Yokohama National University
Doctoral Dissertation

MULTI-ANTENNA SYSTEMS COMMUNICATING THROUGH SUITABLE PROPAGATION PATHS

(適切な伝送路を介して通信を行うマルチアンテナシステム)

A Thesis in
Department of Electrical and Computer Engineering
by
Daisuke Uchida

Submitted in Partial Fulfillment
of the Requirements
for the Degree of

Doctor of Engineering

December 12, 2011

The thesis of Daisuke Uchida was reviewed and approved* by the following:

Hiroyuki Arai
Professor
Thesis Advisor, Chair of Committee

Takehiko Adachi
Professor
Review Committee Member

Toshihiko Baba
Professor
Review Committee Member

Nobuhiro Kuga
Associate Professor
Review Committee Member

Koichi Ichige
Associate Professor
Review Committee Member

*Signatures are on file in the Graduate School.

Perseverance is sure to provide great value.
It may be invisible and hard to quickly notice now.
However, in the future, it will illuminate us with bright light.

Abstract

Communication speed by radio wave has been enhanced, and wired communications have been replaced by wireless communications because of their convenience. We often hear someone talk "Why are high speed communications needed?". He or she thinks that present wireless communications are sufficiently speedy, however, higher speed is still needed. When we consider how informations are efficiently transfered in the limited frequency resources, speeding up is equivalent to high-efficiency. Of course, speeding up is needed for transferring movie, music and image quickly, however, the needs of the speeding up also can be discussed in the view of high-efficiency.

In LTE-Advanced, it is considered that "Heterogeneous network" will be configured. "Heterogeneous network" indicates the combinational network of pico, femto, macrocell, and relay base station. Among them, femtocell base station (BS) is an attractive technology. In femtocell, the coverage area is tens of meter radius, and the BS is located in indoor environments. Since the number of mobile terminals (MTs) accessing femtocell BS is small, comfortable communications without reduction of the speed and without losing connections are achieved. On the other hand, since line capacity is not sufficient for the increase of users in urban area, cellular phone operators want to disperse loads of 3G lines on public W-LAN, which is available in station, airport, cafe and fast food restaurants. Thus, to configure future wireless networks, small-area wireless communications in indoor environments attract much attention.

Then, in LTE and LTE-Advanced, multiple-input multiple-output (MIMO) is a key technology. MIMO technology can enhance communication speed by using multiple antennas on transmitting and receiving sides without expanding frequency band. Hence, it can transmit data efficiently with narrow frequency band. The study of MIMO has been shifted to MU-MIMO, MIMO mesh network, and multihop. However, those researches seem to be at the initiative of software and system, and then it is also important to look toward hardware such as antennas and circuits. This dissertation targets hardware applied to multi-antenna systems, and discussions are focused on single user's communi-

cations, which are the basis for develop researches. As mentioned before, since communications in indoor environments typified by femtocell and W-LAN is an indispensable way to disperse traffic, this dissertation deals with such scenario. Among them, this dissertation specially focuses on indoor base stations and describes the multi-antenna technologies using radiation patterns wisely to improve the performance without increasing the number of streams.

In Chapter 3, channel capacity is introduced as a evaluation factor of MIMO performance, and the relationship between channel capacity, spatial correlation, SNR, received power imbalance, and eigenvalues of spatial correlation matrix are discussed by theory, simulation and measurement. Then, as one example, spatial correlation reduction and channel capacity enhancement by multi-polarization is described. Moreover, just a concept of channel capacity enhancement by SNR increment is shown in this chapter, and the discussion is connected to chapter 4.

Chapter 4 describes the MIMO antenna configuration methodology by using radiation patterns effectively. The discussion is mainly focused on indoor BSs, and the target is enhancement of MIMO performance using fixed radiation patterns. Here, two types of BS positions are assumed, which are BS mounted in the vicinity of wall and at the center of the ceiling. For the former, this dissertation reveals that narrow HPBW of 60°-80° pointed to the corner of the room is effective to obtain large channel capacity by ray-tracing propagation analysis. Based on the design guidelines, a patch antenna array with dual-feeds is fabricated, and then the measurement is conducted in the small room of 6.2 m $\times$ 5.8 m $\times$ 2.7 m. The results shows that the 4 $\times$ 4 MIMO channel capacity is enhanced by about 20% at two out of three typical MT positions, compared to that for sleeve antenna configurations. On the other hand, for the latter, this dissertation presents a low-profile dual-polarized directional MIMO antenna with a thickness of 0.24λ. The antenna is also designed based on guidelines by ray-tracing propagation analysis, and is configured by four cavity-backed slot and four printed dipole antenna elements. Slot and dipole elements radiate vertical and horizontal polarizations, and uni-directional radiation patterns with downward tilt angles are obtained in each polarization. By channel measurements in an actual environment, the SNR and channel capacity are compared with those of the sleeve antenna configuration. The place averaged SNR of the proposed antenna is 14.1 dB, and the improvement factor is 2.6 dB. The place averaged channel capacity of the proposed antenna is 7.1 bits/s/Hz, and improvement factor is 16.2%. The results of this study reveal that the MIMO capacity performance is the same or better than that of the sleeve antenna configuration.

Chapter 5 proposes a novel feeding circuit with switching function of shapes and directions of radiation patterns. First, a technique to realize cardioid and figure of eight radiation patterns is presented. Then, as the modified version, techniques to realize omni-directional and directive radiation patterns are presented. Those techniques are based on array antenna theory, and multi-radiation pattern is generated by switch of feed

elements and phase difference feeding (0°, 180°, -90° and 90°). For the former circuit, the array factors derived from the output signals at 2 GHz shows that two cardioid and two figure of eight radiation patterns are achieved when mutual coupling effects are ignored. When mutual coupling effects are considered, uni-directional with more than 10 dB F/B ratio and bi-directional radiation patterns are obtained. Moreover, the measurement results show that the averaged losses between 1.85 and 2.21 GHz are less than 1.8 dB, and the phase differences agree with simulation data in the vicinity of 2 GHz in the proposed feeding circuit. For the latter, the proposed circuit has five operation modes, and can switch feed to two elements with the phase differences of 0°, 180°, -90° and 90° and feed to a single element. The simulation results show that in all the modes, mismatch losses are less than 0.5 dB, and desired phase differences are obtained at 2 GHz. The output signals lead to the array factor of two cardioid, two figure of eight, and omni-directional radiation patterns. Then, this dissertation reveals that uni-, bi- and omni-directional radiation patterns are obtained in consideration of a combination with a three-element linear monopole array. The variations in the radiation patterns as a function of the frequency are small at 1.88, 2 and 2.06 GHz. Then, since the effect of switching circuits has not been considered in the above simulation and measurement, the design procedures are showed, and the measurement results of the fabricated switching circuit is evaluated. Although frequency shift is caused, good insertion loss and isolation characteristics are observed.

Chapter 6 presents an antenna selection criterion that is suitable for indoor LOS scenarios for two-stream MIMO systems. Since the selection criterion can be applied to algorithm for switching the appropriate radiation patterns, this section is ranked as the system level consideration of chapter 5. In chapter 6, this dissertation demonstrates that the criterion using the square of the absolute value of the determinant of the channel matrix is the most effective one for both BER performance and computational load in an indoor LOS scenario. The investigations of this chapter employ ray-tracing propagation analysis taking into consideration variations in both the amplitude and phase of the channel matrix depending on the selected antenna subsets. The criterion based on the determinant of the channel matrix can be applied to various scenarios, and the effectiveness of the criterion for BER performance is also empirically verified in an actual environment. The computational complexity is lower than criterion based on second eigenvalue, which is target for comparison, and the BER performance is comparable to that.

Table of Contents

Chapter 1

Introduction

1.1 Background

Social trends change at a tremendous speed. In Japan, having a cellular phone has now become quite commonplace, but as little as 15 years ago, most people did not have a cellular phone and the dominant communication tool was a land-line phone. In 1996, the Telecommunications Carriers Association started to disclose information about cellular phone subscribers in the business sector. It reported that the total enrollment was 8,443,800 at the end of January, 1996 [1]. At that time, the pocket pager was popular, with its number exceeding that of cellular phones, being estimated at 10,609,400. However, from around 1996, price reduction and the spread of cellular phones advance rapidly, and the number of cellular phones increased at a rate of ten million. By the end of August, 2011, the total enrollment in Japan was 122,449,400, which signifies a huge change in people's lifestyles.

The history of cellular phones is described. Wireless communication devised by Marconi in 1895 started to be used as an automobile telephone service in America in 1946. Mobile telephone service (MTS) applied to it, and then improved mobile telephone service (IMTS) was introduced in 1964 [2]. However, IMTS was a "pre"-cellular system with service area limited to a radius of 30–40 km. In [3], Kuramoto et al. describe that a "cellular" system with a small radius was first summarized by Bell Laboratory in 1971 [4]. Then, the world's first cellular service was introduced by Nippon Telegraph and

Telephone Public Corporation in Japan in 1979. The demand for using phones outside cars ledto additional Japanese cellular phone services appearing in 1987 [5]. The analog service that was offered at that time is now referred to as the first generation (1G) and was centered on verbal communication. Since the data transmission scheme was based on frequency division multiple access (FDMA), inefficient frequency usage was a problem.

Then, in Japan, digital cellular phone services were introduced by NTT DoCoMo in 1993. This second generation (2G) service included personal digital cellular (PDC) in Japan and the global system for mobile communications (GSM) in Europe. Most wireless communication systems use time division multiple access (TDMA). From the time that the 2G service was offered, cellular phones started to be used for data communication.

Subsequently, third generation (3G) mobile telecommunications complying with the International Mobile Telecommunication 2000 (IMT-2000) standard were introduced by NTT DoCoMo in 2001. Basically, code division multiple access (CDMA) was used in 3G services. Wideband-CDMA (W-CDMA) and the Universal Mobile Telecommunications System (UMTS) used in Japan (NTT DoCoMo and SoftBank) and Europe, respectively, and CDMA2000 developed by Qualcomm, which is used in KDDI, Japan, are included in 3G. As a typical example for NTT DOCOMO, the communication speed was 2.4 kbps in 1993. However, the speed was enhanced to 384 kbps in 2001, allowing the transmission of movies and music and enabling game playing. In 2006, high-speed downlink packet access (HSDPA), with downlink speeds of up to 3.6 Mbps, was introduced as 3.5G. Then, long term evolution (LTE) service ranked as 3.9G, which is called as Xi, started in 2010. Maximum downlink speeds of up to 75 Mbps were developed in some indoor environments. Recently, the use of “smartphone” has spread rapidly, and the fusion of cellular phones and personal computers (PCs) has accelerated.

Now, let us turn our attention from cellular phones to PCs. Nowadays, we can carry on a laptop PC and log onto the Internet without any lines by using a wireless local area network (W-LAN). Even while traveling abroad, we can freely communicate with someone via email, skype, and chat. In 1996, it was doubtful even whether our home had a PC. At that time, the Internet connection speed was slow even with wire lines, and wireless access had not been developed. Although W-LAN started in the early 1980s in America, the main objective was to unwire printer cables, and the transmission rate was less than 9.6 kbps [7]. Then, in 1987, the Federal Communications Commission (FCC)

permitted the private sector to use industrial, scientific, and medical (ISM) bands, which are at 900 MHz, 2.4 GHz, and 5.7 GHz. As a result, vendors made many products and standardization was required to spread the products. In 1990, the IEEE 802.11 working group (WG) began standardization and drew up the first standard (802.11), with a maximum speed of 2 Mbps, in 1997. However, there was a problem of interconnection between products made by different vendors even when the products complied with the standard. Therefore, an industry organization, the Wireless Ethernet Compatibility Alliance (WECA) (later renamed to the Wireless Fidelity (Wi-Fi) Alliance) was set up [8]. Nowadays, we frequently hear the word "Wi-Fi," which refers to the name or brand representing that the Wi-Fi Alliance certificated interconnection between wireless applications in IEEE 802.11a/IEEE 802.11b. Here, IEEE 802.11a and IEEE 802.11b indicate W-LAN standards, which were drawn up in 1999. The IEEE 802.11b and 11a standards set frequencies of 2.4 and 5 GHz, respectively, and maximum speeds of 11 and 54 Mbps, respectively. In 2003, IEEE 802.11g, realizing a maximum speed of 54 Mbps in the 2.4–GHz band, was drawn up, and in 2009, IEEE 802.11n, realizing a maximum speed of 600 Mbps in the 2.4 and 5 GHz bands was drawn up. In 2013, IEEE 802.11ac, with a throughput of over 1 Gbps, will be formulated.

To facilitate easy understanding, the evolution of communication speed is summarized in Fig. 1.1. Over time, the communication speed with radio waves has been enhanced, and wired communications have been replaced by wireless communications because of the convenience of the latter. We often hear someone ask, "Why are higher communication speeds needed?". One might think that the present wireless communication speeds are sufficiently high. However, many researchers think that higher speeds are still needed. As described by Kamatani [9], "Radio waves are a valuable and shared resource because their medium is space. When we consider how to efficiently transfer information using limited frequency resources, speeding up is equivalent to high-efficiency." Of course, increased speed is needed for transferring movies, music, and images quickly; however, these needs can also be discussed from the viewpoint of high-efficiency.

1.2 Future Prospects of Wireless Communications

The fourth generation (4G) is wireless communications complying with IMT-Advanced, which is examined in ITU-R. LTE-Advanced is a standardization proposed to ITU-R by

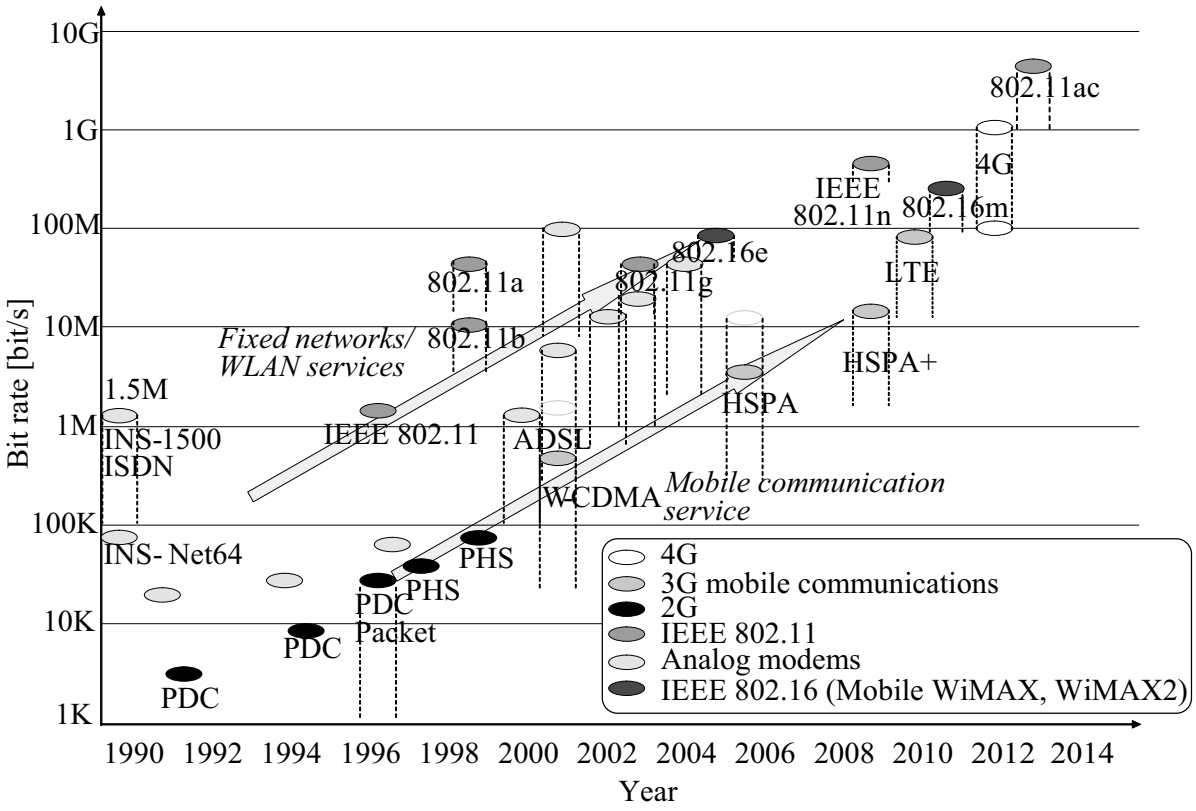

Figure 1.1. Evolution of communication speed (based on [10]). The International Telecommunication Union (ITU) stated that improved 3G systems such as LTE, WiMAX, and HSPA+ can be called 4G in 2010. However, in this figure, they are not categorized as 4G.

the Third-Generation Partnership Project(3GPP) [11]. For IMT-Advanced, 100 Mbps and 1 Gbps are required for high and low mobility, respectively [12], and LTE-Advanced is expected to exceed this requirement. In LTE-Advanced, a "heterogeneous network" (Fig. 1.2) will be configured [13]. A heterogeneous network indicates the combination of picocell, femtocell, macrocell and relay base station [13]–[16]. Networks that connected lines are selected based on time and use applications are also referred to as heterogeneous networks (in cognitive radio) [17]. However, here, we focus only on the former, which has a different cell size. In a heterogeneous network, user terminals communicate using picocell or femtocell networks when possible, and using macrocell networks when not possible.

The advantages of the heterogeneous network are as follows:

1. The throughput in the cell edge and the blind zone are drastically enhanced.

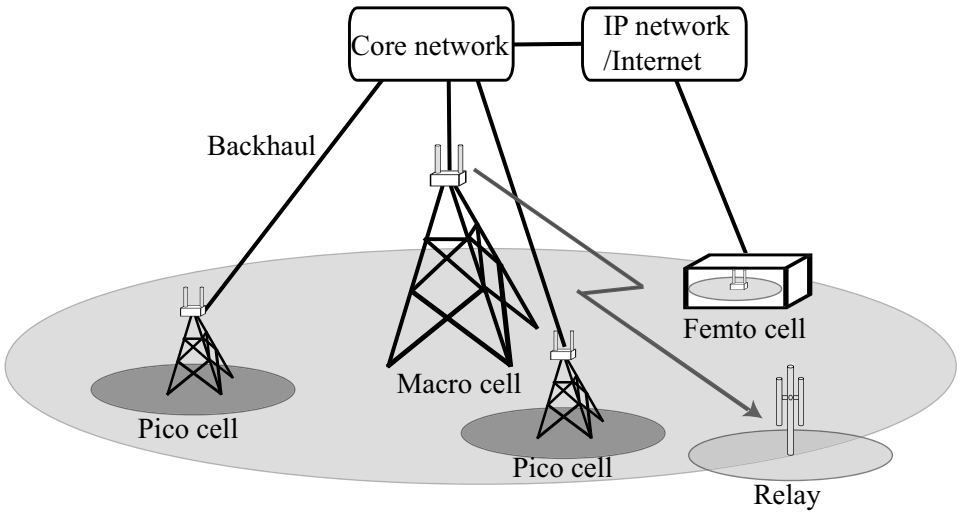

Figure 1.2. Schematic of a heterogeneous network.

2. High-traffic areas can be covered by deploying small base stations (BSs).

3. Low power consumption and low cost are realized by downsizing BSs.

More explanation is in order for item 2 since it is of notable merit. Nowadays, the number of smartphones has dramatically increased, and in August 2010, the MM Research Institute predicted that the number would exceed 40 million in fiscal year 2015 in Japan [18]. Statistical data indicate that traffic for a smartphone is 10 times as high as that for a conventional cellular phone [19]. Let us remember that the available frequency band and the total amount of sendable and receivable data in a fixed time have limitations for the BS. Therefore, the available data amount per mobile terminal is decreased if many smartphones are connected to one BS. In this circumstance, the connection speed becomes slow or the connection cannot be made. This indicates that communication using macrocells could be difficult. Therefore, the recent trend is to employ many BSs covering small areas, each using less output power [19].

One base station scheme generated from this trend is femtocell communication [19]-[21]. A femtocell BS's coverage area is tens of meters in radius, and the BS is located indoors. The femtocell sends or receives data to a core network through broadband lines (Fig. 1.2). Therefore, the traffic load to the wireless network is reduced, and the cost for operation of backhaul lines is suppressed. Since the number of mobile terminals accessing a femtocell BS is small, comfortable communication without the reduction of

speed and lost connections is achieved. Moreover, since line-of-sight (LOS) transmission is realized in indoor environments, the throughput is enhanced.

Meanwhile, since line capacity is not sufficient for the increase in the size of users networks in urban areas, cellular phone operators want to disperse 3G line loads onto public WLANs [22], which are available at train stations, airports, cafes and fast-food restaurants. Thus, to configure future wireless networks, small-area wireless communication in indoor environments is being given much attention.

1.3 Brief Overview of MIMO Systems

In LTE and LTE-Advanced, multiple-input multiple-output (MIMO) is a key technology [23]. MIMO is described briefly here, and the details are described later. MIMO is an attractive technology for enhancing communication speed using multiple antennas on transmitting (Tx) and receiving (Rx) sides without expanding the frequency band. It can transmit data efficiently over a narrow frequency band. In wireless communication, although use of a large frequency band leads to high-speed, the available frequency band is limited. This technology is suitable as a countermeasure of the trade-off between the frequency band and the speed.

The history of MIMO is summarized well in [24]–[27]. In 1995, Telatar derived the MIMO channel capacity based on Shannon's capacity [28] and revealed that the MIMO capacity linearly increased as the rank of the channel was increased in an independent and identically distributed (i.i.d.) Rayleigh fading channel [29]. Then, Foschini proposed a communication architecture to enhance the transmission capacity by spatial multiplexing in 1996 [30]. This scheme is called Bell Laboratories Layered Space-Time (BLAST) or diagonal-BLAST (D-BLAST), and this research became a trigger of subsequent research on MIMO systems. In Bell Laboratories, later, Wolniansky et al. proposed vertical-BLAST (V-BLAST) [31], [32] as a simplified version of D-BLAST, which solved the problem of reduced transmission rate resulting from multiple transmissions of identical signals in D-BLAST. A work by Foschini & Gans [33] published in 1998 and Telatar's work [34] published in 1999 played a big part in evaluations of the MIMO channel capacity, and these papers have been referred to by many MIMO researchers.

Meanwhile, Alamouti [35] and Tarokh [36], [37] proposed a space-time code (STC) as a technique to improve transmission quality in 1998 and 1999. In [35], Alamouti

described that when two transmit and M receive antennas were deployed, it provided a diversity order of $2M$. Here, the diversity order d is defined as the slope of its error probability $P_e(\mathrm{SNR})$ on a log-scale at high signal-to-noise ratio (SNR) regimes [38], and it is given as follows [39]:

$$d = -\lim_{\mathrm{SNR}\to\infty} \frac{\ln P_e(\mathrm{SNR})}{\ln(\mathrm{SNR})} \tag{1.1}$$

For M=2, "full rate" representing a code rate of 1 and "full diversity" representing a diversity order of $2M$ are achieved. Although the SNR was reduced to half, diversity gain (diversity order) by Alamouti's scheme equaled that achieved by a maximal ratio combining (MRC) scheme.

MIMO performance is closely connected with the eigenvalues of the spatial correlation matrix $\mathbf{H}\mathbf{H}^H$, where $\mathbf{H}$ represents a channel response matrix. Here, MRC can be considered as a transmission scheme communicating through only a path of maximum eigenvalue. However, MIMO systems can also generate plural eigenvalue paths (eigenpaths). Therefore, a method of communicating through plural eigenpaths by forming plural beams (eigenbeams) was proposed and examined [40]–[43]. This technique leads to maximum throughput by allocating optimum resources to each eigenbeam.

Because orthogonal frequency division multiplexing (OFDM), which is a modulation scheme with high frequency usage efficiency and large tolerance for frequency selective fading, has a high affinity with MIMO technology, studies of MIMO-OFDM have been conducted [44]–[46]. In fact, MIMO-OFDM is an important technique in recent applications because it is applied to IEEE 802.11n and IEEE 802.16e.

Moreover, a technique called multi-user MIMO (MU-MIMO) [47]–[49] was introduced because there were certain issues with single-user MIMO (SU-MIMO). Generally, since the space required to mount antennas on the BS side is larger than that required on the mobile terminal (MT) side, the number of antenna elements for the BS (N_t) is larger than that for the MT (N_r). In this scenario, downlink communication speed is determined by N_r because MIMO performance depends on the magnitude of $\min(N_t, N_r)$. A solution to this problem is to use multiple MTs with a small number of antenna elements to simultaneously access the BS, so that a large transmission capacity can be achieved by the entire system. This technique is called MU-MIMO, and it will be adapted in the standardization of the next-generation W-LAN, IEEE 802.11ac.

Recently, for example, studies on multihop communication systems, such as MIMO mesh networks [50], multi-cell MIMO (BS cooperation) [51], and near-field MIMO systems with different characteristics from conventional MIMO systems [52], have been conducted. Moreover, as a nontelecommunication application, a sensor system called a "MIMO sensor" [53] has been proposed. Furthermore, studies on security systems using MIMO channels [54] and radar systems using MIMO technologies, referred to as "MIMO radar" [55], have been conducted. Thus, MIMO technologies have been developed, and they have attracted a substantial amount of attention.

1.4 Scope, Objective, and Contributions of the Dissertation

Scope

The study of MIMO has shifted to MU-MIMO, MIMO mesh networks, and multihop communication. However, the research seems to be at the initiative of software and systems, and hence, it is also important to look toward hardware such as antennas and circuits. This dissertation targets hardware applied to multiantenna systems, and discussions are focused on single-user communication, which are the basis for develop research. As mentioned before, since communication in indoor environments typified by femtocells and WLANs is an indispensable method to disperse traffic, this dissertation deals with such scenarios. This dissertation especially focuses on indoor base stations and describes multiantenna technologies using radiation patterns wisely to improve the performance without increasing the number of streams.

Objective

The objective of this dissertation is to present novel multiantenna technologies that utilize radiation patterns wisely. These include the realization of BS enabling high-speed wireless communication and proposed novel radiation-pattern-reconfigurable techniques applied to BSs.

Contributions

The content of this dissertation is divided into two main topics, although this disserta-

tion addresses one united topic: multiantenna technologies that use radiation patterns wisely. The first topic is MIMO systems that utilize radiation patterns effectively. The discussion will focus mainly on

- fabrication of prototype MIMO antennas by using directional antennas effectively and the evaluations in actual environments;
- clarification of suitable design guidelines for radiation patterns in indoor base stations; and
- realization of a low-profile MIMO antenna with good MIMO transmission characteristics.

The second topic is about feeding circuits with the switching function for multiradiation patterns. Discussion of this dissertation will include

- a proposal for a feeding circuit switching function for omnidirectional and directive radiation patterns and
- (related matters (e.g., when the technique of the feeding circuit is expanded to MIMO and actual application is considered)) the clarification of the switching criterion when propagation paths are changed (the details of novelty of this topic are described in Chapter 6).

MIMO Systems that Utilize Radiation Patterns Effectively

MIMO systems are a key technology for the enhancement of communication capacity [56]. For an evaluation of the performance in MIMO systems, the channel capacity has been used as an evaluation index, and many indoor measurement campaigns have been conducted [57]-[60]. When the channel state information (CSI) is unknown on the transmitting side, space division multiplexing (SDM) [61], [62] is the best scheme for obtaining large channel capacity. In this scheme, independent signals with equal power are multiplexed at the same time and frequency.

SDM has been shown to be effective in low-correlation Rayleigh fading channels, such as non-line-of-sight (NLOS) channels [63]. However, the above is evaluated under the condition of a constant received signal-to-noise ratio (SNR). When the transmission power is constant, the received SNR is not constant, and the channel capacity and

bit error rate (BER) have better performance in a LOS environment than in an NLOS environment, despite the higher correlated channel [64], [65]. A high received SNR is effective for achieving large capacity in an LOS environment, i.e., a correlated channel. High received power has been obtained using directional antennas in an appropriate configuration, and the channel capacity obtained using directional antennas was shown to be larger than that obtained using omnidirectional antennas analytically [66], [67] and experimentally [68], [69]. (It is written that low spatial correlation by directional antennas enhances channel capacity in [70]. However, the stance of this dissertation is that the main contribution of directive radiation patterns is to enhance received power or SNR.) Although such evaluations have been conducted for the application of directional antennas to MIMO systems, there is little research on fabricated prototype antennas showing how to use directional antennas effectively and presenting the measured performances.

Here, in addition to a high SNR, low spatial correlation is also a key component with respect to MIMO channel capacity. However, it is difficult to fulfill both of these conditions because the variation between SNR and multipath richness (spatial correlation) is often a trade-off relationship [58], [59]. This indicates that when the radiation patterns are not optimized, directive radiation patterns may lead to the degradation of channel capacity. Therefore, antenna parameters should be optimized along detailed guidelines. To obtain general guidelines, some studies are performed. Quist et al. proposed a method to obtain near-optimal average channel capacity using the stochastic power angular spectrum [71], [72]. Honma et al. proposed a method to obtain an optimum radiation pattern maximizing channel capacity by adjusting the electrical length of parasitic elements in a Yagi-Uda array [73]. However, both schemes need information on channel conditions ahead of time. Although Honma et al.'s [73] scheme reduces the number of necessary measurements of the channel, measuring the channel in typical environments before the fact remains a problem. When a target is confined to indoor BSs, appropriate radiation pattern guidelines are considered to be established without preliminary channel measurement. Such guidelines make antenna design easier for vendors. However, there are no clear design guidelines for indoor BSs.

In the design of MIMO antennas to enhance channel capacity in indoor environments, the main parameters are polarization [74], radiation pattern [72], [73], and array configuration [75]. To this end, MIMO antennas with multipolarization [76], directive radiation patterns [77], and well-configured planar inverted-F antennas (PIFA) [78] have

been proposed. In MIMO antennas, not only high performance but also miniaturization is an important design consideration. For indoor wireless communication in small areas, as typified by femtocell and wireless LAN, BSs are often placed near the ceiling to realize a LOS environment between the BS and the MT. In a BS, compact and low-profile structures are desired for easy installation and improved aesthetics. However, a significant problem in the miniaturization of antennas concerns mutual coupling, as the arrangement of antenna elements with narrow element spacing increases mutual coupling between elements. Although the correlation level is decreased by mutual coupling [79], the radiation efficiency of antennas is also decreased, resulting in a corresponding reduction in channel capacity [80]. As a method to combat mutual coupling, matching networks have been introduced [81]; however, it is difficult to fabricate a matching network with small size, and to effectively realize wide-band matching. Therefore, antenna miniaturization without the reduction of channel capacity has been sought in the design of antenna structures that effectively utilize polarization [82]–[86]. To date, however, few studies have examined miniaturization with the consideration of radiation patterns, particularly the design of low-profile MIMO antennas with directive patterns.

Feeding Circuits with a Switching Function for Multiradiation Patterns

In MIMO systems that utilize radiation patterns effectively, the approach with fixed radiation patterns was considered. In this approach, the general MIMO performance is enhanced, and the same is true of the stochastic approach of [72], [73]. However, upon closer examination, performance degradation is observed at some MT positions, and the stochastic approach is not always sufficient.

In wireless communications, the locations of MTs are usually shifted, and the channel conditions among BSs or access points (APs) and MTs are varied. Since the optimum radiation patterns depend on the propagation channels, the radiation pattern should be changed when the propagation characteristics rapidly degrade. From a different standpoint, these pattern changes are effective in suppressing fading effects and in sustaining a high SNR and low spatial correlation since the propagation path of a radio wave can be changed. Although digital beam forming (DBF) [87] leads to appropriate radiation pattern flexibility, it requires an analog to digital (A/D) converter circuit, a radio-frequency (RF) amplifier circuit, and frequency conversion circuitry with respect to each antenna element [88]. One solution is to use radiation pattern controls at RF stages, and analog

techniques using parasitic elements have been examined in [89], [90]. Such controls were proposed in [91], and involve adjusting the electrical length of parasitic elements. However, for the varactor-diode commonly used to adjust the electrical length [92], a high direct current (DC) voltage supply and variable voltage controls are needed to obtain the desired radiation patterns in some cases.

Analog pattern controls using phase difference feeds have been proposed in [93], [94]. These approaches are based on the Butler matrix [95], in which only hybrid circuits, fixed phase shifters and switches are used. DC biases are required to switch ON and OFF states when the PIN diode is assumed as a switching element. However, the voltage level required for the operation is not high, and the operation for the DC voltage supply is simpler than for the varactor-diode because only two states are switched.

Thus, there are typical types [94] of analog pattern controls, with the former and the latter categorized as "adaptive" and "switched beam" types, respectively. In the "switched-beam" types, there are restrictions for the realizable patterns. For example, although Butler-matrix-based techniques in [93]–[95] can change the direction of the beams, they cannot change the shapes of the beams. When MIMO is assumed as an application, the optimum radiation patterns are not identical in different usage environments and statuses of use [96], [97]. Hence, the shapes of the radiation patterns also need to be changed.

When pattern-reconfigurable techniques are viewed in a slightly broader context, it is noted that various pattern-reconfigurable antennas have been proposed. For diversity applications, an antenna providing an omnidirectional or a directional pattern by switches was proposed in [98]. An antenna that switches the direction of its main beams based on the principle of the Yagi-Uda antenna was proposed in [99]. For MIMO applications, an antenna consisting of two L-shaped slots was proposed in [100]; here, the direction of the radiation pattern was changed by switching the current path. In [101], a MIMO antennas with two reconfigurable microstrip dipole antennas was proposed, and the change in the dipole length led to a level change in the directive pattern. However, there have been few antennas with a switching function for omni-, uni-, and bidirectional radiation patterns. Moreover, there are also few antennas capable of changing both the direction and the shape of the radiation patterns.

1.5 Organization of the Dissertation

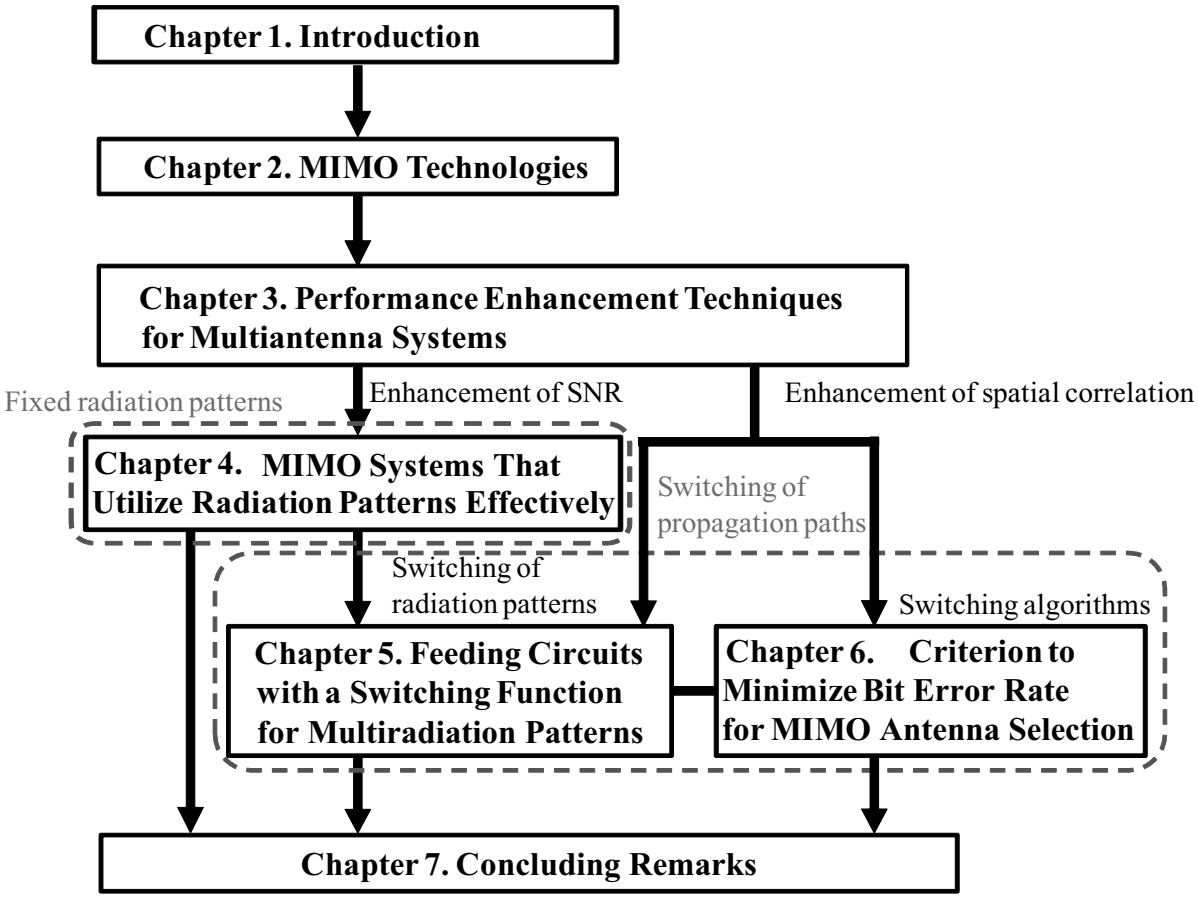

Figure 1.3. Organization of the dissertation.

The remainder of this dissertation is organized as illustrated in Fig. 1.3. Chapter 2 presents an overview of MIMO technologies, including the explanations on MIMO spatial division multiplexing, formulation of MIMO systems, signal processing on the receiving side, and a MIMO testbed used for channel measurements.

In Chapter 3, channel capacity is introduced as an evaluation factor of MIMO performance, and the relationships among channel capacity, spatial correlation, SNR, received power imbalance, and eigenvalues of the spatial correlation matrix are discussed using theory, simulations, and measurements. Generally, channel capacity enhancement is divided into spatial correlation reduction and SNR enhancement. Hence, as one example of the reduction of spatial correlation, measurement-based performance evaluation of

multipolarization is described. For SNR enhancement, only the concept is presented in this chapter, and the discussion is connected to Chapter 4. Chapter 3 is positioned as a basis for the subsequent chapter.

Chapter 4 describes the MIMO antenna configuration methodology that use radiation patterns effectively. The discussion is mainly focused on indoor BSs, and our target is the enhancement of MIMO performance using fixed radiation patterns. First, this chapter describes the BS mounted in the vicinity of a wall, and introduces a two-element patch antenna array with dual feeds, which is designed based on ray-tracing propagation analysis. Second, this chapter describes the BS mounted in the center of the ceiling. Here, a unidirectional, dual-polarized MIMO antenna with a thickness of 0.24λ is proposed on the basis of the design guidelines. This antenna consists of dipole antennas mounted horizontal to the ground plane and cavity-backed slot antennas for vertical polarization. In this chapter, a lower profile BS antenna is also discussed, and the result of investigations on a MIMO handset antenna are also presented.

Chapter 5 proposes a novel feeding circuit with a switching function for shapes and directions of radiation patterns. Since the proposed scheme does not lead to radiation patterns with a high gain, the goal is not to enhance SNR but to prevent SNR reduction. Therefore, when the contents of this chapter are connected with Chapter 3, the proposed scheme is positioned as a technique to reduce spatial correlation. This chapter is also related to Chapter 4. In Chapter 4, channel capacity enhancement by fixed radiation patterns is explored, and then by this approach, general MIMO performance is shown to be enhanced. However, on closer examination, performance degradation is observed at some MT positions, and the stochastic approach is not always sufficient. Therefore, this chapter also presents one countermeasure against the problems relating to Chapter 4.

Chapter 6 presents an antenna selection criterion that is suitable for indoor LOS scenarios for two-stream MIMO systems. The antenna selection is categorized as a technique to reduce spatial correlation by changing propagation paths when the contents of this chapter are linked with Chapter 3. Moreover, this chapter is also associated with Chapter 5, which explores a novel techniques for switching radiation patterns. Since the selection criterion can be applied to an algorithm for switching the appropriate radiation patterns, this section is ranked as a system-level consideration. Finally, concluding remarks are presented in Chapter 7.

Chapter 2

MIMO Technologies

This chapter presents an overview of MIMO technologies. First, an explanation of MIMO spatial division multiplexing is provided by categorizing MIMO systems. Then, MIMO systems are formulated and signal processing on the receiver side is described. These descriptions are mainly based on [27]. Finally, this chapter describes a MIMO testbed used for the channel measurements.

2.1 MIMO Spatial Multiplexing

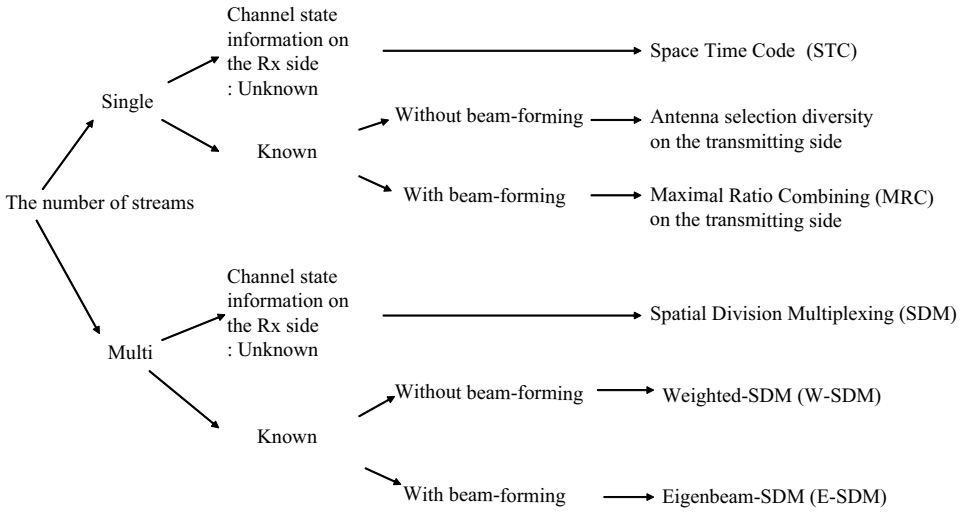

Figure 2.1. Classification of MIMO systems.

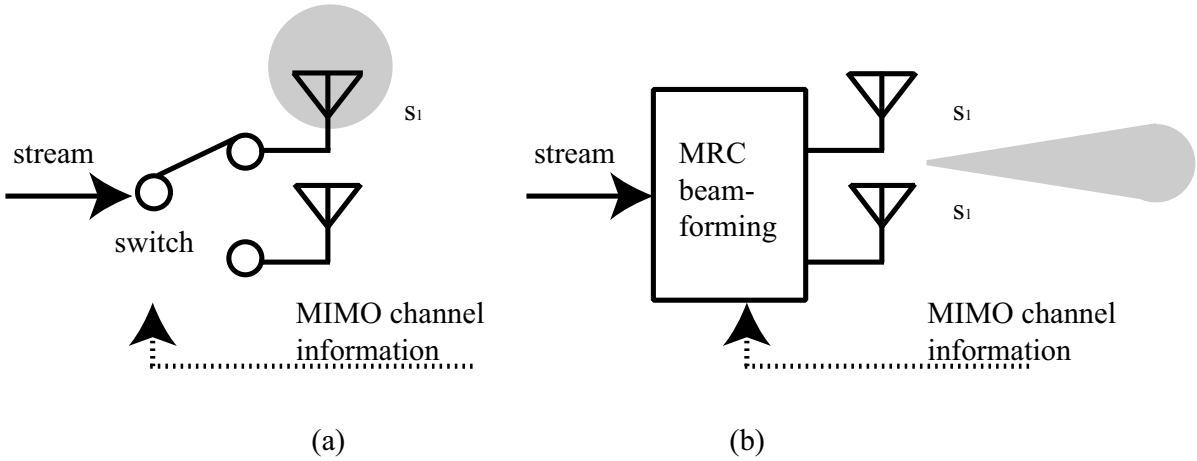

Figure 2.2. Transmission diversity. (a) Antenna selection diversity and (b) maximal ratio combining (MRC).

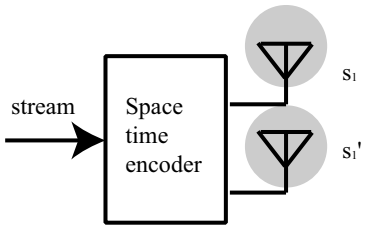

Figure 2.3. Space time code (STC).

MIMO systems are categorized by the transmitting scheme shown in Fig. 2.1. The transmitting signal is called a "stream," and the category is based on whether the number of streams is single or multiple, whether the CSI is known or unknown on the transmitting side, and whether the signal transmission is with or without beam-forming. Here, a single stream means that the number of simultaneous parallel transmission signals is one even when using multiple antennas. Multistream means that the number of signals is two or more. As a next step, the details of single stream MIMO transmission are explained. When the CSI is known on the transmitting side, transmitting schemes include antenna selection diversity (Fig. 2.2(a)) and MRC (Fig. 2.2(b)). In the former, an antenna transmitting a stream is selected from multiple transmitting antennas, and in the latter, a single beam is formed by adjusting the phase and amplitude of the signals, and high SNR is achieved. When the CSI is unknown on the transmitting side, the STC scheme is used (Fig. 2.3). In this scheme, encoding is conducted to transmit

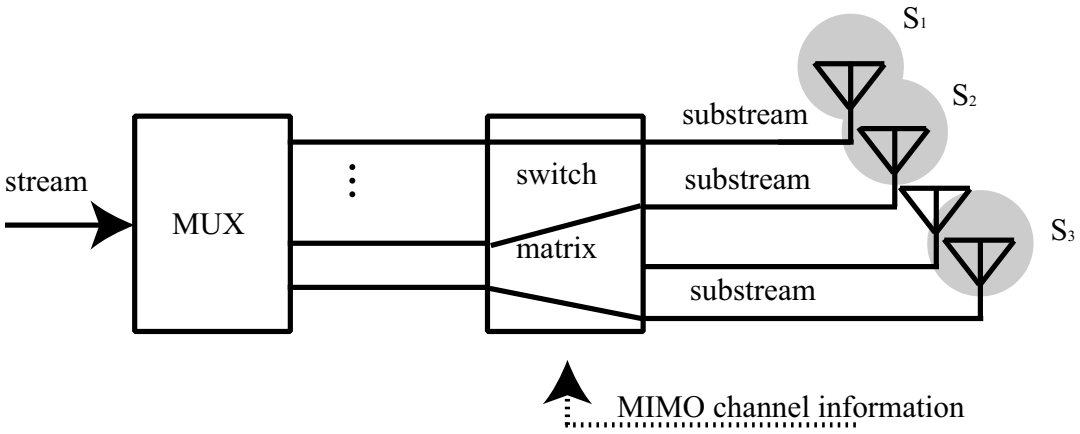

Figure 2.4. Weighted space division multiplexing (W-SDM).

information in transmitting streams from all the antennas. Although different signals are transmitted simultaneously, the number of streams is one. The scheme's objective is to realize highly-dependable communications.

In contrast, the objective of multistream transmission is to enhance the transmission rate. When the CSI is known on the transmitting side, transmitting schemes such as weighted space division multiplexing (W-SDM) (Fig. 2.4) and eigenbeam space division multiplexing (E-SDM) (Fig. 2.5) are used. In the former, K elements are selected from N_t elements, and signals are transmitted by adjusting the transmitting power. In the latter scheme, a multibeam is generated according to conditions of the MIMO channel, and transmitting power control is conducted in each beam. This scheme achieves maximum channel capacity. When the CSI is known on the transmitting side, SDM (Fig. 2.6) is used. In this scheme, substreams with identical transmitting power are transmitted from the antennas. Here, the substream indicates the stream divided into multiplex signals spatially, as shown in Fig. 2.4. My target is SDM without beam-forming, and my approach is to enhance the performance using physical techniques instead of signal processing.

2.2 Formulation of MIMO Systems

The basic model of a MIMO system is shown in Fig. 2.7. In this figure, the numbers of transmitting and receiving antennas are denoted by N_t, and N_r, respectively. A signal

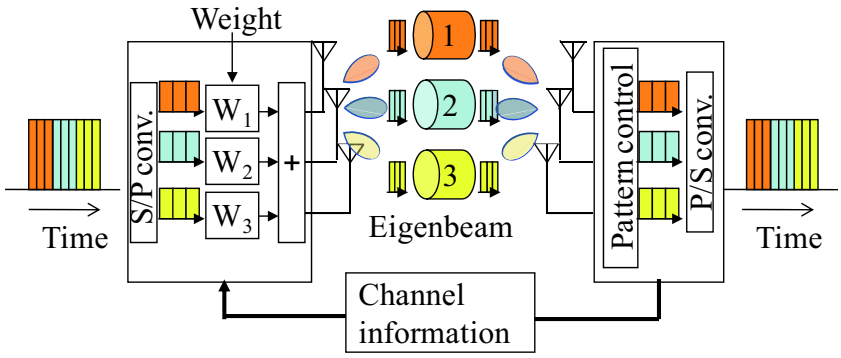

Figure 2.5. Eigenbeam space division multiplexing (E-SDM).

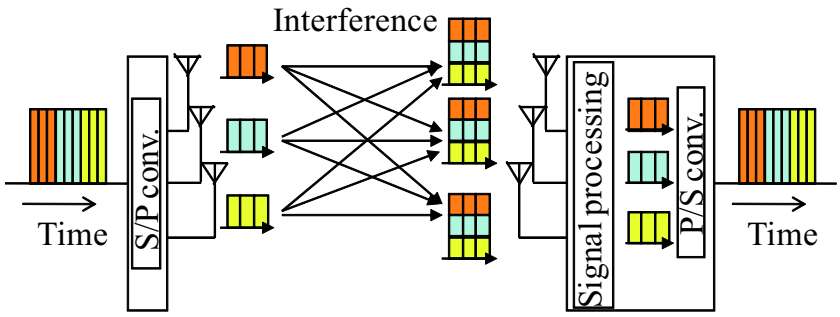

Figure 2.6. Space division multiplexing (SDM).

transmitted at $t = mT$ (where T is the number of symbols) is represented by $s_k(m)$, and then a signal multiplied by a "weight" is represented by $x_j(m)$, where "weight" is used to control phase and amplitude. When the receiving signals and noise are represented by $y_i(m)$ and $z_i(m)$, respectively, the following relationship is satisfied:

$$\begin{aligned} \mathbf{y}(m) &= [y_1(m), y_2(m), ..., y_{N_r}(m)]^T \\ &= \sum_{l=0}^{L-1} \mathbf{H}(l)\mathbf{x}(m-l) + \mathbf{z}(m) \end{aligned} \tag{2.1}$$

where

$$\mathbf{x}(m) = [x_1(m), x_2(m), ..., x_{N_r}(m)]^T \tag{2.2}$$

$$\mathbf{z}(m) = [z_1(m), z_2(m), ..., z_{N_r}(m)]^T \tag{2.3}$$

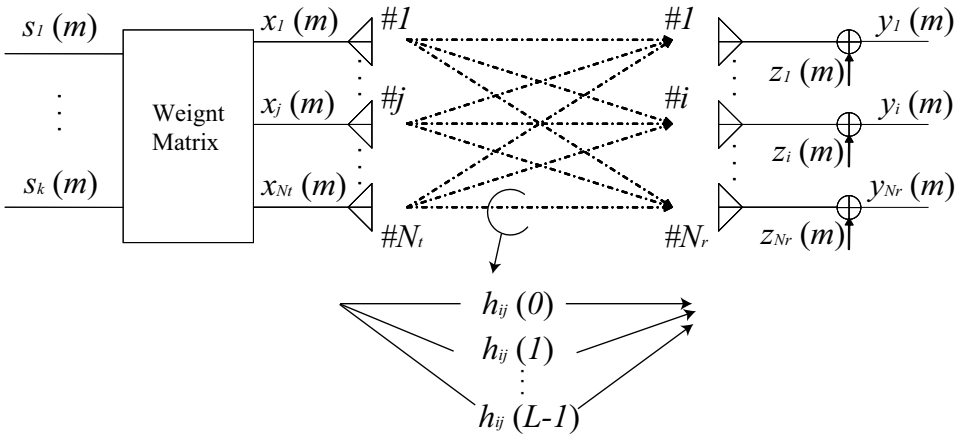

Figure 2.7. Basic model of a MIMO sytem.

Here, each component of the noise vector is an independent complex Gaussian process with average 0 and dispersion $2\sigma^2$. The ensemble average $E[\cdot]$, in terms of $\mathbf{I}_{N_r}$, the N_r $\times$ N_r identity matrix, is given by

$$E[\mathbf{z}(m)\mathbf{z}^H(m)] = 2\sigma^2\mathbf{I}_{N_r} \tag{2.4}$$

$\mathbf{H}(l)$ is an $N_r \times N_t$ channel response matrix, and it is represented by

$$\mathbf{H}(l) = \begin{bmatrix} h_{11}(l) & \cdots & h_{1N_t}(l) \\ & \ddots & \\ \vdots & h_{ij}(l) & \vdots \\ & & \ddots \\ h_{N_r1}(l) & \cdots & h_{N_rN_t}(l) \end{bmatrix} \tag{2.5}$$

Here, $h_{ij}(l)$ is a channel response in the l symbol delay wave from the jth transmitting antenna to the ith receiving antenna. Given a flat-fading channel without delay paths, (2.1) and (2.5) can be simplified, and the following equation is derived:

$$\mathbf{y}(m) \;=\; \mathbf{H}(0)\mathbf{x}(m) + \mathbf{z}(m) \tag{2.6}$$

where

$$\mathbf{H}(0) = \mathbf{H} = \begin{bmatrix} h_{11} & \cdots & h_{1N_t} \\ & \ddots & \\ \vdots & h_{ij} & \vdots \\ & & \ddots \\ h_{N_r1} & \cdots & h_{N_rN_t} \end{bmatrix} \tag{2.7}$$

In SDM, spatially multiplexed signals cause interference on the receiving side, and hence, desired signals should be detected from multiple incoming waves. On the transmitting side, the data inputted to the transmitter are divided into multiple streams $(s_1(m), \ldots, s_{N_t}(m)$ in Fig. 2.7). Since the weight is not multiplied in SDM, the following relationship is satisfied between $\mathbf{s}(m)$ and the transmitting signal $\mathbf{x}(m)$:

$$\mathbf{x}(m) = \mathbf{s}(m) \tag{2.8}$$

2.3 Signal Processing on the Receiving Side

On the receiving side, desired signals are detected using the estimated channel matrix $\mathbf{H}$ as a weight. This section describes zero-forcing (ZF) and minimum mean-square-error (MMSE) algorithms, which are signal detection schemes by linear processing.

2.3.1 The ZF Algorithm

The ZF algorithm is a kind of spatial filtering, in which interference between substreams is completely eliminated. Spatial filtering is also called a adaptive array, and spatial filtering can select signal spatially by pointing strong beams to desired signals or null to undesired signals. In SDM, N_t signals are simultaneously transmitted, and the configuration of the spatial filter to extract jth signals is shown in Fig. 2.8.

When the weight vector $\mathbf{w}_j$ configured by N components is denoted by

$$\mathbf{w}_j = [w_{j,1}, w_{j,2}, \ldots, w_{j,N_r}]^T \tag{2.9}$$

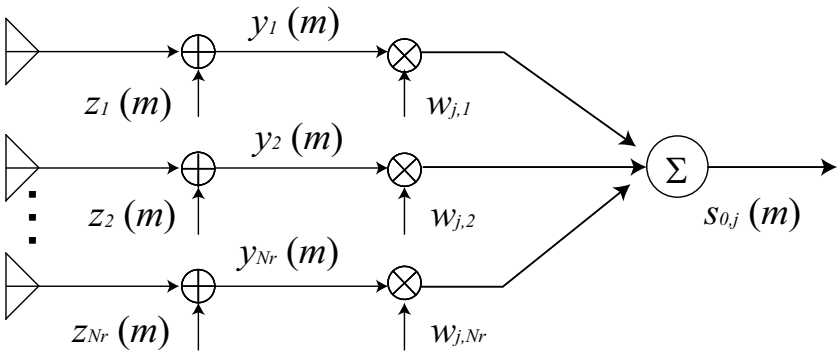

Figure 2.8. Adaptive array.

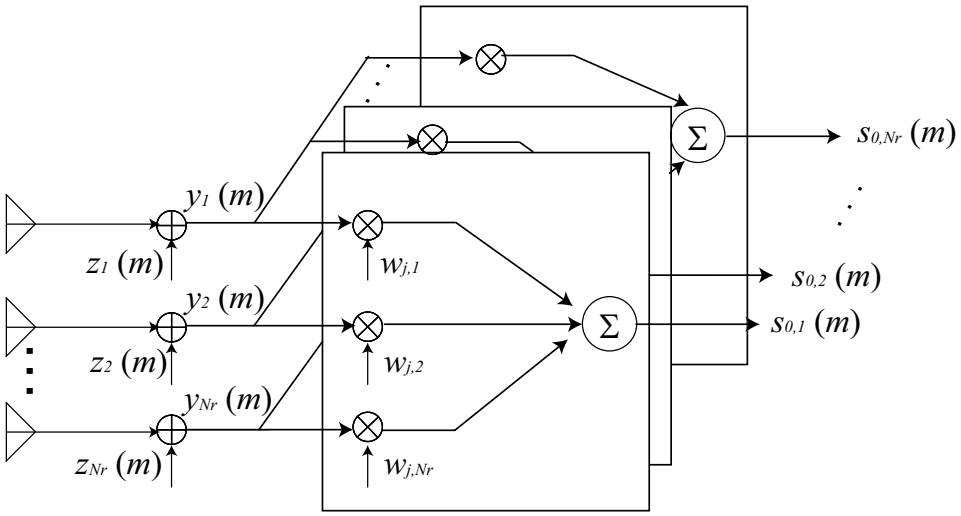

Figure 2.9. Multibeam adaptive array.

the output signal from the spatial filter is given by

$$s_{0,j}(m) = \mathbf{w}_j^T \mathbf{y}(m) \tag{2.10}$$

A spatial filter extended to extract N_t signals is shown in Fig. 2.9. The equation is derived by extending (2.10) to the matrix,

$$\mathbf{s}_0(m) = [s_{0,1}(m), s_{0,2}(m), \ldots, s_{0,N_t}]^T = \mathbf{W}_j^T \mathbf{y}(\mathbf{m}) \tag{2.11}$$

where weight matrix $\mathbf{W}$ is given as follows:

$$\mathbf{W} = \begin{bmatrix} w_{1,1} & \cdots & w_{N_t,1} \\ & \ddots & \\ \vdots & w_{j,i} & \vdots \\ & & \ddots \\ w_{1,N_r} & \cdots & w_{N_t,N_r} \end{bmatrix} \tag{2.12}$$

The ZF and MMSE algorithms are schemes to derive $\mathbf{w}_j$ or $\mathbf{W}$. When (2.6) is substituted into (2.11), and noise is ignored, the following equation is derived:

$$\begin{aligned} \mathbf{s}_0(m) &= \mathbf{W}^T\mathbf{y}(m) \\ &= \mathbf{W}^T\mathbf{H}\mathbf{x}(m) + \mathbf{W}^T\mathbf{z}(m) \\ &= \mathbf{W}^T\mathbf{H}\mathbf{s}(m) + \mathbf{W}^T\mathbf{z}(m) \\ &= \mathbf{W}^T\mathbf{H}\mathbf{s}(m) \end{aligned} \tag{2.13}$$

The ZF algorithm is the method to derive a weight matrix satisfying $\mathbf{s}_0(m) = \mathbf{s}(m)$ in (2.13). When the number of transmitting and receiving antennas is identical, $\mathbf{W}^T$ is given by

$$\mathbf{W}^T = \mathbf{H}^{-1} \tag{2.14}$$

When the number of transmitting and receiving antennas is not identical, $\mathbf{W}^T$ is given using the Moore-Penrose generalized inverse matrix,

$$\mathbf{W}^T = \mathbf{H}^+ = (\mathbf{H}^H\mathbf{H})^{-1}\mathbf{H}^H \tag{2.15}$$

Thus, desired signals are detected by multiplying the weight derived from the estimated $\mathbf{H}$. Note that spatial filtering can eliminate a maximum of $N_r - 1$ interference signals, which is called the degree of freedom of the array. Therefore, interference signals cannot be eliminated completely in $N_r < N_t$.

2.3.2 The MMSE Algorithm

In the ZF algorithm, noise is ignored and then the weight is derived. In the MMSE algorithm, the weight is derived by minimizing the mean square error between the output signal from the spatial filter including noise ($s_{0,j}(m)$ in (2.10)) and the desired signal $s_j(m)$. The weight vector $\mathbf{w}_{m,j}$ is given by the Wiener solution as follows [102]:

$$\mathbf{w}_{m,j} = \mathbf{R}_{yy}^{-1}\mathbf{r}_{ys_j} \tag{2.16}$$

where $\mathbf{R}_{yy}$ is an autocorrelation matrix of $\mathbf{y}$, and $\mathbf{r}_{ys_j}$ is a mutual correlation vector between $\mathbf{y}$ and s_j. Hence, (2.16) is transformed as follows:

$$\begin{aligned}
\mathbf{w}_{m,j} &= \left(E[\mathbf{y}^*(m)\mathbf{y}^T(m)]\right)^{-1}E[\mathbf{y}^*(m)s_j(m)] && (2.17)\\
&= \left(\mathbf{H}^*E[\mathbf{s}^*(m)\mathbf{s}^T(m)]\mathbf{H}^T + E[\mathbf{z}^*(m)\mathbf{z}^T(m)]\right)^{-1}\left(\mathbf{H}^*E[\mathbf{s}^*(m)s_j(m)]\right) && (2.18)\\
&= \left(\frac{P_x}{N_t}\mathbf{H}^*\mathbf{H}^T + P_z\mathbf{I}\right)^{-1}\left(\mathbf{H}^*\frac{P_x}{N_t}\mathbf{e}_j\right) && (2.19)\\
&= \left(\frac{P_x}{N_t}\mathbf{H}^*\mathbf{H}^T + P_z\mathbf{I}\right)^{-1}\left(\frac{P_x}{N_t}\mathbf{h}_j^*\right) && (2.20)\\
&= \left(\mathbf{H}^*\mathbf{H}^T + \frac{N_t\mathbf{I}}{P_x/P_z}\right)^{-1}\mathbf{h}_j^* && (2.21)
\end{aligned}$$

where (2.6) and (2.8) are substituted into (2.17). P_x, P_z, and $\mathbf{I}$ represent the total transmitting power, the noise level, and the identity matrix, respectively. $\mathbf{e}_j$ is a column vector with 1 in the jth component and 0 in the other components. Then, the weight matrix $\mathbf{W}_m$ is given by

$$\begin{aligned}
\mathbf{W}_m &= [\mathbf{w}_{j,1}, \mathbf{w}_{j,2}, \ldots, \mathbf{w}_{j,N_t}] && (2.22)\\
&= \left(\mathbf{H}^*\mathbf{H}^T + \frac{N_t\mathbf{I}}{P_x/P_z}\right)^{-1}[\mathbf{h}_1, \mathbf{h}_2, \ldots, \mathbf{h}_{N_t}]^* && (2.23)\\
&= \left(\mathbf{H}^*\mathbf{H}^T + \frac{N_t\mathbf{I}}{P_x/P_z}\right)^{-1}\mathbf{H}^* && (2.24)
\end{aligned}$$

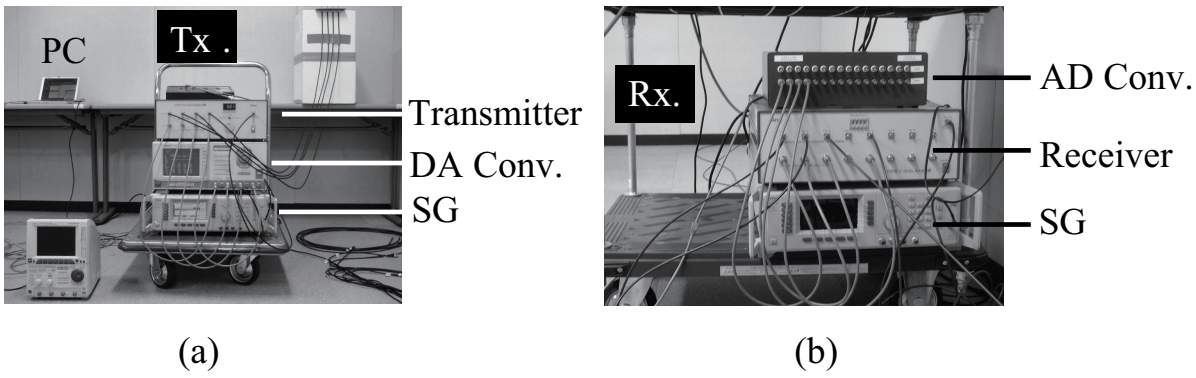

Figure 2.10. Measurement systems at the transmitting side and receiving side, respectively.

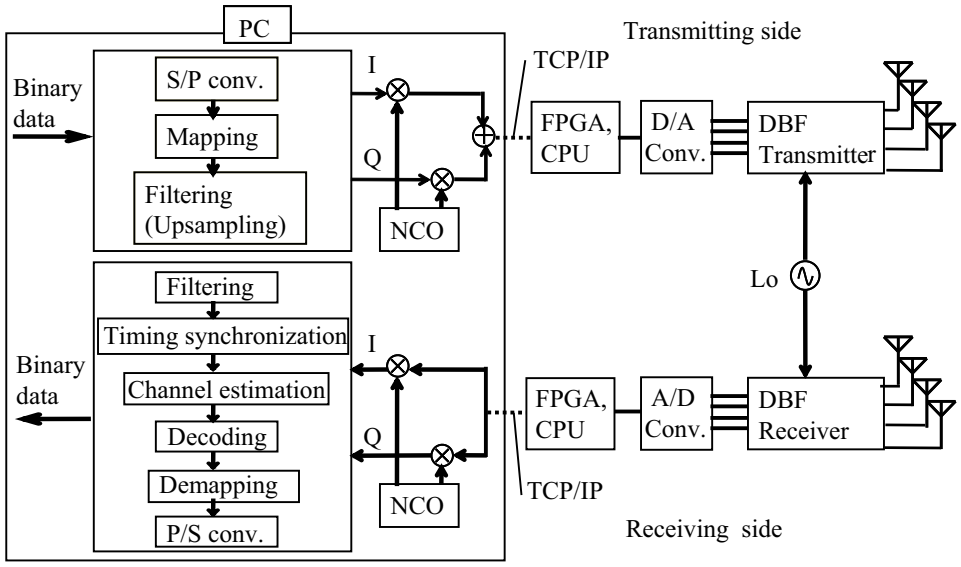

Figure 2.11. Block diagram of the measurement systems.

2.4 MIMO Testbed

This section presents the measurement system to evaluate MIMO performance in an actual environment [103]–[106]. Figures 3.22(a) and 3.22(b) show the photographs of the transmitting and receiving sides, respectively, and Fig. 2.11 depicts the block diagrams.

On the transmitting side, baseband signals and intermediate frequency (IF) signals with a frequency of 10.7 MHz are generated on a PC. Signals consist of header and data,

Table 2.1. Specification of the measurement system.

RF part	Carrier frequency	2〜8 GHz (tunable)
	IF frequency	1st:10.7MHz, 2nd:160.7MHz(transmitter) 1st:160MHz, 2nd:40MHz(receiver)
	Bandwidth	5MHz
	Gain control	0〜-20dB
	Phase control	±90°
Digital part	D/A converter	DAC904 (Burrbrown), 100MHz 14bit (D/A)
	A/D converter	AD9245 (Analog Device), 32MHz, 14bit (A/D)
	FPGAs	ALTERA STRATIX EP1S40(1020pins, 773 I/O) 1 Mega Gates, 3,423,744 memory bits
	CPU	HITACHI SH4, 200 MHz, 360 MIPS, 1.4 GFLOPS
	SDRAM	S133-512MZ (I-O DATA), 512MB

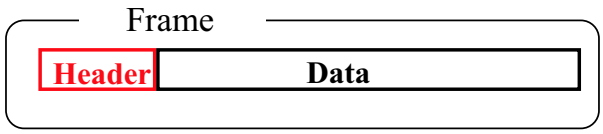

Figure 2.12. Frame format.

and the header is composed of maximum-length sequences (M-sequences). After digital-to-analog (D/A) conversion and two-staged frequency up-conversion in the transmitter, RF signals are simultaneously transmitted from the multiple transmitting antennas. Hence, mutual couplings between antennas must be considered.

On the receiving side, IF signals with a frequency of 8 MHz are obtained after two-staged frequency down-conversion in the receiver and sampling by A/D converters. Then, they are returned to the PC. Timing-synchronization, channel estimation, and demodulation are performed with off-line processing. The specifications of the measurement system are summarized in Table 2.4.

The channel estimation scheme on the receiving side is described next. In this measurement system, as previously explained, the transmitting frame format consists of a header part using M-sequences [107] and a data part (Fig. 2.12). M-sequences with 2^m-1 bits/period are generated by an m stage linear shift register, and the M-sequence for $m = 4$ is shown in Fig. 2.13 as an example.

Channel responses are estimated using a complex sliding correlation. In this scheme, the correlation coefficient (cor_i) between received and reference signals (M-sequences

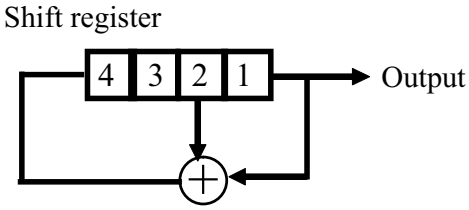

Clock	Shift register				Output
	4	3	2	1	
0	1	0	0	0	
1	0	1	0	0	0
2	0	0	1	0	0
3	1	0	0	1	0
4	1	1	0	0	1
5	0	1	1	0	0
6	1	0	1	1	0
7	0	1	0	1	1
8	1	0	1	0	1
9	1	1	0	1	0
10	1	1	1	0	1
11	1	1	1	1	0
12	0	1	1	1	1
13	0	0	1	1	1
14	0	0	0	1	1
15	1	0	0	0	1

Figure 2.13. Four-step shift register and M-sequences generated from it.

identical to the header part) is derived by a sliding reference signal by one sample (Fig. 2.14). Here, the reference signal is denoted by $\mathbf{r}$, and the received signal extracted to be the same length as the reference signals from the ith sample is denoted by $\mathbf{y}_i$; the correlation coefficient between these is given by

$$cor_i = \frac{\mathbf{y}_i \cdot \mathbf{r}^*}{\sqrt{(\mathbf{y}_i \cdot \mathbf{y}_i^*)(\mathbf{r} \cdot \mathbf{r}^*)}} \tag{2.25}$$

In this process, the autocorrelation characteristic changes rapidly when the position of the reference symbol accords with the header symbol, as shown in Fig. 2.14. Therefore, the head of the frame is detected, and then, the channel response is estimated. Here, the peak correlation coefficient and received signal vectors when the peak value is achieved are denoted by *cor* and $\mathbf{y}_p$, respectively. Since transmitting and receiving signals are

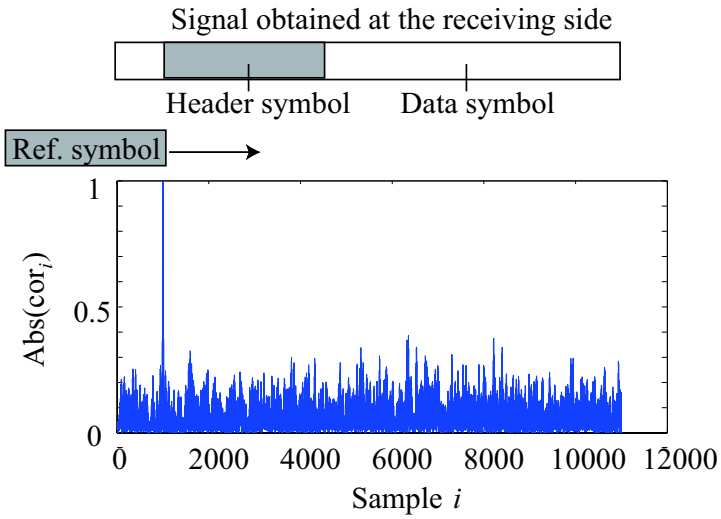

Figure 2.14. Correlation coefficient obtained by a complex sliding correlation.

related by (2.6) and (2.8), the following equation is satisfied:

$$\mathbf{y}_p = H\mathbf{r} + \mathbf{n} \tag{2.26}$$

where H is the channel response in single-input single-output (SISO). When the equation is solved for H by ignoring the noise and multiplying to both sides of (2.26) by $\mathbf{r}$, the following relationship is obtained:

$$H = \frac{\mathbf{r} \cdot \mathbf{y}_p}{|\mathbf{r}|^2} \tag{2.27}$$

Then, the following equation is obtained from the correlation coefficient *cor* and the standard variations σ_r, and σ_{y_p} of $\mathbf{r}$ and $\mathbf{y}_p$:

$$\begin{aligned} cor \times \frac{\sigma_{y_p}}{\sigma_r} &= \frac{\sum_{i=1}^{n}(r_i - \overline{r})(y_{p,i} - \overline{y_p})}{\sqrt{\sum_{i=1}^{n}(r_i - \overline{r})^2}\sqrt{\sum_{i=1}^{n}(y_{p,i} - \overline{y_p})^2}} \times \frac{\frac{1}{n}\sqrt{\sum_{i=1}^{n}(y_{p,i} - \overline{y_p})^2}}{\frac{1}{n}\sqrt{\sum_{i=1}^{n}(r_i - \overline{r_i})^2}} \\ &= \frac{\sum_{i=1}^{n}(r_i - \overline{r})(y_{p,i} - \overline{y_{p,i}})}{\sum_{i=1}^{n}(r_i - \overline{r_i})^2} \approx \frac{\sum_{i=1}^{n} r_i \times y_{p,i}}{\sum_{i=1}^{n} {r_i}^2} = \frac{\mathbf{r} \cdot \mathbf{y}_p}{|\mathbf{r}|^2} \end{aligned} \tag{2.28}$$

where $\overline{r}$ and $\overline{y_p}$ represent the average values of $\mathbf{r}$ and $\mathbf{y_p}$, respectively. In this equation, it was assumed that $\overline{r} = \overline{y_p} \approx 0$. n is the length of the reference signal and the header

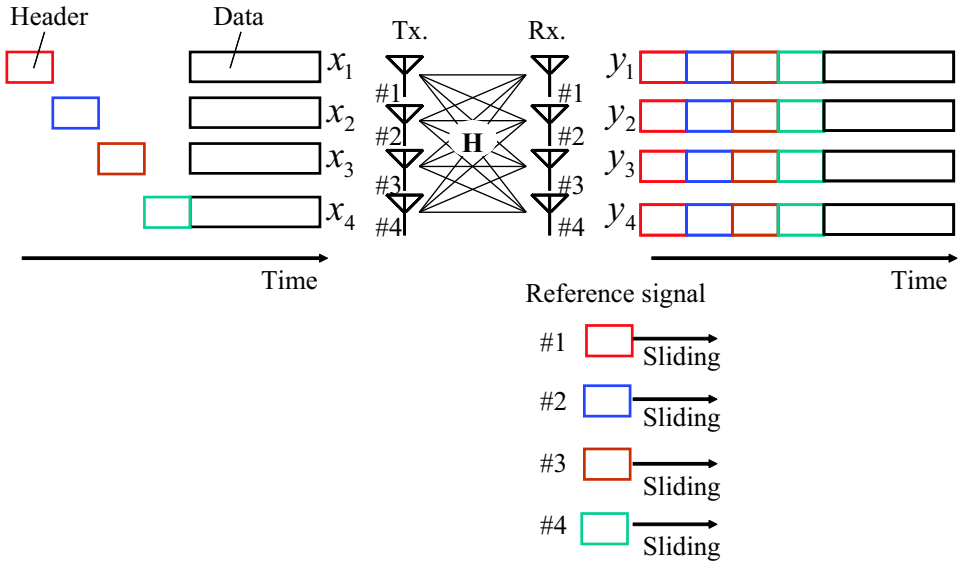

Figure 2.15. Sliding correlation coefficient in a 4 × 4 MIMO system.

part. From (2.28) and (2.29), H is estimated as

$$H = cor \times \frac{\sigma_{y_p}}{\sigma_r} \tag{2.29}$$

As a next step, an estimation method for the MIMO channel using a 4 × 4 MIMO is explained as an example (Fig. 2.15). The header symbol transmitted from each antenna is different, and these are not temporally-overlapped. On the receiving side, four reference signals identical to the header are transmitted from each transmitting antenna. For example, when a complex sliding correlation is applied to y_1 using reference signal #1, h_{11} can be estimated. In a similar way, when it is applied to y_2, y_3, and y_4, h_{21}, h_{31} and h_{41} can be estimated. The combinations of received and reference signals required to estimate each channel response are summarized in Fig. 2.16.

Figure 2.17(a) shows the correlation coefficient obtained by a complex sliding correlation using reference signal #1, which is based on measurement data. Since the peaks appear in this figure, the head of the frame is detected. Figure 2.17(b) shows the constellation pattern of $\mathbf{y}_1$. Since the transmitting signal modulated by quaternary phase-shift keying (QPSK) can be demodulated, the adequacy of the measurement system is confirmed.

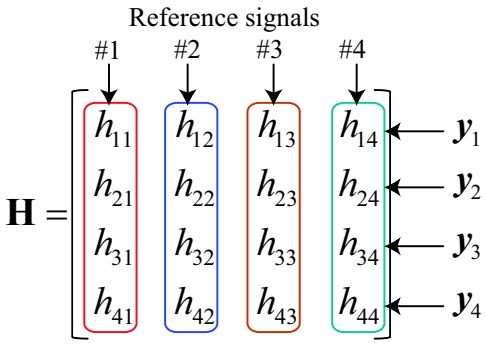

Figure 2.16. Combinations of received and reference signals required to estimate channel response.

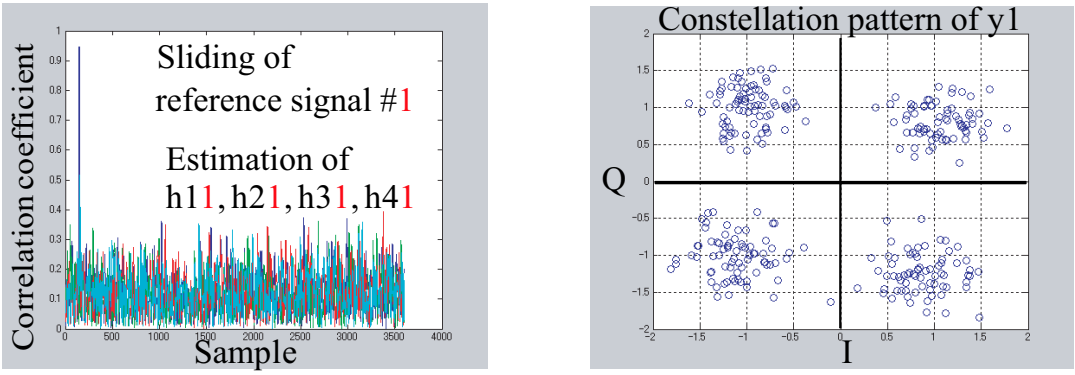

Figure 2.17. (a) Complex sliding correlation based on measurement data, and (b) constellation pattern after signal detection on the receiving side.

Chapter 3

Performance Enhancement Techniques for Multiantenna Systems

3.1 Introduction

Many studies have been conducted to optimize MIMO systems, and the enhancement of channel capacity by altering radiation pattern [72], using multipolarization [74], efficiently configuring antennas [76], and introducing decoupling networks [81] have been reported.

With respect to channel capacity, many theoretical examinations were performed [108]-[112]. In MIMO-SDM, the channel capacity depends on the SNR and the spatial correlation matrix $\mathbf{HH}^H$ of the channel matrix $\mathbf{H}$ if the number of antenna elements is fixed [30]. In the evaluation of channel capacity, $\mathbf{HH}^H$ is replaced by a spatial correlation coefficient γ_s, and high SNR [56] and low $|\gamma_s|$ [110]-[112] are desirable to obtain large channel capacity. However, even if there are two channels with identical SNR and $|\gamma_s|$, those channel capacities are not always identical owing to the effect of received power imbalance between branches, as described in [110]. Ogawa et al. described that the received power imbalance was caused by the user's hand that was holding the MT, and the imbalance then led to a reduction in the channel capacity [113]. Thus, even if the spatial correlation is reduced without changing the SNR, the channel capacity can be decreased by the received power imbalance. In other words, although many researches focus on spatial correlation reduction, the approach is not always appropriate for enhanc-

ing channel capacity. Although a theoretical study [110] revealed that channel capacity depended on the received power imbalance, the authors did not mention the above problem. Moreover, they do not discuss eigenvalues of the spatial correlation matrix, which play a key role for estimating channel capacity. In [113], although simulation-based performance evaluation was conducted to discern the impact of received power imbalance on channel capacity, few theoretical study or measurement were conducted.

Nonetheless, although spatial correlation reduction does not always lead to channel capacity enhancement, spatial correlation is a useful parameter for estimating channel capacity. For example, when the received power imbalances for two situations are similar, spatial correlation reduction is reasonable. Here, an important reminder is that variations in SNR, received power imbalance and spatial correlation should be simultaneously considered for the accurate evaluation of spatial correlation. In fact, considerable SNR enhancement is difficult to achieve on the MT side since the available space for mounting antennas is small. For total system performance, although the received SNR on the MT side is enhanced by applying antenna selection [114] and radiation pattern reconfiguration [115] to the BS side, minimization of SNR enhancement is convenient for enhancing channel capacity. In this scenario, there is often a trade-off between variations in SNR and spatial correlation for two antenna configurations. Take the example of MIMO antenna selection. Given the scenario that the SNR for antenna subset 1 is larger than that for subset 2, the spatial correlation for subset 2 is often lower than that for subset 1. The same holds true for radiation pattern reconfiguration. In such cases, the extent of correlation reduction required to minimize SNR enhancement is unclear.

This chapter presents the relationship among parameters relating to the channel matrix, the SNR, and the channel capacity, in particular, with a focus on 2×2 MIMO systems. First, this chapter describes the relationship among the spatial correlation, received power imbalance, and channel capacity independent of the SNR. Then, this chapter broadens the discussion using eigenvalues and explains the importance of eigenvalues as a parameter estimating channel capacity. The discussion is also confirmed by measurement of MIMO antenna selection. Moreover, by considering the variation in spatial correlation, received power imbalance, and SNR, the correlation reduction requirement is clarified. Then, as an example to reduce spatial correlation, this chapter presents a performance evaluation of a MIMO system with dual-polarized antennas. Here, such discussions about correlation reduction have links with Chapters 5 and 6.

In these chapters, this dissertation's aim is not to present an enhancement of the SNR but to find ways to prevent SNR degradation, and spatial correlation reduction is a dominant factor. Conversely, when the correlation is reduced by techniques such as dual-polarization, SNR enhancement is effective in obtaining a large channel capacity. For this approach, this chapter describes only the concept here and connects it with Chapter 4.

3.2 Channel Capacity

This section describes the basic theory of channel capacity. First, the basic points related to MIMO channel capacity are described. Second, channel capacities of multistream MIMO systems are categorized, and the relationships between the SNR and eigenvalues are summarized. Then, this section demonstrates the relationship among the spatial correlation coefficient, the received power imbalance, and the channel capacity. Third, the channel capacity is divided into two components depending on the SNR and the spatial correlation coefficient. This section corresponds to a preliminary preparation for discussions in the subsequent section.

3.2.1 Channel Capacity in MIMO-SDM

Channel capacity is the maximum amount of information transmitted per unit time. First, the channel capacity in SISO systems is represented by

$$C = \log_2(1 + \gamma) \tag{3.1}$$

where γ is the SNR. If the signal is sufficiently larger than the noise in (3.1), the following equation is obtained.

$$C \approx \log_2 \gamma \tag{3.2}$$

Even if the SNR is doubled in (3.2), the enhancement of the channel capacity is only 1 as follows:

$$C \approx \log_2 2\gamma = \log_2 2 + \log_2 \gamma = 1 + \log_2 \gamma \tag{3.3}$$

However, given two completely parallel transmission paths using MIMO systems, the enhancement of the channel capacity is large. When the transmitting power is allocated equally to two transmitting antennas, the channel capacity for each transmission path is given by

$$C \approx \log_2 \frac{\gamma}{2} = \log_2 \gamma - \log_2 2 = \log_2 \gamma - 1 \tag{3.4}$$

Although the SNR is halved, the decrement of channel capacity is only 1 in each transmission path. The total channel capacity is given by

$$C \approx 2\log_2 \frac{\gamma}{2} = 2\log_2 \gamma - 2\log_2 2 = 2\log_2 \gamma - 2 \tag{3.5}$$

The channel capacity is largely enhanced, compared to (3.2). For example, when a channel capacity of 10 [bits/s/Hz] is obtained for a SISO system, a channel capacity of 18 [bits/s/Hz] is achieved for a MIMO system. Thus, MIMO systems are effective for enhancing channel capacity [116].

The channel capacity in an $N_t \times N_r$ MIMO system is represented as follows [27]:

$$C = \log_2 \det\left(\mathbf{I}_{N_r} + \frac{\mathbf{H}\mathbf{R}_x\mathbf{H}^{\mathbf{H}}}{\sigma^2}\right) \tag{3.6}$$

where $\mathbf{R}_x = E[\mathbf{x}\mathbf{x}^{\mathbf{H}}]$ is the correlation matrix of the transmitting signal vector, σ^2 is the noise power, and $\mathbf{I}_{N_r}$ is an $N_r \times N_r$ identity matrix**.**

When CSI is unknown on the transmitting side, the condition of $\mathbf{R}_x$ required to maximize the channel capacity is given as [27]

$$\mathbf{R}_x = \frac{P_x}{N_t}\mathbf{I}_{\mathbf{N_t}} \tag{3.7}$$

where P_x is the total transmitting power. The following is a detailed expression for $\mathbf{R}_x$.

$$\mathbf{R}_x = \begin{bmatrix} \frac{P_x}{N_t} & 0 & \dots & \dots & 0 \\ 0 & \frac{P_x}{N_t} & \ddots & & \vdots \\ \vdots & \ddots & \frac{P_x}{N_t} & \ddots & \vdots \\ \vdots & & \ddots & \ddots & 0 \\ 0 & \dots & \dots & 0 & \frac{P_x}{N_t} \end{bmatrix} \tag{3.8}$$

Now, when the transmitting signal vector $\mathbf{x}_j$ $(j = 1, 2, \ldots, N_t)$ is noncorrelated mutually, the following is obtained from the definition of $\mathbf{R}_x$.

$$\mathbf{R}_x = \mathbf{x}\mathbf{x}^{\mathbf{H}} = \begin{bmatrix} x_1x_1^* & 0 & \ldots & \ldots & 0 \\ 0 & x_2x_2^* & \ddots & & \vdots \\ \vdots & \ddots & x_3x_3^* & \ddots & \vdots \\ \vdots & & \ddots & \ddots & 0 \\ 0 & \ldots & \ldots & 0 & x_{N_t}x_{N_t}^* \end{bmatrix} \tag{3.9}$$

where $\{\cdot\}^*$ denotes the complex conjugate. From (3.8) and (3.9), the following equations are satisfied:

$$x_1x_1^* = \frac{P_x}{N_t}, \quad x_2x_2^* = \frac{P_x}{N_t}, \quad \ldots, \quad x_{N_t}x_{N_t}^* = \frac{P_x}{N_t} \tag{3.10}$$

Equations (3.10) indicate that the maximum channel capacity is achieved when noncorrelated substreams are transmitted with identical power P_x/N_t. As previously mentioned, this scheme is SDM, which leads to maximum channel capacity when CSI is unknown on the transmitting side. The channel capacity of SDM is given by substituting (3.7) into (3.6).

$$C = \log_2 \det\left(\mathbf{I}_{N_r} + \frac{P_x}{N_t\sigma^2}\mathbf{H}\mathbf{H}^{\mathbf{H}}\right) \tag{3.11}$$

Furthermore, (3.11) is transformed using eigenvalues of $\mathbf{H}^H\mathbf{H}$ (λ_j $(1 \leq j \leq N_t)$) as follows:

$$C = \sum_{j=1}^{N_t} \log_2\left(1 + \frac{P_x\lambda_i}{N_t\sigma^2}\right) \tag{3.12}$$

Figures 3.1 and 3.2 show the variation in channel capacity as a function of the number of antenna elements in SDM. In Fig. 3.1, the number of transmitting antennas is identical to that of receiving antennas, and channel capacity increases in proportion to the number of elements, which is a great advantage in MIMO systems. Figure 3.2 shows the channel capacity when either the number of transmitting or receiving antennas is fixed and the number of the other elements is changed. In these figures, when the

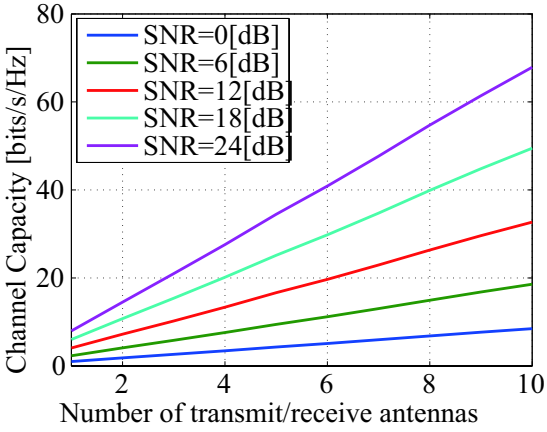

Figure 3.1. Channel capacity as a function of the number of antenna elements. The number of transmitting antennas is identical to that of receiving antennas.

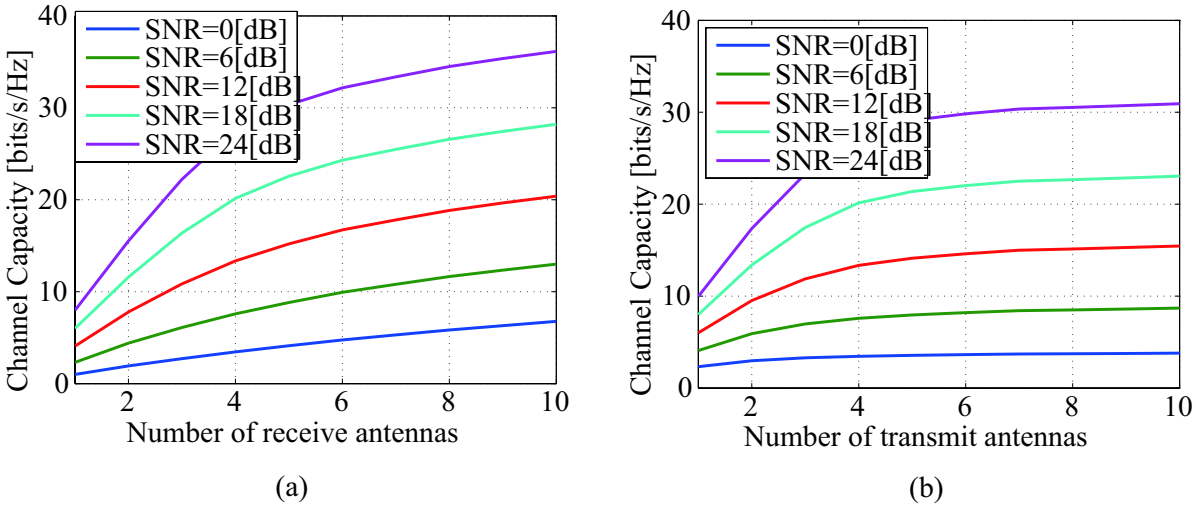

Figure 3.2. Channel capacities as a function of the number of (a) receiving and (b) transmitting antenna elements. In (a) and (b), the number of transmitting and receiving antennas is four, respectively.

numbers of transmitting and receiving antennas are larger than those of receiving and transmitting antennas, respectively, the increase in channel capacities becomes small.

Here, channel matrix $\mathbf{H}$ is decomposed by a singular value decomposition (SVD) as

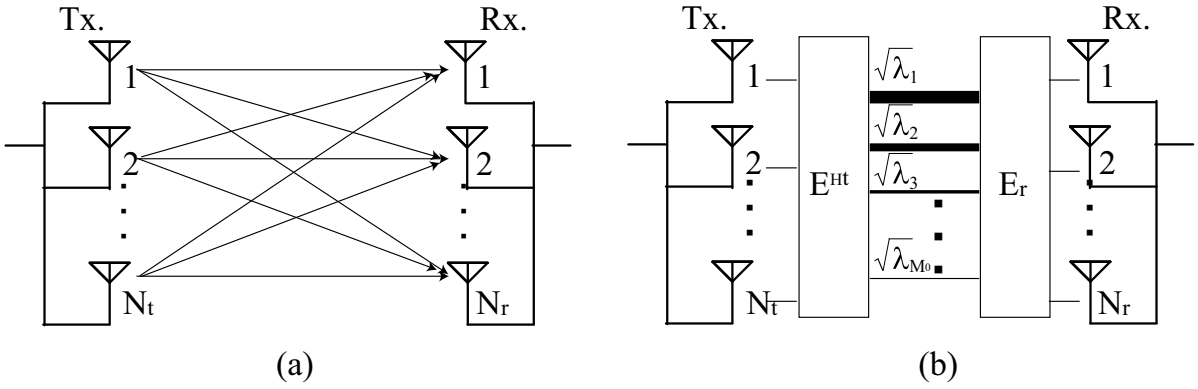

Figure 3.3. Conceptual diagram of (a) MIMO transmission path and (b) the equivalent circuit based on SVD.

(3.13) [117]

$$\mathbf{H} = \mathbf{E}_r \mathbf{D} \mathbf{E}_t^H = \sum_{i=1}^{M_0} \sqrt{\lambda_i} \mathbf{e}_{ri} \mathbf{e}_{ti}^H \tag{3.13}$$

where the λ_i represent eigenvalues of $\mathbf{H}\mathbf{H}^H$ and $\mathbf{H}^H\mathbf{H}$, and $\mathbf{D}$, $\mathbf{E}_t$, $\mathbf{E}_r$, and M_0 are defined by the following:

$$\mathbf{D} = \text{diag}[\sqrt{\lambda_1}, \sqrt{\lambda_2}, \ldots, \sqrt{\lambda_{M_0}}] \tag{3.14}$$

$$\mathbf{E}_t = [\mathbf{e}_{t,1}, \mathbf{e}_{t,2}, \ldots \mathbf{e}_{t,M_0}] \tag{3.15}$$

$$\mathbf{E}_r = [\mathbf{e}_{r,1}, \mathbf{e}_{r,2}, \ldots \mathbf{e}_{r,M_0}] \tag{3.16}$$

$$M_0 = \min(N_t, N_r) \tag{3.17}$$

where $\mathbf{e}_{t,i}$ and $\mathbf{e}_{r,i}$ are eigenvectors of λ_i for $\mathbf{H}^H\mathbf{H}$ and $\mathbf{H}\mathbf{H}^H$, respectively, and $\mathbf{E}_t$ and $\mathbf{E}_r$ are unitary matrices. Figure 3.3 shows the conceptual diagram of MIMO channels and the equivalent circuit based on SVD. In Fig. 3.3(b), signals are transmitted with an amplitude gain of $\sqrt{\lambda_i}$ through virtual transmission paths (eigenpaths). The thickness of the paths can be changed according to the size of the eigenvalues, and the thick paths lead to large channel capacity. Thus, MIMO performance can be characterized by eigenpaths, and the reason for the capacity performance in Fig. 3.2 is because the number of eigenpaths is determined by a small number of elements, namely $M_0 = \min(N_t, N_r)$. This indicates that having identical numbers of elements on the transmitting and receiving

sides is reasonable.

3.2.2 Classification of Channel Capacity in MultiStream MIMO Systems

In multistream MIMO systems, the channel capacities are mainly divided into three equations, although they are essentially identical [118]. As previously indicated, when the channel matrix is unknown on the transmitting side, the channel capacity C is given by the following equation:

$$C = \log_2 \det\left(\mathbf{I} + \frac{P_t}{N_t \sigma^2}\mathbf{H}\mathbf{H}^H\right) \tag{3.18}$$

where P_t and σ^2 are the total transmitting power and noise level, respectively. $\{\cdot\}^H$ represents a complex conjugate transpose, and $\mathbf{I}$ is an identity matrix. $\mathbf{H}$, denoting a channel response matrix, is given by

$$\mathbf{H} = \begin{bmatrix} h_{11} & \dots & h_{1N_t} \\ \vdots & \ddots & \vdots \\ h_{N_r 1} & \dots & h_{N_r N_t} \end{bmatrix} \tag{3.19}$$

where h_{ji} is an impulse response between the ith transmitting and the jth receiving antennas. N_t and N_r are the numbers of transmitting and receiving antennas, respectively. In (3.18), channel capacity is determined on the transmitting side since it depends on P_t. The transmit symbol vector at the ith transmitting antenna element and the received signal at j th receiving antenna element are denoted by s_i and x_j. Since transmitting power from each element is equal in SDM without CSI on the transmitting side, the received power at the jth element is expressed as

$$P_{r,j} = E\left[|x_i|^2\right] = E\left[\left|\sum_{i=1}^{N_t} h_{ji} s_i\right|^2\right] = \sum_{i=1}^{N_t} |h_{ji}|^2 E[|s_i|^2] = P_{t,i} \sum_{i=1}^{N_t} |h_{ji}|^2 \tag{3.20}$$

where $P_{t,i}$ is the transmitting power at the ith transmitting antenna element. The

averaged received power $\bar{P}_r$ is calculated by

$$\bar{P}_r = \frac{\sum_{j=1}^{N_r} P_{r,j}}{N_r} = \frac{P_{t,i}}{N_r} \sum_{i=1}^{N_t} \sum_{j=1}^{N_r} |h_{ji}|^2 \tag{3.21}$$

Hence, the transmitting power at the jth transmitting antenna element is expressed as

$$P_{t,i} = \frac{\bar{P}_r N_r}{\sum_{i=1}^{N_t} \sum_{j=1}^{N_r} |h_{ji}|^2} \tag{3.22}$$

Since each element has the identical tansmitting power from each element is equal, the total transmitting power P_t is represented by

$$P_t = \sum_{i=1}^{N_t} P_{t,i} = \frac{\bar{P}_r N_t N_r}{\sum_{i=1}^{N_t} \sum_{j=1}^{N_r} |h_{ji}|^2} \tag{3.23}$$

By substituting (3.23) in (3.18), the channel capacity is transformed as follows:

$$\begin{aligned} C &= \log_2 \det \left(\mathbf{I} + \frac{P_r}{N_t \sigma^2} \frac{\mathbf{H}}{\sqrt{\frac{1}{N_r N_t} \sum_{i=1}^{N_t} \sum_{j=1}^{N_r} |h_{ji}|^2}} \frac{\mathbf{H}^H}{\sqrt{\frac{1}{N_r N_t} \sum_{i=1}^{N_t} \sum_{j=1}^{N_r} |h_{ji}|^2}} \right) \\ &= \log_2 \det \left(\mathbf{I} + \frac{\rho}{N_t} \mathbf{H}_n \mathbf{H}_n^H \right) \end{aligned} \tag{3.24}$$

where $\rho = P_r/\sigma^2$ is the averaged SNR at each receiving antenna, and $\mathbf{H}_n$ is a normalized channel response matrix denoted by

$$\mathbf{H}_n = \frac{\mathbf{H}}{\sqrt{\frac{1}{N_r N_t} \sum_{i=1}^{N_t} \sum_{j=1}^{N_r} |h_{ji}|^2}} \tag{3.25}$$

In (3.24), the channel capacity is determined on the receiving side since it depends on ρ.

Moreover, when CSI is known on the transmitting side, a channel can be divided into multiple independent eigenpaths. The channel capacity C is given by the sum of the channel capacity in each eigenpath C_k as follows [42]:

$$C = \sum_{k=1}^{K} C_k = \sum_{k=1}^{K} \log_2 \left(1 + \frac{\lambda_k P_k}{\sigma^2} \right) \tag{3.26}$$

where λ_k is the kth eigenvalue derived by the eigenvalue decomposition

$$\mathbf{H}\mathbf{H}^H = \mathbf{V}\mathbf{\Lambda}\mathbf{V}^H, \quad \mathbf{\Lambda} = \mathrm{diag}(\lambda_1, \ldots, \lambda_K) \tag{3.27}$$

$K = \min(N_t, N_r)$ is the number of eigenpaths, and P_k is the transmitting power allocated for kth eigenpath, which is represented by

$$P_k = \max\left(\eta - \frac{\sigma^2}{\lambda_k}, 0\right), \quad \sum_{k=1}^{K} P_k = P_t \tag{3.28}$$

where η is a constant. The SNR of the kth detected substream is expressed as

$$\rho_k = \frac{\lambda_k P_k}{\sigma^2} \tag{3.29}$$

For three types of channel capacity, the relationships between eigenvalue and SNR are summarized. In (3.18), the amplitude level of h_{ji} is related to the received SNR if the total transmitting power is fixed. Therefore, the effect of SNR is included in eigenvalues derived by the eigenvalue decomposition of $\mathbf{H}\mathbf{H}^H$. In contrast, in (3.24), there is no impact of the SNR on eigenvalues derived from the eigenvalue decomposition of $\mathbf{H}_n\mathbf{H}_n^H$ because SNR (ρ) and $\mathbf{H}_n\mathbf{H}_n^H$ are completely separated. In (3.26), the effect of SNR is included in eigenvalues because λ_k is expressed using the SNR from (3.29) ($\lambda_k = \rho_k\sigma^2/P_k$). The next section focuses on the channel capacity of (3.24) defined on the receiving side and the normalized channel matrix to consider correlation and SNR separately.

3.2.3 Relationship between Channel Capacity and Spatial Correlation

The description in this section is based on [110]. In a 2 × 2 MIMO system, the spatial correlation coefficient between received signals is given by

$$\gamma_s = \frac{h_{11}h_{21}^* + h_{12}h_{22}^*}{\sqrt{(|h_{11}|^2 + |h_{12}|^2)(|h_{21}|^2 + |h_{22}|^2)}} \tag{3.30}$$

where $\{\cdot\}^*$ denotes the complex conjugate. Here, the received powers at receiving antennas #1 and #2 are represented by

$$P_{r,1} = |h_{11}|^2 + |h_{12}|^2, \quad P_{r,2} = |h_{21}|^2 + |h_{22}|^2 \tag{3.31}$$

When the received power imbalance between #1 and #2 are defined as $\beta = P_{r,1}/(P_{r,1} + P_{r,2})$, $P_{r,1}$, $P_{r,2}$ and γ_s are transformed using (3.25) as

$$P_{r,1} = 4\beta, \quad P_{r,2} = 4(1-\beta) \tag{3.32}$$

$$\gamma_s = \frac{h_{11}h_{21}^* + h_{12}h_{22}^*}{4\sqrt{\beta(1-\beta)}} \tag{3.33}$$

The following equations are given by substituting (3.32) and (3.33) into the transformed formula of (3.24):

$$C = \log_2 \det \begin{bmatrix} 1+(|h_{11}|^2+|h_{12}|^2)\cdot\rho/2 & (h_{11}h_{21}^*+h_{12}h_{22}^*)\cdot\rho/2 \\ (h_{21}h_{11}^*+h_{22}h_{12}^*)\cdot\rho/2 & 1+(|h_{21}|^2+|h_{22}|^2)\cdot\rho/2 \end{bmatrix} \tag{3.34}$$

$$= \log_2(1 + 2\rho + 4\beta\rho^2(1-\beta)(1-|\gamma_s|^2)) \tag{3.35}$$

In (3.35), the SNR and spatial correlation, as well as the received power imbalance, have an impact on channel capacity. Figure 3.4 shows the relationship among spatial correlation, received power imbalance, and channel capacity with an SNR of 15 dB. The channel capacity is maximized in β=0.5 for each correlation coefficient. Figure 3.4 also indicates that even when the spatial correlation is reduced, the channel capacity can be degraded because of the received power imbalance.

3.2.4 Separation of Channel Capacity Components

In SDM without CSI on the transmitting side, the total received power normalized by the transmitting power from each element is given by

$$P_H = \sum_{i=1}^{N_t}\sum_{j=1}^{N_r} |h_{ji}|^2 = \mathrm{tr}\left(\mathbf{H}\mathbf{H}^H\right) = \sum_{i=1}^{K} \lambda_i \tag{3.36}$$

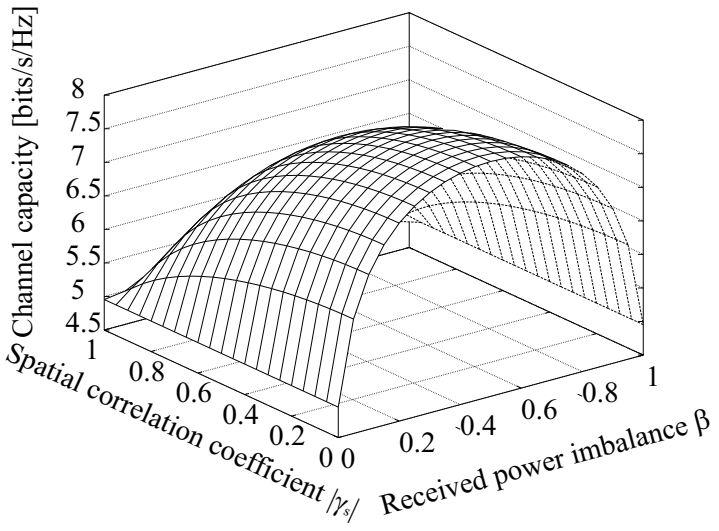

Figure 3.4. Relationship among spatial correlation coefficient, received power imbalance, and channel capacity (SNR=15 dB).

where tr(·) denotes the trace of the matrix. For the normalized channel matrix $\mathbf{H}_n$ in (3.25), the following equation is given:

$$\begin{aligned} \mathrm{tr}\big(\mathbf{H}_n\mathbf{H}_n^H\big) &= \frac{1}{\frac{1}{N_rN_t}\sum_{i=1}^{N_t}\sum_{j=1}^{N_r}|h_{ji}|^2}\mathrm{tr}\big(\mathbf{H}\mathbf{H}^H\big) \\ &= N_rN_t = Const. \end{aligned} \tag{3.37}$$

According to [119], (3.24) is transformed as follows:

$$C = N_r\log_2\left(\frac{\rho}{N_t}\right) + \log_2\det\left(\mathbf{I}\cdot\frac{N_t}{\rho} + \mathbf{H}_n\mathbf{H}_n^H\right) \tag{3.38}$$

$$\approx N_r\log_2\left(\frac{\rho}{N_t}\right) + \log_2\det\big(\mathbf{H}_n\mathbf{H}_n^H\big) \tag{3.39}$$

$$= C_{\mathrm{SNR}} + C_{\mathrm{COR}} \tag{3.40}$$

In (3.39), the approximation is satisfied for $N_r \geq N_t$, high SNR and non-ill-conditioned channels [119]. By the transformations of (3.38) and (3.39), the channel capacity is divided into two elements depending on the SNR (C_{SNR}) and the spatial correlation (C_{COR}).

Figure 3.5 shows the channel capacity of (3.24), (3.38) and (3.39) as a function of

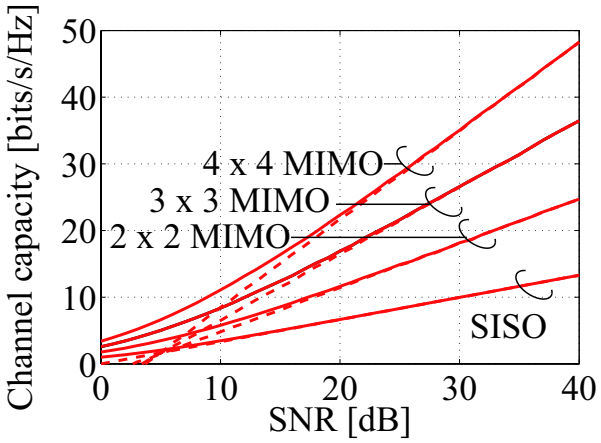

Figure 3.5. Relationship between SNR and channel capacity. The solid curves are for (3.24) and (3.38), and the dashed curves are for (3.39).

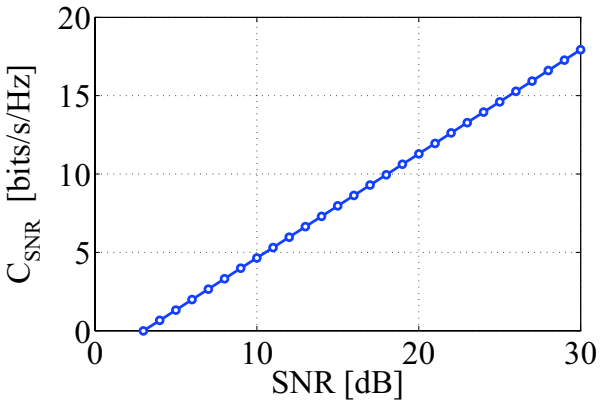

Figure 3.6. Relationship between SNR and C_{SNR}.

SNR. For the channel capacity, an ensemble average of 1,000 patterns of channel matrices with a complex Gaussian distribution are used in each SNR and each number of elements. Here, the approximation is satisfied in the high-SNR regime with a small number of elements. Figure 3.6 shows C_{SNR} as a function of SNR in 2×2 MIMO systems. Since C_{SNR} does not include the channel matrix and the only variable is ρ, C_{SNR} increases in proportion to SNR. The impact of the channel matrix on the channel capacity is discussed in the next section.

3.3 Contribution of the Channel Matrix to Channel Capacity

This section focuses on C_{COR} and describes the relationship among spatial correlation, eigenvalues, and channel capacity. This section presents not only an analysis-based examination using channels with complex Gaussian distributions but also a measurement-based examination by MIMO antenna selection.

3.3.1 Analysis Based Examination Using Channels with Complex Gaussian Distributions

In fact, C_{COR} is not directly related to the spatial correlation coefficient γ_s but is related to $\det(\mathbf{H}_n\mathbf{H}_n^H)$. Figure 3.7 shows the relationship between $\det(\mathbf{H}_n\mathbf{H}_n^H)$ and γ_s. The variation in $\det(\mathbf{H}_n\mathbf{H}_n^H)$ for each γ_s is large, and the distribution of C_{COR} also fluctuates (Fig. 3.8). Although a low $|\gamma_s|$ tends to result in a large channel capacity, it does not always lead to channel capacity enhancement. The examination of two scenarios is described in the following text.

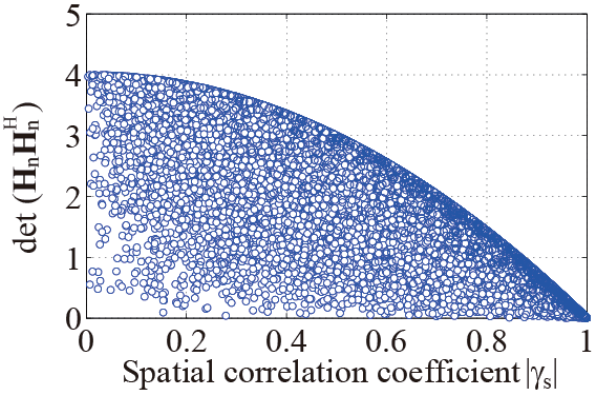

Figure 3.7. Relationship between spatial correlation coefficient and $\det(\mathbf{H}_n\mathbf{H}_n^H)$.

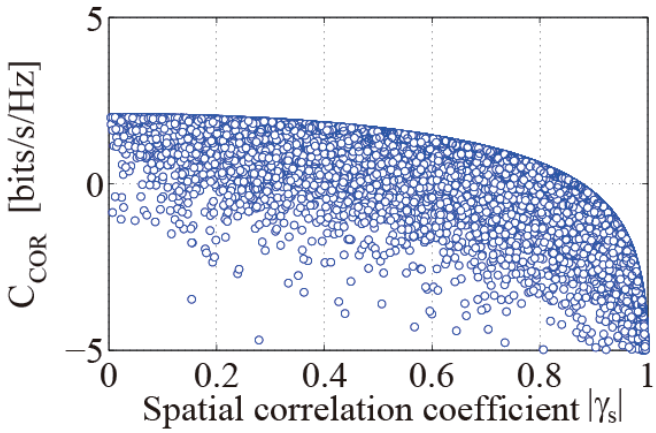

Figure 3.8. Relationship between spatial correlation coefficient and C_{COR}.

Scenario 1

To evaluate the fluctuation, the following two channels are prepared.

$$\mathbf{H}_{n,1} = \begin{bmatrix} 0.2566 - j0.4480 & 0.5748 + j0.8434 \\ 0.4363 + j0.1800 & 1.4799 + j0.5282 \end{bmatrix} \tag{3.41}$$

$$\mathbf{H}_{n,2} = \begin{bmatrix} 1.0985 - j1.2068 & 0.4588 - j0.7584 \\ 0.4457 + j0.4691 & 0.2100 - j0.2973 \end{bmatrix} \tag{3.42}$$

From (3.30), the spatial correlation for each channel is derived as follows:

$$|\gamma_{s,1}| = 0.8004 \quad \left(\gamma_{s,1} = 0.8004 e^{j0.4870}\right) \tag{3.43}$$

$$|\gamma_{s,2}| = 0.8005 \quad \left(\gamma_{s,2} = 0.8005 e^{-j1.3466}\right) \tag{3.44}$$

Although the $|\gamma_s|$s are almost identical, their channel capacities are different, as follows:

$$C_{\mathrm{COR},1} = 0.3395, \quad C_{\mathrm{COR},2} = -0.5505 \tag{3.45}$$

From (3.37), the received powers for $\mathbf{H}_{n,1}$ and $\mathbf{H}_{n,2}$ are identical when the transmitting power is fixed. The difference in channel capacity between two channels with an identical SNR and spatial correlation coefficient is explainable in terms of the received power

imbalance β:

$$\beta_1 = 0.3271, \quad \beta_2 = 0.8622 \tag{3.46}$$

As evidenced by Fig. 3.4, since β for $\mathbf{H}_{n,1}$ is closer to 0.5 than that for $\mathbf{H}_{n,2}$, the C_{COR} for $\mathbf{H}_{n,1}$ is larger. Now, the received power for each branch is calculated as follows:

$$P_{r1,1} = 1.3083, \quad P_{r2,1} = 2.6919 \tag{3.47}$$

$$P_{r1,2} = 3.4487, \quad P_{r2,2} = 0.5512 \tag{3.48}$$

where the received power at element $\#i$ for the channel $\mathbf{H}_{n,k}$ is defined as $P_{ri,k}$. The received power difference between two branches for $\mathbf{H}_{n,2}$ (2.8975) is greater than that for $\mathbf{H}_{n,1}$ (1.3836).

As an alternative view, eigenvalues for $\mathbf{H}_{n,1}$ and $\mathbf{H}_{n,2}$ are derived, respectively, as follows:

$$\lambda_{1,1} = 3.6537, \quad \lambda_{2,1} = 0.3463 \tag{3.49}$$

$$\lambda_{1,2} = 3.8213, \quad \lambda_{2,2} = 0.1787 \tag{3.50}$$

The allocation of the first and second eigenpaths are different in each channel, indicating that the maximization of C_{COR} is achieved by optimizing the allocation of eigenpaths. Here, C_{COR} is transformed as follows [27]:

$$\begin{aligned} C_{\mathrm{COR}} &= \log_2 \det\left(\mathbf{H}_n \mathbf{H}_n^H\right) && (3.51)\\ &= \log_2 \det\left(\mathbf{U}\mathbf{\Lambda}\mathbf{U}^H\right) && (3.52)\\ &= \log_2\left(\det \mathbf{U} \det \mathbf{\Lambda} \det \mathbf{U}^H\right) && (3.53)\\ &= \log_2\left(\det \mathbf{\Lambda}\right) && (3.54)\\ &= \log_2 \lambda_1 \lambda_2 && (3.55) \end{aligned}$$

where matrix diagonalization is conducted in the transformation from (3.51) to (3.52). $\mathbf{U}$ is a unitary matrix, and $\mathbf{\Lambda}$ is a diagonal matrix configured by eigenvalues, which is

given by

$$\mathbf{\Lambda} = \begin{bmatrix} \lambda_1 & 0 \\ 0 & \lambda_2 \end{bmatrix} \tag{3.56}$$

Since C_{COR} was expressed using eigenvalues, as a next step, the range of eigenvalues is examined. In a 2 × 2 MIMO system, the following relationship is satisfied from (3.36) and (3.37):

$$\lambda_1 + \lambda_2 = 4 \tag{3.57}$$

Applying the relational expression between arithmetic and geometric averages to λ_1 and λ_2, the following equation is derived:

$$\lambda_1 + \lambda_2 \geq 2\sqrt{\lambda_1 \lambda_2} \tag{3.58}$$

where the equality in (3.58) holds if λ_1=λ_2. By substituting (3.57) in (3.58), the following relationship is derived:

$$\lambda_1 \lambda_2 \leq 4 \tag{3.59}$$

From $0 \leq \lambda_2 \leq \lambda_1$ and (3.59), the range of λ_2 is derived as

$$0 \leq \lambda_2 \leq 2 \tag{3.60}$$

The range of λ_1 is derived from (3.57) and (3.60) as

$$2 \leq \lambda_1 \leq 4 \tag{3.61}$$

From (3.60) and (3.61), a common range for λ_1 and λ_2 is confirmed only at 2. The distributions of the spatial correlation coefficient as a function of each eigenvalue are shown in Figs. 3.9(a) and 3.9(b). The upper bounds of the spatial correlation coefficient are expressed using straight lines as

$$|\gamma_s| \leq \frac{1}{2}\lambda_1 - 1, \quad |\gamma_s| \leq -\frac{1}{2}\lambda_2 + 1 \tag{3.62}$$

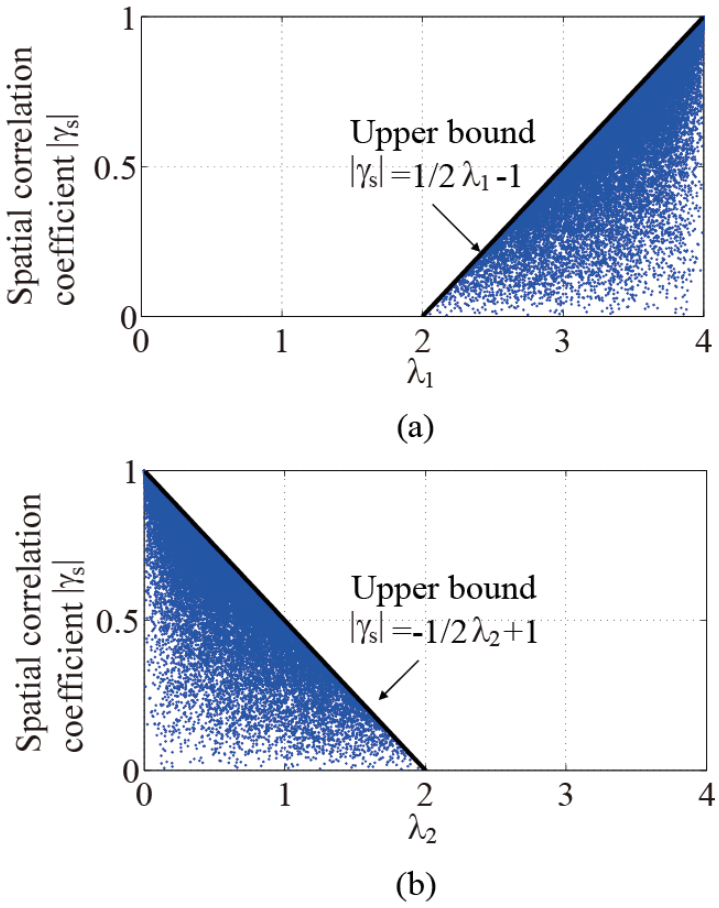

Figure 3.9. Relationship between (a) the first eigenvalue and the spatial correlation coefficient and (b) the second eigenvalues and the spatial correlation coefficient.

The range of the eigenvalues are given as

$$2(|\gamma_s|+1) \le \lambda_1 \le 4, \quad 0 \le \lambda_2 \le 2(-|\gamma_s|+1) \tag{3.63}$$

Equations in (3.63) indicate that the range of eigenvalues in (3.60) and (3.61) are restricted by spatial correlation.

Figure 3.10 is a combined conceptual diagram of Figs. 3.9(a) and 3.9(b). When the upper bounds of Fig. 3.9 are solved for λ_1 and λ_2, $\lambda_1 = 2(|\gamma_s|+1)$ and $\lambda_2 = 2(-|\gamma_s|+1)$ are obtained, as shown in Fig. 3.10. Since the sum of these two straight lines is 4, it

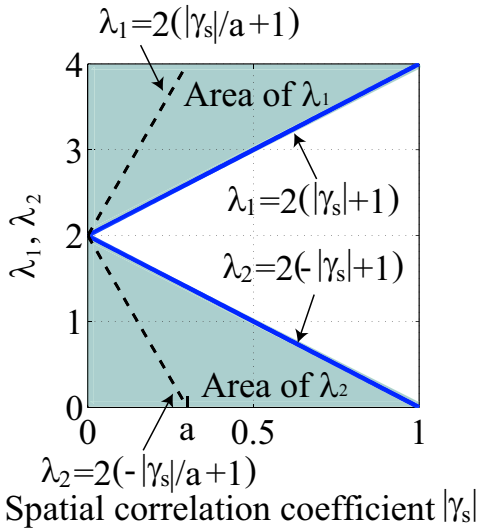

Figure 3.10. Relationship between the spatial correlation coefficient and eigenvalues.

satisfies the condition in (3.57). The product of the eigenvalues is given by

$$\lambda_1\lambda_2 = 4(1 - |\gamma_s|^2) \tag{3.64}$$

Since $\lambda_1\lambda_2$ is maximized when $\lambda_1 = \lambda_2$ from (3.58) and (3.59), the line of the upper bound for $\lambda_1\lambda_2$ passes through (0,2) in Fig. 3.10. Here, the straight line representing λ_2 connecting (0,2) to (a,0): $0 < a \leq 1$ is given by

$$\lambda_2 = 2\left(-\frac{|\gamma_s|}{a} + 1\right) \tag{3.65}$$

The straight line of λ_1 is derived from (3.57) as

$$\lambda_1 = 2\left(\frac{|\gamma_s|}{a} + 1\right) \tag{3.66}$$

These two lines are shown with dotted lines in Fig. 3.10. From (3.66) and (3.65), $\lambda_1\lambda_2$ is calculated as follows:

$$\lambda_1\lambda_2 = 4\left(1 - \frac{|\gamma_s|^2}{a^2}\right) \tag{3.67}$$

Since (3.64) $\geq$ (3.67) is satisfied for all a and $|\gamma_s|$, (3.64) is an upper bound of $\lambda_1\lambda_2$. By

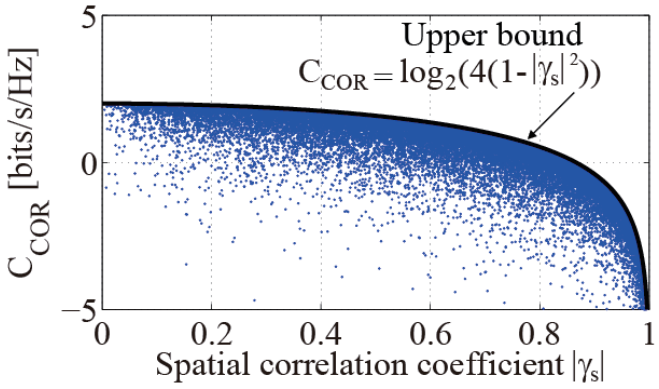

Figure 3.11. Relationship between spatial correlation and C_{COR}.

substituting (3.64) in (3.55), the following relationship is obtained:

$$C_{\mathrm{COR}} \leq \log_2 4(1 - |\gamma_s|^2) \tag{3.68}$$

Since the right side of (3.68) corresponds to the upper bound of Fig. 3.11, the validity of (3.68) is confirmed. Thus, maximum C_{COR} is achieved by minimizing the difference between eigenvalues for each spatial correlation.

Scenario 2

This section discusses the relationship among spatial correlation, received power imbalance, and channel capacity for another scenario. Figure 3.12 shows C_{COR} as a function of the spatial correlation coefficient for channel matrices extracted in target scenarios 1 and 2. $\mathbf{H}_{n,3}$ is a newly extracted channel matrix in scenario 2, which is given by

$$\mathbf{H}_{n,3} = \begin{bmatrix} 0.3639 - j0.0978 & -0.1805 - j0.3313 \\ 0.0301 - j1.0570 & 1.1053 + j1.1730 \end{bmatrix} \tag{3.69}$$

The spatial correlation, C_{COR}, received power imbalance, received power for each branch, and eigenvalues are

$$|\gamma_{s,3}| = 0.5113 \tag{3.70}$$

$$C_{\mathrm{COR},3} = -0.3579 \tag{3.71}$$

$$\beta_3 = 0.0711 \tag{3.72}$$

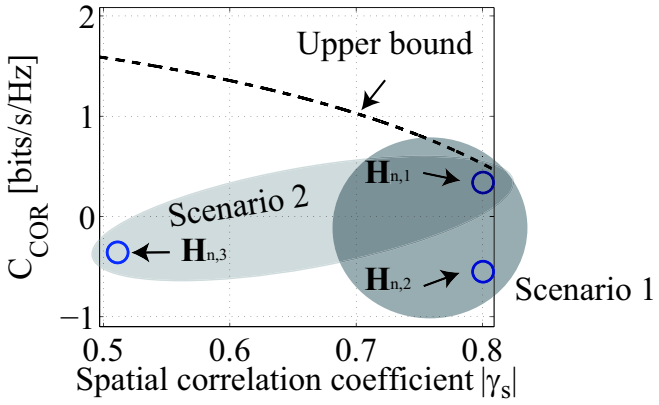

Figure 3.12. C_{COR} as a function of the spatial correlation coefficient in $\mathbf{H}_{n,1}$, $\mathbf{H}_{n,2}$ and $\mathbf{H}_{n,3}$ for scenarios 1 and 2.

$$P_{r1,3} = 0.2843, \quad P_{r2,3} = 3.7157$$
$$(|P_{r1,3} - P_{r2,3}| = 3.4314) \tag{3.73}$$
$$\lambda_{1,3} = 3.7944, \quad \lambda_{2,3} = 0.2056 \tag{3.74}$$

Although the spatial correlation for $\mathbf{H}_{n,3}$ is lower than that for $\mathbf{H}_{n,1}$, the C_{COR} for $\mathbf{H}_{n,3}$ is smaller (Fig. 3.12) because of the received power imbalance β_3. Compared to (3.46)-(3.48), β_3 in (3.72) is farther from 0.5, and the difference in the received power between each branch in (3.73) is larger than that for $\mathbf{H}_{n,1}$. In addition, the difference between eigenvalues in (3.74) is also larger than that in (3.49).

Let us evaluate this scenario further. In the distribution of Fig. 3.11, two points are extracted, and the reduction in spatial correlation and enhancement in C_{COR} are derived from those data. Figure 3.13 shows their distributions for 10,000 random iterations. The tendency is for C_{COR} to increases with a reduction in spatial correlation (the first quadrant,) and for C_{COR} to decreases with an increase in spatial correlation (the third quadrant). However, the distributions also appear in the second and fourth quadrants, indicating that C_{COR} increases (respectively, decreases) despite an increase (respectively, decrease) of spatial correlation, because of the received power imbalance. Figure 3.14 shows the distributions of enhancement in C_{COR} as a function of the increment in λ_2 in a similar manner. Here, an increment in λ_2 is equivalent to a decrement in the difference between λ_1 and λ_2. Because the distributions are concentrated only in the first and third quadrants, magnitude relation in λ_2 completely correspond to those in

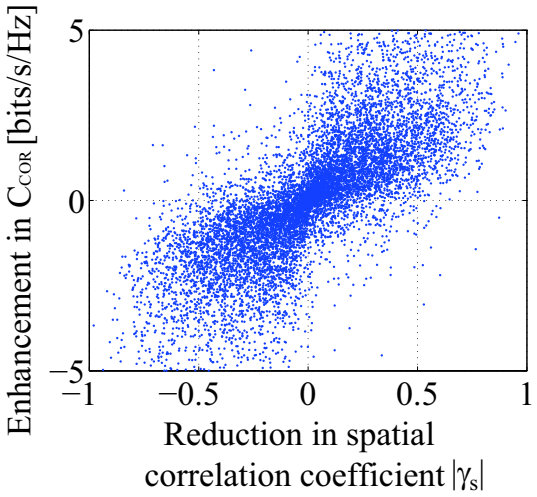

Figure 3.13. Relationship between the reduction in spatial correlation coefficient and the enhancement in C_{COR}.

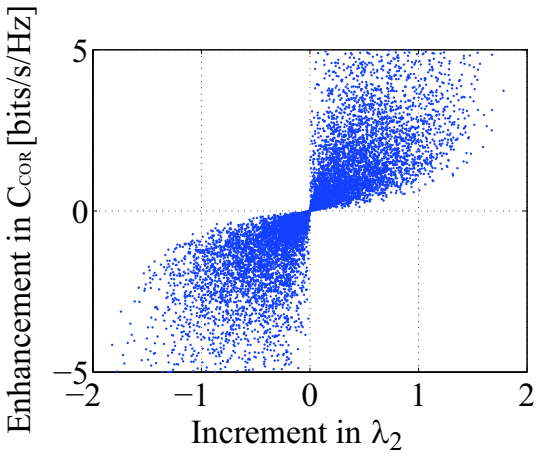

Figure 3.14. Relationship between the increment in the second eigenvalue and the enhancement in C_{COR}.

C_{COR}. Hence, the eigenvalue is a parameter that includes the effects of spatial correlation and power imbalance. Note that spatial correlation reduction does not always lead to C_{COR} enhancement.

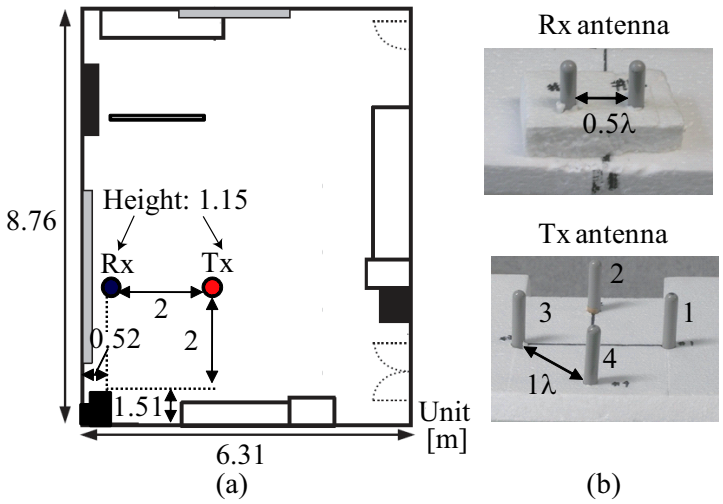

Figure 3.15. Measurement environment.

3.3.2 Measurement-Based Examination

Since the discussion in the previous section was theoretical, it should be confirmed by measurement. This section describes the relationships among C_{COR}, spatial correlation, and received power imbalance. The measurement target is a MIMO system with transmit antenna selection in an indoor environment because multiple combinations of received power imbalance and spatial correlation are generated by physically switching antennas.

As shown in Fig. 6.9, measurement is conducted in a room of 8.76 m × 6.31 m × 2.7 m. On the Tx and Rx sides, sleeve antennas are used, and those positions are fixed as shown in Fig. 6.9(a). Tx is configured using a four-element rectangular array (Fig. 6.9(b)), and a 2×2 MIMO-SDM is performed by selecting two feed elements from four elements. Here, the switching operation is conducted manually and nonfed elements are terminated. In contrast, Rx is configured using a two-element linear array (Fig. 6.9(b)). The heights of Tx and Rx are both 1.15 m, and the measured environment is quasistatic. M-sequences are used for headers of transmitting signals, and channel matrices are estimated based on a complex sliding correlation scheme using reference signals. In this measurement, the carrier frequency is 5 GHz.

The channel matrices estimated for each antenna subset in Fig. 3.16(a) are normalized, and then, C_{COR} values are derived from them. There are multiple sets of data for each antenna selection in Fig. 3.16(b) because the data are acquired several times. In

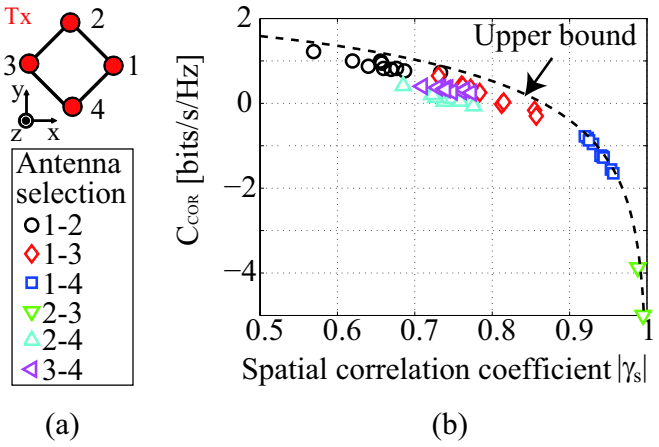

Figure 3.16. (a) Definition of the number of transmitting antenna elements and six antenna subsets. (b) Relationship between the spatial correlation coefficient and C_{COR} for each antenna subset.

Fig. 3.16(b), the data are distributed between 0.5 and 1, and the C_{COR} for antenna selections 2–3 and 1–4 are close to the upper bound. Although the C_{COR} is enhanced overall with a reduction of spatial correlation, it cannot be applied between 0.65 and 0.8. In this regime, C_{COR} is lower than the upper bound. Figure 3.17 shows an enlarged view of Fig. 3.16(b), and focused data (i, ii, and iii) are marked by filled circles and triangles in this figure. The spatial correlation, C_{COR}, received power at elements 1 and 2, and eigenvalues for those data are summarized in Fig. 3.18. In the figure, the dotted line indicates the performance of upper bounds of C_{COR}.

Although the spatial correlation coefficients for i and ii are similar, the C_{COR} for i is larger, as shown in Fig. 3.18(b). This is explainable by using the received power imbalance because β_{i}=0.3377 is closer to 0.5 than β_{ii}=0.1702. As shown in Figs. 3.18(c) and 3.18(d), the difference between the received power for each branch for i is smaller than that for ii, and the difference between eigenvalues for i is also smaller in Figs. 3.18(e) and 3.18(f).

Although the spatial correlation coefficient for iii is lower than that for i, the C_{COR} for iii is smaller in Fig. 3.18(b). This can also be explained by using the received power imbalance because β_{iii}=0.1950 is not closer to 0.5 than β_{i}=0.3377. For iii, the performances of the difference between the received power in each branch and the difference between eigenvalues relative to those for i are similar to the relationship between ii and i. Thus, the performance of C_{COR} for scenario 1 and 2 has been examined empirically,

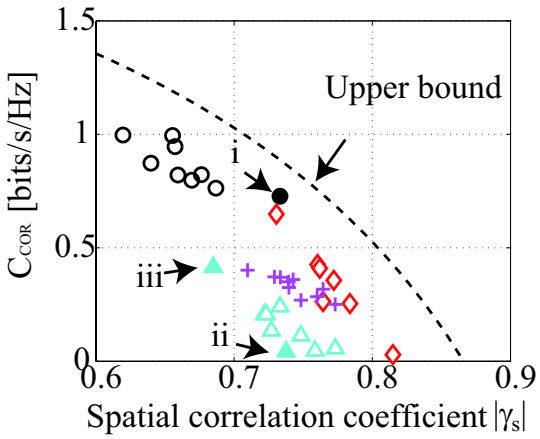

Figure 3.17. Relationship between the spatial correlation and C_{COR} for each antenna selection (The range between 0.6 and 0.9 in Fig. 3.16(b) is expanded.)

and the measurement results also indicate that a low correlation does not always lead to a large channel capacity. The eigenvalue is an appropriate factor for evaluating C_{COR}.

3.4 Requirements for Spatial Correlation Reduction

As described in the preceding section, spatial correlation reduction did not always lead to channel capacity enhancement. However, spatial correlation is an easily-handled parameter for estimating channel capacity because the range is constrained between 0 and 1. Meanwhile, in the preceding section, the impacts of SNR and the spatial correlation coefficient on channel capacity were independently considered. However, in fact, variations in SNR, received power imbalance, and spatial correlation should be simultaneously considered. In particular, since variations in SNR and spatial correlation often have a trade-off relationship, a large increase in SNR is required to enhance channel capacity when spatial correlation and eventually C_{COR} are degraded. To minimize the increase in SNR required for enhancing channel capacity, this section describes a spatial correlation level that should be maintained even when the states of antenna configurations, MT positions, and surrounding environments are changed.

For a change from state 1 to state 2, when C_{SNR} and C_{COR} increase simultaneously, the channel capacity is obviously enhanced. Under this condition, an increase in SNR greater than 0 dB leads to channel capacity enhancement. However, variations in SNR

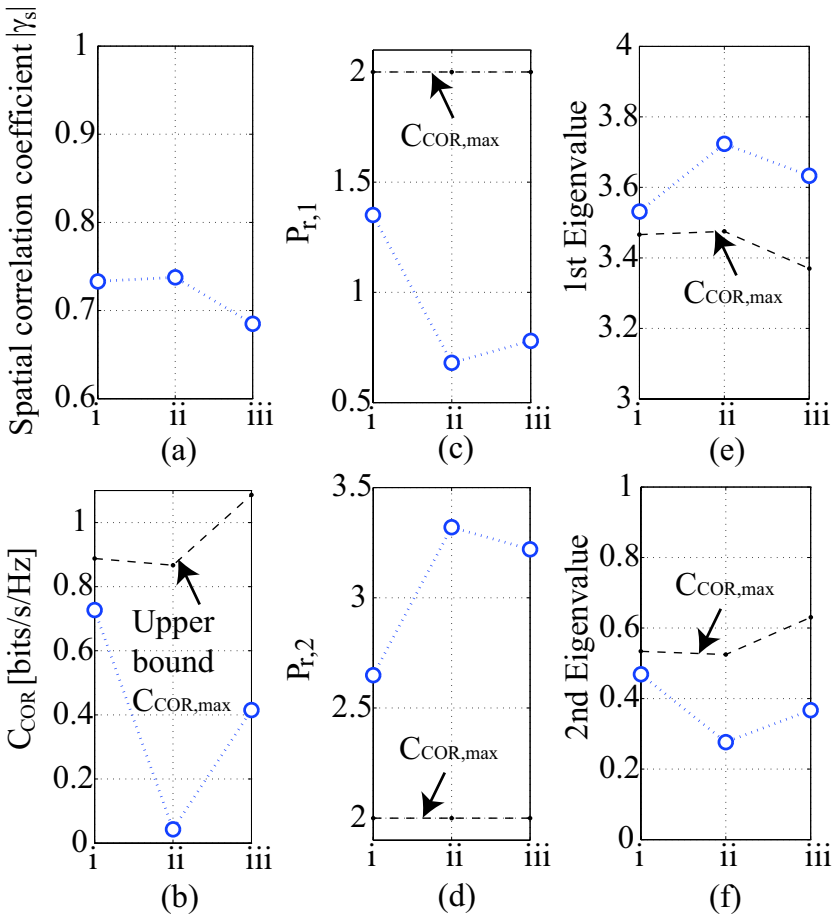

Figure 3.18. (a) Spatial correlation coefficient, (b): C_{COR}, (c) and (d) received power at elements 1 and 2, respectively, and (e) and (f): first and second eigenvalues, respectively, for i, ii, and iii in Fig. 3.17.

and spatial correlation are often in a trade-off relationship for the two configurations. For example, in a MIMO antenna selection or radiation pattern reconfiguration, the following situation is often generated:

$$\rho_1 < \rho_2 \tag{3.75}$$

$$|\gamma_{s,1}| > |\gamma_{s,2}| \tag{3.76}$$

where ρ_1 [dB] and ρ_2 [dB] correspond to the SNR for antenna subsets 1 and 2 or radiation patterns 1 and 2, respectively. In a similar manner, $|\gamma_{s,1}|$ and $|\gamma_{s,2}|$ correspond to the relevant spatial correlation coefficients. As a result, the following condition is often

generated:

$$C_{\mathrm{SNR},1} < C_{\mathrm{SNR},2} \tag{3.77}$$

$$C_{\mathrm{COR},1} > C_{\mathrm{COR},2} \tag{3.78}$$

When the enhancement of channel capacity is defined as C_{UP}, it is given by

$$\begin{aligned} C_{\mathrm{UP}} &= C_2 - C_1 \\ &= (C_{\mathrm{SNR},2} - C_{\mathrm{SNR},1}) + (C_{\mathrm{COR},2} - C_{\mathrm{COR},1}) \end{aligned} \tag{3.79}$$

When the following condition is satisfied in (3.79), $C_{\mathrm{UP}} > 0$ is realized:

$$C_{\mathrm{SNR},2} - C_{\mathrm{SNR},1} > C_{\mathrm{COR},1} - C_{\mathrm{COR},2} \tag{3.80}$$

where $C_{\mathrm{SNR},2} - C_{\mathrm{SNR},1}$ is transformed as follows using (3.39):

$$C_{\mathrm{SNR},2} - C_{\mathrm{SNR},1} = 2\log_2 \frac{10^{\rho_2/10}}{2} - 2\log_2 \frac{10^{\rho_1/10}}{2} \tag{3.81}$$

By substituting (3.81) into (3.80), the following relationship is obtained:

$$\rho_2 - \rho_1 > \frac{5(C_{\mathrm{COR},1} - C_{\mathrm{COR},2})}{\log_2 10} = \rho_{th} \tag{3.82}$$

From (3.82), under the conditions of (3.77) and (3.78), the channel capacity is enhanced when the increase in SNR is greater than ρ_{th}. In other words, ρ_{th} represents the increase in SNR required to enhance the channel capacity. Figure 3.19 shows cumulative distribution functions (CDFs) for ρ_{th} in (3.82). Here, states 1 and 2 satisfying $C_{\mathrm{COR},1} \geq C_{\mathrm{COR},2}$ are randomly selected in $|\gamma_s| \leq 1,\ 0.9,\ 0.8,\ 0.7$, and 0.6. In Fig. 3.19, ρ_{th} at CDF=100% is an important value, which indicates that the channel capacity is always enhanced under any channel when the value of ρ_{th} is used. In Fig. 3.19, the performances of the ρ_{th} distributions become better, with the graph shifting to the left.

Changing from $|\gamma_s| \leq 1$ to $|\gamma_s| \leq 0.6$, causes the distributions to shift to the left and they become saturated around $|\gamma_s| \leq 0.7$. The CDF is approximately 95 % at ρ_{th}=3 dB for $|\gamma_s| \leq 0.7$. This indicates that sustaining $|\gamma_s| \leq 0.7$ during changes from state 1 to 2 minimizes the required increase in SNR for channel capacity enhancement, and the

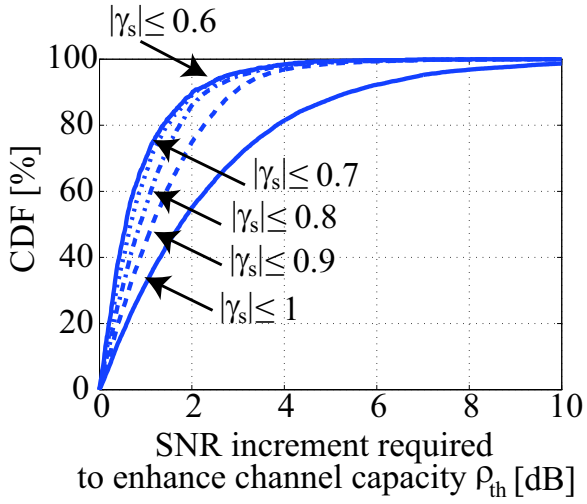

Figure 3.19. Cumulative distribution function of increase in SNR required to enhance channel capacity.

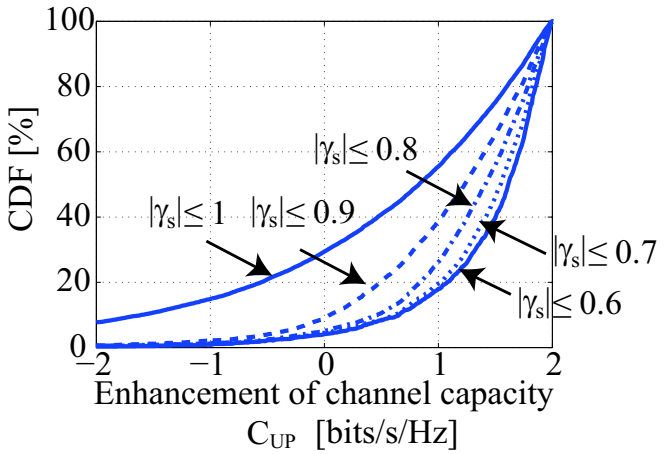

Figure 3.20. Cumulative distribution function of enhancement of channel capacity by 3 dB SNR improvement.

required increase in SNR is approximately 3 dB.

Figure 3.20 shows the CDFs of the channel capacity enhancement C_{UP} when a 3 dB SNR increase is considered for state 2 compared with state 1. In this figure, the CDF at C_{UP}=0 is an important value. When the CDF is greater than 0 at C_{UP}=0 (as in the case of the line representing $|\gamma_s| \leq 1$), this indicates that a 3 dB SNR increase is not sufficient because channel capacity can be degraded. For $|\gamma_s| \leq 0.7$, the CDF at

C_{UP}=0 is approximately 5 % and the decrement is small even when the channel capacity degrades. Thus, the effectiveness of $|\gamma_s| \leq 0.7$ is also verified by this figure.

3.5 Correlation Reduction by Dual-Polarization

When only focusing on the antenna, correlation reduction by suspended lines [120], electromagnetic band-gaps (EBGs) [121], and ground planes with a slit [122] have been considered. Here, an "envelope correlation" is calculated using S-parameters and radiation patterns [123], and the incoming wave is assumed to be identically-distributed to derive the correlation, However, for example in the LOS scenario, the incoming wave is not identically-distributed, and the correlation should be derived by considering both antenna and propagation parts. Schemes to reduce the correlation include the application of matching/decoupling networks [124] [81] and multipolarization [125]. In particular, the method of multipolarization is simpler because, for example, the configuration of matching/decoupling networks for three antenna elements is complicated [126]. Hence, this section discusses the application effect of multipolarization.

For MIMO spatial multiplex transmission systems, many studies have been performed to maximize the channel capacity [72] [73] [127], however, an antenna arrangement with a narrow element spacing causes a decrease in the channel capacity. One scheme to improve the situation is to use orthogonal polarization. Low mutual coupling prevents the decrease in radiation efficiency [76], and low spatial correlation is also obtained [125]. Aimed at indoor environments, various evaluations of MIMO systems using orthogonal polarization have been performed, and measurement campaigns have shown the effect of multipolarization [128]-[130]. The effect of orthogonal polarization depends on whether the environment is LOS or NLOS; however, even if we only focus on the former, the channel capacity can be changed by altering the positions of receiving antennas relative to transmitting antennas. For these MIMO systems, few experimental studies have been conducted on the position dependence of the characteristics in a LOS environment, and therefore, more investigations are needed.

This section presents 4 × 4 MIMO transmission experiments in a small room whose size is 5.80 m × 6.17 m × 2.7 m. Receiving points are changed, and the channel capacity for unipolarized and dual-polarized antennas are compared. This section also demonstrates the advantage of orthogonal polarization in LOS environments.

3.5.1 Measurement Setup

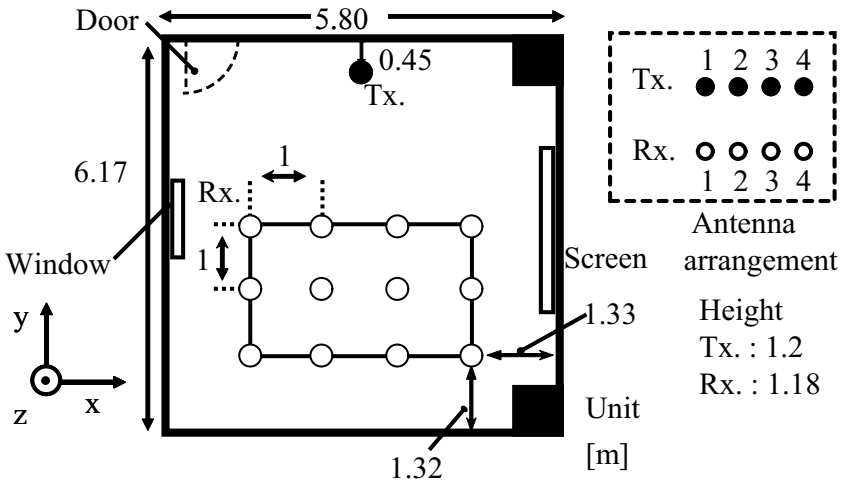

Figure 3.21. Drawing of the top view of the antenna arrangement and the measurement environment.

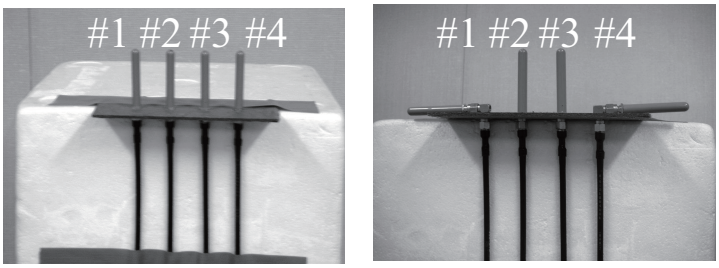

Figure 3.22. Transmitting antenna configurations. (a) Vertical-polarized sleeve antenna array and (b) vertical- and horizontal-polarized sleeve antenna array.

Channel measurement was conducted in a room with the size 5.80 m × 6.17 m × 2.7 m (Fig. 3.21). The transmitting antennas are fixed, while the receiving antennas can be moved, and the channel matrix **H** was estimated at 12 positions, as shown in Fig. 3.21. For transmitting antennas, two kinds of antenna configurations are considered: a four-element vertical-polarized sleeve antenna (V) (Fig. 3.22 (a)) and a four-element vertical- and horizontal-polarized sleeve antennas (V/H) (Fig. 3.22 (b)). In each case, the antenna configuration on the receiving side is identical to that on the transmitting side. The element spacing of the V configuration is a half wavelength, and the spacing is

identical to that of the V/H configuration. The environments between the transmitting and receiving antennas are LOS and quasistatic at all the Rx positions. The received power at each position is measured by a spectrum analyzer. The measurements are performed for a single element for the V configuration and multielements for the V/H configuration (i.e., one by one for each polarization, around 10 times), and maximum values are used in the evaluation. The noise level is -70 dBm, the carrier frequency is 5 GHz, and the transmit frame format consists of a header part with 50 symbols/ch and a data part with 300 symbols/ch.

3.5.2 Position Dependence of the Channel Capacity, Spatial Correlation, and Received Power

The received power, spatial correlation, and channel capacity at each receiving position for both configurations are shown in Fig. 3.23. Here, $(x, y) = (1, 1),\ (1, 2), \ldots,\ (4, 3)$ represent the number of receiving positions, and the meaning of the arrows at several positions is as referred to hereinafter. For spatial correlation, six combinations of the value are calculated for each antenna configuration since the number of receiving antennas is four, Therefore, their average values are used in the evaluation of the spatial correlation. The channel capacity is then normalized by the maximum value in each configuration.

In Fig. 3.23, the position dependence for those parameters is different between V and V/H. The received power at the position near the transmitting antennas is not always high although the measurement is performed in a LOS environment. The spatial correlation does not depend on the distance between the transmitting and receiving antennas. The channel capacity is dependent on the received power level, and its tendency is more clear in V.

Next, the position dependence of the channel capacity is evaluated by eigenvalues $(\lambda_i : i = 1, 2, 3, 4)$ of the spatial correlation matrix $(\mathbf{H}_n\mathbf{H}_n^H)$, where they satisfy $\lambda_1 > \lambda_2 > \lambda_3 > \lambda_4$ at each receiving position. The eigenvalues represent the power gain of virtual channels; in the LOS environment, the first and second–fourth eigenvalues are related to the direct and reflected paths, respectively [131].

Figure 3.24 shows the eigenvalues at each receiving position for V. The characteristics of the first, second, third, and fourth eigenvalues are shown in Figs. 3.24(a)–3.24(d),

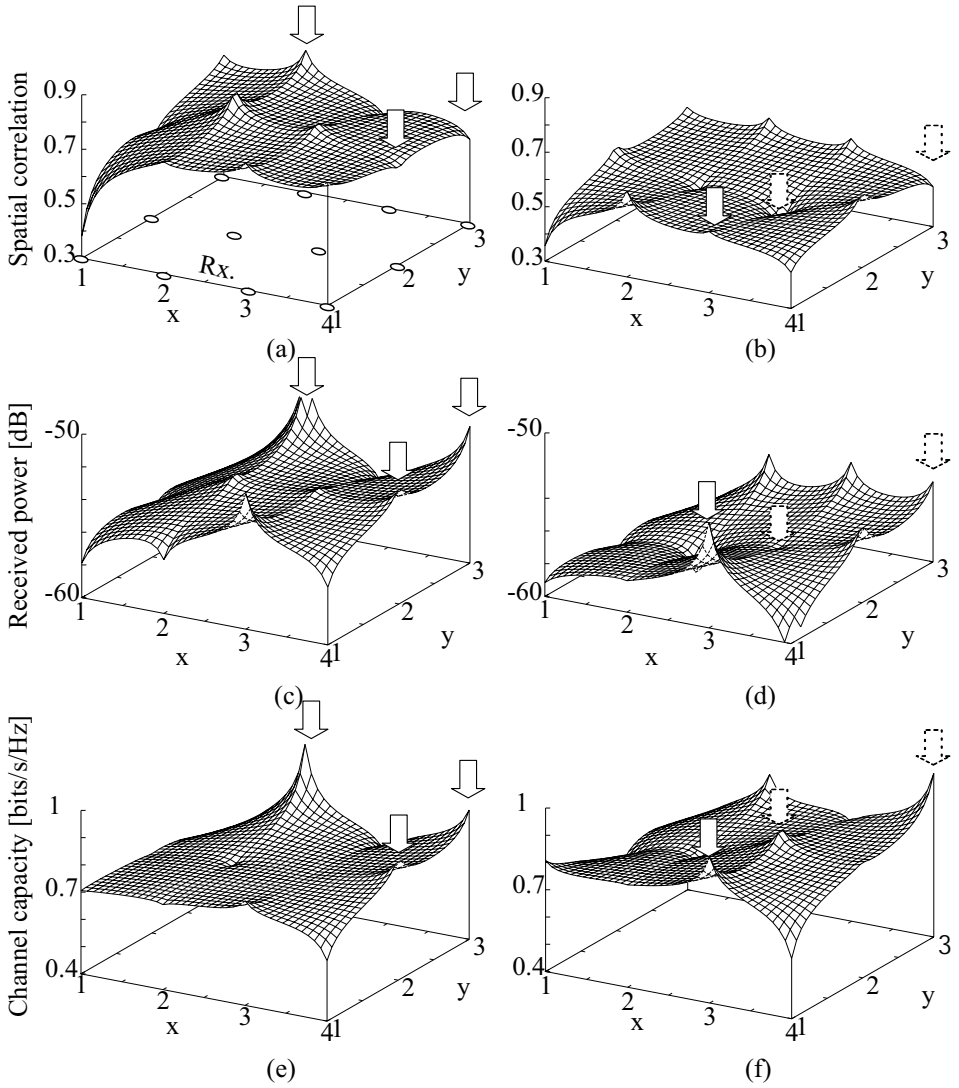

Figure 3.23. Position dependence of the spatial correlation, received power and channel capacity. (a), (c), and (e) are characteristics for V, (b), (d), and (f) are for V/H. (a) and (b) are spatial correlations, (c) and (d) are received power, and (e) and (f) are channel capacities.

respectively. The receiving positions are broadly classified into two groups: those with a large first eigenvalue compared to the other positions and those with small first and large second–fourth eigenvalues. Here, solid arrows indicate the positions with the largest second- and third-largest channel capacity, and the first eigenvalues are large at these positions. Meanwhile, the first eigenvalue is small and the second–fourth ones are large at $(x, y) = (1, 1)$ in Fig. 3.24. The spatial correlation is low at this position as shown in Fig. 3.23 (a); however, this does not significantly contribute to channel capacity

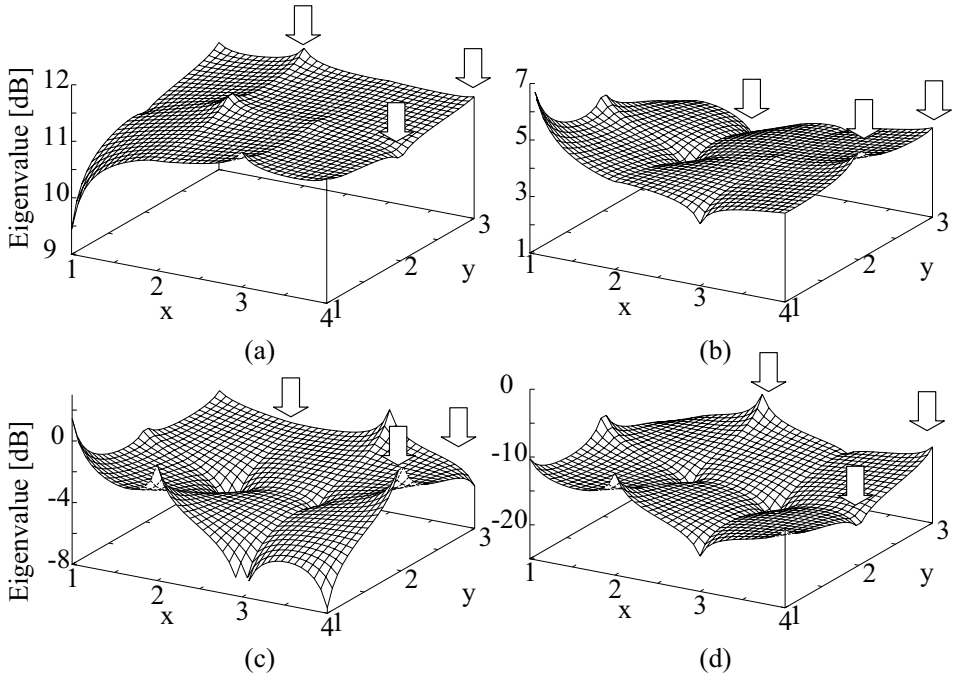

Figure 3.24. Position dependence of the (a) first, (b) second, (c) third, and (d) fourth eigenvalues for V.

enhancement. As a result, the direct wave is the dominant factor and the received power has a significant impact on the channel capacity for V.

In a similar manner, eigenvalues for V/H are shown in Fig. 3.25. The characteristics are divided into two groups, indicated by solid arrows and dotted arrows, respectively. At the former positions, the first eigenvalue is larger than those at the other positions and the influence of the direct wave is strong. The channel capacity enhancement arising from the received power is shown in Fig. 3.23(d). At the latter positions, the first eigenvalue is small and the second–fourth ones are large, and the spatial correlation is low, as shown in Fig. 3.23(b). At the positions indicated by dotted arrows, the decrease in the spatial correlation contributes to channel capacity enhancement, and for V/H, a large channel capacity is also achieved in this case.

3.5.3 Application Effect of Orthogonal Polarization

In the previous section, after measurements for V had been performed at all the receiving positions, an identical procedure was performed for V/H. Therefore, the displacement of

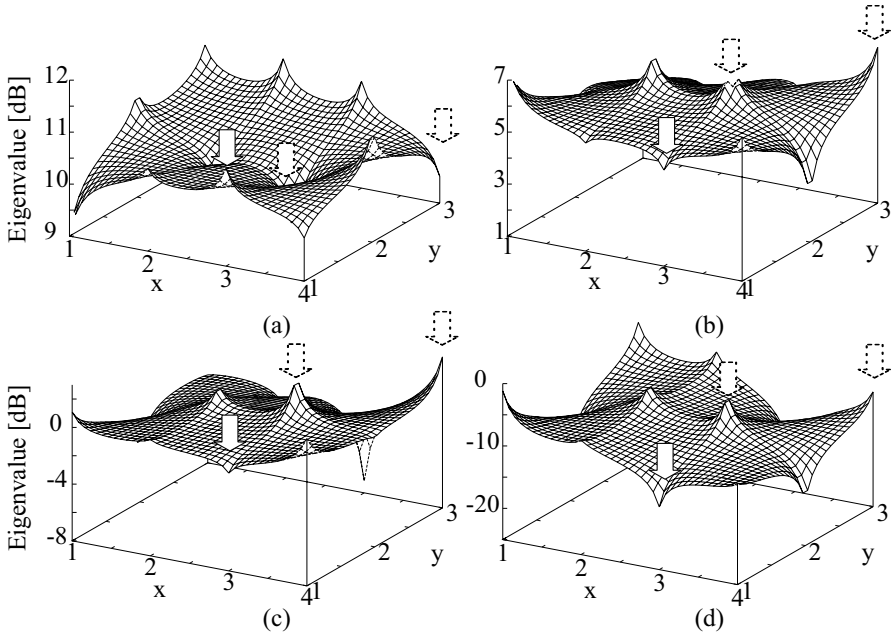

Figure 3.25. Position dependence of the (a) first, (b) second, (c) third, and (d) fourth eigenvalues for V/H.

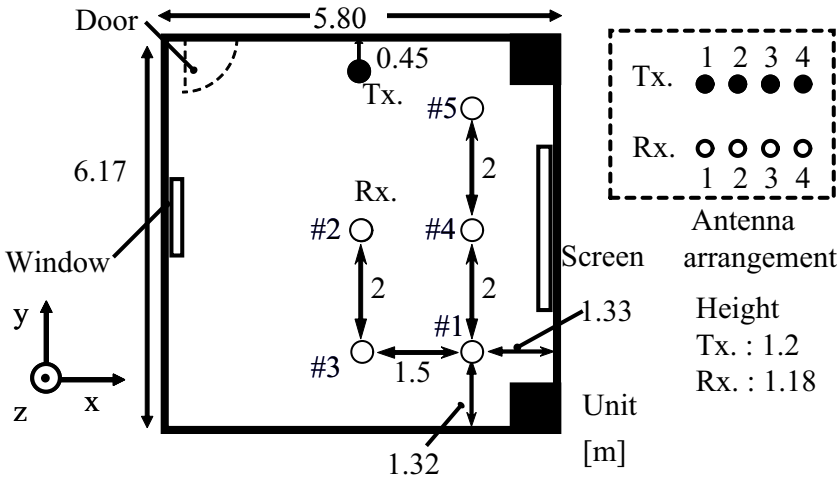

Figure 3.26. Positions of the receiving antennas.

the receiving points in addition to polarization also have an impact on each parameter (eigenvalues, spatial correlation, channel capacity, and received power.) To correctly evaluate the application effect of orthogonal polarization, the V configuration is replaced by a VH configuration with the positions fixed for several receiving positions, as shown

in Fig. 3.26 (#1–#5).

One position is set at the corner of the room, two positions are set in front of the transmitting antennas, and the other two positions are set in the vicinity of the wall. In each position, the SNR is derived by obtaining 10 data per element and averaging those for all the receiving antenna elements. The measurement parameters are identical to those of the previous section. Figure 3.27 shows the SNR, spatial correlation, and channel capacity for V and V/H at five receiving positions. In the SNR, the comparative merits and demerits of V and V/H are different depending on the receiving points, and large variations are confirmed for V (Fig. 3.27(a)). For the V/H configuration, the spatial correlation for VH decreases between approximately 0.2 and 0.4 at all positions, compared to V (Fig. 3.27(a)). Then, for the V/H configuration, the channel capacity increases between approximately 0.1 and 3.1 at all the receiving positions, although the increase is small at positions #3 and #5.

The enhancement effect of the V/H configuration relative to the V configuration is described next. Table 3.1 lists the improvement factor for each parameter obtained by using the V/H configuration. At position #4, both the increase in the SNR and the decrease in the spatial correlation are large, and the enhancement of the channel capacity is also large. In a similar manner, the enhancement of channel capacity is also large at position #2. However, although the SNR decreases at positions #1, #3 and #5, the V/H configuration enhance channel capacity. This indicates that the decrease in spatial correlation by orthogonal polarization works effectively for channel capacity enhancement because the channel capacity slightly increases in spite of the drastic decrease in the SNR at position #3.

Then, investigation is conducted about the difference in the improvement factor of the channel capacity at positions #1 and #5, where denote the similar tendency for the improvement of the spatial correlation and the SNR. The channel capacity is evaluated by eigenvalues normalized by the maximum value (first eigenvalue). By using these parameters, the intensity of the reflected wave relative to the direct wave is assessed. Figures 3.28(a) and 3.28(b) show the normalized eigenvalues for V and V/H at positions #1 and #5, respectively. At position #1, all of the second–fourth eigenvalues for V are larger than those at position #5, and the enhancement of the second and third one for V/H is larger than those at position #5 as well. (Fig. 3.28(a)). Meanwhile, at position #5, the third and fourth eigenvalues are very small and the enhancement by using a

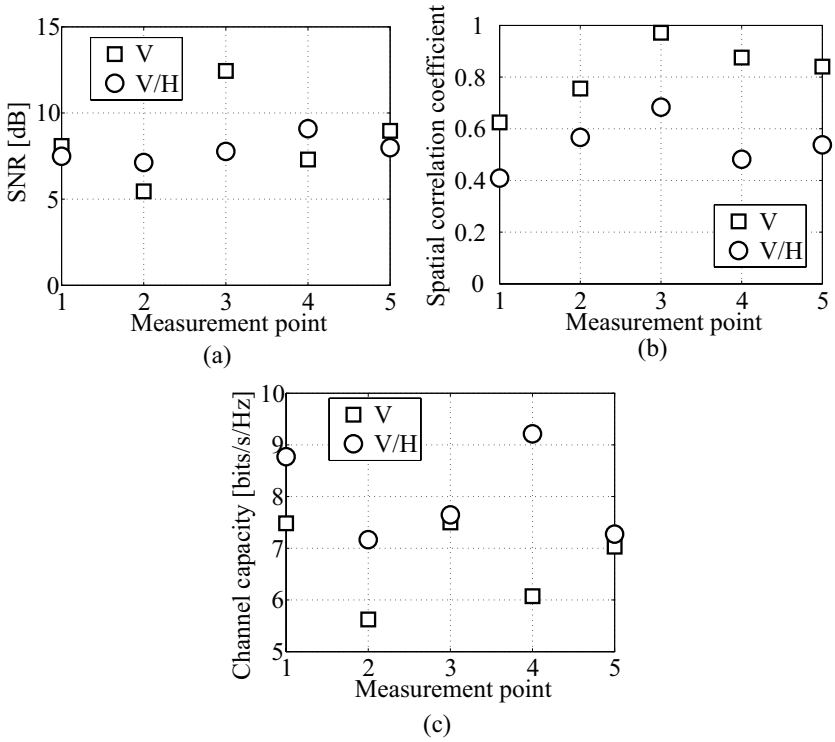

Figure 3.27. Performance comparison between V and V/H: (a) SNR, (b) spatial correlation, and (c) channel capacity.

Table 3.1. Improvement factor of SNR, spatial correlation, and channel capacity by V/H.

Measurement position	Increment in SNR [dB]	Decrement of spatial correlation	Enhancement of channel capacity [%]
1	-0.59	0.22	+ 17.2
2	+1.68	0.19	+ 27.5
3	-4.67	0.29	+ 1.95
4	+1.79	0.39	+ 51.7
5	-0.97	0.30	+ 3.45

V/H configuration is small, as shown in Fig. 3.28(b).

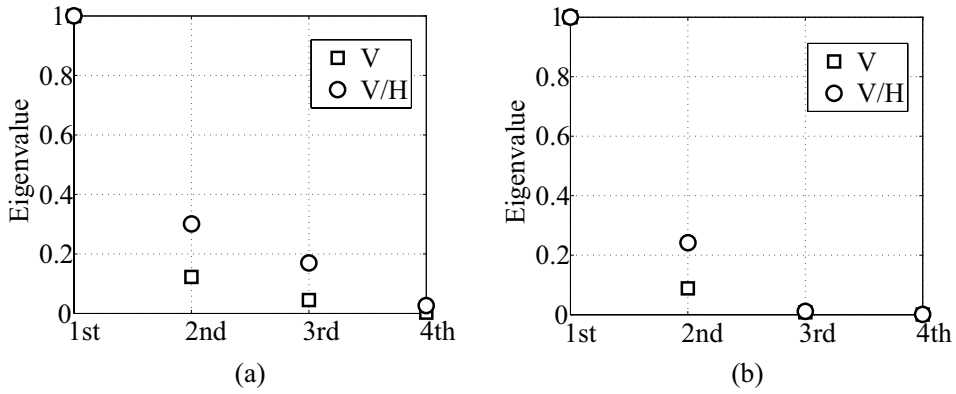

Figure 3.28. Eigenvalues normalized by the first eigenvalue: (a) position #1 and (b) position #5.

3.6 Enhancement of Channel Capacity by Increasing SNR

The previous section mainly focused on the enhancement of channel capacity by reducing the spatial correlation. This section describes the enhancement of channel capacity by increasing the SNR when the spatial correlation is not significantly high. This section only briefly introduces the concept; a more detailed description is provided in the next chapter.

Consider LOS communication, which the channel is a generically correlated channel. From the result of Fig. 3.11, the channel capacity rapidly decreases when the spatial correlation is close to 1. However, when the spatial correlation decreases to some extent, large channel capacity can be expected even in a LOS channel, which is confirmed from the results of Figs. 3.19 and 3.20. Generally, it is considered that channel capacity for i.i.d channel (non-correlated channel) is larger than that for a LOS channel [132]. However, this conclusion is based on the assumption that the received power is fixed. When the transmitting power is fixed, the channel capacity for a LOS channel can outperform that for an NLOS channel with low spatial correlation because of the large received power [65]. Molisch et al. [132] also conclude that this comparison, assuming that the receiving power is fixed, is not realistic.

Figure 3.11 is a conceptual diagram showing the variation in channel capacity as a function of the SNR in MIMO systems. Figure 3.29(a) shows the channel capacity

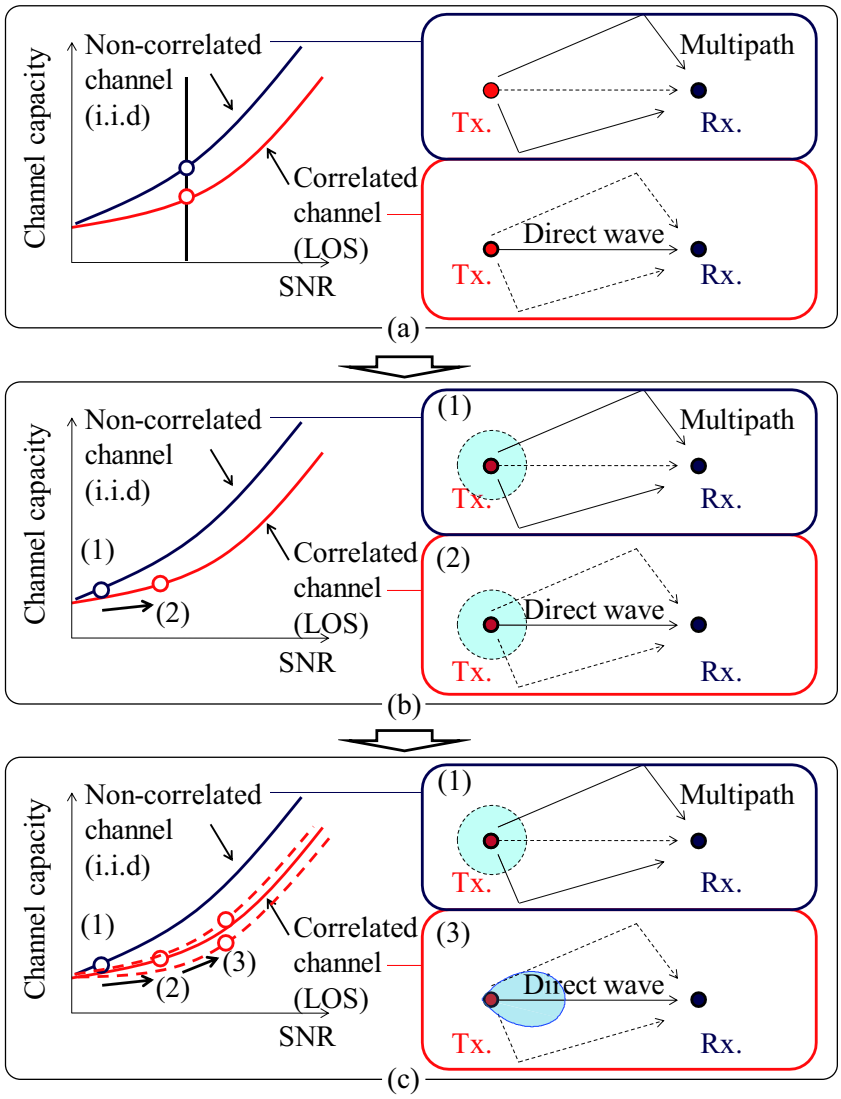

Figure 3.29. Conceptual diagram of the enhancement of channel capacity by increasing SNR in MIMO systems. Channel capacity performance (a) when the received SNR is fixed, (b) when the difference in SNR between i.i.d and LOS channels is considered (omnidirectional radiation patterns), and (c) when the difference in SNR is considered and directional antennas are applied for LOS channels.

performance when the SNR in LOS and i.i.d channels are assumed to be identical. Under this assumption, the channel capacity for the i.i.d channel is larger than that for the LOS channel. However, when the transmitting power is assumed to be fixed, and the difference in received power between the i.i.d and LOS channels is considered, the channel capacity for the LOS channel can be larger than that for the i.i.d. one, as shown

in Fig. 3.29(b). Furthermore, application of directional antennas with appropriate radiation patterns can lead to larger channel capacity in the LOS scenario, as shown in Fig. 3.29(c).

3.7 Summary

This chapter presented the relationship among parameters relating to the channel matrix, SNR, and channel capacity to enhance channel capacity effectively. The evaluation was mainly based on 2×2 MIMO systems. First, this chapter theoretically explained that even if the spatial correlation were reduced, the channel capacity could be degraded because of the received power imbalance. Then, the equation of the channel capacity was divided into two elements depending on the SNR C_{SNR} and the spatial correlation coefficient C_{COR}. For C_{COR}, two scenarios were extracted, and this chapter analytically and empirically revealed that eigenvalues were an important factor for estimating channel capacity. Moreover, this chapter also focused on a spatial correlation reduction under the condition that the SNR and the components of the channel matrix were varied simultaneously. When MIMO antenna selection and radiation pattern reconfiguration are assumed as a concrete example, variations in the SNR and the spatial correlation often have a trade-off relationship. For this scenario, this chapter revealed that the correlation reduction requirement of $|\gamma_s| \leq 0.7$ was effective for channel capacity enhancement.

In association with the above correlation reduction, this chapter presented a measurement based evaluation of a 4×4 MIMO system using unipolarized antennas (V) and dual-polarized antennas (V/H) in a LOS environment. By using the position dependence of the received power, spatial correlation, and eigenvalues, for V, it was demonstrated that the direct wave was a dominant factor, and the received power level contributed to an increase in the channel capacity. For V/H, the receiving positions with large channel capacity were divided into two groups: one with high received power and one with low spatial correlation. Then, for V/H, the decrease in the spatial correlation by orthogonal polarization had a strong impact on the channel capacity enhancement.

Finally, this chapter briefly introduced the concept of enhancing channel capacity by increasing the SNR. Given a fixed SNR, the channel capacity for an i.i.d channel is larger than that for a LOS channel. However, given a fixed transmitting power, the channel capacity for a LOS channel can outperform that for an i.i.d channel because of

the large SNR. Furthermore, the application of directional antennas with appropriate radiation patterns can lead to larger channel capacity. This discussion is relevant to the next chapter, where details are further elaborated upon.

Chapter 4

MIMO Systems That Utilize Radiation Patterns Effectively

4.1 Introduction

In accord with the concept of Chapter 3.6, this chapter describes the MIMO antenna configuration methodology that uses radiation patterns effectively. The discussion is mainly focused on indoor BSs, and the goal is the enhancement of MIMO performance using fixed radiation patterns.

First, this chapter describes the situation in which the BS is mounted in the vicinity of wall. Beneficial use of radiation patterns has been reported to achieve good MIMO performance [66], [67], [72], [73]. As a first step, for vertical-polarized elements, the half-power beam width (HPBW) and the angle between beams are regarded as variables, and a directional antenna configuration suitable for each aspect ratio of the room is derived. This examination is based on ray-tracing propagation analysis, and 2×2 MIMO communications in LOS scenarios are assumed. As a second step, the discussion is extended to 4×4 MIMO communications, and the design guidelines of antennas are determined. In this examination, multipolarization is applied, and changes in the array arrangement for the MT are taken into account. As a third step, a two-element patch antenna array with dual feeds is fabricated based on the design guidelines. The measurement results show that the improvement factor in channel capacity is shown to be approximately +20% at two out of three typical positions, compared to a sleeve

antenna configuration.

Then, this chapter describes the situation in which the BS is mounted in the center of the ceiling. Low-profile, small structures are required to configure the MIMO antenna. First, this chapter assumes downlink transmission in indoor MIMO systems and presents the design guidelines for the radiation pattern to obtain large channel capacity by the ray-tracing method. This chapter then proposes a unidirectional, dual-polarized MIMO antenna with a thickness of 0.24λ based on the design guidelines. The proposed antenna consists of dipole antennas mounted horizontal to the ground plane and cavity-backed slot antennas for vertical polarization. This chapter discusses the application of the proposed antenna to 2×2 MIMO transmission and demonstrates the effectiveness of channel capacity enhancement in an actual environment. The improvement factor is revealed to be +16.2% with a place-averaged value compared to a sleeve antenna configuration. Furthermore, a lower-profile MIMO antenna consisting of a loop and dipole elements is presented. The height of this antenna is 0.16λ (20 mm), and it is designed based on the guidelines derived by a ray-tracing propagation analysis.

Finally, a MIMO handset antenna is examined. As is the case for the BS, enhancement of channel capacity with fixed antenna configurations is examined on the MT side. In a handset MIMO antenna, small numbers of elements and ports are desired. To achieve a large channel capacity in this situation, adjustment of the radiation patterns is important. This examination focuses on analog techniques, and phase-difference feeding is applied to a handset MIMO antenna with human body effects included. The phase difference is determined and fixed based on the mean effective gain (MEG) and the correlation coefficient. The results of a propagation analysis show that channel capacities with optimum phase difference are larger than those without phase difference in all angles of incoming wave. This result indicates that the enhancement can be achieved by using a fixed phase difference, namely, by using simple feeding circuits such as delay lines.

4.2 A BS Antenna Mounted in the Vicinity of a Wall

4.2.1 Determination of Antenna Design Guidelines by Numerical Evaluations

Before antenna design, appropriate parameters of the radiation pattern to obtain large channel capacity are decided using the ray-tracing method. This section shows the assessment strategy.

Channel Modeling

In this section, the handled target is narrow band single user (SU) MIMO systems. The number of transmitting (Tx) and receiving (Rx) antennas are denoted by N_t and N_r, and channel matrix $\mathbf{H}$ with $N_r \times N_t$ elements is modeled by the ray-tracing method. Here, the image method is used to calculate the rays precisely [133]. In the calculation of the received electric field intensity, for simplicity, this analysis considers only reflection waves and do not consider diffraction waves or scattering waves. The composite electric field E used to generate channel matrix $\mathbf{H}$ is given as follows:

$$E = \sum_i \frac{\lambda}{4\pi d(i)} e^{-jkd(i)} G_t(i) G_r(i) \Gamma(i)^{l+m+n} \tag{4.1}$$

where λ is the wavelength, $d(i)$ is the propagation distance of the ith ray, k is the wave number, and $G_t(i)$ and $G_r(i)$ are the Tx and Rx antenna radiation patterns in the direction of ray. The ith ray is assumed to be reflected l, m, and n times in the zx, yz, and xy planes, respectively. Then, $\Gamma(i)$ indicates multiplication by the reflection coefficient of $l + m + n$ times.

In (4.1), the effect of the radiation patterns is considered by G_t and G_r. The use of directional Tx antennas is assumed, and G_t is calculated as described in [134]:

$$\begin{aligned} D(\theta) &= \begin{cases} \cos^{\Theta_h}(\theta), & 0 \le \theta \le \pi/2, 3\pi/2 \le \theta \le 2\pi \\ 0, & \pi/2 \le \theta \le 3\pi/2 \end{cases} \\ \Theta_h &= -\frac{\log_{10} 2}{\log_{10} \cos(\theta'_h/2)} \end{aligned} \tag{4.2}$$

where $D(\theta)$ is directivity function, θ is the radiation angle from the maximum radiation

direction, and θ'_h is the half-power beam width (HPBW) in a certain plane. Equation (4.2) gives the radiation pattern in a certain plane. However, the radiation pattern in an arbitrary plane is the same. The front-to-back (FB) ratio is infinity, and its shape is a pencil beam. The antenna gain G depending on HPBW is defined as in [135]:

$$G = 10 \log_{10} \frac{4\pi}{\theta_h \phi_h} \tag{4.3}$$

where θ_h rad and ϕ_h rad are the HPBW in the θ and ϕ planes, respectively, and, for simplicity in calculation, θ_h and ϕ_h are set to the same angle throughout the simulation.

Determination of Parameters: Examination of 2 × 2 MIMO Systems Considering the Aspect Ratio of the Room

To determine the suitable design guidelines for the MIMO antenna radiation patterns, parameter studies are conducted using ray-tracing propagation analysis based on the scenario presented in Fig. 4.1, where the variable t denotes the aspect ratio of the room. The room size is given by 6 m × 6t m × 2.7 m. In this scenario, the BS is placed near a wall, and the channel matrices are calculated at 25 MT positions (x, y, 1). The environments between the BS and all MT positions are LOS without obstacles. The simulation parameters are shown in Table 4.3. The transmitting and noise powers are -5 dBm/ch and -85 dBm, respectively, and 2×2 MIMO downlink communication is assumed. The inter-element spacing at both BS and MT are half-wavelength of the 5 GHz

Table 4.1. Principal simulation parameters.

The number of Tx antenna	2
The number of Rx antennas	2
Polarization radiated from Tx antennas	Vertical
Carrier frequency	5 GHz
Symbol rate	4 Msps
Modulation scheme	QPSK (header),16QAM (data)
Transmitting power	-5 dBm/ch
Noise power	-85 dBm
Wall material Relative permittivity/Conductivity Reflection times	Concrete 6.76/0.0023 S/m Up to 5 times

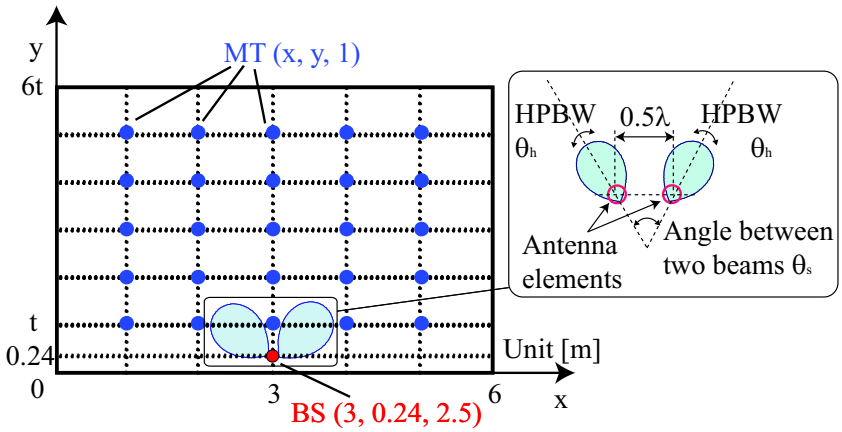

Figure 4.1. Analyzed room model and location of the BS and MT for determining suitable radiation patterns (overhead view). The room height is 2.7 m. t denotes the aspect ratio of the room.

carrier frequency. BS is set in the position of 0.2 m below the ceiling and 0.24 m from the wall.

For reasons of expediency, the room sizes of x-direction and y-direction are denoted by x_{room} and y_{room}, respectively. In this simulation, channel matrices **H** are calculated at 25 points at intervals of $x_{room} \times 1/6$ m and $y_{room} \times 1/6$ m by moving the MT for a certain aspect ratio. The procedure deriving **H** is shown as follows:

1. Signals constituted by header of Maximum-length sequences (M-sequence) and data are transmitted from BS.

2. Signals received by MT through the propagation channel are generated by ray-tracing method.

3. The head of the received frame is searched by a complex sliding correlation using a reference signal.

4. The channel matrix **H** is estimated from the reference signal, received data, and correlation coefficient obtained by a complex sliding correlation.

On the BS side, the HPBW of directional antennas (θ_h) shown in Fig. 4.1 is changed from 30° to 150° at intervals of 30°. Furthermore, the separation angle between two beams (θ_s) is changed from 0° to 180° at intervals of 20°. This operation is repeated by changing t from 0.5 to 2 at intervals of 0.1. Figure 4.2 shows the channel capacity for

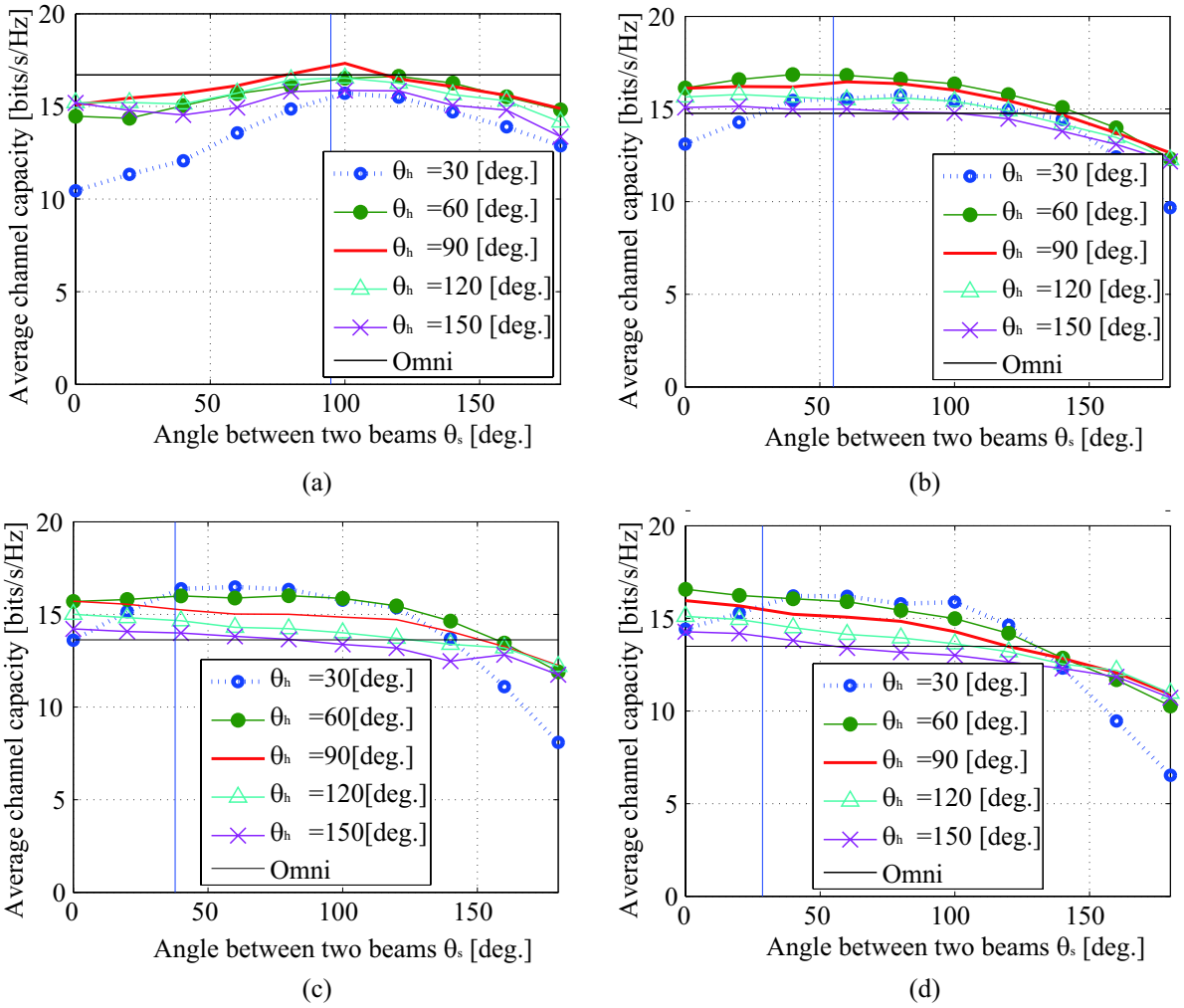

Figure 4.2. Average channel capacity for each HPBW θ_h as a function of angle between two beams θ_s. (a) t=0.5, (b) t=1, (c) t=1.5, and (d) t=2.

each θ_h as a function of θ_s. In each figure, place-averaged channel capacity is used, and the capacity for omni-directional (isotropic) antennas are also evaluated. Here, omni-directional (isotropic) radiation patterns are considered on the MT side. From these graphs, it is confirmed that the channel capacity for appropriate directional antenna configurations outperform that for omni-directional antennas. The radiation pattern has the optimum θ_s to maximize the average channel capacity.

Figure 4.3 shows the HPBW (θ_h) to maximize the average channel capacity as a function of t. The θ_h becomes small as the t increases, and narrow HPBW is effective. The

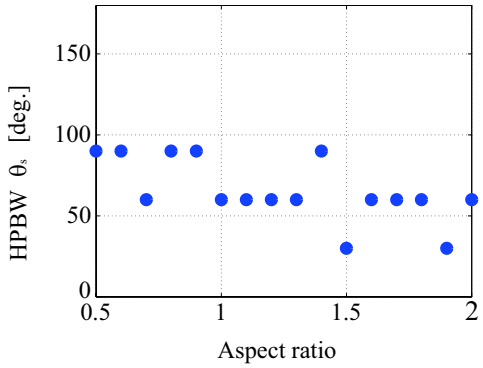

Figure 4.3. Variation in HPBW achieving maximum average channel capacity as a function of the aspect ratio t of the room.

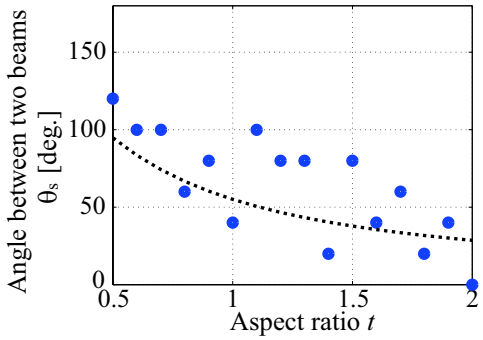

Figure 4.4. Angles between two beams θ_s leading to the maximum space-averaged channel capacity. (θ_h is fixed to 60°, and the dotted line indicates θ_s obtained when the main beams are pointed to the corner of the room.)

distribution is concentrated on $\theta_h = 90°$ and $\theta_h = 60°$ in $t < 1$ and $t \geq 1$, respectively. In these examples, since the channel capacity is considered to be statistically large at $\theta_h = 60°$, as a next step, θ_s is changed with fixed HPBW ($\theta_h = 60°$).

Figure 4.4 shows the relationship between θ_s with the maximum place-averaged channel capacity and the aspect ratio. The distribution following the dotted line indicates that the main beams of the BS should be directed towards the room corners to increase the channel capacity. Here, θ_s when the main beams of the BS is directed towards the room corners is denoted by $\theta_{s,corner}$. Then, place-averaged channel capacity for θ_h=60° and θ_s=$\theta_s, corner$ are derived and are compared with maximum place-averaged channel capacity obtained by selection of optimum θ_h and θ_s. Those channel capacities are denoted by C_{corner} and C_{max}, respectively, and those performances are shown in Fig.

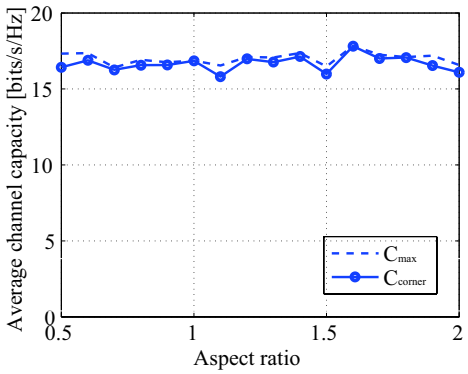

Figure 4.5. Comparison between C_{corner} and C_{max}. Here, C_{corner} indicates place-averaged channel capacity for θ_h=60° and θ_s=$\theta_{s,corner}$. C_{max} indicates maximum place-averaged channel capacity in the case of optimum θ_h and θ_s.

4.5. Since the performances of C_{corner} and C_{max} are similar, The main beams directed towards the room corners is effective as a design guideline of radiation patterns.

Determination of Parameters: Examination of 4 × 4 MIMO Systems

The improvement effect of channel capacity is not limited to 2 × 2 MIMO systems, and it is also confirmed for four streams. Here, considering ease of the realization, the applied HPBW is wider than the previous target HPBW (60°). Then, the inter-element spacing of BS is changed from 0.5λ to 1λ because the antenna spacing for BS is large compared to that for MT, and dual-polarization is applied to reduce spatial correlation. Now, to derive channel capacity, the operation of the channel estimation is omitted, and channel matrices obtained by ray-tracing propagation analysis are directly used. In the simulation, electric fields are decomposed to TE/TM components in the reflection of the propagation wave. Here, BS antennas are mounted at (3, 0.2, 2.5) in the room of 6 m × 6 m × 2.7 m, and the channel matrices are calculated at 121 MT positions in total by moving the positions. The other parameters such as carrier frequency, transmitting and noise power, wall material and reflection times are identical to the previous section.

Figure 4.6 shows the simulation scenario and the directional antenna configuration for BS. Here, two beams are vertical polarization, and the other beams are horizontal polarizations. The radiation patterns for vertical and horizontal polarizations are overlapped. The angle between beams in the horizontal plane is 60°, which leads to beams nearly directed to the corner of the room. The radiation patterns are tilted

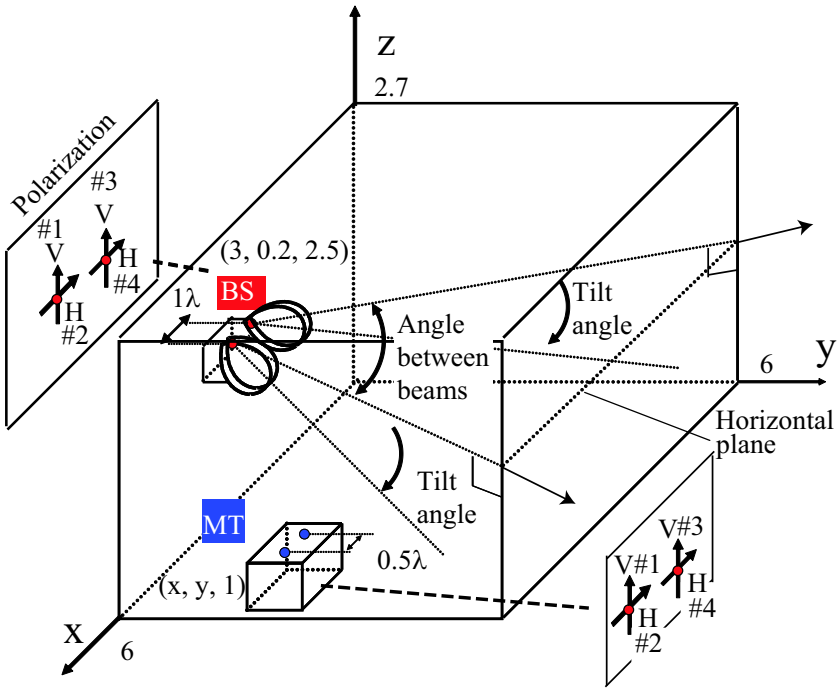

Figure 4.6. Analytical model for directional antenna configurations applied to 4 × 4 MIMO systems.

downward by 30°, and the HPBWs and tilted angles are identical in four beams. Then, this configuration denoted by VH is compared with the other configurations, such as V_i, V_d, V, VH_i, and VH_d. Here, V_i and V_d represents isotropic and dipole radiation patterns for vertical polarization, respectively, and VH_i and VH_d represent those radiation patterns for dual polarization, respectively. In VH_i and VH_d, the positions of vertical and horizontal polarization elements are identical. On the other hand, V is the directional antenna configuration radiating vertical polarization. In V, a four-element linear array parallel to x-axis is used. The beams from each element are pointed to 30°, 60°, 120°, and 150° directions from x-axis in the horizontal plane, respectively. In other words, two beams are pointed to the corner of the room and the other two beams are pointed to the direction to bisect the remaining angles in the horizontal plane. The beams also tilted downward by 30°. On the other hand, on the MT side, the radiation pattern is isotropic, and vertical and horizontal polarization elements mounted at the same positions are applied.

Based on cumulative distribution function (CDF), channel capacity for each antenna

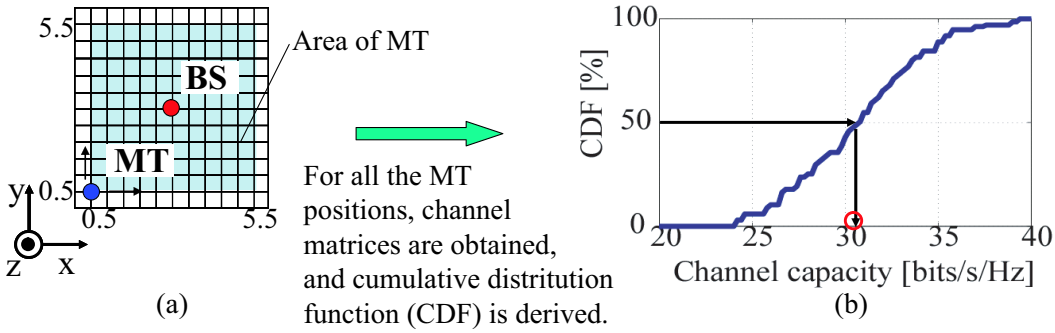

Figure 4.7. Derivation process of median values of channel capacity based on the cumulative distribution function (CDF). (a) Overhead view of the room, and (b) CDF of channel capacity.

Table 4.2. Median values of the channel capacity based on the CDF. Improvement factor indicates the value compared with V_i.

Radiation patterns	Channel capacity [bits/s/Hz]	Improvement factor [%]
V_i	28.51	0
V_d	28.96	+1.58
V	32.66	+14.6
VH_i	29.10	+2.07
VH_d	29.09	+2.03
VH	34.52	+21.1

configuration is evaluated. Figure 4.7 shows the derivation process of median values of channel capacity based on the CDF. For each antenna configuration, the CDF of the channel capacity is derived from channel matrices obtained at plural MT positions, and the value of CDF=50% is extracted. Table 4.2 shows the median value for each antenna configuration. In this table, the channel capacity is enhanced by using orthogonal polarization and directive patterns effectively, and the effectiveness of the radiation patterns shown in Fig. 4.6 is confirmed. In [136], it was confirmed that the beams toward corner of the rooms were effective in 5 m × 8 m × 2.7 m. Therefore, it is considered that this beam configuration can be applied in small scale-rooms.

Consideration of MT Antenna Arrangement

This section describes the antenna configuration for the BS, considering the arrangement of the MT in 4 × 4 MIMO downlink transmission. Here, the main beam directions and

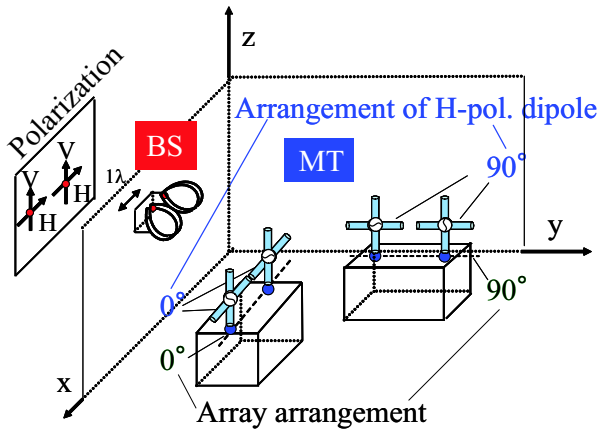

Figure 4.8. Antenna arrangement for MT.

downward tilted angles are identical to those of the previous section. On the MT side, vertical and horizontal polarization elements with dipole radiation patterns are considered, and the arrangement of horizontal polarized (H-pol.) dipole elements and array arrangement (Fig. 4.8) are changed separately.

First, the impact of arrangement of H-pol. dipole elements for the MT on channel capacity is examined. In this simulation, carrier frequency, transmitting and noise power, wall material, and reflection times are identical to those of the previous section. Here, this examination focuses on the BS configuration of HPBW=40°, 60°, 80°, and 100° for the directional antenna configurations (Dir) in Fig. 4.6. This examination also uses BS configurations with dipole radiation patterns (Dip) and with only launched electric field components without considering any antennas (LE). Then, for a certain BS configuration and MT configuration with a certain arrangement angle in H-pol. dipole elements (θ_{H-pol} in Fig. 4.9(a)), the channel capacity is obtained at 121 MT positions just as in the previous section, and the CDF is derived along with Fig. 4.7. Then, CDF values of 10%, 50%, and 90% are extracted. For all the θ_{H-pol}, an identical procedure is performed, and then, for certain BS configurations, the values of CDF=10%, 50%, and 90% in the channel capacity as a function of θ_{H-pol} are obtained as shown in Fig. 4.9. In this figure, only the performances between 0° and 90° are shown because the performances are almost symmetric about θ_{H-pol}=90°.

In Fig. 4.9, channel capacity enhancement by directional antennas is confirmed for all θ_{H-pol}. This indicates that regardless of the arrangement of H-pol. dipole elements

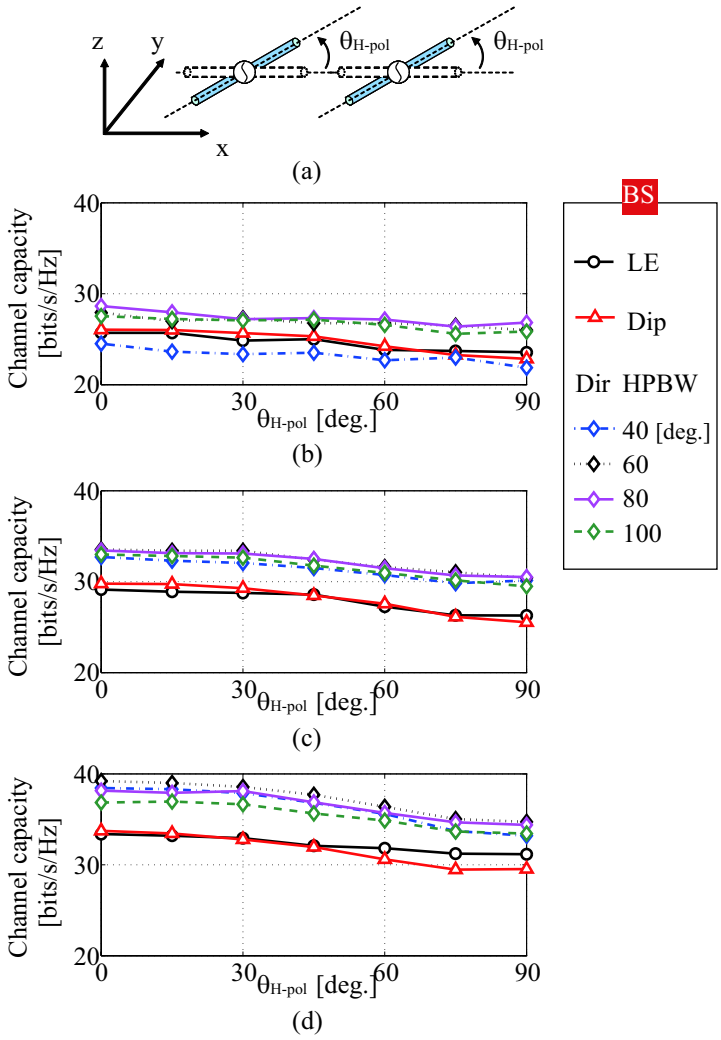

Figure 4.9. (a) Definition of θ_{H-pol}, which represents the arrangement angle of H-pol. dipole elements, and the CDF values of (b) CDF=10%. (c) 50%, and (d) 90% in the channel capacity for each BS configuration as a function of θ_{H-pol}.

for the MT, the effectiveness of directive radiation patterns for the BS remains valid. Here, the channel capacity decreases as θ_{H-pol} increases because the incident electric fields of the MT antennas are changed as θ_{H-pol} becomes large. In fact, the directions of the H-pol. dipole elements for the BS and MT are at right angles to each other at θ_{H-pol}=90°, and in this case, the correlation coefficient becomes large [137]. However, since this tendency appears in all the BS configurations, the comparative merits and demerits of Dir and Dip/LE are not changed.

Variations in the channel capacity as a function of HPBW for CDF=10%, 50%, and

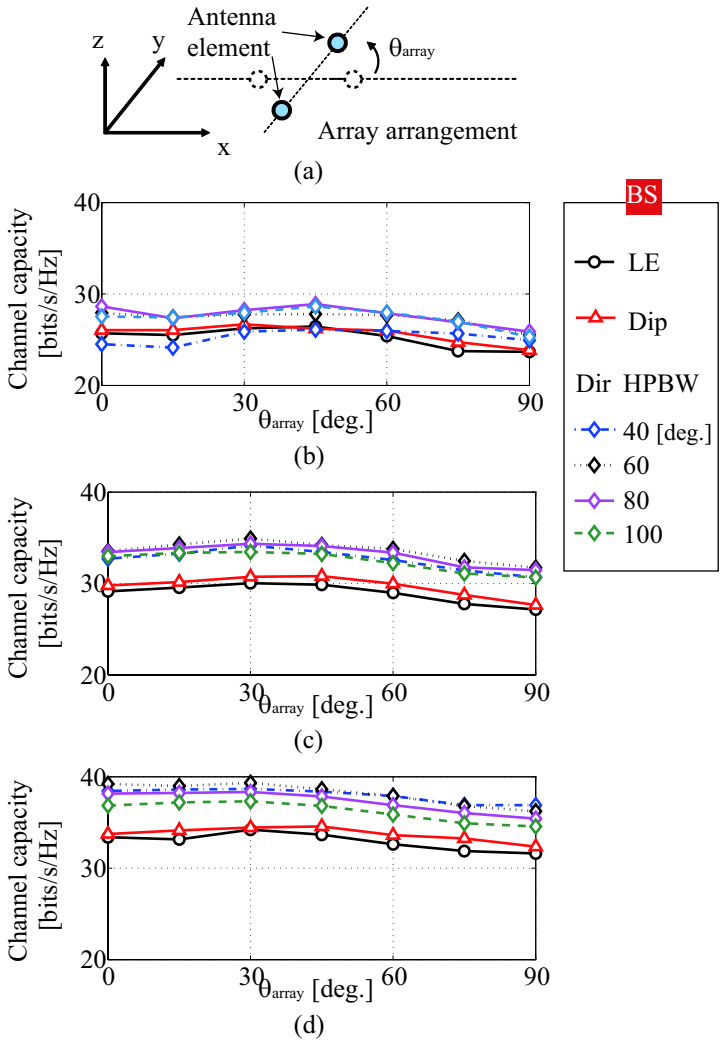

Figure 4.10. (a) Definition of θ_{array}, which represents the angle of array arrangement, and the CDF values of (b) CDF=10%. (c) 50%, and (d) 90% in the channel capacity for each BS configuration as a function of θ_{array}.

90% are now evaluated. In particular, property variation is rapid for CDF=10%, and channel capacity severely degrades for HPBW=40°. The CDF=10% corresponds to MT positions with a small channel capacity. Therefore, this degradation results from the reception level of the direct wave becoming small at some positions when a narrow HPBW is used. However, wide HPBW is not always good, and the optimum HPBW is 60-80°. In contrast, for CDF=90°, the channel capacity for HPBW=40° is similar to that for HPBW=80°. The CDF=90° corresponds to the MT positions with a large

channel capacity. Although gain is enhanced for HPBW=40°, the maximum channel capacity is not changed. This can be explained by problems of balance between SNR and spatial correlation and indicates that SNR and spatial correlation have a trade-off relationship for channel capacity, and that SNR enhancement does not always lead to channel capacity enhancement.

The impact of the array arrangement for the MT on channel capacity is now examined. Figure 4.10 shows the channel capacity as a function of θ_{array} (Fig. 4.10(a)), which is derived in the same manner as Fig. 4.9. As shown in this figure, channel capacity enhancement by directional antennas is also confirmed for all θ_{array} when the angle of the array arrangement is changed. When the channel capacity at θ_{array}=0° is compared with that at θ_{array}=90°, the channel capacity degrades at θ_{array}=90°. Reference [137] focused on the positions with a large difference in the channel capacity between θ_{array}=0° and θ_{array}=90°, and revealed the above reason using eigenvalues. At these positions, the third and fourth eigenvalues are small in θ_{array}=90°. In other words, MIMO transmission is concentrated on the upper eigenvalue. However, since the tendency also appears when the BS configuration is replaced by an LE configuration, the comparative merits and demerits of Dir and Dip/LE are not changed. In this figure, it is also confirmed that an HPBW range of 60°-80° is appropriate.

4.2.2 Fabricated Antenna and Measurement

Before the explanation of the fabricated antenna and the measurement performance, the design guideline for BS based on simulation results are shown as follows,

- Outline is based on Fig. 4.6.
- Target of HPBW and target tilted angle are about 80° and 30°, respectively.
- 4 × 4 MIMO transmission is assumed, and two combinations of two beams overlapped with dual-polarization are pointed to the each corner of the room.

The effectiveness of above guidelines are still valid regardless of array arrangement for MT.

The antenna based on the above design guidelines consists of a two-element patch antenna array with dual feeds, as illustrated in Fig. 4.11(a). Two beams with orthogonal polarizations are radiated from each patch antenna, and those are tilted downward

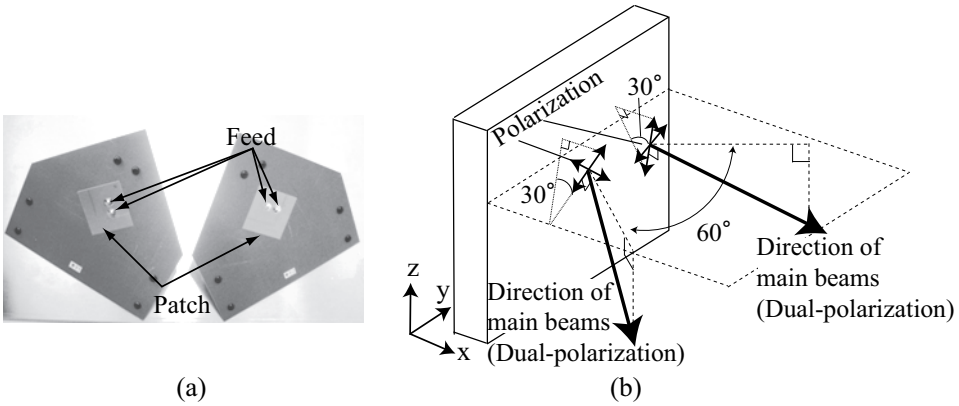

Figure 4.11. (a) Fabricated patch array. (b) Directions of the main beams.

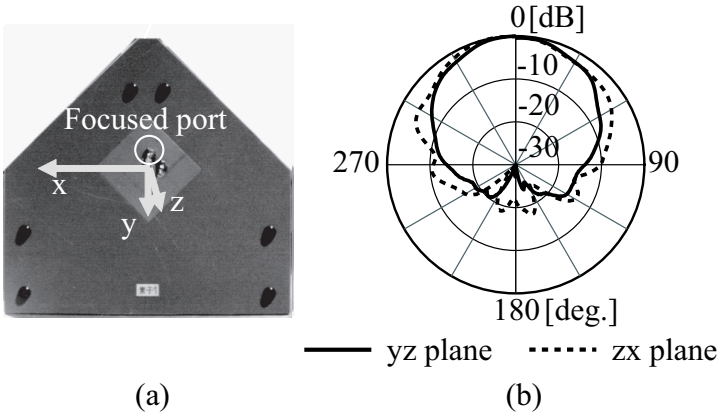

Figure 4.12. (a) Definition of the x, y, and z-axes in the BS patch antenna. (b) Radiation patterns in the yz and zx planes.

mechanically, as shown in Fig. 4.11(b). The angle between beams in the horizontal plane is 60°, and it is appropriate for 6 × 6 × 2.7 m when the BS is mounted near the wall. Figure 4.12 shows the radiation patterns, and the HPBWs in the yz and zx planes are approximately 80° and 90°, respectively, and the antenna gain is 7.0 dBi.

The channel capacity of the BS adopting a patch array was measured under the environment shown in Fig. 4.13. The room size is about 6.2 m × 5.8 m × 2.7 m, and is close to 6 m × 6 m × 2.7 m. As a reference, a sleeve array is also used for a dual-polarization BS antenna, with the spacing between the vertical and horizontal oriented sleeves is equal to 1λ. For MT antennas, a single dipole antenna is used and moved to evaluate sixteen channels' impulse responses by four channels because the measured

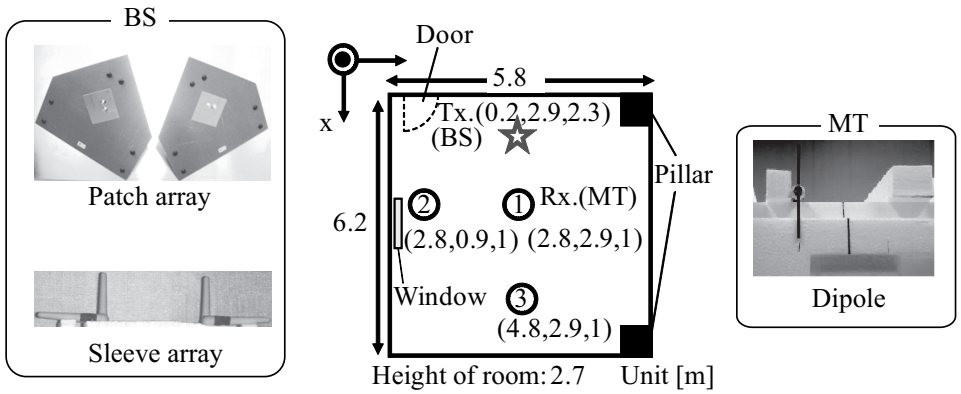

Figure 4.13. Measurement environment.

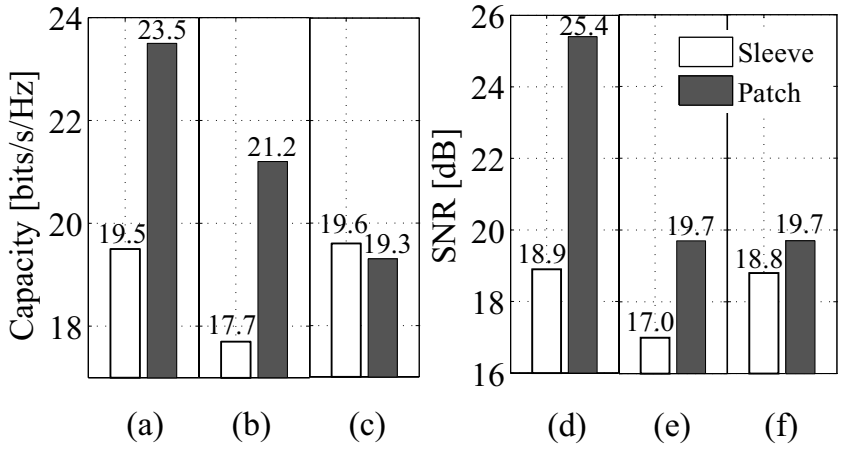

Figure 4.14. (a), (b), and (c) Channel capacities at MT positions 1, 2, and 3, respectively, for patch and sleeve antenna arrays. (d), (e), and (f) respective SNRs at the three positions.

environment is quasi-static and the time variation is small. Under this measurement condition, the element spacing between MT antennas is 0.5λ. The BS antenna is placed on the ceiling near a wall using styrene foam. Since the height for BS (2.3 m) is higher than that for MT (1 m), downward tilt of the beams works well in this scenario. The channel matrices are measured at the three typical positions 1-3 for the MT, as shown in Fig. 4.13. At positions 1 and 3, the signals from the four beams of the BS are received at nearly the identical level, and the SNR at position 1 is higher than that at position 3. At position 2, the signals from the left patch are dominant.

In this measurement, the carrier frequency of 2.45 GHz is used for reasons of expediency, however, it is no problem because the effectiveness of the design guidelines are still

applicable even if the frequency changed (One example is shown in section 4.3.). The channel matrix at each MT position is obtained off-line by complex sliding correlation using reference signal. The detail of the measurement system is described in [103] [104].

Figure 4.14 shows the measured channel capacity and SNR for the three MT positions. At all positions, the SNRs for the patch array-based antenna are higher than those for the reference antenna based on the sleeve array. The channel capacities are enhanced by the patch array, with improvements of 20% at positions 1 and 2. The channel capacity for the patch array is slightly smaller than that for the sleeve array at position 3. This is caused by degradation of the fourth eigenvalue, which is minimum eigenvalue, in the spatial correlation matrix derived from normalized channel matrix. However, the patch antenna array enhances the channel capacity by having a high SNR at the MT positions.

4.3 A BS Antenna Mounted in the Center of the Ceiling

4.3.1 Determination of Antenna Design Guidelines by Numerical Evaluations

Determination of Target HPBW and Tilt Angles in Radiation Patterns

This section considers the case which BS antenna is mounted at the center of the ceiling. The dimensions of the simulation model are 6 m $\times$ 6 m $\times$ 2.7 m, and the characteristics of 4 $\times$ 4 MIMO downlink transmission are examined. Figure 4.15(a) shows an overhead view of the simulation model. The Tx positions are 2.5 meters high and are fixed at the center of the ceiling. The Rx positions are 1 meter high and are moved at 0.5 m intervals in the x and y directions. Channel matrices $\mathbf{H}$ are derived at each Rx position. In this simulation model, there are no obstructions and a LOS condition is assumed, and the simulation parameters are summarized in Table 4.3.

Now, the optimum HPBW (θ_h) and beam direction of the directional antennas are determined. Two Tx antenna configurations are considered to evaluate how to arrange Tx antennas, as shown in Figs. 4.15(b) and 4.15(c). The reasons for using the spatial

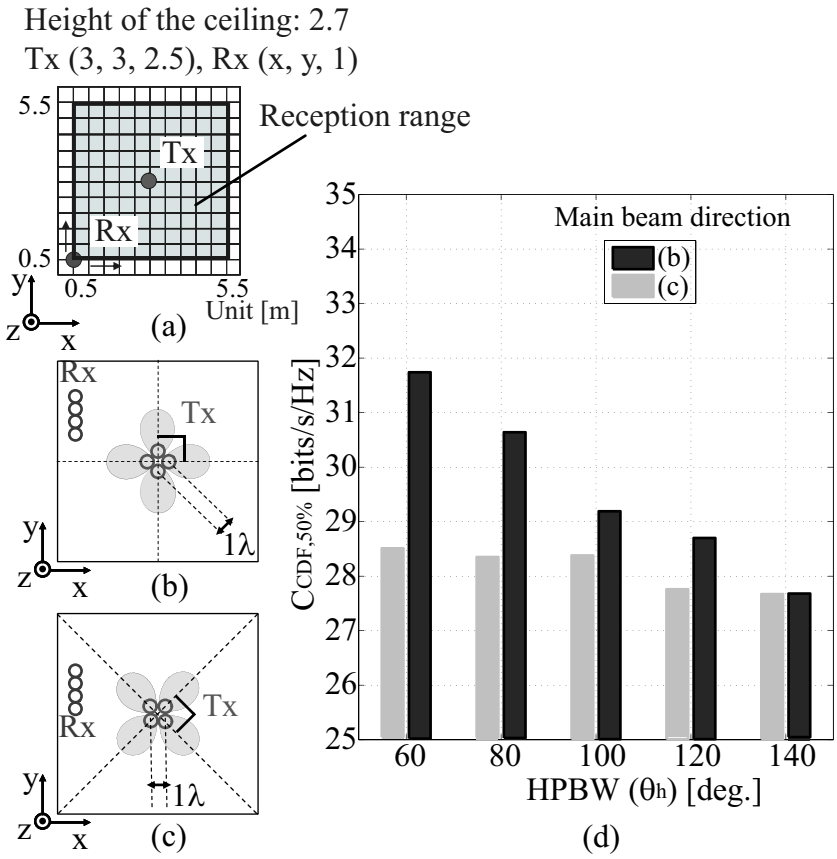

Figure 4.15. (a) Overhead view of the simulation model. (b), (c) Configurations of the vertical-polarized directional antenna with main beams pointed to the side wall and the corner of the room (overhead view). (d) 50% values of capacity at the CDF ($C_{\mathrm{CDF},50\%}$) versus HPBW in the configuration of (b) and (c).

Table 4.3. Primary simulation parameters.

Number of Tx/Rx antennas	4/4
Carrier frequency	5 GHz
Transmitting power	-5 dBm/ch
Noise power	-85 dBm
Wall material	Concrete
Relative permittivity/Conductivity	6.76/0.0023 S/m
Maximum number of reflections	5

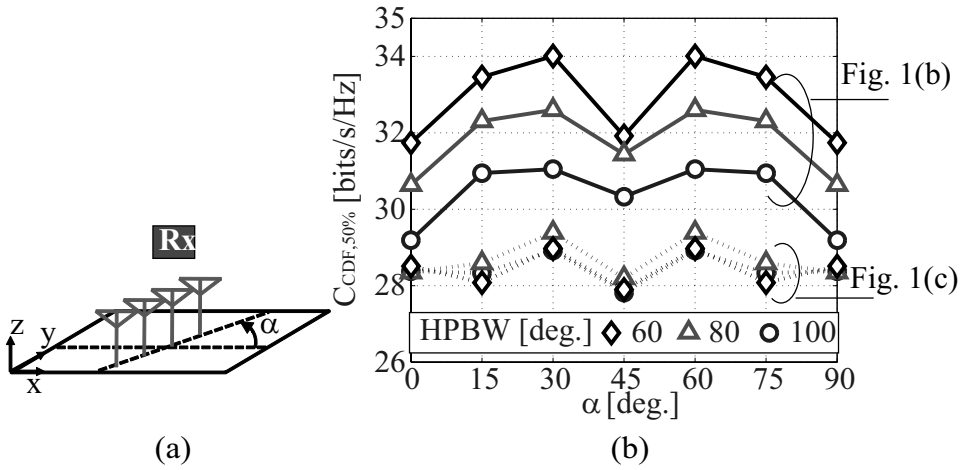

Figure 4.16. (a) Definition of the angle of Rx array arrangements (α). (b) 50% values of capacity at the CDF ($C_{\mathrm{CDF},50\%}$) as a function of α.

orthogonal beams are to realize an orthogonal propagation channel, to realize symmetric property of the channel capacity in the room, and to decrease the spatial correlation. All of the elements radiate vertical polarization. The inter-element spacings at the Tx and Rx antennas are one wavelength and one half of a wavelength of the 5 GHz carrier frequency, respectively. Figure 4.15(d) shows the channel capacity for various θ_h in the configurations shown in Figs. 4.15(b) and 4.15(c). The channel capacity is evaluated by the 50% values at the cumulative distribution function (CDF) ($C_{\mathrm{CDF},50\%}$) in Fig. 4.15(d). The capacity in Fig. 4.15(b) is larger than that in Fig. 4.15(c) and increases as θ_h becomes narrower. Here, although θ_h=60° is the largest, θ_h=80° is selected in consideration of the actual antenna size because a large antenna is required in order to realize narrow θ_h. In above results, the Rx array configuration was linear and arranged parallel to y axis. Figure 4.16 shows $C_{\mathrm{CDF},50\%}$ for Tx array arrangement in Figs. 4.15(b) and 4.15(c) as a function of the angle of Rx array arrangements. The channel capacity of Fig. 4.15(b) is also larger than that of Fig. 4.15(c) when the Rx array arrangement is changed. For these antenna configurations (beam direction of Fig. 4.15(b) and θ_h=80°), the tilt angle shown in Fig. 4.17(a) is also decided. Figure 4.17(b) shows the variation of channel capacity as a function of tilt angle, and 30° is shown to be optimum. Thus, the beam direction of Fig. 4.15(b), θ_h=80°, and the tilt angle=30° are considered as guidelines for the radiation pattern.

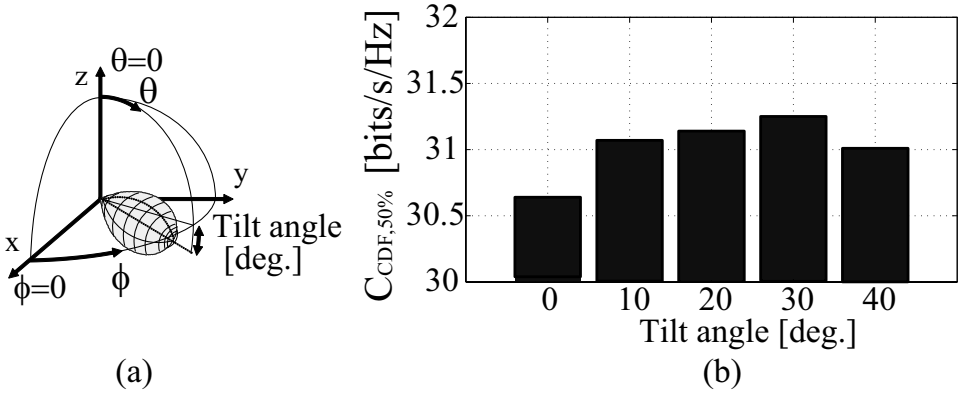

Figure 4.17. (a) Tilt angle. (b) 50% values of capacity at the CDF ($C_{\mathrm{CDF},50\%}$) in the configuration of Fig. 4.15(b) and θ_h=80° versus tilt angle.

Analytical Study of Channel Capacity Enhancement

For the antenna configuration selected in the previous section, which is denoted by V, the enhancement effect of channel capacity is evaluated. The evaluation is also conducted for the effect of applying orthogonal polarization to the selected configuration, which is denoted as VH and is shown in Fig. 4.18. Vertical polarization and horizontal polarization are allocated alternately in the horizontal plane, and this is to avoid high correlation at Rx. As the beam selection method, the case where the beam directions of both vertical and horizontal polarizations are the same is also a candidate. This configuration is denoted as $VH(Same)$ hereafter. The value of $C_{\mathrm{CDF},50\%}$ of the VH configuration shown in Fig. 4.18, 32.5, is similar to that of the $VH(Same)$, 32.3. However, the standard deviations of the channel capacities at all the receiving positions using the VH and $VH(Same)$ configurations are 2.88 and 5.02, respectively. Since the VH configuration can suppress the variation of the channel capacity, the VH configuration is selected in this study.

Here, the designs of the radiation pattern and polarization are considered independently in VH configuration. When orthogonal polarization is applied, there is a possibility that the appropriate HPBW is wider because the coupling effect between adjacent elements is low. Table 4.4 shows 50 % values of the channel capacity and the composite electric field derived from (4.1) in the wider HPBW than 80°. When orthogonal polarization is applied, the capacity of HPBW=80° is also larger than that of the wider HPBW, and this is because of the higher received power.

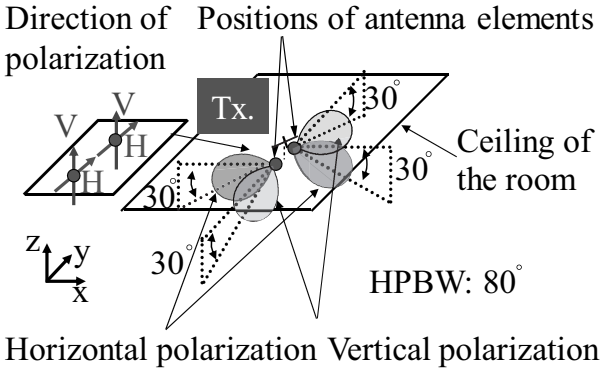

Figure 4.18. VH configuration.

Table 4.4. 50 % values of capacity and composite electric field at the CDF ($C_{\mathrm{CDF},50\%}$, $E_{\mathrm{CDF},50\%}$) for each HPBW in VH configuration.

HPBW	$C_{\mathrm{CDF},50\%}$ [bits/s/Hz]	$E_{\mathrm{CDF},50\%}$ [dB]
80°	32.5	-51.8
100°	31.6	-53.2
120°	30.6	-54.2

The capacity enhancement is demonstrated through comparison with other radiation patterns, which include isotropic (V_i) and dipole (V_d) radiation patterns for vertical polarization and VH_i and VH_d radiation patterns for dual polarization. Each radiation pattern in the vertical and horizontal planes is shown in Figs. 4.19(a) and 4.19(b). Note that configurations V_i and V_d are the same as configuration V, except for the radiation pattern, which is also true for VH_i and VH_d. In V_i, V_d, and V, the Rx antenna is a linear array with four vertical polarized antennas mounted parallel to the y-axis. In VH_i, VH_d, and VH, two couples of vertical and horizontal polarized antennas mounted at the same positions are considered. This array arrangement is also parallel to the y-axis. In both cases, the radiation pattern is isotropic.

Figure 4.20 shows the capacity CDF of the selected antenna configuration for various radiation patterns. Capacity enhancement by directive radiation and orthogonal polarization is confirmed. When V is compared to V_i, the capacity is enhanced in both the high- and low-CDF regions in Fig. 4.20. This suggests that the selected antenna configuration is effective in both high- and low-SNR regions. Here, $C_{\mathrm{CDF},50\%}$ of V_i, V,

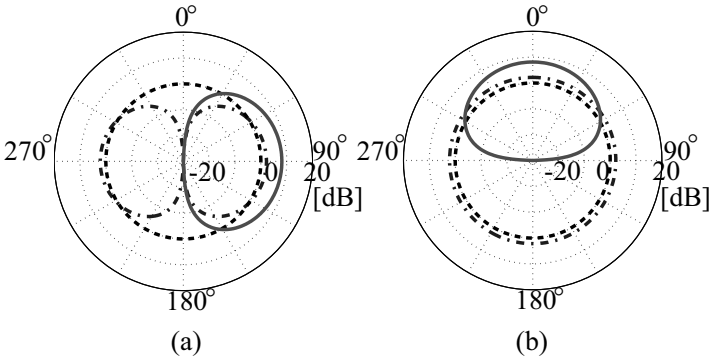

Figure 4.19. Radiation patterns of - - -isotropic, - · - dipole, and — directional antennas with θ_h=80° in the (a) vertical and (b) horizontal planes (Tilt angle is not considered in these figures).

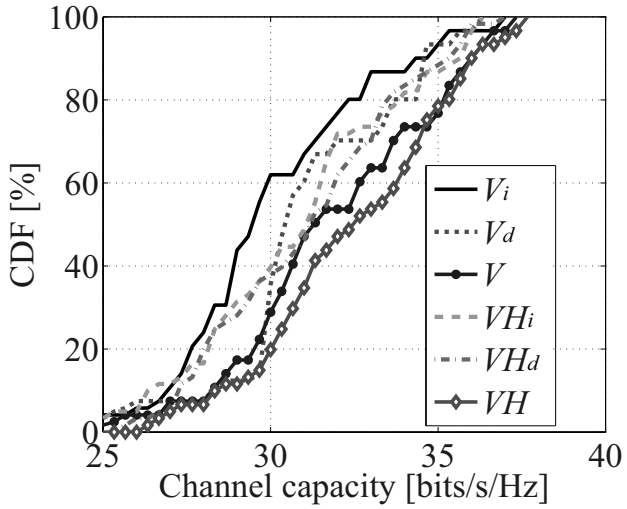

Figure 4.20. Comparison of capacity CDF between antenna configurations with the selected radiation pattern and various other radiation patterns.

and VH are 29.5, 31.4, and 32.5 bits/s/Hz. The improvement factors of V and VH relative to V_i are +5.66% and +10.1%, respectively. In addition to the 6 m × 6 m × 2.7 m simulation model, this analysis also examine the 5 m × 8 m × 2.7 m simulation model in a similar manner. As an afterthought, it was confirmed that the capacity was enhanced by the designed radiation pattern if the room size had minor deviations.

As discussed later, 2.4 GHz band frequency is used in the fabrication of the prototype MIMO antenna and the channel measurement. Wireless local area network (WLAN) is an application example of this study. In WLAN, 5 GHz and 2.4 GHz band frequencies

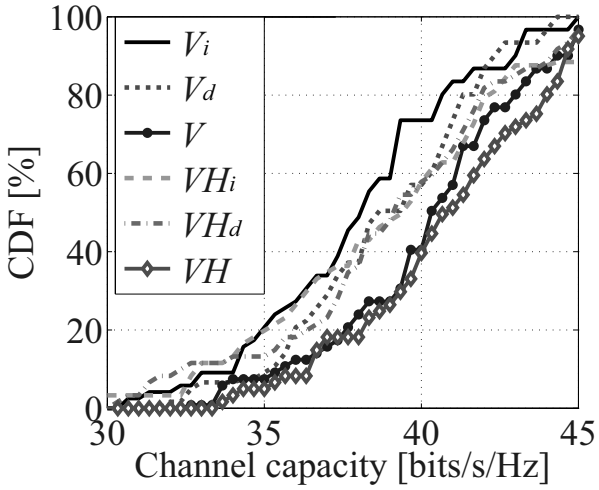

Figure 4.21. Comparison of capacity CDF between antenna configurations with the selected radiation pattern and various other radiation patterns (Carrier frequency is changed to 2.45 GHz).

are allocated, and the miniaturization of the antenna is required for 2.4 GHz band more strongly. Then, the possible application of the above discussion about channel capacity to 2.4 GHz band is examined. Figure 4.21 shows the capacity CDF of the VH configuration shown in Fig. 4.18 for various radiation patterns as well as Fig. 4.20, where the frequency is 2.45 GHz used in the channel measurement. For 2.4 GHz-band, large channel capacity is also obtained by the VH configuration.

Then, the performance of 2 $\times$ 2 MIMO-SDM is also evaluated. Ray-tracing propagation analysis is performed using the frequency of 2.45 GHz, and the simulation model is shown in Fig. 4.22. The model is same as Fig. 4.15 (a), however, the reception range is different. At the Tx side, two elements of V (Vertical polarization) and H (Horizontal polarization) are used, and VH configuration in Fig. 4.18 is compared with VH_d (dipole radiation pattern). In this simulation, Rx antennas are dipole antennas with two elements. One element is inclined parallel to the ground, and the other is arranged perpendicular to the ground, and those elements are arranged in one position. At each receiving position, plural Rx array orientations are considered. Figure 4.23 shows the channel capacity CDF, and the enhancement by the VH configuration is confirmed in CDF 10 %, 50 % and 90 % values. This indicates that in 2 $\times$ 2 MIMO-SDM, the efficacy of the VH configuration is also shown.

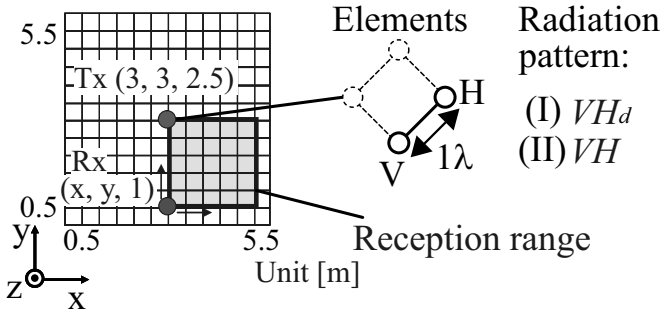

Figure 4.22. Overhead view of the simulation model in 2 × 2 MIMO-SDM.

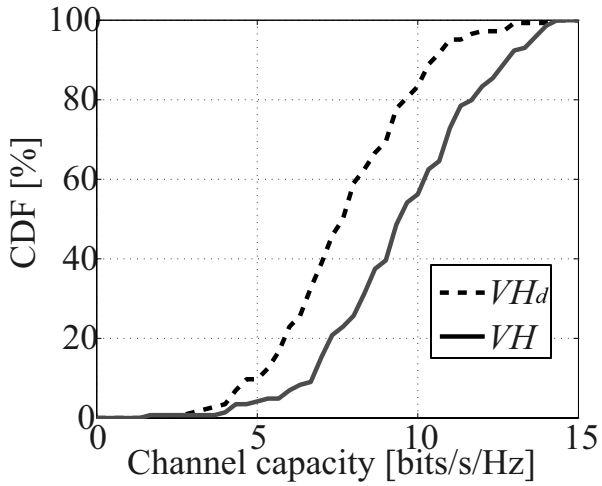

Figure 4.23. Simulation results of channel capacity in 2×2 MIMO-SDM for VH_d and VH configurations.

4.3.2 A Low-Profile MIMO Antenna with Slot and Dipole Antennas

A low-profile MIMO antenna for 2.4 GHz based on the configuration of Fig. 4.18 is presented in this section. The design procedures are described in [138], and the MIMO antenna consists of cavity-backed slot antennas and printed dipole antennas with a complementary relation, as shown in Fig. 4.24. Although the dipole antennas are mounted around the slot antennas, there is little effect on the radiation of the individual antennas because their polarizations are orthogonal and the isolation between the antennas is less than -20 dB. The heights of the slot and dipole antenna elements are 30 mm and 20.5 mm, respectively, as shown in Figs. 4.24(c) and 4.24(d). The number of elements is

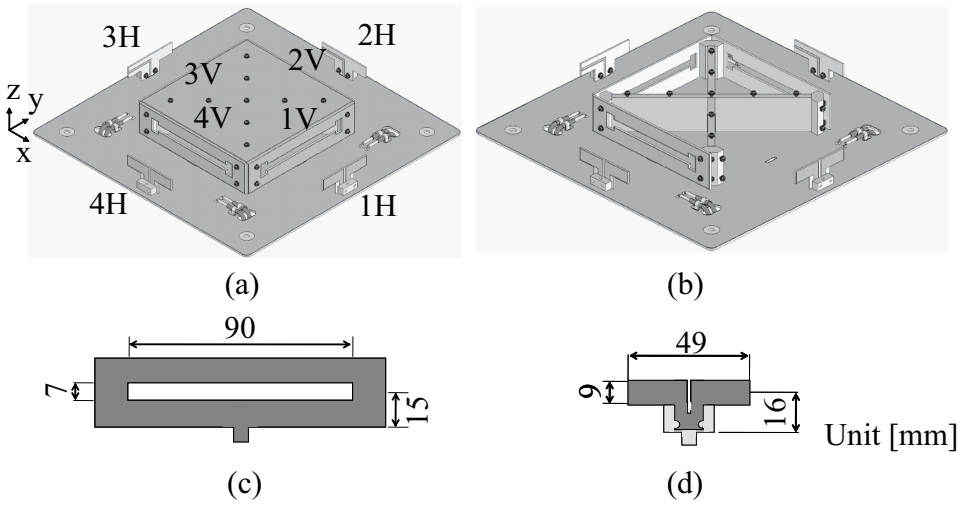

Figure 4.24. (a) Structure of the prototype MIMO antenna. (b) Inner structure of the cavity-backed slot antennas. (c) and (d) Slot and dipole antenna radiating vertical and horizontal polarization.

four, and vertical (V) and horizontal (H) polarizations are radiated from the slot and the dipole, respectively. Partitions are mounted diagonally in the cavity, as shown in Fig. 4.24(b). These partitions suppress the backward radiation, and a uni-directional radiation pattern is achieved for slot antennas. The partitions also reduce mutual coupling between slot antennas. A corner reflector effect by the ground plane and the conducting surface of the cavity provide a uni-directional pattern for the dipole antennas.

The tilt angle of each radiation pattern from the xy plane is influenced by the height of the cavity and the size of the ground plane. Dipole location (height and distance from the cavity) also has an effect on the tilt angle for dipole elements, which is considered independent of the slot elements because the polarizations of the slot and dipole elements are orthogonal. In particular, a small height is desired for a low-profile structure. However, when the height is decreased, a large current flows on the upper surface of the cavity, and the radiation pattern of the slot points toward the z-direction. The radiation pattern of the dipole denotes same tendency because reflections from the conducting surface of the cavity are suppressed. When the ground size is decreased, reflections from the ground plane are suppressed. As a result, the main beam is pointed in the horizontal direction, and the HPBW increases due to diffraction from the edge of the ground plane. The height of the cavity, the location of the dipole elements, and the size of the ground plane are decided in consideration of the above [138]. Figure 4.25 shows the fabricated

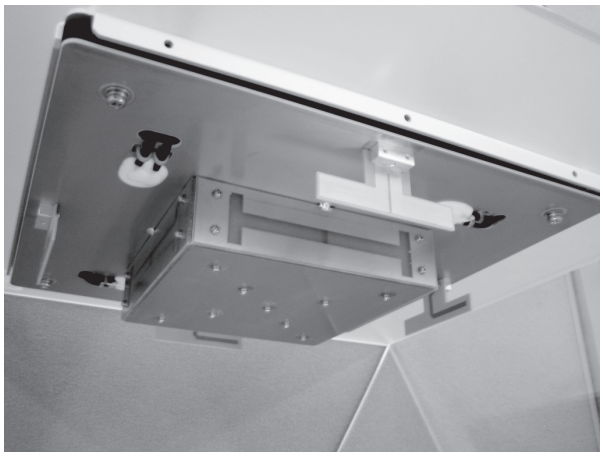

Figure 4.25. Photograph of the prototype MIMO antenna.

prototype MIMO antenna. The antenna is placed upside down on the ceiling when in use, as shown in Fig. 4.25, and the radiation pattern is tilted downward to point toward the Rx antenna, the height of which is lower than that of the Tx antenna.

Next, the measured characteristics of the prototype MIMO antenna are presented. Figure 4.26(a) shows the radiation patterns in the vertical plane of the slot and dipole antenna elements. This figure illustrates the characteristics of a single pair of V and H elements (1V and 1H). Figure 4.26(a) demonstrates that both of the radiation patterns are tilted from the x-direction toward the z-direction. The HPBW of 1V and 1H are 84° and 85.5°, respectively. The angles between the x-direction and the maximum radiation direction for 1V and 1H are 45° and 66.5°, respectively. These values are large because we just focus on the direction of the maximum radiation. However, HPBW is comparatively large, and the gain is sufficient in the 30° tilted direction from the x to z-direction. Therefore, above radiation patterns are suitable. Figure 4.26(b) shows the radiation pattern in the 30° slanted plane from the xy plane toward the z-direction, where 0° indicates the 30° tilted direction from the x-direction toward the z-direction. The HPBW of 1V and 1H are 61° and 53°, respectively. Figures 4.26(a) and 4.26(b) demonstrate that the uni-directional radiation pattern with a narrow HPBW and the tilt angle toward the z-direction are obtained in the slot and dipole elements, the radiation patterns of which are similar. In this antenna structure, the main beams are pointed in four directions with spatial orthogonality in the horizontal plane because four slot/dipole antennas are mounted at right angles to each other.

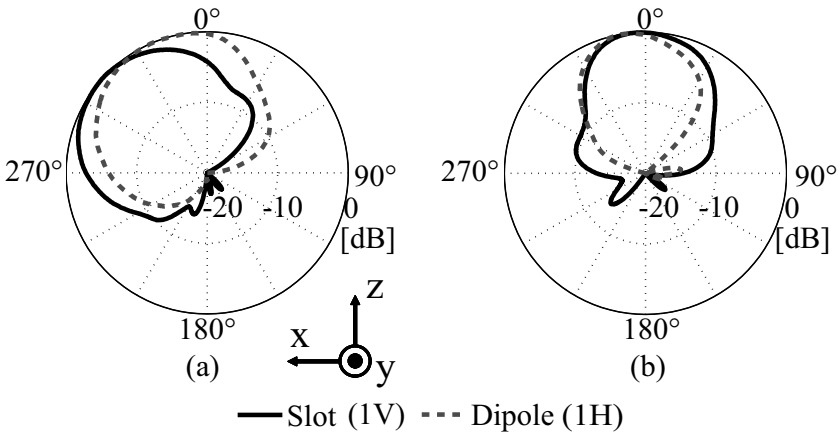

Figure 4.26. Radiation patterns of the prototype MIMO antenna (Elements 1V and 1H). (a) Vertical plane, and (b) 30° tilted horizontal plane toward z axis.

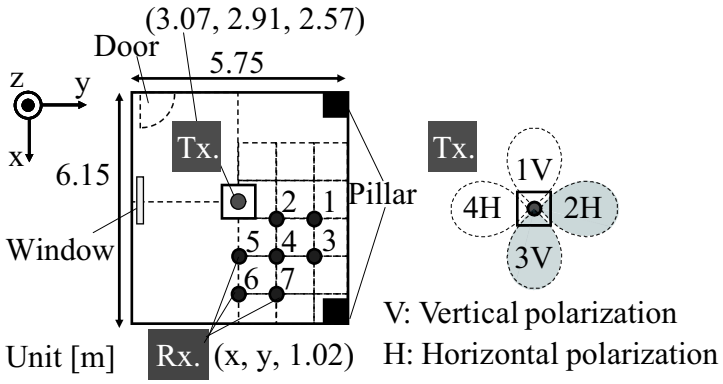

Figure 4.27. Measurement environment and positions of the Tx and Rx antennas.

In addition, VSWR characteristics measured at 2.3-2.6 GHz are evaluated. The VSWR of the slot is less than 2 at 2.3-2.54 GHz, and that of the dipole is less than 1.6 at 2.3-2.6 GHz.

4.3.3 Measurement Based Evaluation for Channel Capacity

Setup of the MIMO Transmission Experiments

Channel measurements are performed in an actual environment using the prototype MIMO antenna. A detailed description of the measurement system is provided in [103]. The measurement space is 5.75 m × 6.15 m × 2.70 m, as shown in Fig. 4.27, and, as

Table 4.5. Examined antenna configurations.

	Target:	Target for comparison:
Tx	Prototype MIMO antenna	Sleeve antennas
Rx	Sleeve antennas	

shown in Fig. 4.25, the prototype MIMO antenna is fixed at the center of the ceiling as the Tx antenna. The height is 2.57 m, and the main beams are pointed toward the side wall of the room. The state of the prototype MIMO antenna is associated with the VH configuration shown in Fig. 4.18, and vertical polarization and horizontal polarization are allocated alternately in the horizontal plane as shown in Fig. 4.27. Channel measurements are performed by changing the Rx positions at intervals of 1 m in the horizontal plane, as shown in Fig. 4.27, in consideration of the symmetric property. The channel matrix at each position is obtained off-line by complex sliding correlation with the maximum length sequence (M-sequence). For simplicity, this measurement assumes 2×2 MIMO transmission at each Rx position, and at the Tx antenna, elements 2H and 3V are used to cover the received area, as shown in Fig. 4.27.

Not only the prototype MIMO antenna but also sleeve antenna configuration are used as the Tx antenna for the performance comparison. The polarization, array arrangement, and element spacing of the sleeve antennas used at Tx side are the same as for the prototype MIMO antenna, and elements 2H and 3V are also used. On the other hand, sleeve antennas are used as the Rx antennas. One element is inclined parallel to the ground, and the other is arranged perpendicular to the ground. They are closely arranged, and the height of the Rx antenna is fixed at 1.02 m. The Tx and Rx configurations are summarized in Table 4.5. For the simplicity of the expression in the following section, the cases using "prototype MIMO antenna" and "sleeve antennas" are represented as S_d and S_l, respectively hereafter. The environments between the Tx and Rx antennas are a LOS and quasi-static at all of the Rx positions. The measurement frequency is 2.45 GHz.

Measurement Results

Figure 4.28(a) shows the time averaged SNRs of S_d and S_l at each Rx position shown in Fig. 4.27. The SNR of S_d changes with the Rx position, and higher SNR is observed

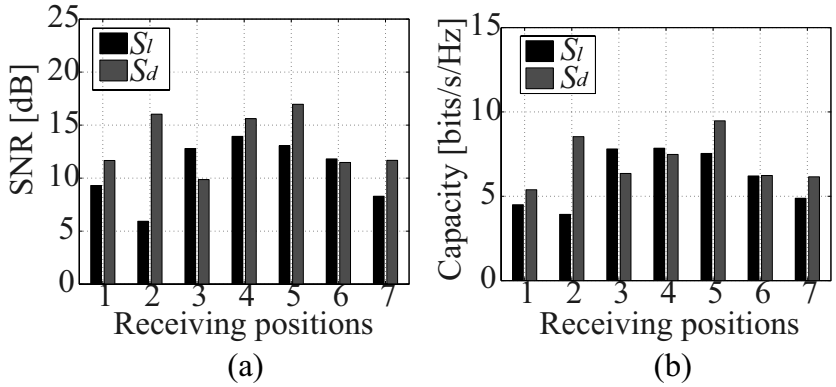

Figure 4.28. Characteristics comparison between S_d and S_l. (a) SNR and (b) channel capacity.

at positions near the Tx antenna, such as positions 2, 4, and 5. At positions 1 and 7, which are far from the Tx antenna, the SNR is lower than at the positions near the Tx antenna but is higher than that of S_l. The SNR is enhanced by S_d at five out of seven positions. The place averaged SNR of S_l and S_d are 11.5 and 14.1 dB, and 2.6 dB enhancement by S_d is confirmed. Figure 4.28(b) shows the channel capacity of S_d and S_l at each Rx position shown in Fig. 4.27. The channel capacity of S_d is larger than that of S_l at the positions with larger SNR, with the exception of position 4. Therefore, the SNR has a great influence on the channel capacity. In particular, a large capacity enhancement (2.18 times) by S_d is confirmed at position 2. This is due to the high SNR, because the spatial correlation of both configurations are almost same (S_l: 0.68, S_d: 0.65). The place averaged channel capacities of S_l and S_d are 6.1 and 7.1 bits/s/Hz, respectively, and the improvement factor by S_d is 16.2 %. The predominant feature is that the capacity is enhanced at positions 1, 2, and 7 with small capacity in the case of S_l because requirement of enhancement at small capacity positions is higher than at large capacity positions. The maximum and minimum capacities at all of the Rx positions of S_l are 7.9 and 3.9 bits/s/Hz, respectively, and those of S_d are 9.5 and 5.4 bits/s/Hz, respectively. Both channel capacities are enhanced by S_d. Consequently, the MIMO capacity performance of S_d is the same or better than that of S_l.

The capacity of S_d is decreased only at position 4, despite the SNR being higher than that of S_l. The reason for it is examined using the eigenvalue of the spatial correlation

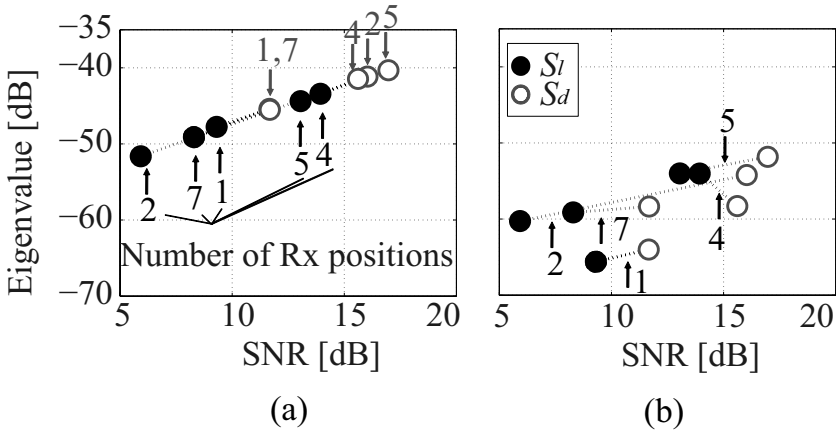

Figure 4.29. (a) First and (b) second eigenvalues of S_l and S_d as functions of SNR.

matrix. The channel capacity shown in (3.18) is transformed as follows:

$$C = \sum_{i=1}^{2} \log_2\left(1 + \frac{P_t \lambda_i}{N_t \sigma^2}\right) \tag{4.4}$$

where λ_i $(i = 1, 2)$ are the eigenvalues of the spatial correlation matrix $\mathbf{HH}^H$, which satisfy $\lambda_1 > \lambda_2$. Figures 4.29(a) and 4.29(b) show the variation in the first and second eigenvalues as functions of the SNR at the positions satisfying the condition in which the SNR of S_d is higher than that of S_l. In Fig. 4.29(a), the first eigenvalue increases with increasing SNR at all of the Rx positions. The second eigenvalue increases in a similar manner at the positions 1, 2, 5, and 7, but decreases at position 4, as shown in Fig. 4.29(b). The decrease of the second eigenvalue of S_d provide channel capacity decrease. The large first eigenvalue has been reported to be obtained by the adjustment of the radiation pattern in directional antennas [139]. Although the first eigenvalue is dominant for the channel capacity, the second eigenvalue is also an important factor for enhancing capacity in directional antennas.

4.3.4 Low-Profile MIMO Antenna with Loop and Dipole Antennas

The previous section evaluated a BS MIMO antenna mounted on the ceiling for downlink transmission, and demonstrated that directive radiation patterns with a tilt angle in the

Table 4.6. Improvement factor of the channel capacities for V and VH compared to those for isotropic antennas.

Configurations	Room size	
	6 m × 6 m × 2.7 m	5 m × 8 m × 2.7 m
V	+6.34	+3.78
VH	+10.1	+5.88

downward direction were effective for enhancing SNR and channel capacity compared to a sleeve antenna configuration. The MIMO antenna was constructed using cavity-backed slot antennas and dipole antennas. Here, this antenna structure is modified, and a lower profile antenna with a height of 0.16λ (20 mm) is presented. This is for use with a 2.4 GHz BS and consists of loop and dipole elements for vertical and horizontal polarizations, respectively. The structure provides uni-directional radiation patterns in four orthogonal directions in the horizontal plane, which were designed considering previously described propagation characteristics.

Target Specifications of the Designed Antenna and a Method to Achieve Them

As described before, the assumption is that the Tx was mounted on the center of the ceiling in a hexahedron room. Four beams with downward tilt were radiated in four orthogonal directions in the horizontal plane. Table 4.6 summarizes the improvement factor of 4 × 4 MIMO channel capacities for the configurations derived from Figs. 4.15 and 4.17 (V), which has only vertical polarized elements, 80° HPBW, and 30° downward tilt angle, and the configurations in Fig. 4.18 (VH), compared to the capacities for isotropic antennas.

As indicated in Table 4.6, capacity enhancement by V and VH were confirmed in both 6 m × 6 m × 2.7 m and 5 m × 8 m × 2.7 m rooms, indicating that the appropriate settings for directional antennas and polarization are effective for channel capacity enhancement. From these results, design guidelines for the radiation patterns and polarizations are set based on VH. For HPBW, the target angle range is set as 60-80°. Figure 4.24 presented the MIMO antenna based on the design guideline of Fig. 4.18, which were constructed by slot and dipole elements. The goal of this section is to reduce the MIMO antenna height to 20 mm with the desired radiation patterns. In

Fig. 4.24, the antenna height was determined by the slot antennas, which were vertical polarization elements. However, a lower-profile antenna cannot be achieved using this structure because a large current flows on the upper surface of the cavity, and the radiation patterns of the slot antennas point toward the z-direction. Therefore, the use of other low-profile vertical polarization elements is required to reduce the height. As a result, slot antennas are replaced by different antennas in an attempt to realize a low-profile MIMO antenna.

Antenna Design: Examinations of Vertical-Polarization Elements

For vertical polarization elements mounted on the ground, candidates for low-profile wire antennas are inverted-F antennas and transmission line antennas, namely loop antennas (Figs. 4.30(a) and 4.30(b)). The radiations to the z and y directions for the loop antenna are suppressed, as compared to those for the inverted-F antenna. As mentioned, the assumption is that the MIMO antenna would be placed upside down on the ceiling when in use. In this situation, an obliquely upward beam tilt and narrow HPBW are required in the radiation patterns to obtain large channel capacity. To realize these conditions, suppression of the radiation in the z and y directions of the loop is readily achievable. In addition, as loop antennas have a wider bandwidth than inverted-F antennas, loop antennas are selected for the vertical elements [140]-[142].

To generate a uni-directional radiation pattern, a reflector was mounted on the ground. Moreover, as shown in Fig. 4.30(c), four loop antenna with reflectors arranged at right angles on the ground are set in a similar way to slot antennas in Fig. 4.24. With the addition of the reflector, a uni-directional radiation pattern with vertical polarization is obtained, and the cross polarization and mutual coupling between elements are sufficiently low [140].

Antenna Design: Combinational Antenna With Vertical- and Horizontal-Polarization Elements

For horizontal polarized elements, dipole antennas are set in a similar way to Fig. 4.24. Specifically, dipole antennas printed on both sides of a glass epoxy dielectric substrate (ε_r=4.8) with 1.6 mm thickness are used as shown in Fig. 4.31. On the ground side of the substrate, the conductor increases in width from 4 to 12 mm forming a tapered shape, and functions as a balun.

Figure 4.32 shows a designed MIMO antenna, which is constituting of loop and dipole

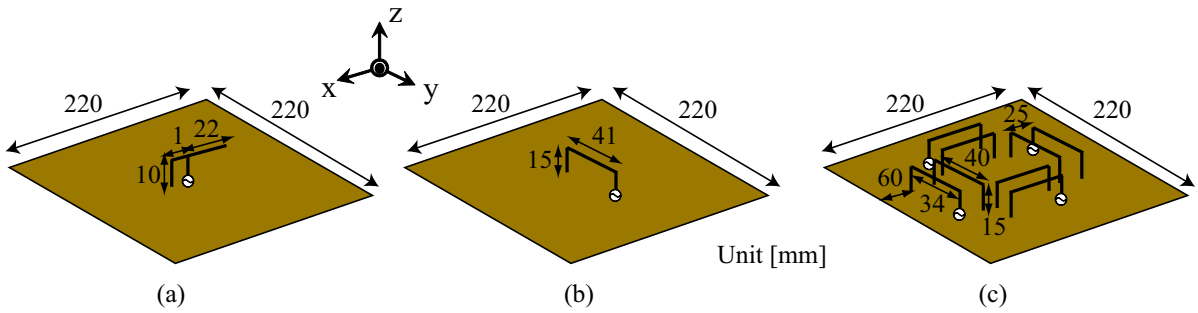

Figure 4.30. Layout of (a) a single inverted-F antenna, (b) a single loop antenna (c) four loop antennas with reflectors [140] mounted on the ground.

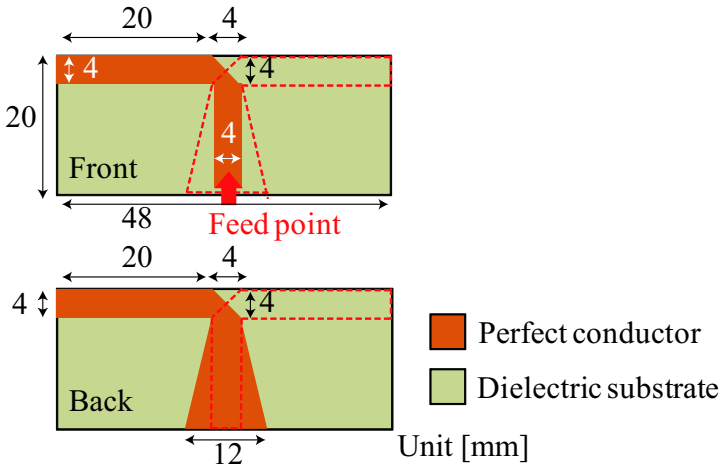

Figure 4.31. Printed dipole antenna used for horizontal polarization elements. Conductor and substrate thicknesses are 0.035 and 1.6 mm, respectively. The relative permittivity of the glass epoxy substrate is 4.8.

elements [143]. To obtain the desired radiation patterns, directors and reflectors are added in horizontal polarized elements. The length (mm) and location of each element are shown in the two-dimensional model. The feeding elements and reflectors for the loop antennas are 1 mm wide, and the directors and reflectors for the dipole antennas are 4 mm wide. All of the elements are made of perfect conductors. The heights of the loop and dipole elements are 15 and 20 mm, respectively. Fig. 4.33 shows the fabricated antenna, for which a copper plate is used for the ground plane, loop antennas, directors, and reflectors. Feedings to loop and dipole antennas are conducted from beneath the ground by feed pins. The directors and reflectors of the dipole antennas are fixed using

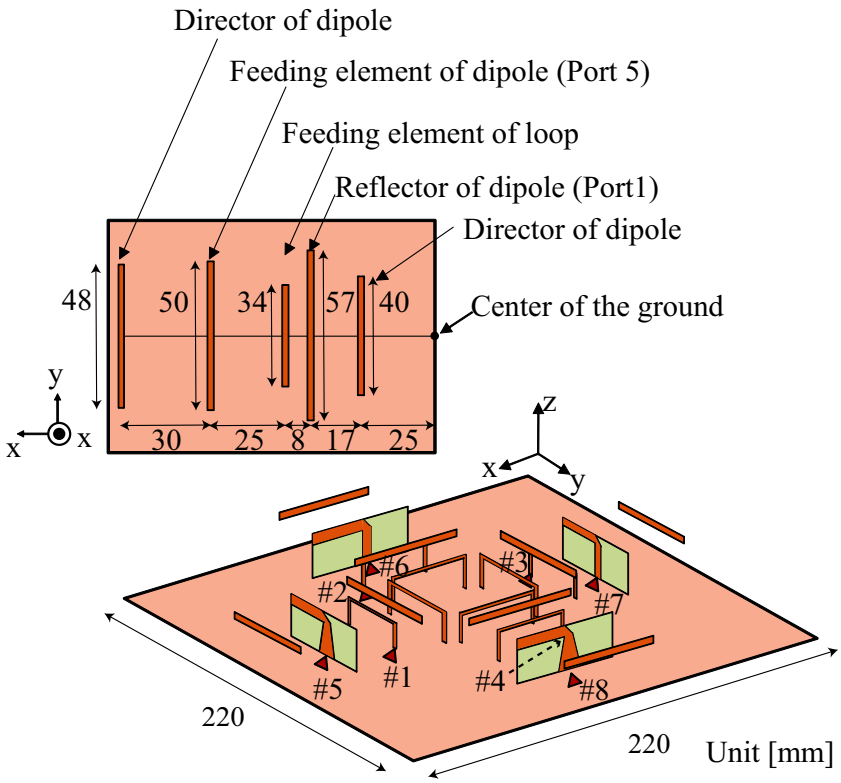

Figure 4.32. Simulation model of the proposed MIMO antenna assuming the experimental conditions of the dipole element. The digits (#i) denote port numbers.

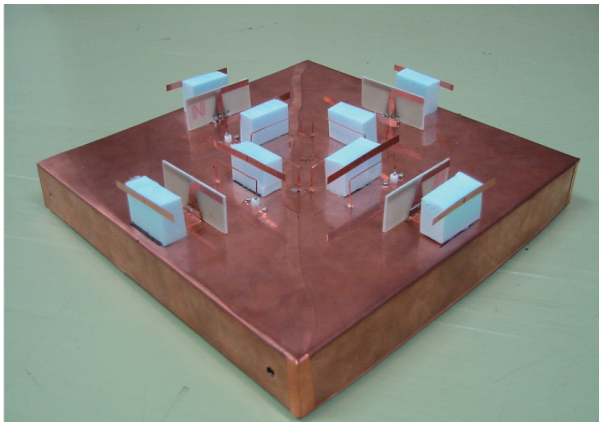

Figure 4.33. Photograph of the fabricated MIMO antenna consisting of loop and dipole elements.

styrene foam.

Figure 4.34 shows the comparison between calculated and measured S-parameters of

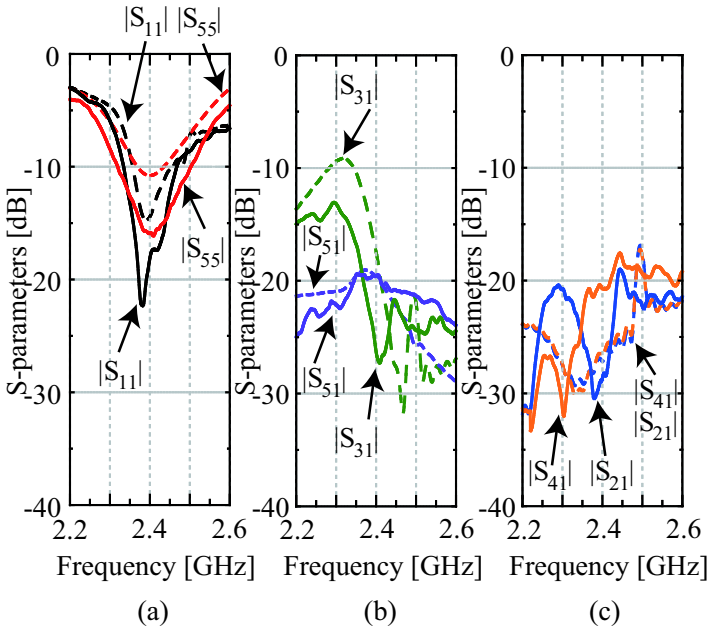

Figure 4.34. (a) Reflection characteristics for the loop and dipole elements of the proposed MIMO antenna. (b) Mutual coupling between vertical and horizontal polarization elements, and between facing vertical polarization elements. (c) Mutual coupling between adjacent vertical elements. Dotted and solid lines represent simulation and experimental data, respectively.

the MIMO antenna, which correspond to dotted and solid lines. As seen in Fig. 4.34(b), the reflection characteristics (S_{11} and S_{55}) of the loop and dipole elements are less than -10 dB at 2.4 GHz in both the calculated and measured data. Mutual coupling between the vertical and horizontal polarization elements (S_{51}) is approximately -20 dB at 2.4 GHz, which is sufficiently low. Although the mutual coupling between the facing vertical polarization elements (S_{31}) is slightly strong in the calculated data, all of the isolation characteristics, including mutual coupling between the adjacent vertical elements shown in Fig. 4.34(c), are nearly less than -20 dB in the measured data.

Figure 4.35 shows the comparison between the calculated and measured radiation patterns in the zx plane for the loop and dipole antennas. The cross polarizations are sufficiently low, and uni-directional radiation patterns with suppressed backward radiations are obtained. According to the simulations, the tilt angles of the loop and dipole antennas are 61.0° and 52.0°, respectively, and the HPBWs are 55.5° and 70.9°, respectively. Although the calculated radiation patterns are normalized with the maximum value in Figs. 4.35(a) and 4.35(b), the maximum gain for the loop and dipole elements

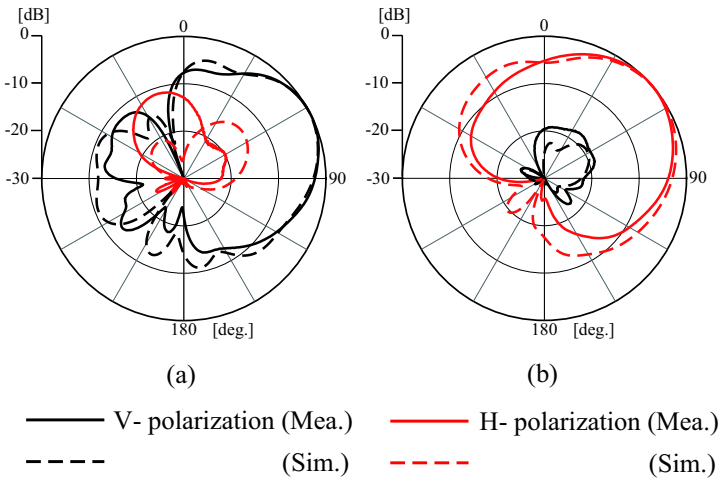

Figure 4.35. Calculated and measured radiation patterns for (a) loop (port 1) and (b) dipole (port 5) elements. The calculated radiation pattern is normalized with the maximum value in each figure.

are 8.0 dBi and 8.2 dBi, respectively. Notably, the measured radiation patterns are similar to the calculated radiation patterns. The tilt angles for the loop and dipole antennas are 63° and 50°, respectively, and the HPBWs are 61° and 78°, respectively. As indicated by these results, the desired radiation patterns were achieved based on the design guidelines of 60-80° HPBW and a 30° downward tilt angle, and a MIMO antenna with a thickness of 20 mm has been realized.

In this section, the antenna design was based on the assumption of 4×4 MIMO transmission by dual-polarization. However, this antenna is capable of transmitting up to eight streams, and up to four streams with vertical or horizontal polarization depending on the state of MT. In addition, the proposed antenna can be used as a pattern diversity antenna, and vertical and horizontal polarizations can be radiated in the identical directions. Thus, the potential applications of the proposed antenna cover a wide range of possibilities.

4.4 A Handset Antenna with Phase Difference Feeding

In upcoming cellular phone services, high-speed data transmission is expected and the MIMO system is a key technology. Large channel capacity is achieved using many antenna elements. However, it is difficult to mount many built-in antennas owing to space constraints in the handset. In addition, a small number of ports is desired to realize a simple receiver. To enhance channel capacity effectively for a small number of antenna systems, antenna pattern control is an appropriate solution. Antenna patterns can be changed by analog techniques as shown in [91] and [92], and the cost and complexity are lower than those of digital techniques.

To evaluate handset antennas, the effect of the cellular phone chassis and the human body should be considered. Channel capacity of a handset MIMO antenna is evaluated by including these effects in [144]. However, there are few studies applying radiation pattern changes by analog techniques to a handset MIMO antenna. In [145] and [146], the application of analog phase shifters to the antenna for pattern control was considered. Channel capacity enhancement was confirmed by optimizing the phase difference based on MEG and the correlation coefficient. This section shows the enhancement by these schemes including human body effects and reveals that the enhancement can be achieved by a fixed phase difference, namely, by using simple feeding circuits such as delay lines.

A Multiantenna for a Handset and a Human Phantom Model

This section focuses on downlink communications, and a handset MIMO antenna is used on the receiving side. The antenna consists of inverted F-shaped wire antennas (IFAs), and is mounted on top of a conducting box imitating a handset terminal, as shown in Fig. 4.36. The structure is slightly different from that of [146] because the target frequency is different, being 2 GHz, as will be used for next-generation high-speed data communication. In Fig. 4.36, the arrangements of array 1 and array 2 are mutually orthogonal because larger capacity was obtained this way than with parallel arrangements [146]. Four antennas combined through phase-difference feeding structures provide two output ports to the receiver in Fig. 4.36. The conducting wires of the IFA are bent and the IFA parameters are optimized to resonate at 2 GHz. The shorting

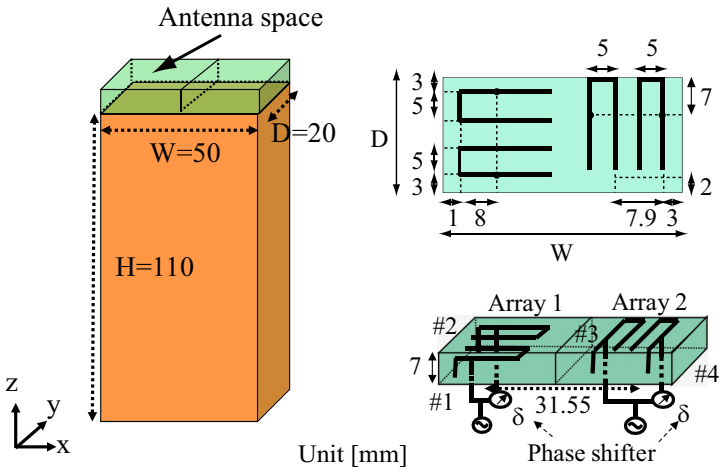

Figure 4.36. Geometry of the handset antenna.

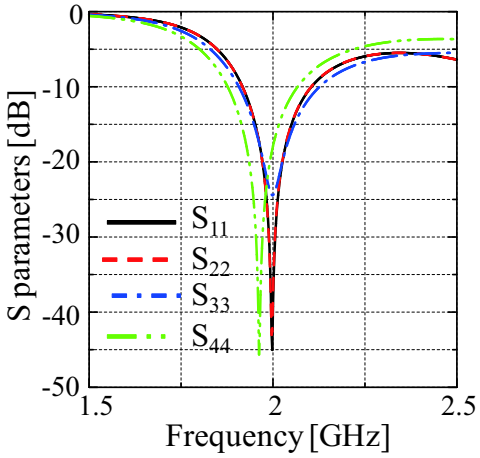

Figure 4.37. S-parameters of the handset antenna.

pin of the IFA is adjusted to suppress the S_{11} to less than -10 dB, and the S_{11} of each element has good performance, as shown in Fig. 4.37. The antenna characteristics in this section are calculated by FEKO [147].

In the analysis of the handset antenna, human body effects are considered by the viewer mode human phantom shown in Fig. 4.38. The head model is based on COST 244 [148], and the shape is a sphere with a radius of 100 mm, a relative permittivity (ε_r) of 40, and a conductivity (σ) of 1.4 S/m. For the other parts of the human body, ε_r and σ are 54 and 1.45 S/m determined based on the electric constant of muscle. Figures 4.39(a) and 4.39(b) show radiation patterns in the xy plane of array 1 and array 2,

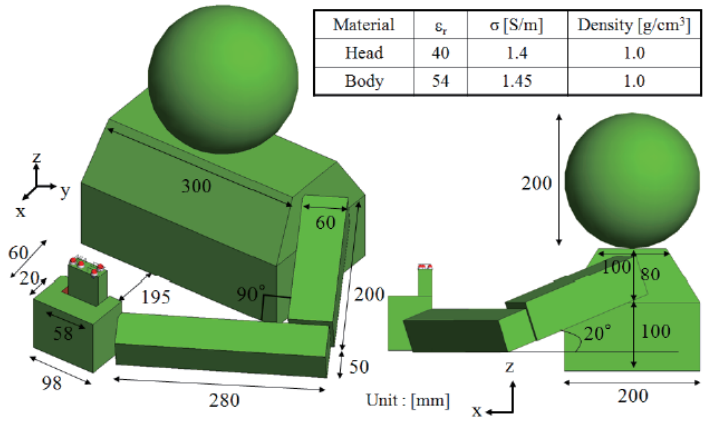

Figure 4.38. Human phantom.

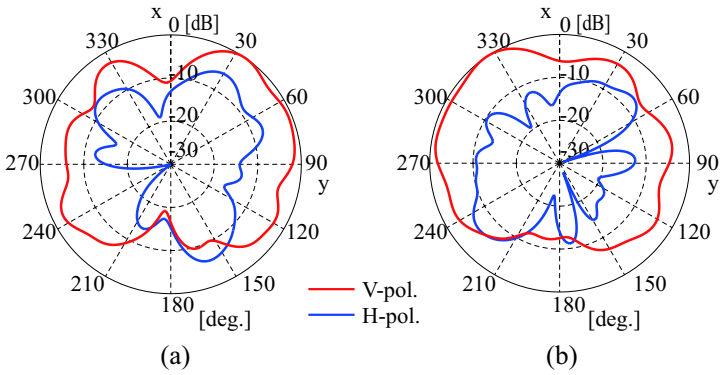

Figure 4.39. Radiation patterns in the xy plane (δ=0°) for (a) array 1, (b) array 2.

where the phase difference is 0°. The radiation pattern is distorted because reflection and absorption are caused by the hand and the body.

Procedure for Determining the Phase Difference and Channel Capacity

The phase difference of the handset MIMO antenna is determined by MEG (G_e) and the correlation coefficient (ρ). In Rayleigh fading environments, they are given by [149], [150],

$$G_e = \int_0^{2\pi} \int_0^{\pi} \left(\frac{XPR}{1+XPR} G_\theta P_\theta + \frac{1}{1+XPR} G_\phi P_\phi \right) \cdot \sin\theta d\theta d\phi \tag{4.5}$$

$$\rho = \frac{g_{12}(\theta,\phi)\cdot e^{j2\pi dx\cdot r(\theta,\phi)/\lambda}}{\sqrt{g_{11}(\theta,\phi)}\sqrt{g_{22}(\theta,\phi)}} \tag{4.6}$$

$$g_{ij} = \int_0^{2\pi}\int_0^{\pi}(XPR\cdot E_{\theta i}^{*}E_{\theta j}P_{\theta} + E_{\phi i}^{*}E_{\phi j}P_{\phi})\sin\theta d\theta d\phi \tag{4.7}$$

where XPR is the cross polarization power ratio. G_θ, G_ϕ, P_θ and P_ϕ are the θ and ϕ components of the antenna power gain pattern and the angular density functions of incoming plane waves, which are assumed to be uniform distribution (P_θ =P_ϕ=1/4 π). $E_{\theta k}$ and $E_{\phi k}$ (k=1, 2) are θ and ϕ components of the complex electric field radiation pattern of each array. $e^{j2\pi dx\cdot r(\theta,\phi)/\lambda}$ shows the phase difference depending on the positions of the elements.

Phase differences with maximum MEG and minimum correlation coefficient are derived. Here, there are two MEG values for two output ports in the array geometry of Fig. 4.36, and the two MEG values for the evaluation factor are simply added. This criterion is equivalent to the sum of received signal strength indicator (RSSI) levels by the two receivers. As shown in Fig. 4.36, the phase difference is denoted by δ, and the δ between #1 and #2 is identical to that between #3 and #4. Sum of MEGs, which is denoted by (MEG), and the correlation coefficients (ρ) as a function of δ at 30° intervals are evaluated. The maximum MEG is 2.23 dBi at δ=-30° (ρ=0.03), and the minimum ρ is 0.01 at δ=30° (MEG=2.15 dBi). As a reference, MEG and ρ at δ=0° are 1.15 dBi and 0.38. The results show that low spatial correlation is also obtained by the maximization of MEG. The radiation patterns in the xy plane at δ=-30° and δ=30° are similar, as shown in Figs. 4.40 and 4.41. The radiation patterns are changed, compared to those at δ=0° of Figs. 4.39(a) and 4.39(b). In both Figs. 4.40 and 4.41, the directions of the strong (weak) radiation in array 1 and the weak (strong) radiation in array 2 are identical. It is known that orthogonal radiation patterns lead to good diversity performance [151], and it is also a common view that the orthogonal radiation patterns typified by E-SDM lead to good MIMO performance. This results in Fig. 4.40 and 4.41 meet the results of the previous works.

The channel capacity is calculated next. The propagation model is a Nakagami-Rice propagation model together with the Kronecker scattering assumption [152]. The number of transmission antennas is 2, and no correlation exists between the antennas.

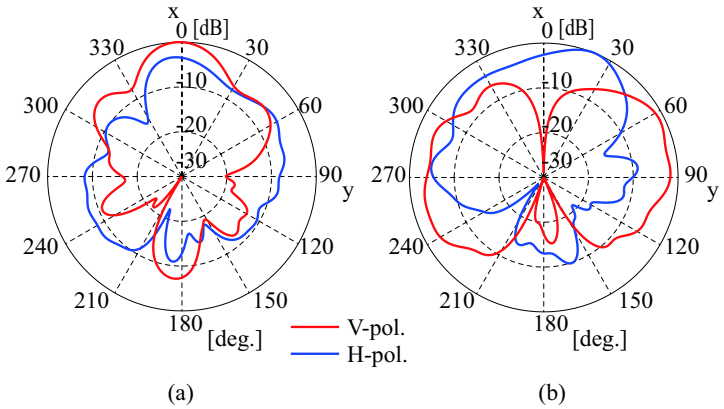

Figure 4.40. Radiation patterns in the xy plane (δ=-30°) for (a) array 1 and (b) array 2.

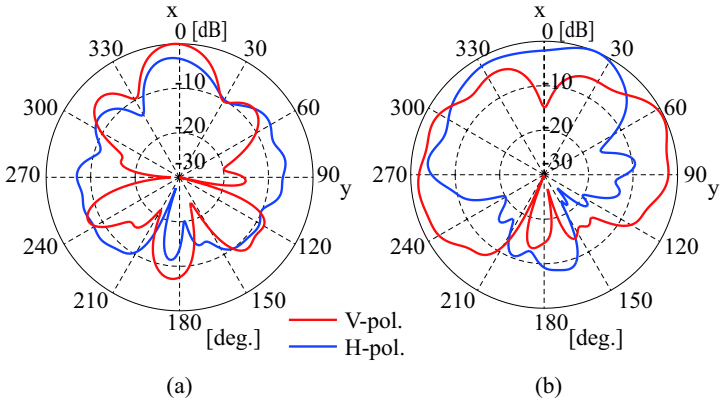

Figure 4.41. Radiation patterns in the xy plane (δ=30°) for (a) array 1 and (b) array 2.

The SNR is 20 dB, the cross-polarization power ratio (XPR) is 0 dB, and Rician factor is 3 dB. The details of the propagation analysis are described in [146]. For simplicity, the simulation assumes that all the incoming waves are concentrated in the xy plane, and the angle of the incoming wave ϕ is defined in Fig. 4.42(a). Since Nishimori et al. observed strong received signals from the horizontal directions in an indoor measurement[153], this two-dimensional model is not unrealistic. Figure 4.42(b) shows the channel capacity of the handset MIMO antenna with the phase difference determined by MEG and ρ as a function of ϕ. Channel capacities with optimum phase difference are larger than those without phase difference for all incoming wave angles. The maximum and average improvement factors by the MEG criterion (δ=-30°) are 20.6 % and 14.7 %, respectively. Those by the ρ criterion (δ=30°) are 20.2 % and 15.2 %, respectively.

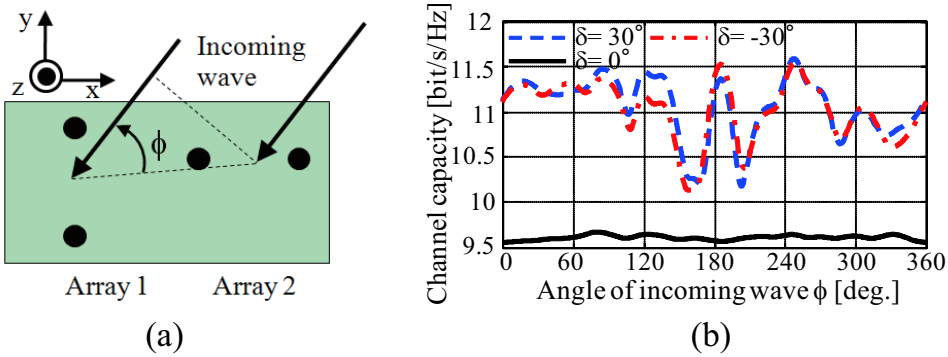

Figure 4.42. (a) Definition of the angle of the incoming wave and (b) channel capacity as a function of the angle of the incoming wave.

4.5 Summary

This chapter presented the MIMO antenna configuration methodology by using radiation patterns effectively. First, this chapter focused on MIMO downlink transmission in an indoor BS mounted in the vicinity of the wall. Then, by using a ray-tracing propagation analysis, it was revealed that a narrow HPBW of 60°-80° pointed to the corner of the room was effective in obtaining large channel capacity. In this analysis, the design guidelines were derived by considering various elements, such as polarization, positions and array arrangements of the MT and the aspect ratio of the room. Based on the design guidelines, a patch antenna array with dual-feeds was fabricated, and then the measurement was conducted in the small room measuring 6.2 m × 5.8 m × 2.7 m. The results showed that the 4 × 4 MIMO channel capacity was enhanced by approximately 20% at two out of three typical MT positions, compared to that for sleeve antenna configurations. This enhancement was attributed to the increased SNR.

Then, this chapter presented a low-profile dual-polarized directional MIMO antenna for transmission. Guidelines for the radiation pattern based on the channel capacity were derived using ray-tracing propagation analysis. The following design guidelines were obtained: The main beam directions are orthogonalized in the horizontal plane and are tilted 30° downward in the vertical plane, and the HPBW is 80°. These design guidelines are applicable for conditions in which the Tx antennas are mounted in the center of a room ceiling to realize a LOS environment to the Rx antenna and the room is small-sized, as typified by 6 m × 6 m × 2.7 m. Then, the MIMO antenna for the 2.4-GHz band

was configured by four cavity-backed slot and four printed dipole antenna elements to achieve the above parameters. Slot and dipole elements radiate vertical and horizontal polarizations, respectively. This chapter presented the measured characteristics and revealed that a unidirectional radiation pattern with a tilt angle in the vertical plane was obtained in these structures. Channel measurements in an actual environment were also performed, and the SNR and channel capacity were compared with those of the sleeve antenna configuration. The place-averaged SNR of the proposed antenna was 14.1 dB, and the improvement factor was 2.6 dB. The place-averaged channel capacity of the proposed antenna was 7.1 bits/s/Hz, and improvement factor was 16.2%. The results of the present study revealed that the MIMO capacity performance was the same or better than that of the sleeve antenna configuration. A low-profile MIMO antenna for the 2.4-GHz band with a thickness of only 0.16λ (20 mm) was also developed. This antenna consisted of loop and dipole elements, and it was also based on the design guidelines derived by the ray-tracing propagation analysis. The reflection characteristics of the loop and dipole antennas were less than -10 dB, and mutual coupling between vertical polarization elements, and between vertical and horizontal polarization elements were nearly less than -20 dB in the measured data.

Finally, this chapter briefly examined the MT side. Here, fixed-phase-difference feeding was applied to a MIMO handset antenna and the channel capacity was evaluated by a propagation analysis including human body effects. The results revealed that when human body effects were considered, the channel capacity was also enhanced by optimum fixed phase difference based on the mean effective gain and the correlation coefficient. The enhancement was confirmed for all incoming wave angles, and the average improvement factor from each criterion was 14.7 % and 15.2 %, respectively. The enhancement can be achieved by fixed phase difference, namely, by using simple feeding circuits such as delay lines.

Chapter 5

Feeding Circuits with a Switching Function for Multiradiation Patterns

5.1 Introduction

This chapter proposes a novel feeding circuit with a switching function to alter the shapes and directions of radiation patterns. First, techniques to realize cardioid and figure 8 radiation patterns are presented. Then, as modified versions, techniques to realize omnidirectional and directive radiation patterns are presented. Those techniques are based on array antenna theory, and the multiradiation pattern is generated by the switching of feed elements and phase-difference feeding.

Since the proposed scheme does not lead to radiation patterns with high gain, the function is not to enhance the SNR but to prevent SNR reduction. Therefore, when the contents of this chapter are connected with Chapter 3, the proposed scheme is positioned as a technique to reduce the spatial correlation. This chapter is also related to Chapter 4. In Chapter 4, channel capacity enhancement by fixed radiation patterns was discussed, and by using this approach, overall MIMO performance is enhanced. However, a closer examination reveals positions of degraded performance's, and the approach is not always sufficient. Therefore, the content of this chapter is also positioned as one countermeasure against the problem raised in Chapter 4. Furthermore, system-level examinations relevant to beam switching are discussed in Chapter 6.

5.2 Switching of Cardioid and Figure 8 Radiation Patterns

5.2.1 Concept and Structure

As is well-known from theory [154], in a two-element linear array arranged at $1/4\lambda$ intervals, cardioid radiation patterns with opposite orientations to each other are obtained by phase-difference feeds of $\pm 90°$. In a two-element linear array arranged at $1/2\lambda$ intervals, figure 8 radiation patterns oriented orthogonal to each other are obtained by phase-different feeds of $0°$ and $180°$ (Table 5.1).

This theory is explained well in [155] as follows. The radiation pattern of an array antenna in the horizontal plane $E(\theta)$ is given by

$$E(\theta) = g(\theta) f(\theta) \tag{5.1}$$

Table 5.1. Relation among interelement spacings, phase differences, and radiation patterns in a two-element linear array.

Interelement spacing	$1/4\lambda$		$1/2\lambda$	
Phase difference	-90°	90°	0°	180°
Radiation pattern	Cardioid (Type 1)	Cardioid (Type 2)	Figure of eight (Type 1)	Figure of eight (Type 2)

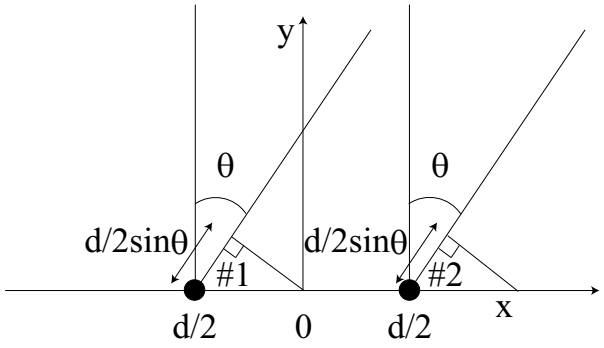

Figure 5.1. A two-element array assuming isotropic wave sources.

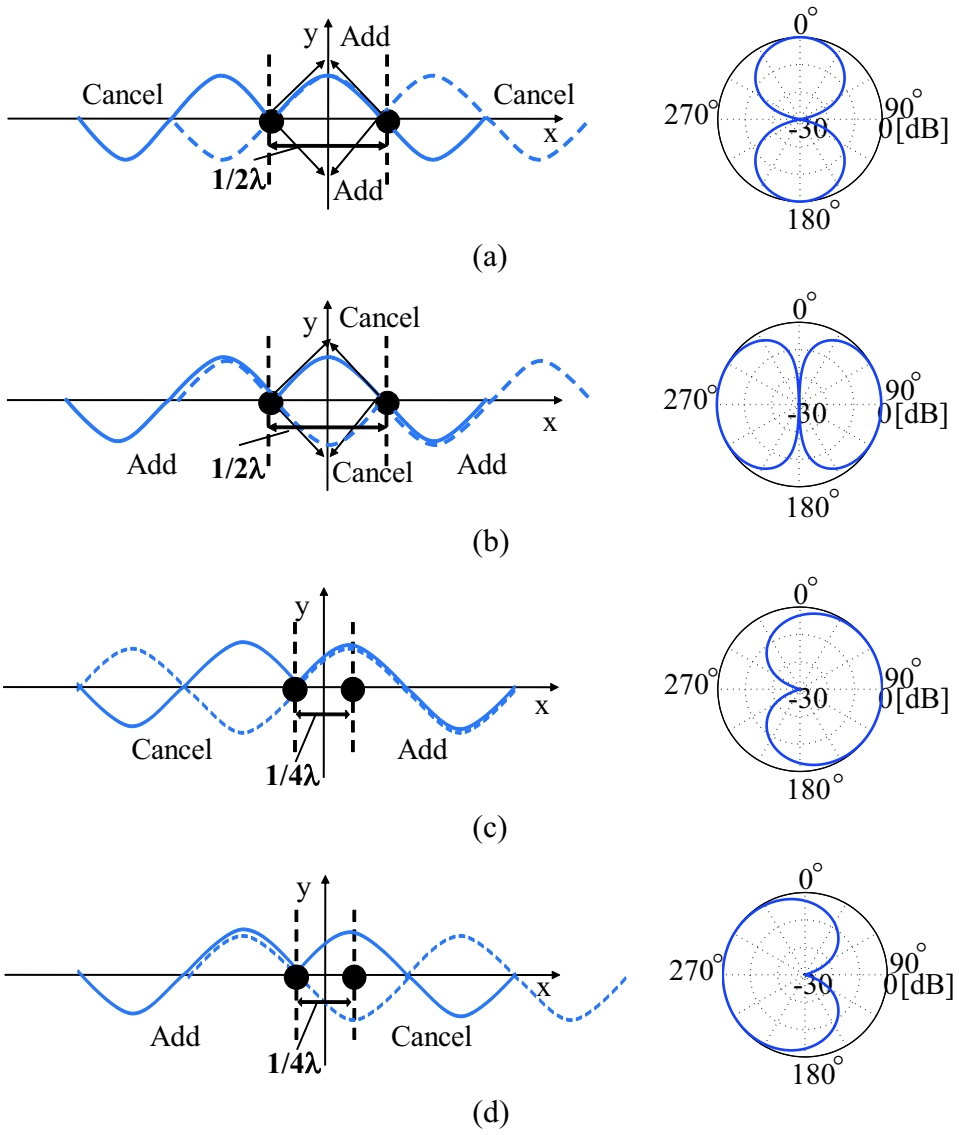

Figure 5.2. Conceptual diagrams of the radiation and the radiation patterns when interelement spacing and excitation conditions are changed in a two-element array. (a) $d = 1/2\lambda$, $\phi_1 = 0°$, $\phi_2 = 0°$, (b) $d = 1/2\lambda$, $\phi_1 = -180°$, $\phi_2 = 0°$, (c) $d = 1/4\lambda$, $\phi_1 = 0°$, $\phi_2 = -90°$, and (d) $d = 1/4\lambda$, $\phi_1 = 0°$, $\phi_2 = 90°$. Here, each radiation pattern is normalized by each maximum value.

where $g(\theta)$ and $f(\theta)$ indicate the radiation pattern of each element and that when an isotropic wave source is assumed, respectively. The latter is called as the array factor. When two isotropic wave sources are assumed, as shown in Fig. 5.1, the array factor

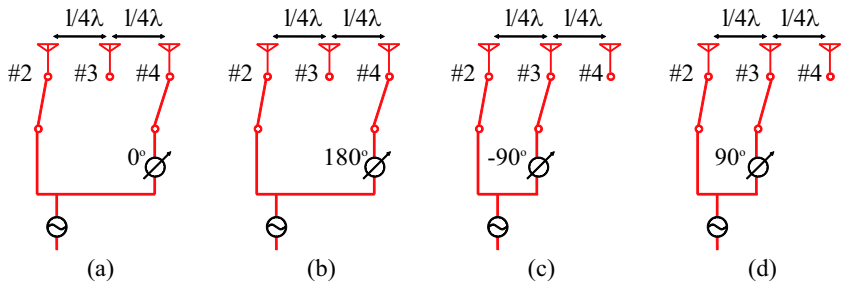

Figure 5.3. Design policy to realize the radiation patterns of Fig. 5.2.

$f(\theta)$ is given by

$$f(\theta) = e^{j(-k_0 d/2 \sin\theta + \alpha_1)} + e^{j(k_0 d/2 \sin\theta + \alpha_2)} \tag{5.2}$$

where d, k_0, and θ denote the interelement spacing, the wave number, and the angle of arrival (angle of radiation), respectively. α_1 and α_2 denote the excitation phases at positions #1 and #2, respectively,

Figure 5.2 shows conceptual diagrams of the radiation and the radiation patterns when the interelement spacing ($d = 1/2\lambda$ or $1/4\lambda$) and excitation conditions (($\alpha_1,\ \alpha_2$) = ($0°,\ 0°$), ($-180°,\ 0°$), ($0°,\ -90°$), or ($0°,\ 90°$)) are changed. The radiation patterns are derived from (5.2). For $d = 1/2\lambda$ and ($\alpha_1,\ \alpha_2$) = ($0°,\ 0°$) (Fig. 5.2(a)), the radiation in the y direction is enhanced because the waves from the two elements are in-phase, and the radiation in the x direction cancels out because the waves from the two elements are out-of-phase. Hence, a figure 8 pattern radiating in the y direction is generated. In contrast, for $d = 1/2\lambda$ and ($\alpha_1,\ \alpha_2$) = ($-180°,\ 0°$) (Fig. 5.2(b)), the radiations in the y and to x directions are canceled and enhanced, respectively, and then a figure 8 pattern radiating in the x direction is generated. For $d = 1/4\lambda$ and ($\alpha_1,\ \alpha_2$) = ($0°,\ -90°$), the radiations in the positive and negative x directions are enhanced and canceled, respectively, and then, a cardioid radiation pattern pointed in the positive x direction is generated. In contrast, for $d = 1/4\lambda$ and ($\alpha_1,\ \alpha_2$) = ($0°,\ -90°$), a cardioid radiation pattern pointed in the negative x direction is generated.

These four radiation patterns are obtained using a three-element linear array with interelement spacings of $1/4\lambda$. As shown in Fig. 5.3, 0° and 180° phase difference feeding between #2 and #3 generate a figure 8, and -90° and 90° phase difference feeding between #3 and #4 generate cardioid radiation patterns. This is just a concept,

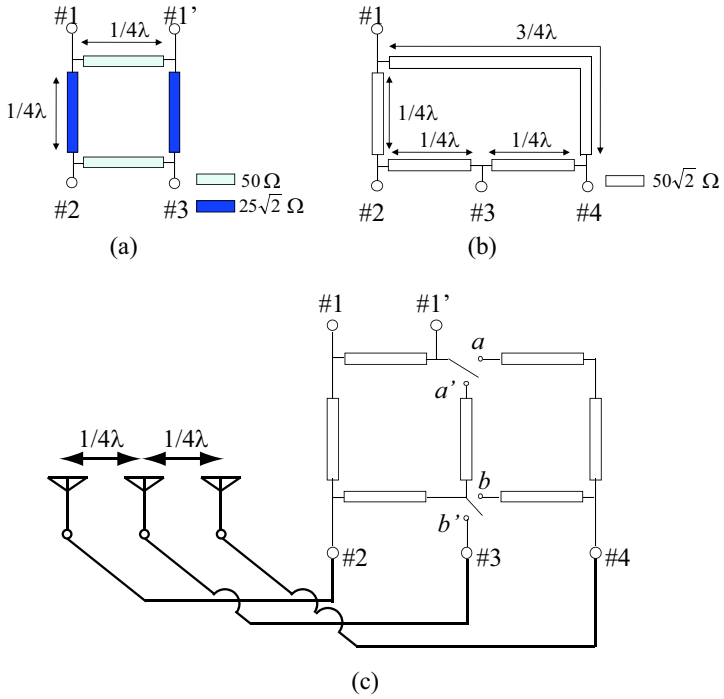

Figure 5.4. (a) 90° and (b) 180° hybrid circuits. (c) Feeding circuit for the proposed antenna array.

and the detailed method to realize the change in radiation patterns is shown in Fig. 5.4. The ±90° and 0/180° phase differences between two ports are obtained by the 90° and 180° hybrid circuits (Figs. 5.4(a) and 5.4(b)) [156]. In Fig. 5.4(a), inputs from #1 and #1' lead to -90° and 90° phase differences between #2 and #3, respectively. In Fig. 5.4(b), inputs from #3 and #1 lead to 0° and 180° phase differences between #2 and #4, respectively. The proposed circuit shown in Fig. 5.4(c) is essentially structured by combinations of these two hybrid circuits, and each operation of Table 5.1 is changed by switches. However, the simple combination increases mismatch losses and complicates the feed structure because the input from #3 in Fig. 5.4(b) is needed to obtain the in-phase feed, and the number of input ports become three (i.e., #1, #1' and #3). In fact, in the proposed feeding circuit, countermeasures are taken against these problems. The mismatch losses are suppressed by adjusting line impedance, and the input from #1' leads to the in-phase feed.

The #2, #3, and #4 ports in Fig. 5.4(c) are connected to a three-element linear array with interelement spacing of $1/4\lambda$ intervals. Here, two ports are simultaneously

excited in each operation of Table 5.1. When an input is from #1', and switches are connected to a and b (mode 1), the current path length to outputs #2 and #4 becomes equal because the current flows symmetrically. As a result, an in-phase feed is obtained between #2 and #4 (with #3 being open). Mode 1 corresponds to Fig. 5.3(a), and leads to a figure 8 pattern with a main beam in a broadside direction. When an input is changed from #1' to #1, and the states of the switches are identical to mode 1, the proposed feeding circuit works as a 180° hybrid circuit with an open stab (mode 2). An out-of-phase feed is obtained between #2 and #4 (with #3 being open). Mode 2 corresponds to Fig. 5.3(b), and leads to a figure 8 pattern with a main beam in an end-fire direction. In addition, when an input is from #1, and each switch is connected to a' and b' (mode 3), the proposed circuit works as a 90° hybrid circuit. A phase difference of -90° is obtained in #3 relative to #2 (with #4 being open). Mode 3 corresponds to Fig. 5.3(c), and leads to a cardioid pattern with a main beam in an end-fire direction. In contrast, when input is changed from #1 to #1', and the states of the switches are identical to mode 3 (mode 4), a phase difference of 90° is obtained in #3 relative to #2 (with #4 being open). Mode 4 corresponds to Fig. 5.3(d) and leads to a cardioid pattern with a main beam in an end-fire direction, which is the opposite of mode 3.

5.2.2 Numerical Evaluation

Figure 5.5 shows the detailed structures of the proposed circuit constructed of microstrip lines, for 2 GHz. The electric permittivity of the substrate is 4.8, and the thicknesses of the substrate and the conductor are 1.6 and 0.035 mm, respectively. In this structure, the widths of the lines are optimized to suppress mismatch losses. There are six switches (Sw), and modes 1-4 shown in the previous section are performed by the switching operations listed in Table 5.2. The switch's states and the current flow in each mode are depicted in Fig. 5.6. When the states of Sw 1 and Sw 2 are ON and OFF, respectively, this corresponds to the input from #1 in Fig. 5.4(c), and when those are OFF and ON, respectively, this corresponds to the input from #1'. In the latter situation, since the end of the line connected to port 1 is open, as shown in Figs. 5.6 (a) and 5.6 (d), the lines are bent to suppress the loss of the current flowing through Sw 2. In this design, switches are replaced by 1 mm × 2 mm microstrip lines for the ON state and gaps for the OFF state for simplicity,

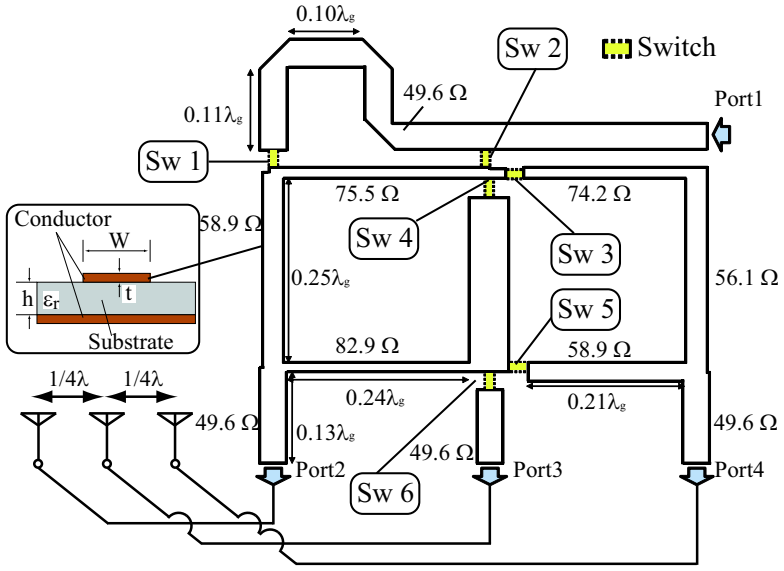

Figure 5.5. Detailed structure of the feeding circuit. (λ_g represents the center wavelength in a substrate.)

Table 5.2. Switching operations in the feeding circuit.

Mode	Sw 1	Sw 2	Sw 3 & 5	Sw 4 & 6	Phase difference (Desired value)
1	OFF	ON	ON	OFF	0°
2	ON	OFF	ON	OFF	180°
3	ON	OFF	OFF	ON	-90°
4	OFF	ON	OFF	ON	90°

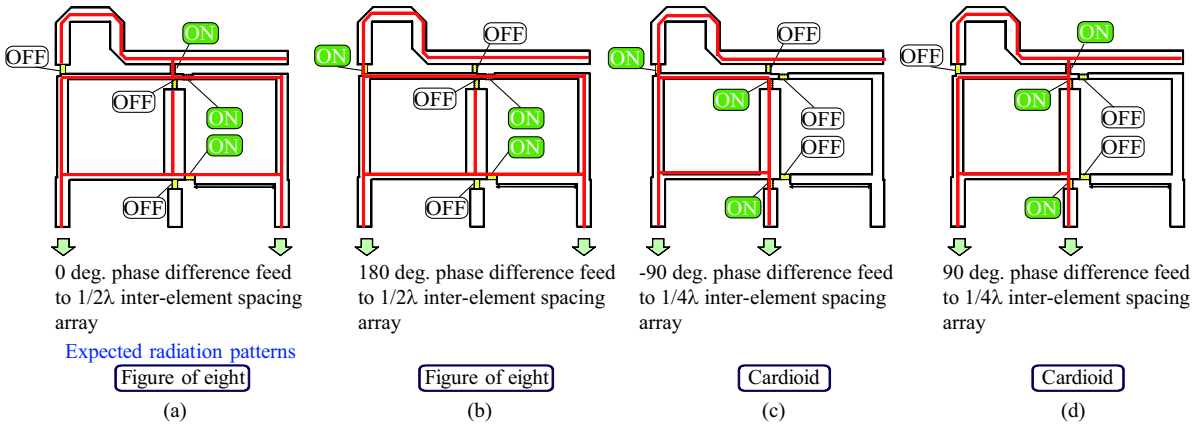

Figure 5.6. Switch states and the current flow in each mode of the proposed feeding circuit for modes (a) 1, (b) 2, (c) 3, and (d) 4, respectively.

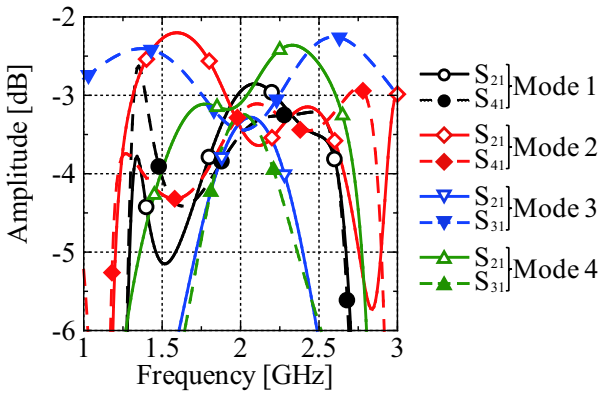

Figure 5.7. Amplitude components of the transmission characteristics ($|S_{j,1}|$).

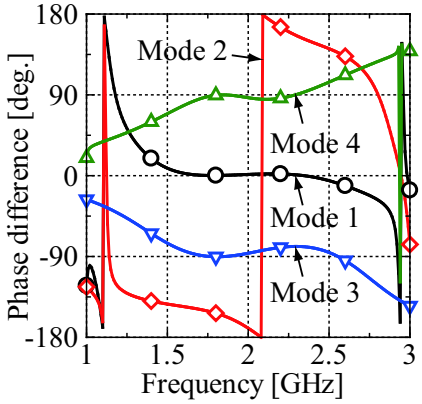

Figure 5.8. Phase difference between the output signals.

To check the operation of the proposed circuit, simulations are conducted using Microwave Office. Figure 5.7 shows the amplitude components of the transmitting characteristics ($|S_{j,1}|$) in each mode. The amplitudes are more than -4 dB; in other words, mismatch losses are less than 1 dB between 1.85 and 2.21 GHz in all modes. Figure 5.8 shows the phase difference between the output signals, and those values in the 1.85 to 2.21 GHz range are 0.40∼1.98°, 164.4∼203.9°, -90.1∼-79.7° and 85.0∼90.0° for modes 1-4, respectively. Although the variation is large for mode 2, they are small for modes 1, 3, and 4. In mode 2, the phase difference is nearly 180° at 2.08 GHz. Table 5.3 shows the $|S_{j,1}|$, the losses, and the phase differences at 2 GHz. In all modes, the $|S_{j,1}|$ are more than -3.6 dB, and the losses are less than 0.4 dB. For the phase difference, the difference between the obtained and the desired values are 1.4°, 10.1°, 3.6° and 3.2° for modes 1-4, respectively.

Next, the array factor is evaluated using the S-parameters in the proposed feeding

Table 5.3. $|S_{j,1}|$, losses, and phase differences between the output signals at 2 GHz.

Mode	1		2		3		4	
Output port	#2	#4	#2	#4	#2	#3	#2	#3
$\|S_{j,1}\|$ [dB]	-3.0	-3.5	-3.4	-3.2	-3.3	-3.4	-3.1	-3.3
Loss [dB]	0.21		0.31		0.38		0.16	
Phase difference [deg.]	1.39		190		-86.4		86.8	

circuit. Since the element spacing is narrow, and therefore mutual coupling effects should be considered, a $1/4\lambda$ monopole array is designed by using CST Microwave Studio. The array configurations shown in Figs. 5.9(a) and 5.9(b) correspond to modes 1 and 2 and to modes 3 and 4, respectively, and the port of one element is open in both configurations. Figures 5.9(c) and 5.9(d) show the S-parameters in the array configurations of Figs. 5.9(a) and 5.9(b). The reflection characteristics are less than -10 dB at 2 GHz in both arrays, and the isolation characteristics are more than -10 dB in Fig. 5.9(b) because of the narrow interelement spacing. The scattering matrices ($\mathbf{S}_1$, $\mathbf{S}_2$) at 2 GHz for Figs. 5.9(a) and 5.9(b) are given by

$$\mathbf{S}_1 = \begin{bmatrix} -0.11 + j0.060 & -0.17 - j0.18 \\ -0.17 - j0.18 & -0.11 + j0.060 \end{bmatrix} \tag{5.3}$$

$$\mathbf{S}_2 = \begin{bmatrix} -0.066 + j0.21 & 0.17 - j0.28 \\ 0.17 - j0.28 & -0.085 + j0.21 \end{bmatrix} \tag{5.4}$$

If a load (Z_L) is connected to each port (ports 1 and 2), a scattering matrix is converted into a Z-matrix as follows:

$$\mathbf{Z} = \begin{bmatrix} Z_{11} & Z_{12} \\ Z_{21} & Z_{22} \end{bmatrix} = Z_L(\mathbf{I} - \mathbf{S})^{-1}(\mathbf{I} + \mathbf{S}) \tag{5.5}$$

where $\mathbf{I}$ is an identity matrix. Now, since the $1/4\lambda$ monopole is a single mode antenna,

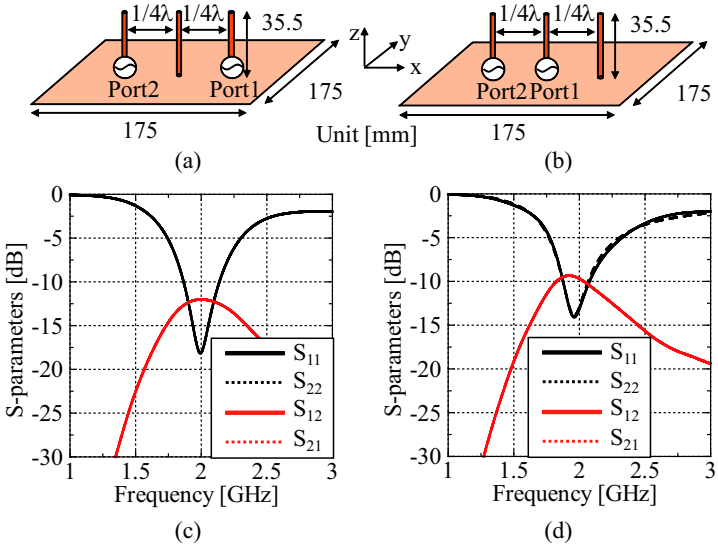

Figure 5.9. Monopole array designed using CST Microwave Studio. The array configurations are for (a) modes 1 and 2 and (b) modes 3 and 4. (The radius of the wire is 0.15 mm.) (c) and (d) are S-parameters of the configurations of (a) and (b), respectively.

the following equation is satisfied [157], [158]:

$$\mathbf{v} = \mathbf{Z}_c^{-1}\mathbf{v}_{open} = \mathbf{C}\mathbf{v}_{open} \tag{5.6}$$

where $\mathbf{v}$ and $\mathbf{v}_{open}$ represent received voltage vectors with and without mutual coupling effects, respectively, and $\mathbf{C}$ denotes the mutual coupling matrix of the array. Here, $\mathbf{Z}_c$ is given by

$$\mathbf{Z}_c = \begin{bmatrix} 1 + \frac{Z_{11}}{Z_L} & \frac{Z_{12}}{Z_L} \\ \frac{Z_{21}}{Z_L} & 1 + \frac{Z_{22}}{Z_L} \end{bmatrix} \tag{5.7}$$

Thus, the mutual coupling matrices $\mathbf{C}$ are derived from scattering matrices, and therefore mutual coupling effects can be considered by (5.6).

Figure 5.10 shows the array factors obtained by the proposed feeding circuit. First, let us focus on the characteristics at 2 GHz. To derive the array factors, the $|S_{j,1}|$ and phase differences in Table 5.3 are used. The ideal array factors denoted by "Ideal" are also shown for comparison. In the "Ideal" situation, the amplitudes of the two output signals are identical, and the phase differences between two output signals are just 0, 180, -90 and 90°. When mutual coupling is ignored, the array factors of the proposed

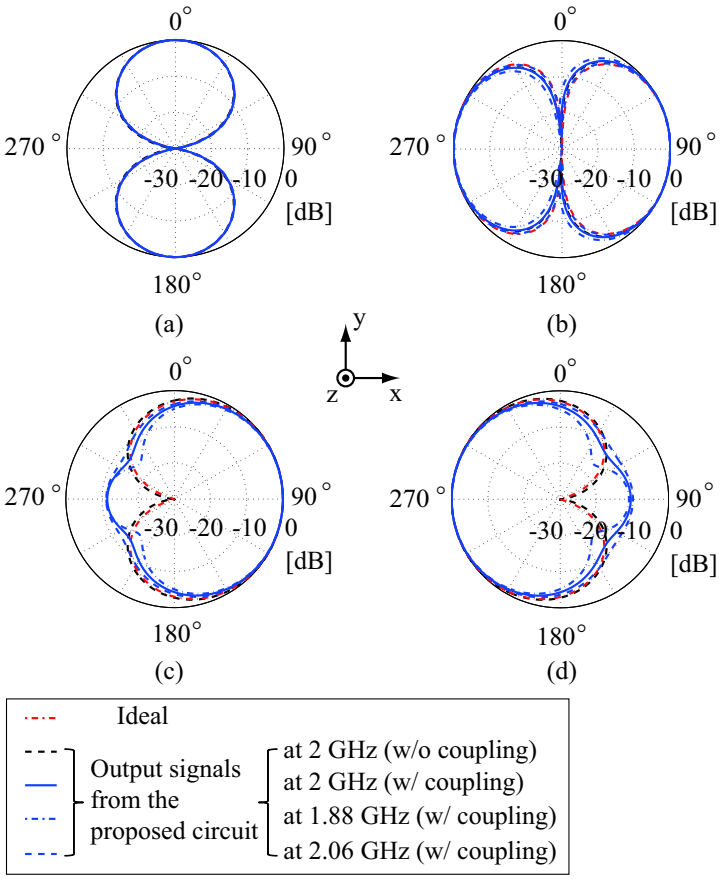

Figure 5.10. Array factors in the proposed antenna array. (a)-(d) correspond to modes 1-4.

array are similar to the "Ideal" ones and cardioid and figure 8 radiation patterns with two beam directions are obtained.

After mutual coupling is considered, good characteristics are also obtained for figure 8 radiation patterns (modes 1 and 2) because the mutual coupling effect is not significant. In modes 3 and 4, the null of the cardioid patterns do not appear because the mutual coupling effect is strong. However, the front-to-back (F/B) ratios, which are defined as the proportion of 90° and 270° to 270° or 90° directions, respectively, are more than 10 dB. This indicates that uni- and bidirectional radiation patterns with two main beam directions can be switched by the proposed feeding circuit.

Next, the variation in the radiation patterns is evaluated in the range of 1.89 and 2.03 GHz with reflection characteristics of less than -10 dB. The radiation patterns at 1.89, 2, and 2.03 GHz are shown in Fig. 5.10. In mode 1, the variations in the radiation

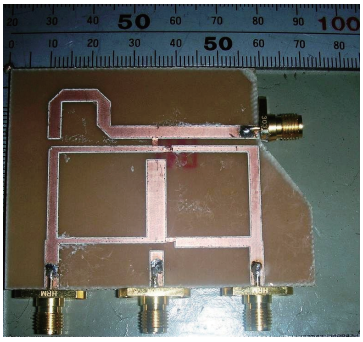

Figure 5.11. Photograph of the fabricated feeding circuit.

pattern at 2 and 2.03 GHz compared with 1.89 GHz are 0.23 and 0.44 dB, respectively. Here, the variation is derived based on the average absolute value of the difference in radiation level between each frequency at all angles. Those variations in mode 2-4 are 1.40 and 2.62 dB, 0.87 and 1.53 dB, and 1.31 and 2.20 dB, respectively. Although the variation is large in modes 2 and 4, figure 8 radiation patterns are still obtained in mode 2, and the F/B ratios are nearly more than 10 dB in each frequency in mode 4.

5.2.3 Measurement Based Performance Evaluation

This section evaluates the performance of the proposed feeding circuit empirically by fabricating it as shown in 5.11. The fabricated circuit is made of a glass epoxy dielectric substrate (FR-4, with an electric permittivity of 4.8 and a substrate thickness of 1.6 mm). In the measurement, the nonmeasured ports are terminated, and copper tape is used as a substitute for the switches. Although the microstrip lines are connected with the copper tape for the ON states, they are not connected for the OFF states. Figure 5.12 shows the comparison between simulation and measurement results of the S-parameters in the feeding circuit. For the phase characteristics, measurement data agree with simulation data in the vicinity of 2 GHz. Although the measurement data for mode 3 are slightly different from the simulation data, the trends in characteristics are identical. For the amplitude characteristics, the losses of measurement data are larger than those of the simulation data. This is because of the losses from the copper tape and the solder in the feeding circuit. Although the two microstrip lines are closely arranged near the input port (port 1 in Fig. 5.5), it was confirmed that the coupling between the two ports was low. The measured losses averaged between 1.85 and 2.21 GHz for modes 1-4 are

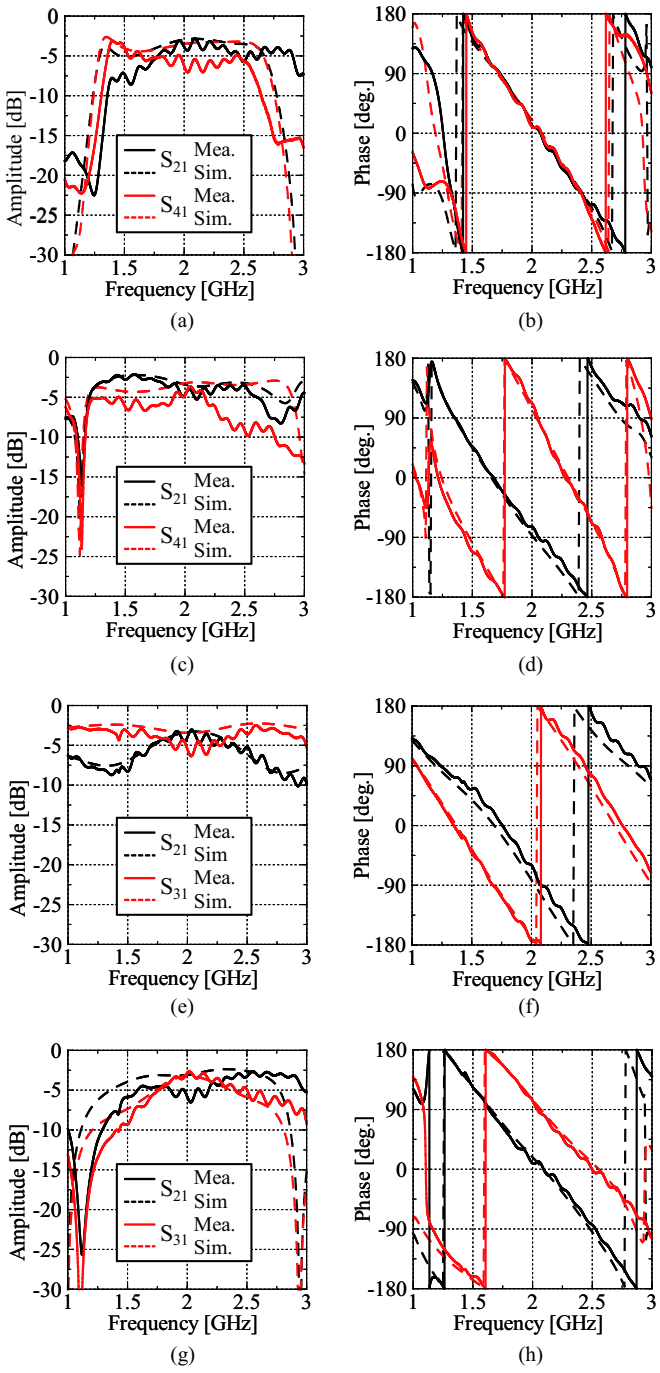

Figure 5.12. The amplitude components of transmission characteristics for modes (a) 1 (c) 2 (e) 3, and (g) 4 and the phase components of the transmission characteristics for modes (b) 1. (d) 2, (f) 3, and (h) 4.

1.72, 1.41, 1.48, and 1.21 dB, respectively. Although the measured losses increases by 1.47, 1.10, 1.08 and 1.02 dB for their modes, compared with the simulated losses, the

averaged measured losses of the feeding circuit are less than 1.8 dB.

5.3 Switching of Omnidirectional and Directive Radiation Patterns

5.3.1 Structure and Numerical Evaluation

The previous section proposed a feeding circuit with a switching function for uni- and bidirectional radiation patterns. However, a switch between omnidirectional and directive patterns is more useful. This section proposes a feeding circuit for switching an omnidirectional pattern in addition to the previously realized pattern shapes.

Figure 5.13 shows the schematic view of the proposed feeding circuit. The circuit is similar to Fig. 5.5, and the number of switches is identical to that in Fig. 5.5. However, the impedance (width) of each microstrip line is different from that in Fig. 5.5, and a new mode is added (mode 5). Here, the switches (Sw) are also represented by 1 mm $\times$ 2 mm microstrip lines for the ON states and gaps for the OFF states for simplicity, Figure 5.14 shows the current flow for each operation mode. The operation principle of modes 1-4 is identical to that shown in Fig. 5.6, and in mode 5, feed to a single element

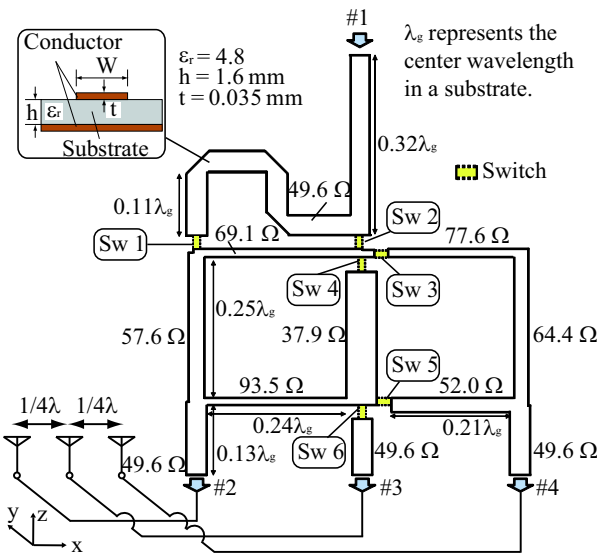

Figure 5.13. Detailed structure of the proposed feeding circuit constituting of microstrip lines.

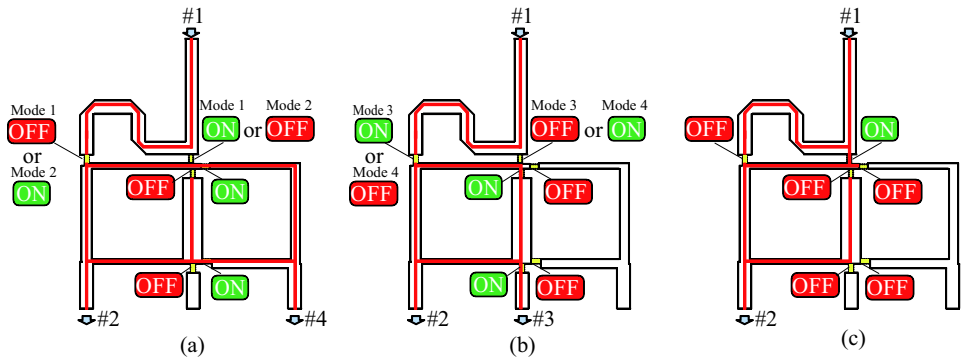

Figure 5.14. Current flow for each mode in the proposed feeding circuit.

Table 5.4. Operations in the feeding circuit.

Mode	Excited output port	Inter-element spacing between the excited ports	Operation	Phase difference between output ports	Radiation pattern
1	#2 and #4	$1/2\lambda$	Symmetrical current flow	0°	Figure of eight
2	#2 and #4	$1/2\lambda$	180° hybrid with an open stub	180°	Figure of eight
3	#2 and #3	$1/4\lambda$	90° hybrid	-90°	Cardioid
4	#2 and #3	$1/4\lambda$	90° hybrid	90°	Cardioid
5	#2	NA	Feed to a single element	NA	Omni

by switching provides an omnidirectional pattern. Table 5.4 summarizes the operations for all modes.

Figures 5.15(a) and (b) show the transmission characteristics ($|S_{j1}|$) and the phase differences between the output signals for all modes. The $|S_{j1}|$s are more than -3.6 dB, and the losses are less than 0.5 dB in all modes at 2 GHz. For the phase differences in modes 1-4, the differences between the obtained and the desired values in Table 5.2 are 1.8°, 4.8°, 2.7° and 2.5°, respectively, and these are sufficiently small. Next, the variation in those characteristics as a function of frequency is described. The losses are less than 1 dB between 1.86 and 2.48 GHz in all modes. For the phase difference, the differences between the obtained and the desired value are less than 10° between 1.70 and 2.36 GHz in modes 1, 3 and 4. In mode 2, this condition is satisfied between 1.96 and 2.11 GHz, and the variation in the phase difference as a function of frequency is large. Figure 5.16

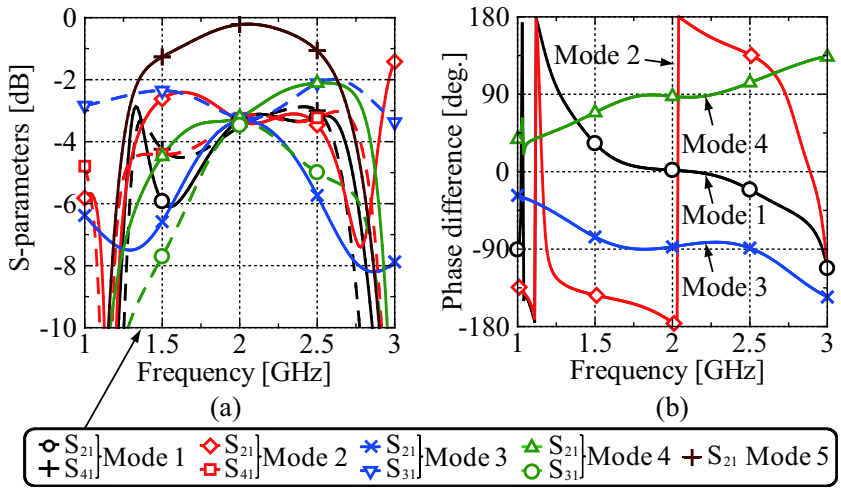

Figure 5.15. (a) Transmission characteristics ($|S_{ij}|$) and (b) phase differences between output signals in the proposed feeding circuit.

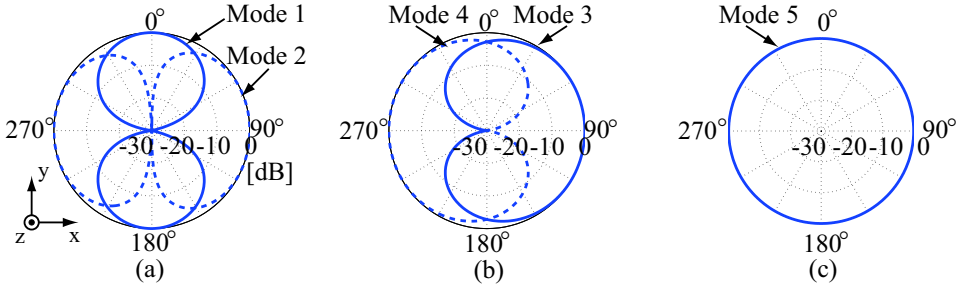

Figure 5.16. Array factors derived from the output signals. Here, mutual coupling effects are not considered.

shows the array factors at 2 GHz derived from the output signals of the proposed circuit. Here, for simplicity, mutual coupling between elements is not considered. For this figure, two figure 8's and two cardioid radiation patterns and omnidirectional radiation pattern are realized.

Now the radiation patterns are evaluated by combining the proposed circuit and an antenna array. Figure 5.17(a) shows the three-element monopole array with $1/4\lambda$ interelement spacing. In this figure, the allocations of the port in modes 1-5 are also shown, and at least one port is opened in each mode. Figure 5.17(b) shows the S-parameters of the monopole array in each mode. In modes 3 and 4, since the interelement spacing between two excited ports is $1/4\lambda$, the isolation ($|S_{12}|$) is low, and the value is

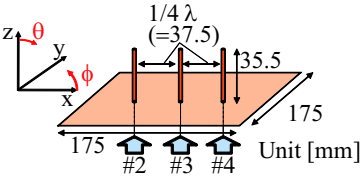

	#2	#3	#4
Modes 1 and 2	Port 2	Open	Port 1
Modes 3 and 4	Port 2	Port 1	Open
Modes 5	Port 1	Open	Open

(a)

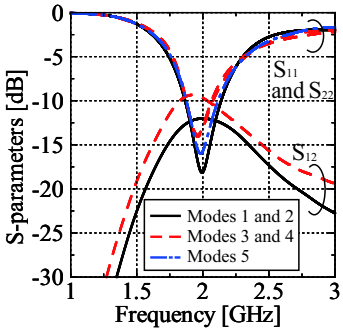

(b)

Figure 5.17. (a) Three-element monopole with 1/4λ interelement spacing and the feed methods for each mode, and (b) the S-parameters of the monopole array.

more than -10 dB. Then, the reflection characteristics between 1.88 and 2.06 GHz are less than -10 dB in all modes.

Figure 5.18 shows the radiation patterns of E_θ in $\theta = 90°$ for each mode. To derive them, CST Microwave Studio was used, and the ports are excited under the conditions of Fig. 5.17(a). The radiation patterns obtained in each element are synthesized based on the amplitude and phase of the output signals in the proposed feeding circuit. As shown in Fig. 5.18, one omni-, two bi-, and two unidirectional radiation patterns are confirmed in the horizontal plane although the null in modes 1, 3, and 4 do not appear because of mutual coupling effects. The radiation patterns at 1.88 GHz are different from those at 2 and 2.06 GHz in modes 3 and 4. As a supplementary note, it was confirmed that as the output amplitude moves further from the value required to form a cardioid radiation pattern considering mutual coupling effects, the shape of the radiation pattern becomes smoother. Additionally, when the phase difference between output ports is far from the desired value, the null of the radiation patterns does not disappear. Therefore, the difference in the amplitude between the obtained and the desired value is small at 1.88 GHz. In this figure, the important aspects are that the radiation patterns in modes 1 and 2 are quasiorthogonal to each other and that the radiation patterns in modes 3 and 4 are oppositely directed. The radiation patterns are changed significantly by switching because the correlation coefficients between modes 1 and 2 and between modes 3 and 4 are expected to be small. This demonstrates the versatility of the proposed technique for various scenarios.

Figure 5.19 shows the radiation patterns in the vertical plane. The differences of

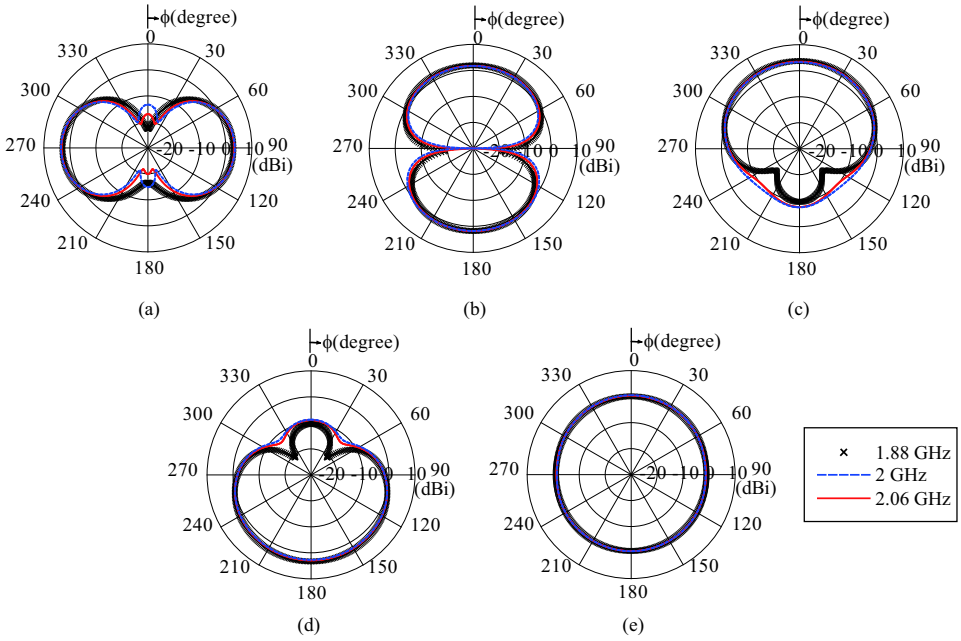

Figure 5.18. Radiation patterns (E_θ) of the array with E_θ=90°. (a)-(e) correspond to modes 1-5, respectively.

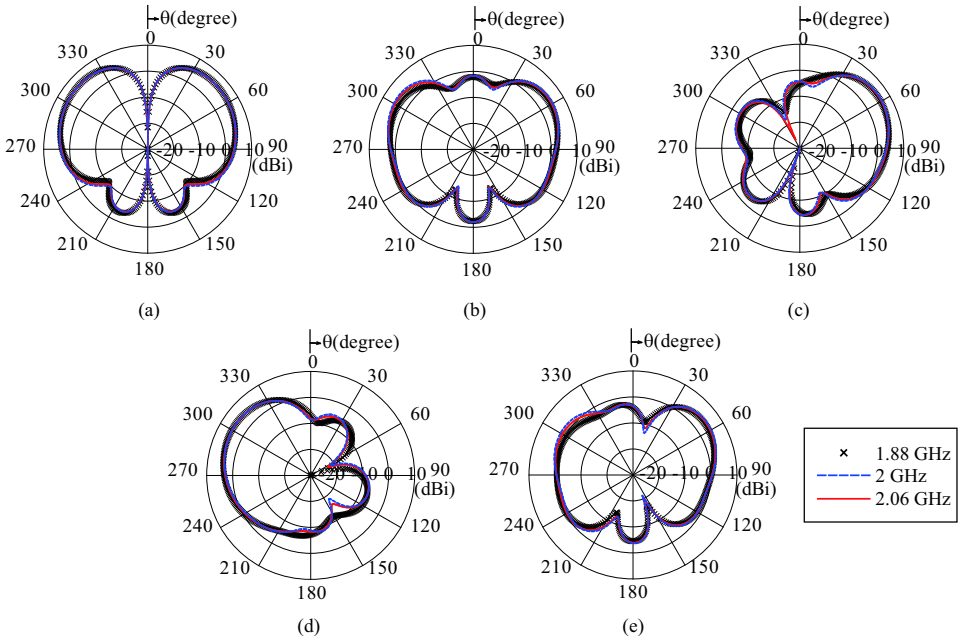

Figure 5.19. Radiation patterns (E_θ) of the array with (a) ϕ=90° and (b)-(e) ϕ=0°. (a)-(e) correspond to modes 1-5, respectively.

the radiation patterns depending on the frequency are small. The radiation patterns have upward tilt angles because of the ground of the array. In mode 1, the maximum

radiation directions (MRDs) at 2 GHz are 47° between 0-180° and 313° between 180-360°. In addition, the maximum gains (MGs) are 6.0 dBi in mode 1. In mode 2, their MRDs are 57° and 302°, and their MGs are 4.9 dBi and 4.8 dBi, respectively. In modes 3 and 4, the MRDs are 57° and 304°, respectively, and the MGs are 6.3 dBi and 4.9 dBi, respectively. In these results, for example in modes 3 and 4, the radiation patterns are tilted toward the zenith direction. These characteristics are suitable for indoor base stations, as shown in Chapter 4.

5.3.2 Examination of the Switching Circuit

Thus far, the switches have been represented by the existence or nonexistence of microstrip lines. This section details the design of switching circuits, describe the design procedure and shows the characteristics of the output signals.

Switches applied to microwaves are mainly divided into mechanical and semiconductor types. Generally, mechanical types offer low insertion loss; however, their application is not realistic in the proposed feeding circuit. Although microelectromechanical systems (MEMS) devices are expected as a new technology in mechanical switches, the necessity of a high voltage for operating these device is a problem. Semiconductor-type switches include PIN diode switches and field-effect transistor (FET) switches. Here, PIN diode switches are used because FET switches suffer from the following problems: (1) the control signal power required must be higher than that for switched RF signals and (2) there is a large insertion loss because the internal resistance is high [159].

The PIN diode used is HVC131 (Renesas Electronics Corporation) and ON and OFF states are switched by the existence or nonexistence of an external bias. First, an equivalent circuit of a PIN diode is constructed. The measurement setup is shown in Fig. 5.20, and the procedure is as follows [160]:

1. A feed pin is connected to port 1 of a network analyzer, and the electrical length is adjusted in this state. Here, the end of the feed pin is abridged.

2. A PIN diode is soldered between the feed pin and ground, as shown in Fig. 5.20.

3. A DC power supply is connected to the bias input in Fig. 5.20, and an appropriate bias is added.

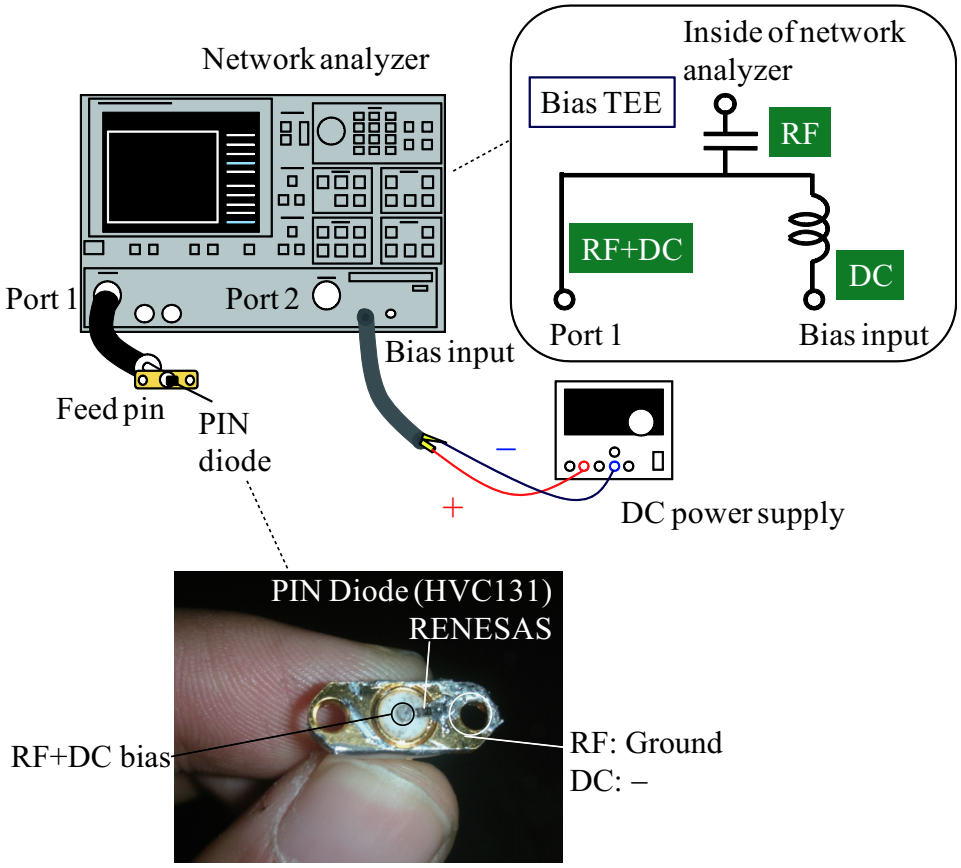

Figure 5.20. Measurement setup for obtaining the equivalent circuit of a PIN diode.

4. An equivalent circuit is made from the impedance data obtained from a Smith chart.

Here, since bias tee is configured in the network analyzer, as shown in Fig. 5.20, the RF signals and DC bias are superimposed in port 1 and the DC bias is added to the PIN diode.

Figures 5.21(a) and 5.21(b) show the measured Smith chart in ON and OFF states, respectively, and the change in characteristics caused by the external bias is confirmed. Here, an impedance Z obtained at a certain frequency is denoted as

$$Z = R + jX \tag{5.8}$$

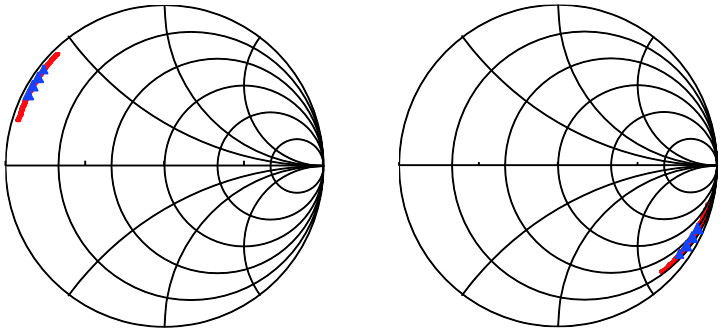

Figure 5.21. Smith chart in the ON state (with a forward current of 10 mA) and in the OFF state (with a forward current of 0 mA).

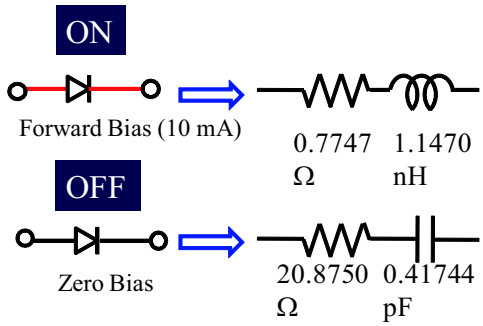

Figure 5.22. Equivalent circuit of a PIN diode in the ON and OFF states at 2 GHz.

Then, the impedances in the ON and OFF states, Z_{ON}, and Z_{OFF} are given by

$$Z_{ON} = R_f + j\omega L_f, \;\; Z_{OFF} = R_{zero} + j\omega C_{zero} \tag{5.9}$$

By comparing (5.8) with (5.9), the equivalent circuits in the ON and OFF states at 2 GHz are derived as shown in Fig. 5.22. Figures 5.23(a) and 5.23(b) show the variations in R_F and L_F as a function of forward current. Since those values are stable in the vicinity of 10 mA, the value assumed as the ON state in Figs. 5.21 and 5.22 is appropriate.

Figure 5.24(a) shows the switching circuit using the PIN diode [161]. The functions of each element and the position of bias are also shown in this figure, and RF signals from #1 go through to #2. In Figs. 5.24(b) and 5.24(c), a part of the PIN diode is replaced by the equivalent circuit of Fig. 5.22. Here, the reason that the equivalent circuit was derived is because a rough insertion loss is estimated and breaking characteristics—

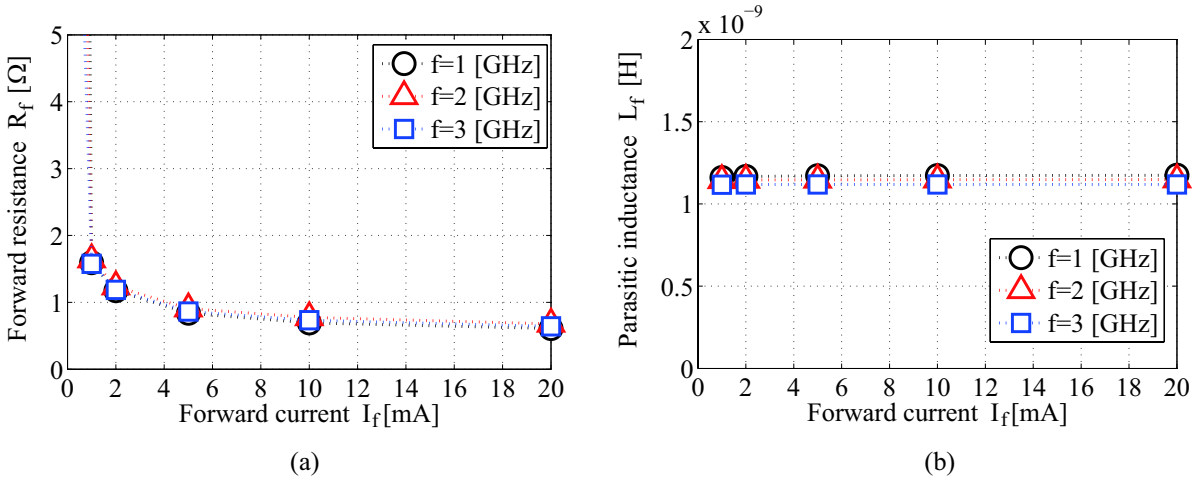

Figure 5.23. Variation in forward resistance R_f and parasitic inductance L_p as a function of forward current I_f.

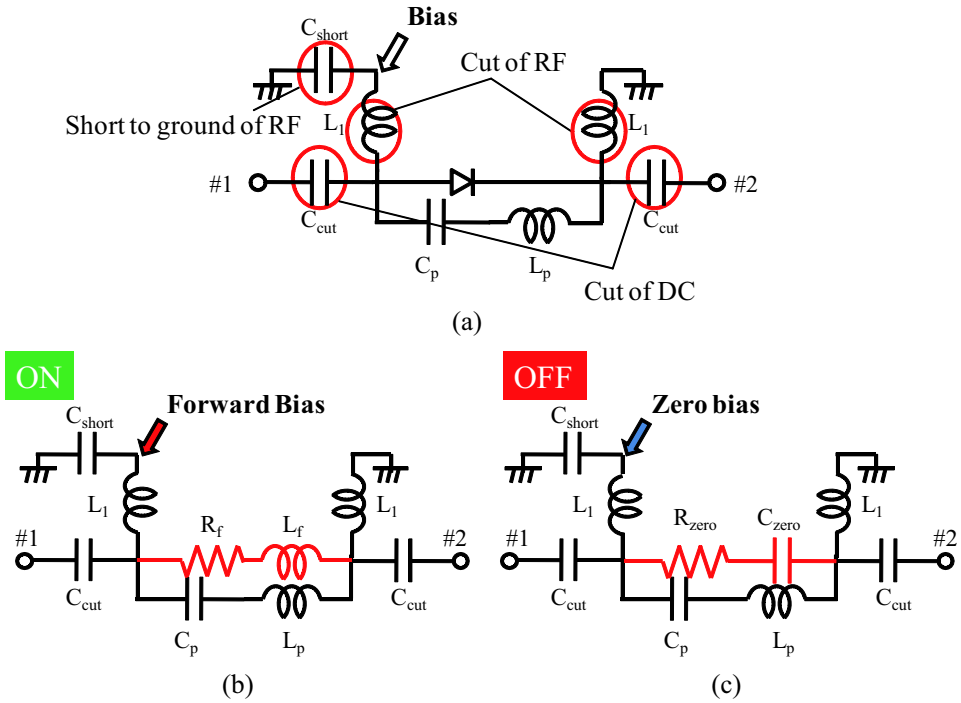

Figure 5.24. (a) Design of a switching circuit using a PIN diode. (b) and (c) represent the circuit in the ON and OFF states, respectively, and the equivalent circuit is used for the PIN diode in these figures. R_f=0.7748 Ω, L_f=1.1470 nH, L_p=15 nH, C_{cut}=C_p=C_{short}=100 pF, L_1=22 nH, R_{zero}=20.8750 Ω, and C_{zero}=0.41744 pF.

namely, isolation characteristics in OFF states—can be enhanced using the equivalent circuit. For the latter, when there are no C_p and L_p connected in parallel with the PIN diode, the isolation characteristics are not good. For simplicity, a parallel circuit constructed using only C_{zero} and L_p is considered. In this circuit, the equation for the impedance $|Z_p|$ is given by

$$|Z_p| = \frac{\omega L_p}{1 - \omega^2 C_{zero} L_p} \tag{5.10}$$

When $1 - \omega^2 C_{zero} L_p = 0$ is satisfied in (5.10), $|Z_p|$ becomes ∞. This indicates that when the above condition is satisfied at the target frequency (2 GHz), RF signals cannot go through to #2. Therefore, the requirement for L_p is given by

$$L_p = \frac{1}{4\pi^2 f^2 C_{zero}} = \frac{1}{4\pi^2 \times (2 \times 10^9)^2 \times 0.41744 \times 10^{-12}} \approx 15 \text{ nH} \tag{5.11}$$

Since C_{zero} is used to determine L_p, the equivalent circuit has important implications. Here, the reason for the addition of C_p is to prevent the circuit from shorting out the DC bias. As a reference, in a simple circuit simulation with only lumped elements (without considering microstrip lines), S_{21}=-0.44 dB (ON) and S_{21}=-25.4 dB (OFF) at 2 GHz are obtained. The insertion loss is sufficiently low since the diode's impedance is low, and then an addition of LC circuit has a small impact on the transmission characteristics in the ON state. In addition, the isolation characteristics are also good.

Figure 5.25 shows the fabricated switching circuit based on Fig. 5.24. The lumped elements are soldered between microstrip lines, and a bias is added by the power supply. Figure 5.26 shows the measured amplitude and phase characteristics of S_{21}. In Fig. 5.26(a), although the best isolation characteristics are shifted in the vicinity of 1.64 GHz, the insertion losses are less than 1 dB at both 1.64 and 2 GHz. Moreover, the S_{21} values at 1.64 and 2 GHz for the OFF states are -21.0 dB and -12.6 dB, respectively; they are less than -10 dB. Although the phase is largely changed at 1.64 and 2 GHz in Fig. 5.26(b), it is confirmed that this can be compensated by optimization of the length of the microstrip lines in the feeding circuit.

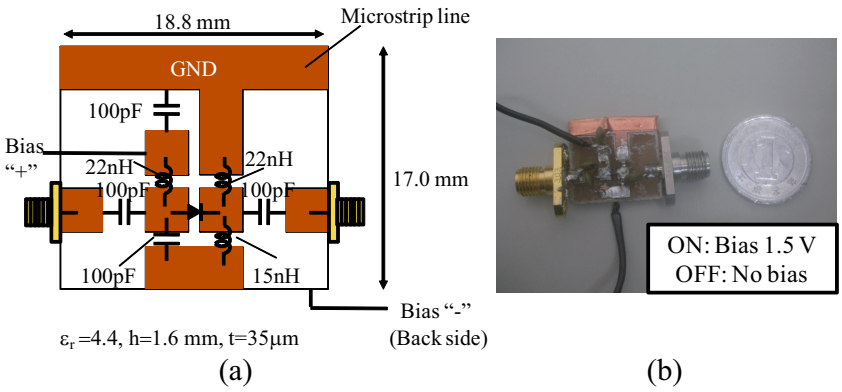

Figure 5.25. Fabricated switching circuit. (a) Circuit schematic and (b) photograph of the fabricated circuit.

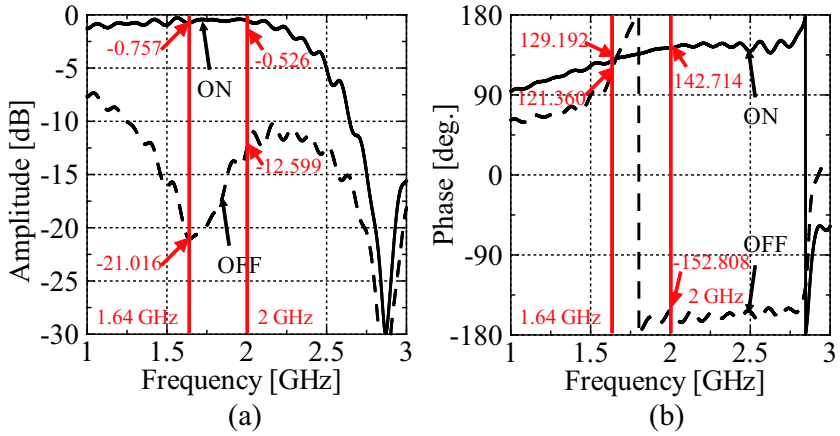

Figure 5.26. (a) Amplitude and (b) phase characteristics of S_{21} for the switching circuit.

5.4 Summary

First, this chapter proposed a novel feeding circuit with a switching function for cardioid and figure 8 radiation patterns. The two main beam directions are switched in each pattern. The operation principle was described, and an explanation was given on how to use the phase-difference feeds and switch the feed elements effectively. The analysis showed that the mismatch losses of the output signals were less than 1 dB between 1.85 and 2.21 GHz, and the phase differences between two output ports were close to 0°, 180°, -90° and 90° for each operation mode at 2 GHz. The array factors derived from the output signals at 2 GHz showed that two cardioid and two figure 8 radiation patterns

were achieved when mutual coupling effects were ignored. When mutual coupling effects were considered, a unidirectional radiation pattern with more than 10 dB F/B ratio and a bidirectional radiation pattern were obtained. Moreover, the measurement results showed that the averaged losses between 1.85 and 2.21 GHz were less than 1.8 dB, and the phase difference agreed with simulation data in the vicinity of 2 GHz in the proposed feeding circuit.

Second, this chapter proposed a novel feeding circuit with a switching function for omnidirectional and directive radiation patterns. The proposed circuit has five operation modes, and it can switch feed to two elements with phase differences of 0°, 180°, -90° and 90° and feed a single element. The simulation results showed that, in all modes, mismatch losses were less than 0.5 dB and the desired phase differences were obtained at 2 GHz. The output signals led to the array factor of one omnidirectional, two cardioid, and two figure 8. Then, this chapter considered a combination with a three-element linear monopole array and revealed that uni-, bi- and omnidirectional radiation patterns were obtained. The variation in the radiation patterns as a function of the frequency was small at 1.88, 2 and 2.06 GHz. Since the effect of switching circuits had not been considered in the simulation and measurement, the design procedures were shown, and the measurement results of the fabricated switching circuit was evaluated. Although a frequency shift was occured, good insertion loss and isolation characteristics were observed.

Chapter 6

Criterion to Minimize Bit Error Rate for MIMO Antenna Selection

6.1 Introduction

This chapter presents an antenna selection criterion that is suitable for indoor LOS scenarios for two-stream MIMO systems. The aim of antenna selection techniques is not to enhance the SNR because antenna gain is not changed but to prevent SNR reduction. The results presented in this chapter will show that adjustment of both the SNR and the spatial correlation is required to achieve a low bit error rate (BER); however, antenna selection is categorized as a technique to reduce spatial correlation by changing propagation paths, which links the contents of this chapter with Chapter 3. Moreover, this chapter is also related to Chapter 5, which presents a novel techniques for switching radiation patterns. Since the selection criterion can be applied to algorithms for switching the appropriate radiation patterns, this topics ranks as a system-level consideration. For evaluating MIMO performance, many researchers have used channel capacity as an evaluation indicator, and this dissertation has followed the same strategy. Although the evaluation by channel capacity is valid, there is a view that channel capacity is an upper limit of the transmitting rate and that BER is a more practical evaluation evaluation index [64]. Therefore, this chapter presents the evaluation of MIMO performance using the BER.

In MIMO systems, the use of a large number of antenna elements improves the

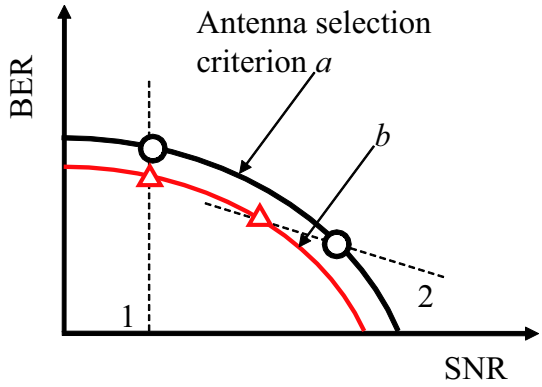

Figure 6.1. Basic concept of evaluation of BER performance as a function of SNR.

performance of channel capacity and the BER [30], [162]. However, in some cases, such as at MTs, fewer elements are desirable in order to save space for mounting antennas and reduce the power, cost, and complexity of the front-end [163]. As a result, the maximum number of streams is often decided at the MT side. As an effective countermeasure, antenna selection can be conducted at the BS side, which typically has a larger space for mounting. When the channel conditions are unfavorable, antenna selection can help to change the conditions, and MIMO performance is then enhanced without an increase in the number of streams.

Many studies have been conducted on antenna selection in MIMO systems, and the BER performances achieved have been evaluated. As antenna selection criteria, the SNR [114], minimum eigenvalue of the spatial correlation matrix [114], [164], and determinant of the channel matrix [165] have been examined. In addition, the phase components of the channel matrix can also be a selection criterion [164].

Several previous studies, for example [114], have compared MIMO performances in terms of the antenna selection criteria. However, the performances have been evaluated as a function of the SNR, and the changes in the SNR resulting from the selected antenna subset have not been considered appropriately. Figure 6.1 shows the basic concept of evaluating the BER performance as a function of the SNR for antenna selection criteria a and b. Although it is determined that the criterion b is better under a fixed SNR (i.e., for dotted line 1), the performances should be compared using different SNRs, because for different antenna selection criteria, the selected antenna subsets are also different. In other words, we should consider variations in both the amplitude and the phase of the

channel matrix depending on the selected antenna subsets. The evaluations under this condition correspond to the dotted line 2 in Fig. 6.1, and the BER of the selection criterion a outperforms b in some cases. In addition, in [114], [165], performance evaluations were conducted in the Rayleigh fading channel, and there have been few evaluations in LOS scenarios. Although [164] has focused on LOS environments, the simulations were conducted under special conditions, and the discussion cannot be applied to an indoor LOS scenario.

This chapter considers transmitting antenna selection from four to two elements applied to MIMO spatial multiplexing with two streams in an indoor LOS scenario. In the numerical analysis, SNR variations depending on the selected antenna subsets are considered by using ray-tracing propagation analysis. On this basis, this chapter clarifies that the square of the absolute value of the determinant of the channel matrix is the most effective selection criterion. Then, this chapter shows the effectiveness of the criterion by a measurement in an actual environment and evaluates the computational complexity.

6.2 Relation between Channel Conditions and BER

In 2×2 MIMO SDM system, the channel matrix $\mathbf{H}$ is given by

$$\mathbf{H} = \begin{bmatrix} h_{11} & h_{12} \\ h_{21} & h_{22} \end{bmatrix} = \begin{bmatrix} r_{11}e^{j\theta_{11}} & r_{12}e^{j\theta_{12}} \\ r_{21}e^{j\theta_{21}} & r_{22}e^{j\theta_{22}} \end{bmatrix} \tag{6.1}$$

where h_{ij} is the transmission function. ϕ is defined as follows:

$$\phi = \theta_{11} + \theta_{22} - \theta_{12} - \theta_{21} \tag{6.2}$$

The first and second eigenvalues of the spatial correlation matrix $\mathbf{HH}^H$ (where $\{\cdot\}^H$ represents the complex conjugate transpose) denoted by λ_1 and λ_2 ($\lambda_1 > \lambda_2$), respectively, are given using h_{ij}, and they are approximated as follows [166] [167]:

$$\begin{aligned} \lambda_1 &= \frac{1}{2}\Big(|h_{11}|^2 + |h_{12}|^2 + |h_{21}|^2 + |h_{22}|^2 \\ &+ \sqrt{(|h_{11}|^2 + |h_{12}|^2 + |h_{21}|^2 + |h_{22}|^2)^2 - 4|h_{11}h_{22} - h_{12}h_{21}|^2}\Big) \end{aligned}$$

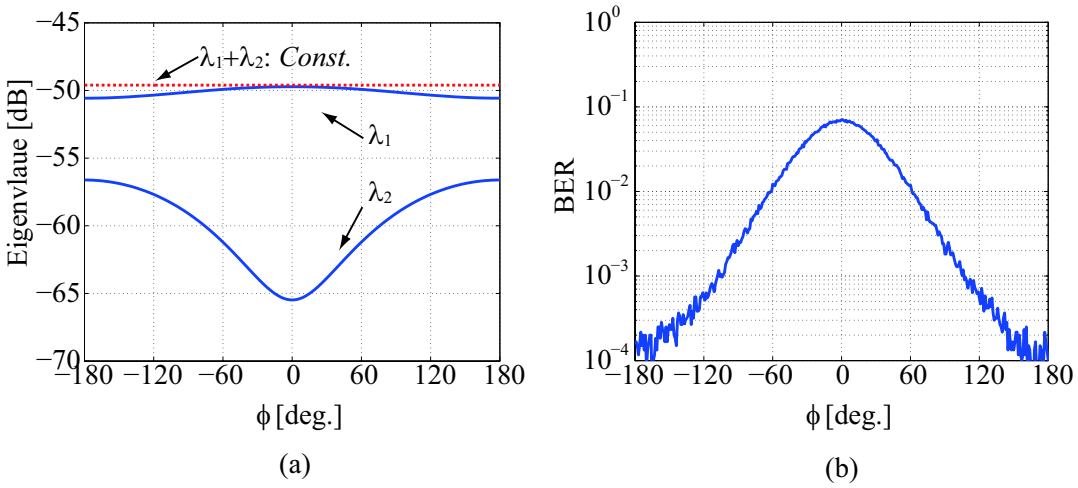

Figure 6.2. (a) Eigenvalues and (b) BER as a function of ϕ with $\lambda_1 + \lambda_2 = Const.$

$$\begin{aligned} &\approx |h_{11}|^2 + |h_{12}|^2 + |h_{21}|^2 + |h_{22}|^2 - \frac{|h_{11}h_{22} - h_{12}h_{21}|^2}{|h_{11}|^2 + |h_{12}|^2 + |h_{21}|^2 + |h_{22}|^2} \\ &= r_{11}^2 + r_{12}^2 + r_{21}^2 + r_{22}^2 - \frac{r_{11}^2 r_{22}^2 + r_{12}^2 r_{21}^2 - 2r_{11}r_{12}r_{21}r_{22}\cos\phi}{r_{11}^2 + r_{12}^2 + r_{21}^2 + r_{22}^2} \end{aligned} \tag{6.3}$$

$$\begin{aligned} \lambda_2 &= \frac{1}{2}\Big(|h_{11}|^2 + |h_{12}|^2 + |h_{21}|^2 + |h_{22}|^2 \\ &- \sqrt{(|h_{11}|^2 + |h_{12}|^2 + |h_{21}|^2 + |h_{22}|^2)^2 - 4|h_{11}h_{22} - h_{12}h_{21}|^2}\Big) \\ &\approx \frac{|h_{11}h_{22} - h_{12}h_{21}|^2}{|h_{11}|^2 + |h_{12}|^2 + |h_{21}|^2 + |h_{22}|^2} \\ &= \frac{r_{11}^2 r_{22}^2 + r_{12}^2 r_{21}^2 - 2r_{11}r_{12}r_{21}r_{22}\cos\phi}{r_{11}^2 + r_{12}^2 + r_{21}^2 + r_{22}^2} \end{aligned} \tag{6.4}$$

Both eigenvalues are dependent on r_{ij} and ϕ components. Figure 6.2(a) shows the eigenvalues as a function of ϕ; they are calculated based on (6.3) and (6.4). Here, λ_1 and λ_2 are derived by changing only ϕ with a fixed r_{ij} in the random channel matrix $\mathbf{H}$. The following equation is satisfied in this case:

$$P = \sum_{j=1}^{2}\sum_{i=1}^{2} |h_{ij}|^2 = \lambda_1 + \lambda_2 = Const. \tag{6.5}$$

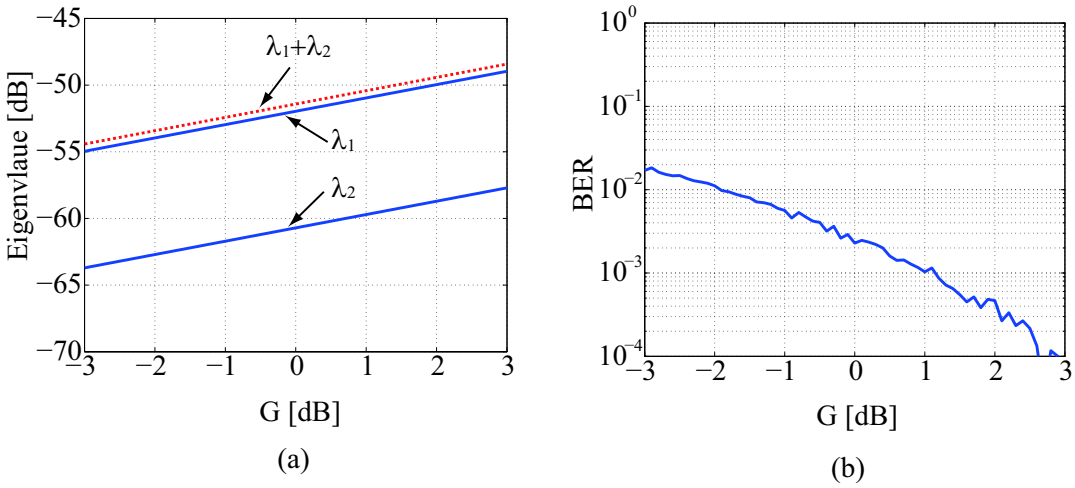

Figure 6.3. (a) Eigenvalues and (b) BER as a function of G with $\phi = 90°$.

In (6.5), P corresponds to the total received power normalized by the transmitting power from each element. Figure 6.2(b) shows the BER performance calculated under the condition that the energy per bit to noise power spectral density ratio E_b/N_0 is 10 dB, the modulation method is quadrature phase-shift keying (QPSK), and signal detection is performed by ZF method. As shown in Fig. 6.2, the λ_1 and λ_2 characteristics are symmetric about $\phi = 0$ and λ_2 is maximum at $|\phi| = 180°$. The variations in λ_1 are small, and the BER performances are dependent on λ_2 to a significant extent. Our primary-focus is on the selection of transmitting antennas from four to two elements, while the number of receiving antennas is two. For convenience, numbers from #1 to #4 and from #1 to #2 are assigned for the transmitting and receiving antennas, respectively. Six transmitting antenna subsets are selected – (#1–#2), (#1–#3), (#1–#4), (#2–#3), (#2–#4) and (#3–#4) – and the channel formed in each case is given by

$$\mathbf{H}_k = \begin{bmatrix} h_{1m} & h_{1n} \\ h_{2m} & h_{2n} \end{bmatrix} \tag{6.6}$$

Here, m and n denote the number of selected antenna elements, and k is 1, 2, ... 6. When the various selected antenna subsets lead to identical SNRs, $\mathbf{H}_k$ satisfies the condition of (6.5). This evaluation corresponds to dotted line 1 in Fig. 6.1. Under this condition, a low BER is obtained by the antenna selection with $|\phi|$ close to 180° (Figs. 6.2(a) and 6.2(b)). In addition, antenna selections with large λ_2 also lead to low BER. As described

in Appendix A, since the relationship between the minimum eigenvalue and the symbol error rate (SER) is represented by several inequalities, focusing on λ_2 makes sense.

However, P in (6.5) is not always constant and changes depending on the selected antenna subsets because of multipath effects in indoor environments. Hence, such changes are considered by evaluating $\mathbf{H}' = G\mathbf{H}$, where G is a real number and a factor providing amplitude variations. All the amplitude components of the channel are varied depending on each other for the simplicity of evaluation. Figures 6.3(a) and 6.3(b) show the eigenvalues and BER performance as a function of G, which are evaluated using a random channel matrix $\mathbf{H}$ with $\phi = 90°$. In the BER calculations, E_b/N_0 is 10 dB at $G = 0$ dB, and the modulation and signal detection schemes are QPSK and ZF, respectively. As shown in these figures, both λ_1 and λ_2 increase with G, and a low BER is obtained in the high-G regime owing to the increase in the eigenvalues.

Now, the discussion is extended to antenna selection. When for ϕ, there are no variations resulting from changes in the selected antenna subsets, that is, ϕ is constant at all $\mathbf{H}_k$ values, a low BER is obtained by selecting antenna with high amplitudes (high received power). Moreover, antenna selections with large λ_1 and λ_2 also lead to low BER.

However, the BER performance for each antenna selection should be evaluated under the condition that both ϕ and amplitude are changed. For example, the antenna selection maximizing $|\phi|$ can lead to lower amplitudes, that is, lower total received power than for other selection criteria, and the BER performance may be inferior to that obtained using other selection criteria. Since the optimum antenna selection criterion cannot be derived easily in this situation, the next section clarifies the optimum selection using a ray-tracing propagation analysis.

6.3 Performance Evaluation of BER Using a Ray-Tracing Propagation Analysis

This section investigates the analytical BER performance of a 2×2 MIMO-SDM with antenna selection by using ray-tracing propagation analysis.

6.3.1 Basic Examination

As a first step, one example is shown for evaluating the antenna selection criterion to minimize BER. Figure 6.4(a) shows the analytical model; the room size is 6 m × 6 m × 2.7 m. The height of the Tx antenna (BS) is 2.5 m, and the antenna is fixed at the center of the ceiling. The configuration is a four-element rectangular array arranged at 1λ-intervals as shown in Fig. 6.4(b). The Rx antenna (MT) is a two-element linear array parallel to the y-axis and arranged at 0.5λ-intervals. The array positions are changed at 0.125-m intervals in the xy plane, and the channel matrices are derived by ray-tracing propagation analysis in each position [168]. Dipole radiation patterns are considered at Tx and Rx antenna elements. In the ray-tracing propagation analysis, the carrier frequency is 5 GHz, and up to five reflections are considered. The transmission power is -15 dBm/ch, and the noise level is -85 dBm. Since the transmission power is fixed, the received power varies with the Rx positions and selected antenna subsets. For the channel estimation, a perfect CSI is assumed. The modulation method is QPSK, and the ZF algorithm is used as the signal detection scheme.

For the Tx antenna, the selection from four elements to two elements is performed at all the Rx positions, and the transmission power is divided equally in the selected antenna elements. Figure 6.5 shows the CDF of ϕ for the target scenario in Fig. 6.4 and ϕ under each channel condition. To derive the distribution of ϕ in the target scenario,

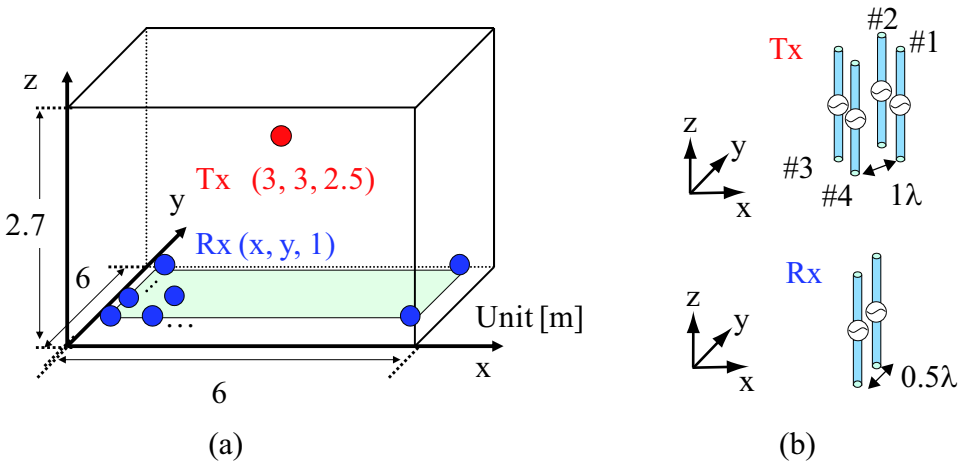

Figure 6.4. (a) Analytical model applying ray-tracing propagation analysis, and (b) transmitting and receiving antenna configurations.

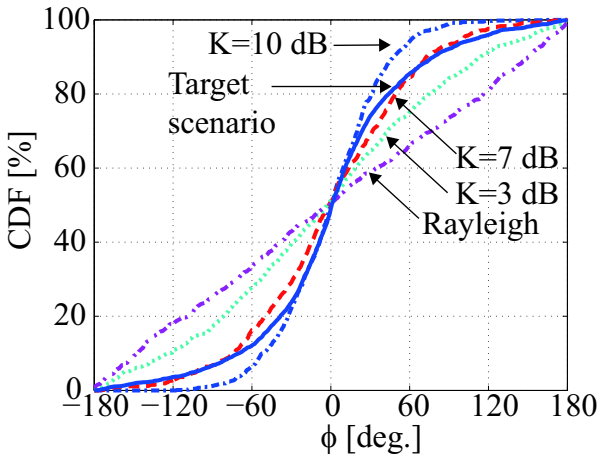

Figure 6.5. Cumulative distribution function (CDF) of ϕ for the target scenario and ϕ under each channel condition.

this analysis uses data from all the antenna selection subsets at all Rx positions. In Fig. 6.5, the distribution of ϕ in the target scenario is compared with that of Nakagami-Rice fading under a Rice factor K = 3, 7, or 10 dB, and Rayleigh fading conditions. Here, the Nakagami-Rice fading environment is generated in accordance with [169] by,

$$\mathbf{H} = \sqrt{\frac{K}{K+1}}\mathbf{H}_D + \sqrt{\frac{1}{K+1}}\mathbf{H}_{i.i.d} \tag{6.7}$$

$$\mathbf{H}_D = \begin{bmatrix} 1 & 1 \\ 1 & 1 \end{bmatrix} \tag{6.8}$$

where $\mathbf{H}_{i.i.d}$ is a matrix with a complex Gaussian distribution. Although ϕ is distributed uniformly under the Rayleigh fading condition, the distribution is concentrated close to 0° under Nakagami-Rice fading conditions including the target scenario. From Fig. 6.5, the statistical Rice factor is approximately 7 dB in the target scenario. Since the measurement results show that the Rice factor for cluster housing in LOS scenarios is 7 dB in [170], this simulated value is valid.

Now, evaluation is conducted for $P = \sum_{j=1}^{2}\sum_{i=1}^{2}|h_{ij}|^2$, which is equivalent to the total received power in the analyzed environment. Here, $\max(P)$ and $\min(P)$ are derived from P for six combinations of the antenna selection at each Rx position. This evaluation

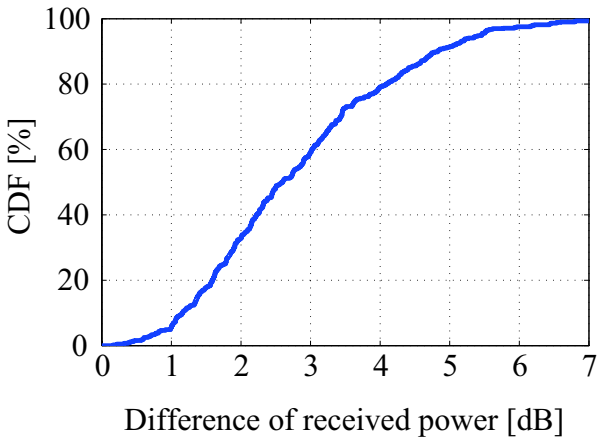

Figure 6.6. CDF of the difference in received power depending on the selected antenna subsets ($\max(P) - \min(P)$).

uses $\max(P) - \min(P)$ at each Rx position as the difference in P depending on the selected antenna subsets. Figure 6.6 shows the CDF of $\max(P) - \min(P)$; the level is more than 6 dB at some positions, and the 50 % value of the CDF is 2.60 dB. Thus, the differences in the received power cannot be ignored.

Figure 6.7(a) shows the CDFs of the BER obtained by antenna selection. In the case of the antenna selection criteria, *Opt* denotes the selection achieving minimum BER at all Rx antenna positions. *Fixed* denotes the case without antenna selection, and the #2 and #4 elements in Fig. 6.4(b) are always used. $|\phi|_{max}$, P_{max} and $\lambda_{2,max}$ denote the selection achieving $\max(|\phi|)$, $\max(P)$ and $\max(\lambda_2)$, respectively, of ${}_4C_2 = 6$ selection candidates at each Rx antenna position. For the convenience of explanation, $|\det(\mathbf{H})|^2_{max}$ is described later. In Fig. 6.7(a), the BER performance for $\lambda_{2,max}$ is almost identical to that for *Opt*, and it is considerably better than the performance for *Fixed*. *Fixed* indicates that the selection criterion based on the second eigenvalues is effective. However, although BER for $|\phi|_{max}$ is better than that for *Fixed*, minimum BER is not obtained. In the case of P_{max}, antenna selection causes a degradation of the BER performance rather than enhancement.

Figure 6.7(b) shows the CDFs of the eigenvalues for each antenna selection criterion. For *Opt*, there are positions realizing BER = 0 in more than two selected antenna subsets. Hence, the distributions are divided into two cases, such as, for example, the selection of $\min(\lambda_2)$ and $\max(\lambda_2)$ at those positions. These distributions are denoted by

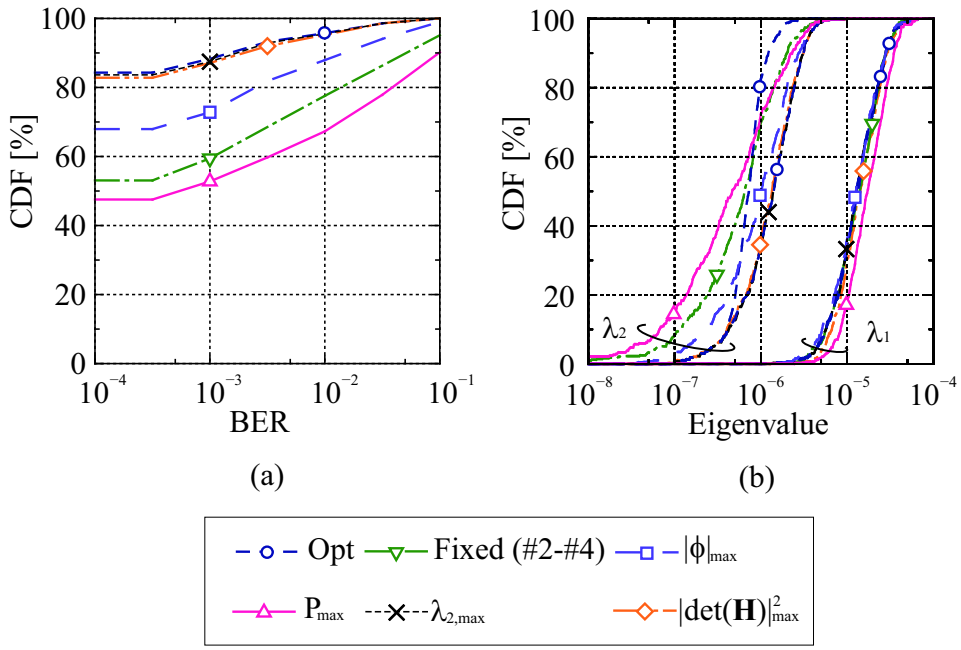

Figure 6.7. CDFs of (a) BER and (b) eigenvalues for each antenna selection criterion.

Opt_{min} and Opt_{max}, respectively. In an indoor LOS scenario, λ_1 shows small variations between each selection criterion, as shown in Fig. 6.7(b), and λ_2 determines the BER performance. In these situations, P_{max} is assumed to be unfavorable because λ_2 in (6.4) is represented by

$$\lambda_2 \approx \frac{|\det(\mathbf{H})|^2}{P} \tag{6.9}$$

Then, the denominator in (6.9) (P) becomes large. In fact, as shown in Figs. 6.7(a) and 6.7(b), BER is degraded by the decrease in λ_2 although λ_1 increases because λ_1 in (6.3) is represented by

$$\lambda_1 \approx P - \frac{|\det(\mathbf{H})|^2}{P} \tag{6.10}$$

As a supplementary note, for the antenna selection based on $\min(P)$, it was confirmed that the BER performance was degraded less than P_{max}.

When the distribution of λ_2 was included in the area surrounded by Opt_{min} and Opt_{max}, a nearly minimum BER was achieved. Although λ_2 is maximized using $|\phi|_{max}$

under condition (6.5), the maximum λ_2 is not achieved when amplitude variations with selected antenna subsets are considered. The distribution of λ_2 for $|\phi|_{max}$ in the low-CDF regime was not included in the area surrounded by Opt_{min} and Opt_{max}. As a result, a minimum BER was not obtained by $|\phi|_{max}$.

For antenna selection in an indoor LOS scenario, optimizations in the phase components of $\mathbf{H}$ are more effective for BER enhancement than those in the amplitude components of $\mathbf{H}$. However, the best BER performance is not obtained under favorable conditions for either phase or amplitude; rather, it is obtained when both components are operated well, and this can be judged using λ_2.

Now, to simplify the $\lambda_{2,max}$ criterion, $\lambda_{2,max}$ is replaced by $|\det(\mathbf{H})|^2_{max}$ based on (6.9). Here, $|\det(\mathbf{H})|^2_{max}$ is defined as the antenna selection for maximizing $|\det(\mathbf{H})|^2$. The reason that $|\det(\mathbf{H})|^2$ is considered is because the changes in the denominator (P) were not effective in obtaining low BER or large λ_2, as mentioned previously. In Fig. 6.7(b), the distribution of λ_2 for $|\det(\mathbf{H})|^2_{max}$ is almost identical to $\lambda_{2,max}$, and a nearly optimum BER is achieved as shown in Fig. 6.7(a).

6.3.2 Examinations of Various Scenarios

As a second step, it is evaluated whether the above discussions also can be applied to antenna selections in various scenarios. Here, the BER performances are evaluated by changing several parameters from the basic scenario described in Section 6.3.1. Those performances are shown in Fig. 6.8, and only $|\det(\mathbf{H})|^2_{max}$ and $\lambda_{2,max}$ leading to good performances in Fig. 6.7 are extracted in Figs. 6.8(a)-(d).

Figure 6.8(a) shows the BER performances when (i) the transmitting power is reduced from -15 to -20 dBm/ch, (ii) 16QAM is used as a modulation scheme instead of QPSK, and (iii) the Rx array is changed from an arrangement parallel to the y-axis to one parallel to $y = x$ (-45° rotation in the xy plane). Figure 6.8(b) shows those when (iv) the MMSE algorithm is used instead of the ZF algorithm as a signal detection scheme at the Rx and when (v) the location of the Tx antenna is changed from the center of the ceiling to the vicinity of a wall. Figures 6.8(c) and (d) show BER performances when (vi) the height of the Tx antenna is changed from 2.5 m to 1 m and when (vii) the size of the room is changed from 6 m × 6 m × 2.7 m to 6 m × 8 m × 2.7 m. In (vii), the location of the Tx antenna is also changed from (3, 3, 2.5) to (3, 4, 2.5) to place the Tx

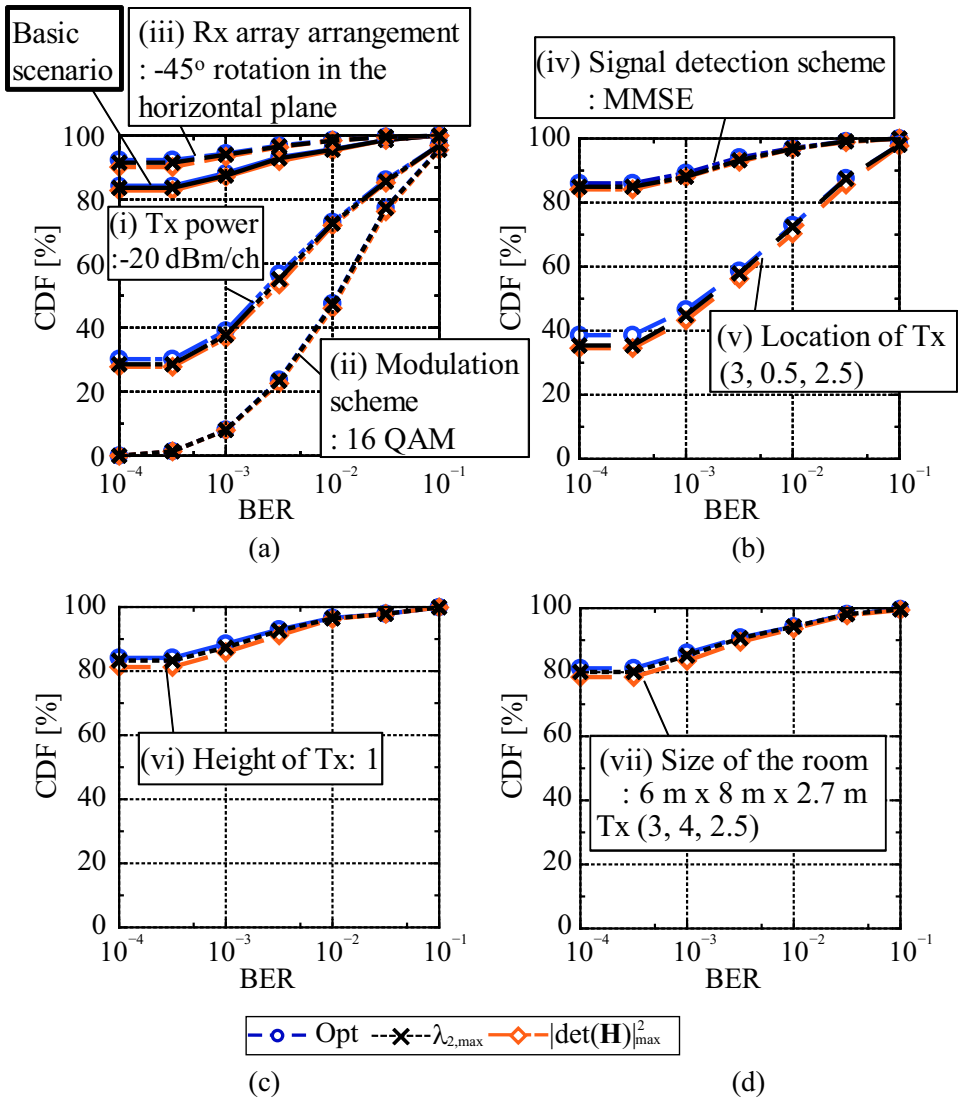

Figure 6.8. CDFs of BER when several parameters are changed.

antenna at the center of the ceiling.

(i), (ii), and (iv) and (iii), (v), (vi), and (vii) are parameter changes relating to systems and environments surrounding the systems, respectively. As shown in Figs. 6.8(a)-(d), $|\det(\mathbf{H})|^2_{max}$ and $\lambda_{2,max}$ are still effective criteria although the distribution of the BER in each scenario is changed from that in the basic scenario. Since $|\det(\mathbf{H})|^2_{max}$ and $\lambda_{2,max}$ are applicable regardless of the size of the room, the transmitting power, and the location of the Tx antenna, the measurement scenario in Section 6.4 is different from the basic scenario in the analysis of Section 6.3.1.

6.4 Measurement Based Performance Evaluation

In the room of 8.76 m × 6.31 m × 2.7 m shown in Fig. 6.9(a), the BER performance is empirically evaluated by including channel estimation and propagation characteristics in an actual environment. For Tx and Rx antennas, four-element rectangular and two-element linear sleeve arrays are respectively used (Fig. 6.9(b)). For the Tx antenna, the number of elements fed simultaneously is two. The feeding elements are switched manually, and nonfeed elements are terminated. The location of the Tx antenna is fixed, and the radiated signals are received at multiple Rx positions (8 in total). Here, the heights of the Tx and Rx antennas are both 1.15 m. The measured environment is quasistatic, and all the Rx positions are in the LOS from the Tx position. In the measurement, the transmitting frame format consists of a header of 50 symbol/ch and data of 400 symbol/ch. M-sequences are applied to the header of the transmitting signals, and the channels are estimated by a complex sliding correlation using reference signals [104]. Then, the signals are detected by ZF algorithm. In this measurement, no error-correcting code is used for simplicity. The measurement systems are described in detail in [104] and [103].

Figure 6.10 shows the transmitting antenna subset achieving minimum BER at each

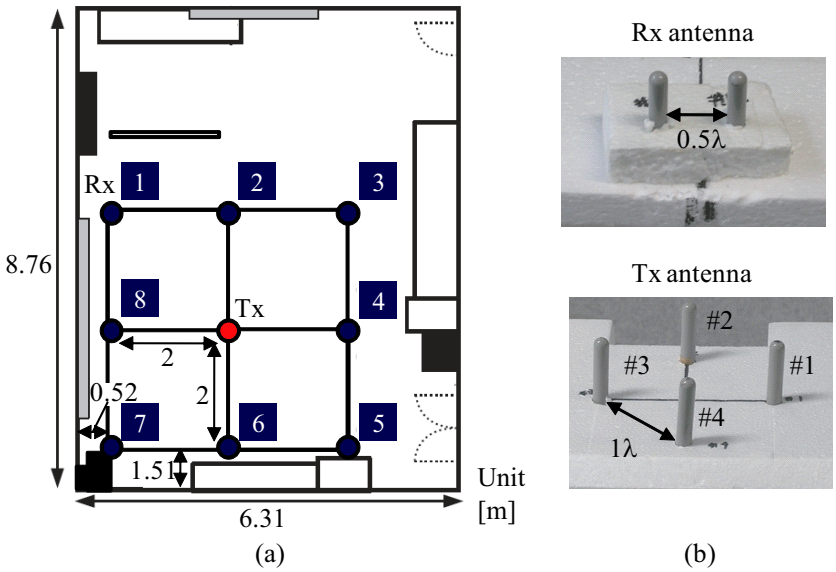

Figure 6.9. (a) Measurement environment and (b) array arrangements.

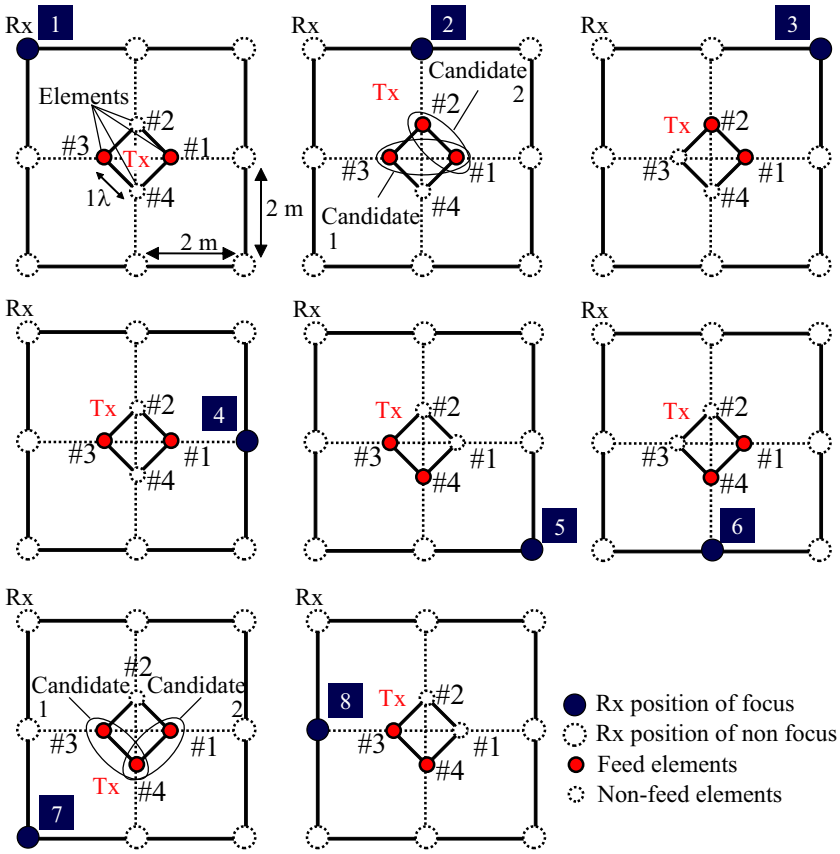

Figure 6.10. Antenna subset leading to minimum BER at each Rx position. $\#i$ denotes the number of Tx antenna elements.

Rx position. Here, at positions 2 and 7, two candidates exist. The optimum antenna selection is different at each Rx position, and there is no clear relationship between Rx positions and optimum Tx antenna subsets, indicating that the antenna subset should be selected based on some criteria. Figure 6.11 shows the CDF of the measured BER for antenna subsets selected at each Rx position and fixed antenna subset. Here, $\#i$ denotes the number of selected feed elements in Fig. 6.9(b), and $\#i$–$\#j$ indicates that the antenna subset is fixed to $\#i$ and $\#j$ at all Rx positions. In Fig. 6.11, the BERs for the antenna selection outperform those for nonantenna selection. Since the BER for $\lambda_{2,max}$ is almost identical to that for *Opt* except for the regime in the vicinity of 10^{-1}, a high λ_2 is effective for obtaining low BER in this measurement scenario. As with the simulation results in Section 6.3, $|\det(\mathbf{H})|^2$ also leads to good BER performance.

Figure 6.12 shows the BER for each antenna selection as a function of Rx positions.

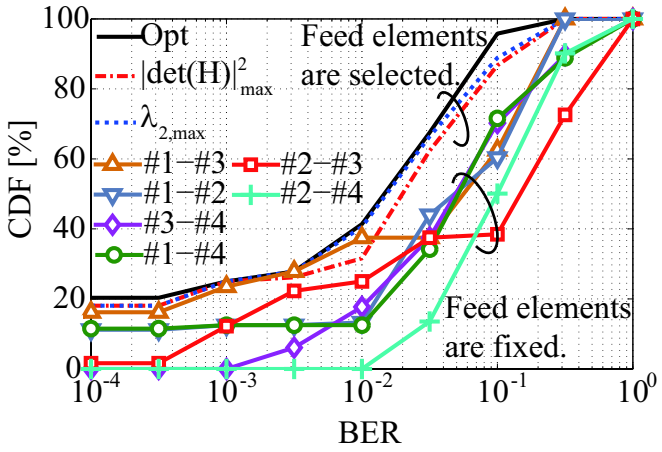

Figure 6.11. CDFs of BER for each antenna selection and for fixed antenna combinations.

Since λ_2 values at positions 5, 6, and 7, which are close to the wall, are less than λ_2 values at the other positions, BER performances are degraded at positions 5, 6, and 7. With respect to the antenna selection effect, BERs for $\lambda_{2,max}$ and $|\det(\mathbf{H})|^2_{max}$ are almost identical to those for *Opt* at positions 3–8. Although BERs for $\lambda_{2,max}$ and $|\det(\mathbf{H})|^2_{max}$ are worse than those for *Opt* at position 2, that is acceptable because those BERs are sufficiently low ($< 1 \times 10^{-4}$) despite not using an error-correcting code. The differences in BER between each selection criterion at position 1 cause the difference in the vicinity of 10^{-2} for the CDF in Fig. 6.11.

Figure 6.13 shows the eigenvalues for $\lambda_{2,max}$ and $|\det(\mathbf{H})|^2_{max}$, which are normalized by the eigenvalues for *Opt* defined as $\lambda_{i,opt}$. This evaluation reveals how large the eigenvalues for $\lambda_{2,max}$ and $|\det(\mathbf{H})|^2_{max}$ are in comparison to *Opt*. When $\lambda_1 - \lambda_{1,opt}$ ($\lambda_2 - \lambda_{2,opt}$) is greater than 0, the first (second) eigenvalue for $\lambda_{2,max}$ or $|\det(\mathbf{H})|^2_{max}$ is greater than that for *Opt*. In Fig. 6.13(b), although $\lambda_2 - \lambda_{2,opt}$ for $\lambda_{2,max}$ are greater than or equal to 0 at all Rx positions, $\lambda_2 - \lambda_{2,opt}$ for $|\det(\mathbf{H})|^2_{max}$ is less than 0 at position 1. It indicates that λ_2 for $|\det(\mathbf{H})|^2_{max}$ is smaller than that for *Opt* at this position, and the degradation of λ_2 is caused by the large P from (6.9). The large P also leads to a large $\lambda_1 - \lambda_{1,opt}$ at position 1 from (6.10) (Fig. 6.13(a)), and the large difference between λ_1 and λ_2 causes the degradation of BER for $|\det(\mathbf{H})|^2_{max}$. Although there are exceptions to consider, $|\det(\mathbf{H})|^2_{max}$ is a suitable criterion to achieve low BER.

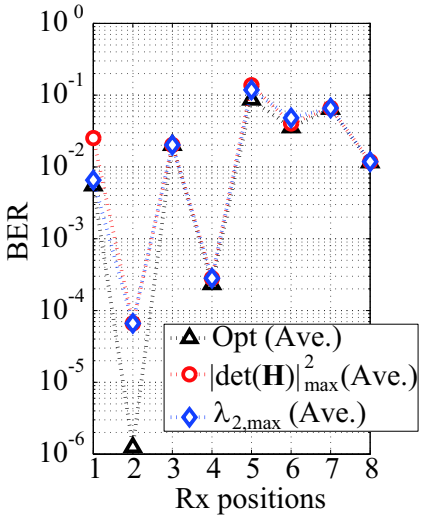

Figure 6.12. Averaged BER performances at each Rx position.

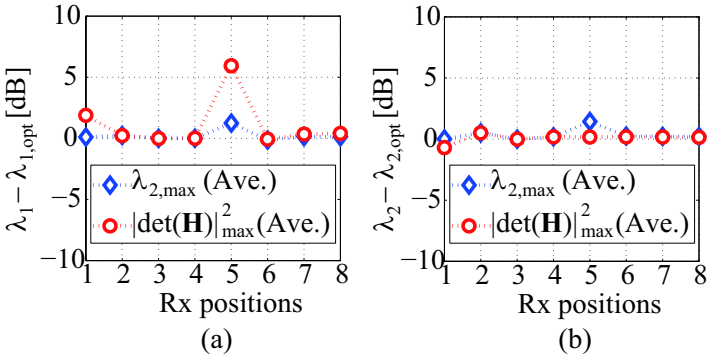

Figure 6.13. (a) First and (b) second eigenvalues normalized by the eigenvalues for *Opt*.

6.5 Evaluation of Computational Load

This section evaluates the antenna selection of *Opt*, $\lambda_{2,max}$ and $|\det(\mathbf{H})|^2_{max}$ alone, which had led to good BER performance, as described in Sections 6.3 and 6.4. First, we compare the system complexity between the criteria when the BER is used directly (*Opt*) and when channel conditions ($\lambda_{2,max}$ and $|\det(\mathbf{H})|^2_{max}$) are used.

Figure 6.14 shows the block diagram of a MIMO system with transmitting antenna selection based on channel conditions. As shown in Fig. 6.14, compared to when the BER is used directly, the processes of "Linear Receiver" and "Symbol Detector" are not necessary for antenna selection based on channel conditions, thereby reducing the

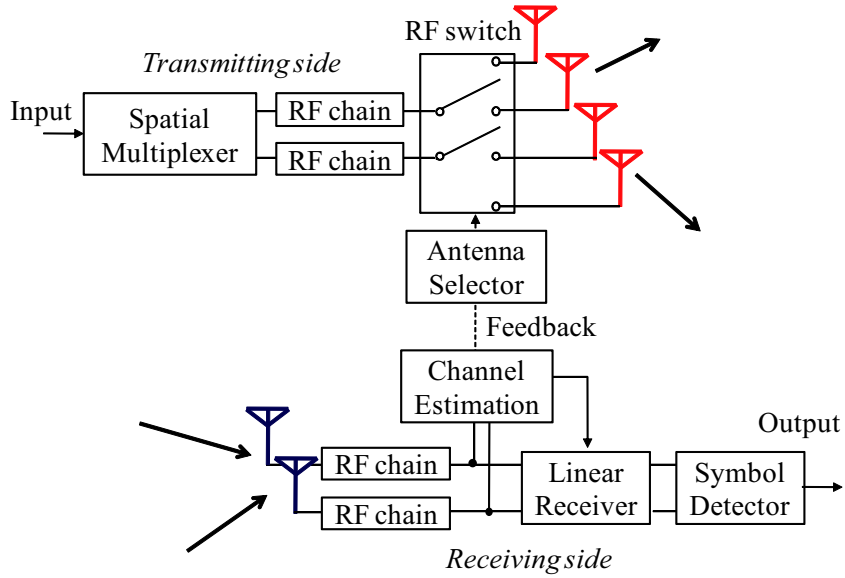

Figure 6.14. Block diagram of a MIMO system with transmitting antenna selection based on channel conditions.

computational load. Moreover, when a high-speed switch is applied to the Tx side, the 4 × 2 channel matrix can be estimated at one time on the Rx side using pilot signals with time difference and reference signals. This is equivalent to the situation in which the Tx side has more antenna elements than the Rx side, and decoding cannot be realized by linear processing such as ZF and MMSE methods owing to the lack of degrees of freedom. In the case of nonlinear processing, although decoding can be realized using maximum likelihood detection (MLD) [171], exponential increases in the complexity as a function of the number of antennas and modulation levels are a problem. Hence, the system complexity for ($\lambda_{2,max}$ and $|\det(\mathbf{H})|^2_{max}$) is lower than that for *Opt*.

Now, the calculation amounts of $\lambda_{2,max}$ and $|\det(\mathbf{H})|^2_{max}$ are evaluated. In general, since the eigenvalue derivation by QR decomposition is widely used in the communications field, the derivation process of the eigenvalue is considered as follows:

1. Generate a correlation matrix $\mathbf{A} = \mathbf{H}\mathbf{H}^H$.

2. Construct the Householder transformation.

3. Perform the QR decomposition.

4. Repeat step 2 and 3 until $\mathbf{A}$ approaches an upper triangular matrix or a diagonal

matrix

Now, the detailed process is described in accordance with [172]. First, the correlation matrix $\mathbf{A}$ is calculated as follows:

$$\begin{aligned}
\mathbf{A} &= \mathbf{H}\mathbf{H}^H && (6.11)\\
&= \begin{bmatrix} |h_{11}|^2 + |h_{12}|^2 & h_{11}h_{21}^* + h_{12}h_{22}^* \\ h_{21}h_{11}^* + h_{22}h_{12}^* & |h_{21}|^2 + |h_{22}|^2 \end{bmatrix} && (6.12)\\
&= \begin{bmatrix} a_{11} & a_{12} \\ a_{21} & a_{22} \end{bmatrix} && (6.13)
\end{aligned}$$

where $\{\cdot\}^*$ denotes the complex conjugate. Subsequently, vector $\mathbf{v}$ is calculated using $\mathbf{x} = [a_{11}, a_{21}]^T, \mathbf{z} = [1, 0]^T$ as follows:

$$\begin{aligned}
\mathbf{v} &= \mathbf{x} + \|\mathbf{x}\|\mathbf{z} && (6.14)\\
&= \begin{bmatrix} a_{11} + \sqrt{|a_{11}|^2 + |a_{21}|^2} \\ a_{21} \end{bmatrix} = \begin{bmatrix} v_1 \\ v_2 \end{bmatrix} && (6.15)
\end{aligned}$$

By using vector $\mathbf{v}$, the Householder matrix $\mathbf{H}_t$ is given by

$$\begin{aligned}
\mathbf{H}_t &= \mathbf{I} - 2 \times \frac{\mathbf{v}\mathbf{v}^T}{\|\mathbf{v}\|^2} && (6.16)\\
&= \begin{bmatrix} 1 - \frac{2|v_1|^2}{|v_1|^2+|v_2|^2} & -\frac{2v_1v_2}{|v_1|^2+|v_2|^2} \\ -\frac{2v_1v_2}{|v_1|^2+|v_2|^2} & 1 - \frac{2|v_2|^2}{|v_1|^2+|v_2|^2} \end{bmatrix} && (6.17)\\
&= \begin{bmatrix} h_{t,11} & h_{t,12} \\ h_{t,21} & h_{t,22} \end{bmatrix} && (6.18)
\end{aligned}$$

where $\mathbf{I}$ denotes a unit matrix, and $\mathbf{H}_t$ satisfies $\mathbf{H}_t = \mathbf{H}_t^T = \mathbf{H}_t^{-1}$. Any $\mathbf{A}$ with $\mathrm{rank}(\mathbf{A}) = 2$ is decomposed by an orthogonal matrix ($\mathbf{Q}$) and an upper triangular matrix ($\mathbf{R}$), which means that the relationship of $\mathbf{A} = \mathbf{Q}\mathbf{R}$ holds. Here, $\mathbf{R}$ is given by

$$\begin{aligned}
\mathbf{R} &= \mathbf{H}_t\mathbf{A} && (6.19)\\
&= \begin{bmatrix} h_{t,11}a_{11} + h_{t,12}a_{21} & h_{t,11}a_{12} + h_{t,12}a_{22} \\ h_{t,21}a_{11} + h_{t,22}a_{21} & h_{t,21}a_{12} + h_{t,22}a_{22} \end{bmatrix} && (6.20)
\end{aligned}$$

Table 6.1. Number of arithmetic operations to calculate each parameter used as antenna selection criteria.

Parameter	Addition /subtraction	Multiplication	Division	Square root
λ_2 (QR)	47+33(k-1)	65+52(k-1)	6+4(k-1)	1+(k-1)
λ_2 (Eq. (6.4))	14	18	5	0
$\lvert\det(\mathbf{H})\rvert^2$	7	10	1	0

$$= \begin{bmatrix} r_{d,11} & r_{d,12} \\ 0 & r_{d,22} \end{bmatrix} \tag{6.21}$$

and $\mathbf{Q}$ is equal to $\mathbf{H}_t$ since $\mathbf{H}_t^{-1} = \mathbf{H}_t$. Here, $\mathbf{A}$ decomposed by these processes is denoted as $\mathbf{A}_1$. In the next stage, the processes from (6.14) are repeated for $\mathbf{A}_2 = \mathbf{RQ}$, where the positions of $\mathbf{Q}$ and $\mathbf{R}$ are exchanged. This operation is continued until $\mathbf{A}$ approaches an upper triangular matrix or a diagonal matrix ($\mathbf{A}_k$), and the diagonal components of $\mathbf{A}_k$ are eigenvalues (λ_1 and λ_2). To evaluate the calculation amount, Table 6.1 lists the number of arithmetic operations required to derive λ_2 from the QR decomposition (λ_2 (QR)) and to derive $\lvert\det(\mathbf{H})\rvert^2$. Here, the number of arithmetic operations for λ_2 derived from the second equation of (6.4) (λ_2 (Eq. (6.4))) are also shown as a reference. In this table, k represents the number of repeated operations required to obtain $\mathbf{A}_k$. The number of arithmetic operations is calculated by considering each component h_{ij} of the channel matrix as a complex value [173].

The results in Table 6.1 indicate that the calculation amount for the eigenvalue derivation is reduced by using (6.4) because the number of arithmetic operations for λ_2 (Eq. (6.4)) is smaller than that for λ_2 (QR) in all the operations. Furthermore, the number of arithmetic operations for $\lvert\det(\mathbf{H})\rvert^2$ is smaller, and therefore, it is concluded that the square of the absolute value of the determinant of the channel matrix is most effective from the viewpoint of BER performance and computational load.

6.6 Summary

This chapter has demonstrated that in 2×2 MIMO-SDM systems with antenna selection from four to two elements, the criterion using the square of the absolute value of the

determinant of the channel matrix was the most effective one for both BER performance and computational load in an indoor LOS scenario. For the investigations, this chapter employed ray-tracing propagation analysis, taking into consideration variations in both the amplitude and the phase of the channel matrix depending on the selected antenna subsets. The optimum BER performance was not obtained with either only a phase or only an amplitude criterion. The second eigenvalue of the spatial correlation matrix was a dominant factor in achieving low BER, and the determinant based criterion is a simplified one of the second eigenvalue. The criterion based on the determinant of the channel matrix could be applied to various scenarios, and the effectiveness of the criterion for BER performance was also verified empirically in an actual environment. The computational complexity was lower than that of a criterion based on the second eigenvalue, and the BER performance was comparable to that.

Chapter 7

Concluding Remarks

This dissertation has focused on indoor base stations and has described novel multi-antenna technologies using radiation patterns wisely to improve performance without increasing the number of streams.

In Chapter 3, channel capacity was introduced as a evaluation factor of MIMO performance, and the relationships among channel capacity, spatial correlation, SNR, received power imbalance, and eigenvalues of the spatial correlation matrix were discussed with a focus on 2×2 MIMO systems. First, this dissertation theoretically explained that even if spatial correlation were reduced, channel capacity could be degraded because of the received power imbalance. Then, the equation for the channel capacity was divided into two elements depending on the SNR C_{SNR} and the spatial correlation coefficient C_{COR}. For C_{COR}, two scenarios were extracted, and it was revealed analytically and empirically that eigenvalues are an important factor in estimating channel capacity. Moreover, this dissertation also focused on a spatial correlation reduction under the condition in which the SNR and the components of the channel matrix are varied simultaneously. When MIMO antenna selection and radiation pattern reconfiguration are assumed as a concrete example, variations in the SNR and the spatial correlation often have a trade-off relationship. For this scenario, it is revealed that a correlation reduction requirement of $|\gamma_s| \leq 0.7$ was effective for channel capacity enhancement. Then, as one example, spatial correlation reduction and channel capacity enhancement by multipolarization was clarified empirically. Moreover, the concept of channel capacity enhancement by increasing SNR was shown in this chapter, and the discussion was connected to Chapter 4.

Chapter 4 described the MIMO antenna configuration methodology by using radi-

ation patterns effectively. The discussion was mainly focused on indoor BSs, and the goal of this dissertation was enhancement of MIMO performance using fixed radiation patterns. Here, two types of BS positions are assumed: mounted in the vicinity of a wall and mounted at the center of the ceiling. For the former, this dissertation revealed by ray-tracing propagation analysis that a narrow HPBW of 60°–80° pointed to the corner of the room was effective in obtaining large channel capacity. Based on the design guidelines, a patch antenna array with dual-feeds was fabricated, and then, measurements were conducted in a small room of 6.2 m × 5.8 m × 2.7 m. The results showed that the 4 × 4 MIMO channel capacity was enhanced by approximately 20% at two out of three typical MT positions, compared to that for sleeve antenna configurations. For the latter, this dissertation presented a low-profile dual-polarized directional MIMO antenna with a thickness of 0.24λ. Design guidelines of the antenna derived by ray-tracing propagation analysis were as follows: The main beam directions are orthogonalized in the horizontal plane and are tilted 30° downward in the vertical plane, and the HPBW is 80°. The antenna was configured by four cavity-backed slots and four printed dipole antenna elements, and slot and dipole elements radiate vertical and horizontal polarizations, respectively. Measurement of the antenna characteristics showed that a unidirectional radiation pattern with a tilt angle was obtained in each polarization. Then, channel measurements were conducted in the room of 5.75 m × 6.15 m × 2.70 m under LOS conditions, and the SNR and channel capacity were compared with those of the sleeve antenna configuration. The place-averaged SNR of the proposed antenna was 14.1 dB, and the improvement factor was 2.6 dB. The place-averaged channel capacity of the proposed antenna was 7.1 bits/s/Hz, and the improvement factor was 16.2%. The results of the present study revealed that the MIMO capacity performance was the same or better than that of the sleeve antenna configuration.

Chapter 5 proposed a novel feeding circuit with a switching function for shapes and directions of radiation patterns. First, a technique to realize cardioid and figure 8 radiation patterns was presented. Then, as a modified version, techniques to realize omnidirectional and directive radiation patterns were presented. Those techniques were based on array antenna theory, and a multiradiation pattern was generated by switching feed elements and phase difference feeding (0°, 180°, -90° and 90°). For the former circuit, the array factors derived from the output signals at 2 GHz showed that two cardioid and two figure 8 radiation patterns were achieved when mutual coupling effects

were ignored. When mutual coupling effects were considered, unidirectional (with more than a 10 dB F/B ratio) and bidirectional radiation patterns were obtained. Moreover, the measurement results showed that the averaged losses between 1.85 and 2.21 GHz were less than 1.8 dB, and the phase difference agreed with simulation data in the vicinity of 2 GHz in the proposed feeding circuit. For the latter, the proposed circuit has five operation modes and can switch feed to two elements with phase differences of 0°, 180°, -90° and 90° and feed to a single element. The simulation results showed that, in all the modes, mismatch losses were less than -0.5 dB and desired phase differences were obtained at 2 GHz. The output signals led to the array factor of two cardioid, two figure 8, and omnidirectional radiation patterns. Then, this dissertation revealed that uni-, bi- and omnidirectional radiation patterns were obtained by considering a combination with a three-element linear monopole array. The variation in the radiation patterns as a function of the frequency was small at 1.88, 2 and 2.06 GHz. Then, since the effect of switching circuits had not been considered in the above simulation and measurement, the design procedures were shown, and the measurement results of the fabricated switching circuit was evaluated. Despite a resulting frequency shift, good insertion loss and isolation characteristics were observed.

Chapter 6 presented an antenna selection criterion that was suitable for indoor LOS scenarios for two-stream MIMO systems. Since the selection criterion could be applied to a switching algorithm appropriate for radiation patterns, this section was ranked as a system-level consideration of Chapter 5. In Chapter 6, this dissertation demonstrated that the criterion using the square of the absolute value of the determinant of the channel matrix was the most effective one for both BER performance and computational load in an indoor LOS scenario. For the investigations, this dissertation employed ray-tracing propagation analysis by taking into consideration variations in both the amplitude and phase of the channel matrix depending on the selected antenna subsets. The criterion based on the determinant of the channel matrix could be applied to various scenarios, and the effectiveness of the criterion for BER performance was also verified empirically in an actual environment. The computational complexity was lower than the criterion based on the second eigenvalue, and the BER performance was comparable to it.

From these results, the effectiveness of a prototype MIMO antenna using directional antennas effectively was confirmed empirically, and suitable design guidelines for radiation patterns in indoor base stations were clarified. Then, a low-profile MIMO antenna

with good MIMO transmission characteristics was realized. Furthermore, this dissertation proposed a novel feeding circuit with a switching function for multiradiation patterns including the change of direction and shape. Then, this dissertation also clarified a switching criterion when propagation paths are changed. The accomplishments provide novel multiantenna technologies to enhance transmission characteristics. Finally, it is desired that this finale will generate new prelude.

Appendix A

Relationship between Eigenvalues and SER

Appendix A describes relational expressions between eigenvalues and symbol error rate (SER).

When $\mathbf{s}(t)$ and $\mathbf{r}(t)$ are defined as the transmitting and receiving signal vectors, respectively, the following equation is satisfied in narrow band single user (SU) MIMO system.

$$\mathbf{r}(t) = \mathbf{H}\mathbf{s}(t) + \mathbf{n}(t) \tag{A.1}$$

where $\mathbf{n}(t)$ is the receiver noise vector, and N_t and N_r are the number of Tx and Rx antennas, respectively. When ZF algorithm is applied to the received signals as a signal detection scheme, the receiving side weight vector $\mathbf{W}$ is given by

$$\mathbf{W} = [\mathbf{w}_1, \mathbf{w}_2, \ldots, \mathbf{w}_j, \ldots] = \mathbf{H}^*(\mathbf{H}^T\mathbf{H}^*)^{-1} \tag{A.2}$$

Then, output signals are represented by the following equations:

$$\begin{aligned} \mathbf{y}(t) &= \mathbf{W}^T\mathbf{r}(t) \\ &= \mathbf{W}^T(\mathbf{H}\mathbf{s}(t) + \mathbf{n}(t)) \\ &= \mathbf{s}(t) + \mathbf{W}^T\mathbf{n}(t) \end{aligned} \tag{A.3}$$

Assuming the same power transmission P_s from each Tx antenna. the SNR after signal

detection for the signals from jth transmitting antenna (SNR_j) is given by

$$\mathrm{SNR}_j = \frac{P_s}{|\mathbf{w}_j^T \mathbf{n}(t)|^2} = \frac{P_s}{||\mathbf{w}_j||^2 \sigma^2} \tag{A.4}$$

where $||\cdot||$ is the Euclidean norm. Minimum SNR_j is given by

$$\min_{1 \le j \le N_t} \mathrm{SNR}_j = \frac{1}{\max_{1 \le j \le N_t} ||\mathbf{w}_j||^2} \cdot \frac{P_s}{\sigma^2} \tag{A.5}$$

where

$$\begin{aligned}
\max_{1 \le j \le N_t} ||\mathbf{w}_j||^2 &= \max_{1 \le j \le N_t} (\mathbf{H}^H \mathbf{H})^{-1}_{jj} && \text{(A.6)} \\
&= \max_{1 \le j \le N_t} \mathbf{e}_j^T (\mathbf{H}^H \mathbf{H})^{-1} \mathbf{e}_j && \text{(A.7)} \\
&\le \max_{\mathbf{x}^T \mathbf{x} = 1} \mathbf{x}^T (\mathbf{H}^H \mathbf{H})^{-1} \mathbf{x} && \text{(A.8)} \\
&= \lambda_{max}[(\mathbf{H}^H \mathbf{H})^{-1}] && \text{(A.9)} \\
&= \lambda_{min}^{-1}[\mathbf{H}^H \mathbf{H}] && \text{(A.10)}
\end{aligned}$$

where $\mathbf{e}_j$ is the jth column of unit matrix $\mathbf{I}_{N_r, N_t}$ in (A.7). (A.9) is derived by applying Rayleigh-Ritz theorem to (A.8), and $\lambda[\mathbf{A}]$ in (A.9) and (A.10) is eigenvalue of matrix $\mathbf{A}$ [114]. Based on (A.9) and (A.10), the following equation is derived.

$$\min_{1 \le j \le N_t} \mathrm{SNR}_j \ge \lambda_{min}[\mathbf{H}^H \mathbf{H}] \cdot \frac{P_s}{\sigma^2} \tag{A.11}$$

Let symbol error rate (SER) for jth transmitting signals be P_j. $P_j(\mathrm{SNR}_{min})$ is P_j corresponding to minimum SNR_j, which is given by the nearest neighbor union bound (NNUB) as follows:

$$P_j(\mathrm{SNR}_{min}) \le N_e Q\left(\sqrt{\min_{1 \le j \le N_t} \mathrm{SNR}_j \frac{d_{min}^2}{2}}\right) \tag{A.12}$$

where d_{min} denotes the minimum Euclidean distance between signal points, and N_e is the average number of nearest neighbors of the per antenna constellation [114], [174].

$Q(\cdot)$ is the Q-function given by the following equation:

$$Q(x) = \frac{1}{\sqrt{2\pi}} \int_x^\infty \exp\left(-\frac{t^2}{2}\right) dt \tag{A.13}$$

$Q(x)$ is the monotone decreasing function in $x > 0$. The right-hand value in (A.12) depends on the minimum value of SNR_j if modulation method is fixed. If λ_{min} is large, low $P_j(\mathrm{SNR}_{min})$ is expected because minimum SNR_j also becomes large in (A.11), and the value of Q-function in (A.13) becomes small.

Acknowledgments

In fact, when I was a master's student, I really debated whether or not to proceed Ph.D. course since I had no confidence to bring off the task. But, I determined to proceed Ph.D. course at that time. Now, I strongly feel that the decision was a correct answer because I have spent invaluable time. The source forming the irreplaceable life is encounter with various people. I would like to extend my appreciation for all the people I met.

In particular, I would like to express my sincere gratitude to my supervisor, Professor Hiroyuki Arai. During my Ph.D. course, he took care of me, and gave me shrewd advice not only to my research but also to student's life. Then, he gave me various chances, for example, international conferences, internship in Korea, and session chair in IEEE VTC 2010-Spring. I could enhance my research skill and communication ability thanks to their experiences.

I would like to express my appreciation to the committee members of Professor Takehiko Adachi, Professor Toshihiko Baba, Associate Professor Nobuhiro Kuga, and Associate Professor Koichi Ichige. In particular, I would like to express my sincere gratitude to Associate Professor Koichi Ichige. He gave me good advice about my research through joint seminar and provided consultation for future planning after Ph.D. course.

Then, I would like to thank Dr. Keizo Cho and Dr. Yuki Inoue of NTT DOCOMO, Inc. for their fruitful discussion and support in the measurements. The collaborative investigation with them was stimulating for me. I also would like to thank Nihon Dengyo Kosaku Co., Ltd., which fabricated prototype MIMO antennas for us. The antenna is indispensable in this dissertation.

I would like to express my sincere gratitude to Professor Young Joong Yoon of Yonsei University, Korea. Totally, I stayed for about two months in Microwave & Antenna Lab, Yonsei University, and he was a supervisor of me during the term. Although my stay was not so long, he gave me many advice. One-on-one meeting in his room was impressive for me. I also would like to express my sincere gratitude to Professor Jaehoon Choi of Hanyang University, Korea. I also visited his laboratory as a internship for two weeks. It was the first time to visit Korea, and I spent a precious time, which I cannot experience

in Japan.

Through conferences, I met many professors, industry people, and students. In particular, I would like to thank Associate Professor Kei Sakaguchi of Tokyo Institute of Technology, Associate Professor Kentaro Nishimori of Niigata University, and Associate Professor Naoki Honma of Iwate University, and Riichi Kudo of NTT Corporation for giving me helpful advice to develop this research. In addition, their presentation was attractive for me, and I learned a lot from them through the presentation and talks about researches with them. Then, I would like to thank Mischa Dohler of CTTC, Barcelona, Spain. Although maybe he does not remember me, I talked a little bit with him and listened to his talk because surprisingly, my seat was next to him when I ate lunch in IEEE VTC 2009-Spring. He is a great researcher, and I want to become a great person with intelligence and humor like him. I also would like to thank Dr. Naobumi Michishita of National Defence Academy. He always took care of me and gave me good advice when I went to domestic and international conferences.

Moreover, I am deeply grateful to Dr. Minseok Kim of Tokyo Institute of Technology. He kindly taught me about measurement systems, and he found and fixed the flaw in the system. Then, my deep appreciation goes to Mr. Taihei Michihata of Sony Corporation. I started to study about MIMO systems when I was an undergraduate student. At that time, I did not know about MIMO systems at all. Thanks to his kindly teaching, I could advance this research.

Furthermore, I would like to express my gratitude to Mr. Chomora Mikeka, who is both my good friend and a rival. He is my English teacher, and he has helped me a lot with preparation of international conferences and papers. Then, I am always amazed by him since his research speed is so high, and he have had great achievement in energy harvesting. In addition, he has been pulled off multitasking. He always stimulates my thinking. I think that his personality, such as always keeping a smile, attracts many people. I hope he will become a president of Malawi and invite me to Malawi by his private plane.

I would like to give a special thanks to my colleagues, Mr. Atsushi Suyama of Fujitsu Toshiba Mobile Communications Limited, Mr. Shumpei Fuse of Sharp Corporation, Mr. Mitsuhiro Tsukamoto of Odakyu Electric Railway Co., Ltd., and Mr. Junichi Ohno of Sony Ericsson Mobile Communications Japan, Inc., and Mr. Mitsuki Sagara, Mr. Atsuki Mizuno, Mr. Shen Wang, Mr. Takero Asai and Mr. Yusuke Hori of Arai Laboratory for their research corporation. My appreciation goes to Dr. SeungWook Nah of Samsung Thales, Dr. Fumiyo Sato of Sharp Corporation, Dr. Hironori Kakefuda of Nihon Dengyo Kosaku, Dr. Ryotaro Tamaki and Dr. Jun Yaezawa of Ministry of Defense, Mr. Naoto Ito of Toshiba Corporation, Dr. Hiromi Matsuno of KDDI R&D Laboratories, Dr. Kunsun Eom of Samsung Advanced Institute of Technology, Dr. Akiko Yamada of Toshiba Corporation, Mr. Noriyuki Mukai & Mr. Hiroshi Yamaguchi of Sony Corporation, Mr. Yutaka Hasegawa of Denso Corporation, Mr. Toshitsugu Jouduka of Mitsui Fudosan Co., Ltd., Mr. Takao Sekiguchi of Ericsson Japan K.K., Mr. Takayuki Moteki, Mr. Senanayaka Shashika Shaminda, and Mr. Kenta Abe, Mr. Hiroki Ohta,

Mr. Takuto Izumi, Mr. Naoki Yoneyama, Mr. Takashi Uesaka, Mr. Takuya Ohkura, Mr. Kenji Hagiwara, Mr. Minoru Yoshida, Ms. Eiko Shioda, Ms. Kumiko Harada, and Ms. Yumiko Terashima of students and secretaries of Arai Laboratory.

I also would like to give a special thanks to Dr. Tommy Lee, Dr. Minseok Han, Mr. Nackgyun Seong, Mr. Haeil Chung, Mr. Jaegeun Ha, and Mr. Kyeol Kwon of the alumini and the members Antennas & RF Devices Lab, Hanyang University. Then, I would like to give a special thanks to the alumni and the members of Microwave & Antenna Lab, Professor Jaeheung Kim, Ms. Hyun Ju Park, Dr. Hyung-Gook Yoon, Dr. Sang-Heun Lee, Mr. Man-Joong Ko, Mr. Jae Rim Oh, Mr. Kyoung Sun Hwang, Mr. Jae-Bok Lee, Mr. Won Yong Lee, Mr. Hyun-Wook Moon, Mr. Woo-Sung Lee, Mr. Yo-Han Lim, Mr. Ji-Hwan Ahn, Mr. Ki-Wook Lee, Mr. Ki-Joon Kim, Mr. Ji-Hwan Yoon, Mr. Young-Sub Kim, Mr. Sung-Hoon Moon, Ms. Eun-Young Kim, Mr. Min-Ho Kim, Mr. Seong-Cheol Lee, Mr. Hyung-Pil Seo, Mr. Woo-Joong Kim, Mr. Jae-Sik Kim, and Ms. Se-Mi Lee.

I would like to thank Yokohama National University and Global COE Program for financial support. The support was indispensable to complete this study. Moreover, I would like to thank JKCF, JKF, JISTEC, and KJCF for giving me a chance to study in Korea as a member of fourth Summer Institute and supporting the expenses.

Finally, I would like to express my sincere gratitude to my father, Shuji, my mother, Takako, and my younger brother, Yosuke. Thanks to their warm support and encouragement, I could reach this day.

Daisuke Uchida

8th February, 2012

Bibliography

[1] Telecommunications Carriers Association (in Japanese). [Online]. Available: http://www.tca.or.jp/database/index.html

[2] M. Morishima, "Systematic survey of technological developments in mobile communication terminals/portable telephones," *Systematized Investigation Report about Techniques by National Science Museum*, vol. 6, pp. 239-301, Mar. 2006 (in Japanese). [Online]. Available: http://sts.kahaku.go.jp/diversity/document/system/pdf/024.pdf

[3] M. Kuramoto and K. Kinoshita, "The dawn of mobile communication systems : from car phones to handheld phones," *J. IEICE (Japanese Edition)*, vol. 89, no. 8, pp. 740-745, Aug. 2006.

[4] Bell Laboratories, "High-capacity mobile telephone system – technical report," *Submitted to the FCC*, Dec. 1971.

[5] NTT DOCOMO History Square (in Japanese). [Online]. Available: http://history-s.nttdocomo.co.jp/list.html

[6] NTT DoCoMo Report No. 40 (in Japanese). [Online]. Available: http://www.nttdocomo.co.jp/binary/pdf/info/news_release/report/060223.pdf

[7] M. Morikura and S. Kubota (Supervising Editor), *802. 11 High-Speed Wireless LAN Textbook (Improved Edition)*, Impress, Dec. 2004 (in Japanese).

[8] K. Nagata, Y. Kojima, T. Hiraguri, Y. Takatori, "Standardization trend about wireless LAN in IEEE802.11 and Wi-Fi alliance," *NTT Technical Journal*, vol. 22, no. 2, pp. 77-80, Feb. 2010 (in Japanese).

[9] Y. Kamatani, "Why is R&D of high-speed wireless networks important?," *TOSHIBA Review*, vol. 61, no. 4, pp. 27, Apr. 2006 (in Japanese).

[10] T. Ohya, K. Cho, S, Narahashi, "Key wireless technologies for future high-speed and large-capacity communications," *NTT DOCOMO Technical Journal*, vol. 10, no. 2, pp. 23-30, Sep. 2008.

[11] 3GPP The Mobile Broadband Standard, [Online]. Available: http://www.3gpp.org/lte-advanced

[12] ITU-R Report M.2134: "Requirements related to technical performance for IMT-Advanced radio interface(s)," 2008.

[13] Qualcomm Incorporated, "LTE Advanced: heterogeneous networks," Jan. 2011. [Online]. Available: http://www.qualcomm.com/documents/lte-advanced-heterogeneous-networks-0

[14] S. Landstrom, A. Furuskar, K. Johansson, L. Falconetti, and F. Kronestedt, "Heterogeneous networks – increasing cellular capacity," *Ericsson Review*, Jan. 2011. [Online]. Available: http://www.ericsson.com/res/thecompany/docs/publications/ericsson_review/2011/heterogeneous_networks.pdf

[15] K. Nishimori, K. Kitao, S. Komatsubara, and T. Imai, "Performance evaluation on interference temperature using measured propagation data in heterogeneous networks," *IEICE Technical Report*, AP2011-32, pp. 29-34, July 2011 (in Japanese).

[16] K. Sakaguchi, "Heterogeneous wireless distributed networks," *IEICE Technical Report*, SR2008-61, pp. 159-164, Oct. 2008 (in Japanese).

[17] J. Akhtman, L. Hanzo, "Heterogeneous networking: an enabling paradigm for ubiquitous wireless communications", in *Proceedings of the IEEE*, vol. 98, no. 2, pp. 135-138, Feb. 2010.

[18] MM Research Institute, [Online]. Available: http://www.m2ri.jp/newsreleases/main.php?id=010120100831500 (in Japanese).

[19] TDK Techno Magazine, [Online]. Available: http://www.tdk.co.jp/techmag/knowledge/201009u/index.htm (in Japanese).

[20] T. Watanabe, H.Ohyane, N. Nakaminami, and Y Hiramoto, "Super-compact base station for femtocells," *NTT DOCOMO Technical Journal*, vol. 10, no. 2, pp. 64-68, Sept. 2008.

[21] V. Chandrasekhar, J. G. Andrews, and A. Gatherer, "Femtocell networks: a survey," *IEEE Commun. Mag.*, vol. 46, no. 9, pp. 59-67, Sept. 2008.

[22] *Nikkei Personal Computing*, Nikkei Business Publications, Inc., no. 630, July 2011 (in Japanese).

[23] K. Kusume, G. Dietl, T. Abe, and H. Taoka, "System level performance of downlik MU-MIMO transmission for 3GPP LTE-advanced," *Proc. IEEE Veh. Technol. Conf. (VTC 2010-Spring)*, May 2010.

[24] H. Nishimoto, "Studies on MIMO spatial multiplexing for high-speed wireless communications," *Doctoral Dissertation*, Hokkaido University, Dec. 2007.

[25] K. Sakaguchi, "MIMO channel measurement and analysis for future wireless communications," *Doctoral Dissertation*, Tokyo Institute of Technology, June. 2006.

[26] M. Dohler, "Virtual Antenna Arrays," *Doctoral Dissertation*, King's College London, U.K., Nov. 2003.

[27] T. Ohgane, "Base and element technology of MIMO system," *IEICE Workshop*, No. 29/30, 2004 (in Japanese).

[28] C. E. Shannon, "A mathematical theory of communication," *The Bell System Technical Journal*, vol. 27, pp. 379-423, 623-656, July, Oct. 1948.

[29] E. Telatar, "Capacity of multi-antenna Gaussian channels," *AT&T Bell Labs Tech. Rep.*, June 1995.

[30] G. J. Foschini, "Layered space-time architecture for wireless communication in fading environment using multi-element antennas," *Bell Labs Tech. J.*, pp. 41-59, Autumn 1996.

[31] P. W. Wolniansky, G. J. Foschini, G. D. Golden, and R. A. Valenzuela, "V-BLAST: An architecture for realizing very high data rates over the rich-scattering wireless channel," *Proc. URSI ISSSE*, pp. 295-300, Sep. 1998.

[32] G. D. Golden, J. G. Foschini, R. A. Valenzuela, and P. W. Wolniansky, "Detection algorithm and initial laboratory results using V-BLAST space-time communication architecture," *Electron. Lett.*, vol. 35, pp. 14-15, Jan. 1999.

[33] G. J. Foschini and M. J. Gans, "On limits of wireless communications in a fading environment when using multiple antennas," *Wireless Personal Commun.*, vol. 6, pp. 311-335, 1998.

[34] E. Telatar, "Capacity of multi-antenna Gaussian channels," *European Trans. on Telecommun.*, vol. 10, no. 6, pp. 585-595, Nov./Dec. 1999

[35] S. Alamouti, "A simple transmit diversity technique for wireless communications," *IEEE J. Sel. Areas Commun.*, vol. 16, pp. 1451-1458, Oct. 1998.

[36] V. Tarokh, N. Seshadri, A. Calderbank, "Space time codes for high data rate wireless communication: performance criterion and code construction," *IEEE Trans. Inform. Theory*, vol 44, no. 2, pp. 744-765, Mar. 1998.

[37] V. Tarokh, H. Jafarkhani, A. Calderbank, "Space-time block codes from orthogonal design," *IEEE Trans. Inform. Theory*, vol 45, no. 5, pp. 1456-1466, July 1999.

[38] H. Zhang, H. Dai, and Q. Zhou, "A geometrical analysis on transmit antenna selection for spatial multiplexing systems with linear receivers," *Proc. IEEE International Symposium on Information Theory (ISIT 2005)*, pp. 1558-1562, Sep. 2005.

[39] L. Zheng, D. N. C. Tse, "Diversity and multiplexing: a fundamental tradeoff in multiple antenna channels," *IEEE Trans. Inform. Theory*, vol. 49, no. 5, pp. 1073 -1096, May 2003.

[40] J. B. Andersen, "Array gain and capacity for known random channels with multiple element arrays at both ends," *IEEE J. Sel. Areas Commun.*, vol. 18, no. 11, pp. 2172- 2178, Nov. 2000.

[41] H. Sampath, P. Stoica, and A. Paulraj, "Generalized linear precoder and decoder design for MIMO channels using the weighted muse criterion," *IEEE Trans. Commun.*, vol. 49, no. 12, pp. 2198-2206, Dec. 2001.

[42] K. Miyashita, T. Nishimura, T. Ohgane, Y. Ogawa, Y.Takatori, and K. Cho, "High data-rate transmission with eigenbeam-space division multiplexing (E-SDM) in a MIMO channel," *Proc. IEEE Veh. Technol. Conf. (VTC 2002-Fall)*, vol. 3, pp. 1302-1306, Sep. 2002.

[43] K. Sakaguchi, S. Ting, and K. Araki, "Initial measurement on MIMO eigenmode communication system," *IEICE Trans. Commun. (Japanese Edition)*, vol. J87-B, no. 9, pp. 1454-1466, Sep. 2004.

[44] H. Bolcskei, D. Gesbert, and A. J. Paulraj, "On the capacity of OFDM based spatial multiplexing systems," *IEEE Trans. Commun.*, vol. 50, no. 2, pp. 225-234, Feb. 2002.

[45] S. Kurosaki, Y. Asai, T. Sugiyama and M. Umehira, "A SDM-COFDM scheme employing a simple feed-forward inter-channel interference canceller for MIMO based broadband wireless LANs," *IEICE Trans. Commun.*, vol. E86-B, no. 1, pp. 283-290, Jan. 2003.

[46] G.L. Stuber, J.R. Barry, S.W. McLaughlin, Y. Li, M.A. Ingram, and T.G. Pratt, "Broadband MIMO-OFDM wireless communications," in *Proc. IEEE*, vol. 92, no. 2, pp. 271-294, Feb. 2004.

[47] Q. H. Spencer, C. B. Peel, A. L. Swindlehurst, and M. Haardt, "An introduction to the multi-user MIMO downlink," *IEEE Comm. Mag.*, vol. 42, no. 10, pp. 60-67, Oct. 2004.

[48] Q. Spencer, A. L. Swindlehurst, and M. Haardt, "Zero-forcing methods for downlink spatial multiplexing in multiuser MIMO channels," *IEEE Trans. Signal Process.*, vol. 52, no. 2, pp. 461-471, Feb. 2004.

[49] K. Nishimori, R. Kudo, Y. Takatori, and M. Mizoguchi, "Results of 1 Gbit/s indoor transmission experiment using multi-user MIMO testbed," *NTT Techinical Journal*, pp. 56-59, July 2006. [Online]. Available: http://www.ntt.co.jp/journal/0906/files/jn200906056.pdf (in Japanese).

[50] G. K. Tran, K. Sakaguchi, F. Ono, and K. Araki, "2D MIMO network coding with inter-route interference cancellation," *IEICE Trans. Commun.*, vol. E92-B, no. 12, Dec. 2009.

[51] D. Gesbert S. Hanly, H. Huang, S. S. Shitz, O. Simeone, and W. Yu, "Multi-cell MIMO cooperative networks: A new look at interference," *IEEE J. Sel. Areas Commun.*, vol. 28, no. 9, pp. 1380-1408, Dec. 2010.

[52] N. Honma, K. Nishimori, T. Seki, and M. Mizoguchi, "Short range MIMO communication," in *Proc. 3rd European Conference on Antenna and Propagation (EuCAP 2009)*, pp. 1763-1767, Mar. 2009.

[53] K. Nishimori, Y. Koide, D. Kuwahara, N. Honma, H. Yamada, and M. Hideo, "MIMO sensor – evaluation on antenna arrangement –," in *Proc. 5th European Conference on Antenna and Propagation (EuCAP 2011)*, pp. 2771-2775, Apr. 2011.

[54] J. W. Wallace and R. K. Sharma, "Automatic secret keys from reciprocal MIMO wireless channels: Measurement and analysis," *IEEE Trans. Inf. Forensics and Security*, vol. 5, no. 3, pp. 381-392, Sept. 2010.

[55] C.-Y. Chen and P. P. Vaidyanathan, "MIMO radar space-time adaptive processing using prolate spheroidal wave functions," *IEEE Trans. Signal Process.*, vol. 56, no. 2, pp. 623-635, Feb. 2008.

[56] A. J. Paulraj, D. A. Gore, R. U. Nabar, and H. Bolcskei, "An overview of MIMO communications - A key to gigabit wireless", in *Proc. IEEE*, vol. 92, no. 2, pp. 198-218, Feb. 2004.

[57] K. Yu, M. Bengtsson, B. Ottersten, D. McNamara, P. Karlsson, and M. Beach, "Second order statistics of NLOS indoor MIMO channels based on 5.2 GHz measurements," in *Proc. IEEE Global Telecommunications Conf. (GLOBECOM 2001)*, vol. 1, pp. 156-160, Nov. 2001,

[58] J. W. Wallace, M. A. Jensen, A. L. Swindlehurst, and B. D. Jeffs, "Experimental characterization of the MIMO wireless channel: data acquisition and analysis," *IEEE Trans. Wireless Commun.*, vol. 2, no. 2, pp. 335-343, Mar. 2003.

[59] T. Svantesson and J. W. Wallace, "On signal strength and multipath richness in multi-input multi-output systems," in *Proc. IEEE Int. Conf. Commun. (ICC 2003)*, vol. 4, pp. 2683-2687, May 2003.

[60] R. Stridh, K. Yu, B. Ottersten, and P. Karlsson, "MIMO channel capacity and modeling issues on a measured indoor radio channel at 5.8 GHz," *IEEE Trans. Wireless Commun.*, vol. 4, no. 3, pp. 895-903, May 2005.

[61] A. van Zelst, "Space division multiplexing algorithms," in *Proc. 10th Mediterranean Electrotech. Conf. (MELECON 2000)*, vol. 3, pp. 1218-1221, May 2000.

[62] A. van Zelst, R. van Nee, and G. A. Awater, "Space division multiplexing (SDM) for OFDM systems," in *Proc. IEEE Veh. Technol. Conf. (VTC 2000-Spring)*, pp. 1070-1074, May 2000.

[63] G. G. Raleigh and J. M. Cioffi, "Spatio-temporal coding for wireless communication," *IEEE Trans. Commun.*, vol. 46, no. 3, pp. 357-366, Mar. 1998.

[64] Y. Ogawa, H. Nishimoto, T. Nishimura, and T. Ohgane, "Performance of MIMO spatial multiplexing in indoor line-of-sight environments," in *Proc. IEEE Veh. Technol. Conf. (VTC 2005-Fall)*, vol. 4, pp. 2398-2402, Sep. 2005.

[65] H. Nishimoto, Y. Ogawa, T. Nishimura, and T. Ohgane, "Measurement-based performance evaluation of MIMO spatial multiplexing in a multipath-rich indoor environment," *IEEE Trans. Antennas Propagat.*, vol. 55, no. 12, pp. 3677-3689, Dec. 2007.

[66] Y. Ge, M. Chuta, M. Fujimoto, and T. Hori, "Channel capacity improvement of MIMO system by using directional antennas," in *Proc. Int. Symp. on Antennas Propagat. (ISAP 2007)*, POS2-14, pp. 1154-1157, Aug. 2007.

[67] K. Saito, Q. Chen, and K. Sawaya, "Study of relation between MIMO channel capacity and directivity of receiving antenna," *IEICE Trans. Commun. (Japanese Edition)*, vol. J92-B, no. 9, pp. 1373-1380, Sep. 2009.

[68] W. Yamada, N. Kita, A. Ando, and T. Ito, "MIMO channel characteristics using directional antennas for transmission between base stations in a street micro-cell environment at 5.2-Ghz band, and prediction method for its propagation characteristics," *IEICE Trans. Commun. (Japanese Edition)*, Vol. J91-B, no. 3, pp. 260-271, Mar. 2008.

[69] C. Hermosilla, R. Feick, R. A. Valenzuela, and L. Ahumada, "Improving MIMO capacity with directive antennas for outdoor-indoor scenarios," *IEEE Trans. Wireless Commun.*, vol. 8, no. 5, pp. 2177-2181, May 2009.

[70] N. Razavi-Ghods, M. Abdalla, and S. Salous, "Characterisation of MIMO propagation channels using directional antenna arrays," in *Proc. IEE International Conference on 3G Mobile Communication Technologies*, pp. 163-167, 2004.

[71] B. T. Quist and M. A. Jensen, "Optimal antenna pattern design for MIMO systems," in *Proc. IEEE Antennas Propagat. Soc. Int. Symp. (APS 2007)*, pp. 1905-1908, June 2007.

[72] B. T. Quist and M. A. Jensen, "Optimal antenna radiation characteristics for diversity and MIMO systems," *IEEE Trans. Antennas Propagat.*, vol. 57, no. 11, pp. 3474-3481, Nov. 2009.

[73] N. Honma, K. Nishimori, R. Kudo, Y. Takatori, T. Hiraguri, and M. Mizoguchi, "A stochastic approach to design MIMO antenna with parasitic elements based on propagation characteristics," *IEICE Trans. Commun.*, vol. E93-B, no. 10, pp. 2578-2585, Oct. 2010.

[74] P. Kyritsi, D. C. Cox, R. A. Valenzuela, and P. W. Wolniansky, "Effect of antenna polarization on the capacity of a multiple element system in an indoor environment," *IEEE J. Sel. Areas Commun.*, vol. 20, no.6, pp. 1227-1239, Aug. 2002.

[75] T. Mitsui, M. Otani, C. H. Y. Eugene, K. Sakaguchi, and K. Araki, "Indoor MIMO channel measurements for evaluation of effectiveness of array antenna configurations," in *Proc. IEEE Veh. Technol. Conf. (VTC 2003-Fall)*, vol. 1, pp. 84-88, Oct. 2003.

[76] C. Y. Chiu, J. B. Yan, and R. D. Murch, "24-port and 36-port antenna cubes suitable for MIMO wireless communications," *IEEE Trans. Antennas Propagat.*, vol. 56, no. 4, pp. 1170-1176, Apr. 2008.

[77] A. -D. Capobianco, F. M. Pigozzo, A. Assalini, M. Midrio, S. Boscolo, and F. Sacchetto, "Compact MIMO array of planar end-fire antennas for WLAN applications," *IEEE Trans. Antennas Propagat.*, vol. 59, no. 9, pp. 3462-3465, Sep. 2011.

[78] L. Ndikumasabo, "MIMO antenna configuration for femtocell application," in *Proc. 2009 Loughborough Antennas & Propagation Conf.*, pp. 125-128, Nov. 2009.

[79] T. Svantesson and A. Ranheim, "Mutual coupling effects on the capacity of multielement antenna systems," in *Proc. IEEE Int. Conf. Acoustics, Speech, and Signal Processing (ICASSP 2001)*, vol. 4, pp. 2485-2488, May 2001.

[80] P. S. Kildal and K. Rosengren, "Correlation and capacity of MIMO systems and mutual coupling, radiation efficiency, and diversity gain of their antennas: simulations and measurements in a reverberation chamber," *IEEE Commun. Mag.*, vol. 42, no. 12, pp. 104-112, Dec. 2004.

[81] J. W. Wallace and M. A. Jensen, "Mutual coupling in MIMO wireless system: a rigorous network theory analysis," *IEEE Trans. Wireless Commun.*, vol. 3, no. 4, pp. 1317-1325, July 2004.

[82] M. A. Andrews, P. P. Mitra, and R. Carvalho, "Tripling the capacity of wireless communications using electromagnetic polarization," *Nature*, vol. 409, pp. 316-318, Jan. 2001.

[83] B. N. Getu and J. B. Andersen, "The MIMO cube - a compact MIMO antenna," *IEEE Trans. Wireless Commun.*, vol. 4, no. 3, pp. 1136-1141, May 2005.

[84] N. K. Das, T. Inoue, T. Taniguchi, and Y. Karasawa, "An experiment on MIMO system having three orthogonal polarization diversity branches in multipath-rich environment," in *Proc. IEEE Veh. Technol. Conf. (VTC 2004-Fall)*, vol. 2, pp. 1528-1532, Sep. 2004.

[85] C.-Y. Chiu, J.-B. Yan, and R. D. Murch, "Compact three-port orthogonally polarized MIMO antennas," *IEEE Antennas Wireless Propagat. Lett.*, vol. 6, pp. 619-622, Dec. 2007.

[86] J. Sarrazin, Y. Mahe, S. Avrillon, and S. Toutain, "Investigation on cavity/slot antennas for diversity and MIMO systems: the example of a three-port antenna," *IEEE Antennas Wireless Propagat. Lett.*, vol. 7, pp. 619-622, May. 2008.

[87] J. Litva and T. Lo, *Digital Beamforming in Wireless Communications*, Artech House, London, 1996.

[88] T. Ohira and K. Iigusa, "Electronically steerable parasitic array radiator antenna," *IEICE Trans. Commun. (Japanese Edition)*, vol. J87-C, no.1, pp. 12-31, Jan. 2004.

[89] T. Ohira and K. Gyoda, "Electronically steerable passive array radiator antennas for low-cost analog adaptive beamforming," *IEEE Int. Conf. Phased Array Syst. Tech.*, pp. 101-104, May 2000.

[90] N. Honma, K. Nishimori, Y. Takatori, A. Ohta, and S. Kubota, "Proposal of compact MIMO terminal antenna employing Yagi-Uda array with common director elements," in *Proc. IEEE Antennas Propagat. Soc. Int. Symp. (APS 2007)*, pp. 2405-2408, June 2007.

[91] R. F. Harrington, "Reactively controlled directive arrays," *IEEE Trans. Antennas Propagat.*, vol. AP-26, pp. 390-397, May 1978.

[92] R. J. Dinger "A planar version of a 4.0 GHz reactively steered adaptive array," *IEEE Trans. Antennas Propagat.*, vol. AP-34, no. 3, pp. 427-431, Mar. 1986.

[93] M. Tsuji, H. Miyagawa, T. Nishikawa, K. Wakino, and T. Kitazawa, "Compact array antenna with hybrid matrix controlling beams to three directions including boresight," *IEICE Trans. Commun. (Japanese Edition)*, vol. J90-B, no. 3, pp. 280-287, Mar. 2007.

[94] M. Nedil, T. A. Denidni, and L. Tarbi, "Novel Butler matrix using CPW multilayer technology," *IEEE Trans. Microw. Theory Tech.*, vol. 54, no. 1, pp. 499-507, Jan. 2006.

[95] J. Butler and R. Lowe, "Beamforming matrix simplifies design of electronically scanned antennas," *Electron. Design*, vol. 9, pp. 170-173, Apr. 1961.

[96] H. Arai, "Adaptive pattern controlled handset antenna by analog phase shifters," in *Proc. 3rd European Conference on Antenna and Propagation (EuCAP 2009)*, pp. 2536-2540, Mar. 2009.

[97] D. Uchida, J. Ohno, and H. Arai, "Capacity enhancement using fixed phase difference feeding in a handset MIMO antenna including human body effects," in *Proc. Int. Conf. on Applications of Electromagnetism and Student Innovation Competition Awards (AEM2C 2010)*, 240, pp. 235-238, Aug. 2010.

[98] W. S. Kang, J. A. Park and Y. J. Yoon, "Simple reconfigurable antenna with radiation pattern," *Electronics Letters*, vol. 44, no. 3, Jan. 2008.

[99] S. Zhang, G. H. Huff, J. Feng, and J. T. Bernhard, "A pattern reconfigurable microstrip parasitic array," *IEEE Trans. Antenna Propagat.*, vol. 52, no. 10, pp. 2773-2776, Oct. 2004.

[100] M.-I. Lai, T.-Y. Wu, J.-C. Hsieh, C.-H. Wang, and S.-K. Jeng, "Design of reconfigurable antennas based on an L-shaped slot and PIN diodes for compact wireless devices," *IET Microw. Antennas Propagat.*, vol. 3, Iss. 1, pp. 47-54, Feb. 2009.

[101] D. Piazza, N. J. Kirsch, A. Forenza, R. W. Heath, Jr., and K. R. Dandekar, "Design and evaluation of a reconfigurable antenna array for MIMO systems," *IEEE Trans. Antenna Propagat.*, vol. 56, no. 3, pp.869-881, Mar. 2008.

[102] N. Kikuma, *Apaptive Signal Processing with Array Antenna*, Science and Technology Publishing Company, Inc., 1998 (in Japanese).

[103] Y. Inoue, N. Ito, and H. Arai, "4 × 4 MIMO prototype system and measurement of indoor environment," in *Proc. Int. Symp. on Antennas Propagat. (ISAP 2005)*, WA3-4, pp. 59-62, Aug. 2005.

[104] D. Uchida, H. Arai, Y. Inoue, and K. Cho, "Experimental assessment of the channel capacity in indoor MIMO systems using dual-polarization," in *Proc. IEEE Veh. Technol. Conf. (VTC 2009-Spring)*. April 2009.

[105] K. Shimizu, "A study on evaluation of adaptive signal processing and receiver signal using array antenna measurement system," *Master Thesis*, Yokohama National University, Feb. 2005 (in Japanese).

[106] T. Michihata, "Evaluation of downlink transmission performance for transmitter weight control in actual indoor environment in single and multi-user MIMO systems," *Master Thesis*, Yokohama National University, Feb. 2008 (in Japanese).

[107] S. Sasaoka, *Mobile Communications*, Ohmsha Press, May 1998 (in Japanese),

[108] A. Goldsmith, S. A. Jafar, N. Jindal, and S. Vishwanath, "Capacity limits of MIMO channels," *IEEE J. Sel. Areas Commun.*, vol. 21, no. 5, pp. 684-702, June 2003.

[109] D. J. Love, R. W. Heath Jr., V. K. N. Lau, D. Gesbert, B. D. Rao, and M. Andrews, "An overview of limited feedback in wireless communication systems," *IEEE J. Sel. Areas Commun.*, vol. 26, no. 8, pp. 1341-1365, Oct. 2008.

[110] S. L. Loyka, "Channel capacity of two-antenna BLAST architecture," *Electron. Lett.*, vol. 35, no. 17, pp. 1421-1422, Aug. 1999.

[111] S. L. Loyka and J. R. Mosig, "Channel capacity of N-antenna BLAST architecture," *Electron. Lett.*, vol. 36, no. 7, pp. 660-661, Mar. 2000.

[112] S. L. Loyka, "Channel capacity of MIMO architecture using the exponential correlation matrix," *IEEE Commun. Lett.*, vol. 5, pp. 369-371, Sept. 2001.

[113] K. Ogawa, S. Amari, H. Iwai, and A. Yamamoto, "Effects of received power imbalance on the channel capacity of a handset MIMO," in *Proc. IEEE Int. Symp. Pers. Indoor Mobile Radio Commun. (PIMRC 2007)*, Sep. 2007.

[114] R. W. Heath Jr., S. Sandhu, and A. Paulraj, "Antenna selection for spatial multiplexing systems with linear receivers," *IEEE Commun. Lett.*, vol. 5, no. 4, pp. 142-144, April 2001.

[115] J. D. Boerman and J. T. Bernhard, "Performance study of pattern reconfigurable antennas in MIMO communication systems," *IEEE Trans. Antennas Propagat.*, vol. 56, no. 1, pp. 231-236, Jan. 2008.

[116] Y. Karasawa, "Close up to potential of MIMO systems," *Technical report of SPC ELECTRONICS CORP.*, no. 16, pp. 6-14, Sep. 2005. [Online]. Available: http://www.spc.co.jp/spc/info_16.html (in Japanese).

[117] Y. Karasawa, "Innovative antennas and propagation studies for MIMO systems," *IEICE Trans. Commun.*, vol. E90-B, no. 9, pp. 2194-2202, Sep. 2007.

[118] M. A. Jensen and J. W. Wallace, "A review of antennas and propagation for MIMO wireless communications," *IEEE Trans. Antennas Propagat.*, vol. 52, no. 11, pp. 2810-2824, Nov. 2004.

[119] D. P. McNamara, M. A. Beach, P. N. Fletcher, and P. Karlsson, "Capacity variation of indoor multiple-input multiple-output channels," *Electron. Lett.*, vol. 36, pp. 2037-2038, Nov. 2000.

[120] A. Diallo, C. Luxey, P. L. Thuc, R. Staraj, and G. Kossiavas, "Study and reduction of the mutual coupling between two mobile phone PIFAs operating in the DCS1800 and UMTS bands," *IEEE Trans. Antennas Propagat.*, vol. 54, no. 11, pp. 2063-3074, Nov. 2006.

[121] F. Yang and Y. Rahmat-Samii, "Microstrip antennas integrated with electromagnetic band-gap (EBG) structures: a low mutual coupling design for array applications," *IEEE Trans. Antennas Propagat.*, vol. 51, no. 10, pp. 2936-2946, Oct. 2003.

[122] T. Ohishi, N. Odachi, S. Sekine, and H. Shoki, "Low pattern correlation and low mutual coupling diversity antenna with a slit," *IEICE Trans. Commun. (Japanese Edition)*, vol. J90-B, no. 9, pp. 844-853, Sep. 2007.

[123] J. Thaysen and K. B. Jakobsen, "Envelope correlation in (N,N) MIMO antenna array from scattering parameters," *Microw. Opt. Tech. Letts.*, vol. 48, no. 5, pp. 832-834, May 2006.

[124] J. Weber, C. Volmer, K. Blau, R. Stephan, and M. A. Hein, "Miniaturized antenna arrays using decoupling networks with realistic elements," *IEEE Trans. Microwave Theory Tech.*, vol.54, no.6, pp. 2733-2740, June 2006.

[125] K. Nishimori, Y. Makise, M. Ida, R. Kudo, and K. Tsunekawa, "Channel capacity measurement of 8×2 MIMO transmission by antenna configurations in an actual cellular environment," *IEEE Trans. Antennas Propagat.*, vol. 54, no. 11, pp. 3285-3291, Nov. 2006.

[126] K. Kagoshima, S. Obote, A. Kagaya, K. Nishimura, and N. Endo, "An array antenna for MIMO system with a decoupling network using bridge susceptances," *2nd International Conference on Wireless Commun. Veh. Technol. Information Theory and Aerospace & Electronic Systems Technol. (Wireless VITAE 2011)*, Mar. 2011.

[127] A. M. Sayeed and V. Raghavan, "Maximizing MIMO capacity in sparse multipath with reconfigurable antenna arrays," *IEEE J. Sel. Topics Signal Process.*, vol. 1, no. 1, pp. 156-166, June 2007.

[128] J. P. Kermoal, L. Schumacher, F. Fredericksen, and P. E. Mogensen, "Experimental investigation of the joint spatial and polarization diversity for MIMO radio channel," in *Proc. 4th Int. Symp. Wireless Personal Multimedia Commun. (WPMC 2011)*, pp. 147-152. Sep. 2001.

[129] V. R. Anreddy and M. A. Ingram, "Capacity of measured Ricean and Rayleigh indoor MIMO channels at 2.4 GHz with polarization and spatial diversity," in *Proc. IEEE Wireless Communications and Networking Conference (WCNC 2006)*, vol. 2, pp. 946-951, Apr. 2006,

[130] L. R. Nair and B .T. Maharaj, "Capacity analysis of an indoor industrial environment using a dual-polarized MIMO system at 2.4 GHz and 5.2 GHz," in *Proc. IEEE AFRICON 2007*, Sep. 2007.

[131] M. Tsuruta and Y. Karasawa, "Simplified estimation method of the largest eigenvalue distribution in Nakagami-Rice MIMO channel," *IEICE Trans. Commun. (Japanese Edition)*, vol. J87-B, no. 9, pp. 1486-1495, Sep. 2004.

[132] A. F. Molisch, M. Steinbauer, M. Toeltsch, E. Bonek, and R. S. Thoma, "Capacity of MIMO systems based on measured wireless channels," *IEEE J. Sel. Areas Commun.*, vol. 20, no. 3, pp. 561-569, April 2002.

[133] T. Imai, "Prediction of propagation characteristics in tunnels using ray-tracing method," *IEICE Trans. Commun. (Japanese Edition)*, vol. J85-B, no. 2, pp. 216-226, Feb. 2002.

[134] K. Uehara, T. Seki, and K. Kagoshima, "Indoor propagation calculation considering antenna patterns using geometrical optics method," *IEICE Trans. Commun. (Japanese Edition)*, vol. J78-B-II, no. 9, pp. 593-601, Sept. 1995.

[135] J. D. Kraus, *A*ntennas, 2nd ed., New York: McGraw-Hill, 1988.

[136] D. Uchida, T. Michihata, H. Arai, Y. Inoue, and K. Cho, "Antenna configuration using directivity and orthogonal polarization in the indoor MIMO systems assuming the wireless LAN," *IEICE Technical Report*, AP2007-131, pp. 51-56, Jan. 2008 (in Japanese).

[137] D. Uchida, H. Arai, Y. Inoue, and K. Cho, "Optimum conditions in indoor MIMO systems using directional antennas at the access point," *IEICE Technical Report*, AP2008-122, pp. 61-66, Nov. 2008 (in Japanese).

[138] A. Suyama, D. Uchida, H. Arai, Y. Inoue, and K. Cho, "A dual polarization 8-port MIMO antenna with dipole and slot antennas," *IEICE Technical Report*, AP2008-234, pp. 113-116, Mar. 2009.

[139] M. Chuta, M. Fujimoto, and T. Hori, "Effect of radiation pattern of transmission antenna on indoor MIMO system," *IEICE Technical Report*, AP2006-85, pp. 53-56, Oct. 2006 (in Japanese).

[140] S. Fuse, H. Arai, Y. Inoue, and K. Cho, "Four-way switching vertical polarization antenna for cellular communication," in *Proc. IEICE Society Conf.*, B-1-74, Sep. 2009 (in Japanese).

[141] S. Fuse, "Four-way switching dual polarization antenna considering polarization and directivity for cellular antenna system," *Master Thesis*, Yokohama National University, Mar. 2010 (in Japanese).

[142] D. Uchida, S. Fuse, H. Arai, Y. Inoue, and K. Cho, "A low-profile dual-polarized directional antenna for an indoor MIMO transmission," in *Proc. IEEE Antennas Propagat. Soc. Int. Symp. (APS 2010)*, July 2010.

[143] S. Fuse, H. Arai, Y. Inoue, and K. Cho, "Four-way switching dual polarization antenna for cellular communication," in *Proc. IEICE General Conf.*, B-1-127, Mar. 2010 (in Japanese).

[144] K. Ogawa, H. Iwai, A. Yamamoto, and J. Takada, "Channel capacity of a handset MIMO antenna influenced by the effects of 3D angular spectrum, polarization, and operator," in *Proc. IEEE Antennas and Propagat. Society Int. Symp. (APS 2006)*, pp. 153-156, July 2006.

[145] J. Ohno and H. Arai, "MIMO channel capacity enhancement by antennas using phase control," in *Proc. Int. Symp. on Antennas Propagat. (ISAP2009)*, WB1, pp. 49-52, Oct. 2009.

[146] H. Arai, and J. Ohno, "Channel capacity enhancement by pattern controlled handset antenna," *Radioengineering*, vol.18, no.4, pp.413-417, Dec. 2009.

[147] www.feko.info

[148] G. d' Inzeo, "Proposal for numerical canonical models in mobile communications," in *Proc. COST 244 Meeting on Reference Models for Bioelectro-magnetic Test of Mobile Communication Systems*, Nov. 1994

[149] T. Taga, "Analysis for mean effective gain of mobile antennas in land mobile radio environments," *IEEE Trans. Veh. Technol.*, vol. 39, no. 2, pp. 117-131, May 1990.

[150] T. Taga, "Characteristics of space diversity branch using parallel dipole antennas in mobile radio communications," *IEICE Trans. Commun. (Japanese Edition)*, vol. J75-B-II, no.6, pp.370-378, June 1992.

[151] R. G. Vaughan and J. B. Andersen, "Antenna diversity in mobile communications," *IEEE Trans. Veh. Technol.*, vol. VT-36, no. 4, pp. 149-172, Nov. 1987.

[152] J. P. Kermoal, L. Schumacher, K. I. Pedersen, P. E. Mogensen, and F. Frederiksen, "A stochastic MIMO radio channel model with experimental validation," *IEEE J. Sel. Areas Commun.*, vol. 20, no. 6, pp.1211-1226. Aug 2002.

[153] K. Nishimori, N. Tachikawa, Y. Takatori, R. Kudo, and K. Tsunekawa, "Frequency correlation characteristics due to antenna configurations in broadband MIMO transmission," *IEICE Trans. Commun.*, vol. E88-B no. 6, pp. 2438-2445, June 2005.

[154] W. L. Stutzman and G. L. Thiele, *Antenna Theory and Design*, John Wiley & Sons, 1998.

[155] T. Hori, "Base of array antenna design," *IEICE Workshop*, no. 34, May 2007 (in Japanese).

[156] D. M. Pozar, *Microwave Engineering*, 3rd ed., John Wiley & Sons, Inc. 2005.

[157] H. Yamada, Y. Ogawa, and Y. Yamaguchi, "On mutual impedance of a receiving array antenna and its calibration matrix," *IEICE Technical Report*, AP2004-332, pp. 173-178, Mar. 2005 (in Japanese).

[158] I. J. Gupta and A. A. Ksienski, "Effect of mutual coupling on the performance of adaptive arrays," *IEEE Trans. Antennas Propagat.*, vol. AP-31, no. 5, pp. 785-591, Sep. 1983.

[159] *Transistor Gijutsu*, CQ Publishing Co., Ltd. Dec. 2004. (in Japanese).

[160] *Transistor Gijutsu*, CQ Publishing Co., Ltd. Dec. 2000. (in Japanese).

[161] *Transistor Gijutsu*, CQ Publishing Co., Ltd. Nov. 2003. (in Japanese).

[162] T. Ohgane, T. Nishimura, and Y. Ogawa, "Applications of space division multiplexing and those performance in a MIMO channel," *IEICE Trans. Commun.*, vol. E88-B, pp. 1843-1851, May 2005.

[163] S. Sanayei and A. Nosratinia, "Antenna selection in MIMO systems," *IEEE Commun. Mag.*, vol. 42, pp. 68-73, Oct. 2004.

[164] Y. Murakami, K. Kobayashi, M. Orihashi, and T. Matsuoka, "Performance analysis based on channel matrix eigenvalue for MIMO systems in LOS environments," *IEICE Trans. Fundamentals*, vol. E88-A, no. 10, pp. 2926-2936, Oct. 2005.

[165] T. Onizawa, A. Ohta, and Y. Asai, "Experiments on FPGA-implemented eigenbeam MIMO-OFDM with transmit antenna selection," *IEEE Trans. Veh. Technol.*, vol. 58, no. 3, pp. 1281-1291, Mar. 2009.

[166] Y. Karasawa, T. Taniguchi, and Y. Zhang, "On multiple-input-multiple-output (MIMO) maximal ratio combining (MRC) and optimal data transmission for OFDM," *IEICE Technical Report*, AP2001-196, pp. 45-52, Jan. 2002 (in Japanese).

[167] R. Shimura and I. Sasase, "Transmit phase control to increase the minimum eigenvalue of the channel correlation matrix in the ETD system," *IEICE Trans. Commun., (Japanese Edition)*, vol. J89-B, no. 3, pp. 337-350, Mar. 2006.

[168] W. D. Burnside and K. W. Burgener, "High frequency scattering by a thin lossless dielectric slab," *IEEE Trans. Antennas Propagat.*, vol. AP-31, no. 1, pp. 104-110, Jan. 1983.

[169] A. Paulraj, R. Nabar, and D. Gore, *Introduction to Space-Time Wireless Communications*, Cambridge, UK: Cambridge University Press, May 2003.

[170] N. Kita, W. Yamada, K. Itokawa, A. Sato, D. More, T. Takao, and H. Watanabe, "Intensity variation of the dominant wave of delay profile in indoor environments at 5-GHz band," in *Proc. IEICE General Conf.*, B-1-13, Mar. 2004 (in Japanese).

[171] R. van Nee, A. van Zelst, and G. Awater, "Maximum likelihood decoding in a space division multiplexing system," in *Proc. IEEE Veh. Technol. Conf. (VTC 2000-Spring)*, pp. 6-10, May 2000.

[172] G. Strang, *Linear Algebra and its Applications*, Academic Press, Inc., New York, 1976.

[173] M. Iri and K. Fujino, *Common Sense on Numerical Computing*, Kyoritsu Shuppan Co., Ltd., Japan, 1985 (in Japanese).

[174] J. G. Proakis, *Digital Communications*, New York: McGraw-Hill, 1995.

List of Publications and Awards

Related Works

Journal Papers

1. Daisuke Uchida, Hiroyuki Arai, Yuki Inoue and Keizo Cho, "A Low-Profile Dual-Polarized Directional Antenna for Enhancing Channel Capacity in Indoor MIMO Systems," IEICE Trans. Commun., vol. E93-B, no. 10, pp. 2570-2577, Oct. 2010.

2. Hiroyuki Arai and Daisuke Uchida, "Design of MIMO Antennas for Indoor Base Station and Mobile Terminal," IEICE Trans. Commun., vol. E95-B, no. 1, pp. 10-17, Jan. 2012.

International Conferences

1. Daisuke Uchida, Taihei Michihata, Hiroyuki Arai, Yuki Inoue, Keizo Cho, and T. Maruyama, "Optimum Beam Direction and Width for Directional Antenna Indoor MIMO systems," International Symposium on Antennas and Propagation (ISAP 2007), 1D5-2, pp.165-168, Toki Messe, Niigata, Japan, Aug. 2007.

2. Daisuke Uchida, Taihei Michihata, Hiroyuki Arai, Yuki Inoue, and Keizo Cho, "Channel Capacity Enhancement by Polarization and Pattern of Access Point Antenna in Indoor MIMO Systems," IEEE Antennas and Propagation Society International Symposium (APS 2008), 321.9, Manchester Grand Hyatt, San Diego, CA, USA, July 2008.

3. Daisuke Uchida, Hiroyuki Arai, Yuki Inoue, and Keizo Cho, "Experimental Assessment of the Channel Capacity in Indoor MIMO Systems Using Dual-Polarization," The 69th IEEE Vehicular Technology Conference (VTC-2009 Spring), 2P-17, Hilton Diagonal Mar Barcelona, Barcelona, Spain, April 2009.

4. Daisuke Uchida, Hiroyuki Arai, Yuki Inoue, and Keizo Cho, "A Low Profile Dual-Polarized Directional Antenna for Enhancing Channel Capacity in Indoor MIMO Systems," International Symposium on Antennas and Propagation (ISAP2009), WB1, pp. 53-56, Imperial Queen's Park Hotel, Bangkok, Thailand, Oct. 2009.

5. Daisuke Uchida, Hiroyuki Arai, Yuki Inoue, and Keizo Cho, "Antenna Selection Based on Minimum Eigenvalue in Dual-Polarized Directional MIMO Antenna," The 71st IEEE Vehicular Technology Conference (VTC-2010 Spring), 3Pa-6, Grand Hotel, Taipei, Taiwan, May 2010.

6. Daisuke Uchida, Shumpei Fuse, Hiroyuki Arai, Yuki Inoue, and Keizo Cho, "A Low-profile Dual-polarized Directional Antenna for an Indoor MIMO Transmission," IEEE Antennas and Propagation Society International Symposium (APS-2010), 404.6, The Sheraton Centre Toronto Hotel, Toronto, Canada, July 2010.

7. Daisuke Uchida, Junichi Ohno, and Hiroyuki Arai, "Capacity Enhancement Using Fixed Phase Difference Feeding in a Handset MIMO Antenna Including Human Body Effects," International Conference on Applications of Electromagnetism and Student Innovation Competition Awards (AEM2C 2010), 240, pp. 235-238, Oriental Institute of Technology, Taipei, Taiwan, Aug. 2010.

8. Daisuke Uchida, Hiroyuki Arai, and Young Joong Yoon, "A Pattern Reconfigurable Antenna with Switching Function of Shape and Direction," The 5th European Conference on Antennas and Propagation (EuCAP 2011), pp. 420-424, EUR Congressi, Rome, Italy, April 2011.

9. Daisuke Uchida, Hiroyuki Arai, Yuki Inoue, and Keizo Cho, "Antenna Selection Criterion Suitable for Indoor LOS Scenarios for Two-Stream MIMO Systems," IEEE Antennas and Propagation Society International Symposium (APS-2011), pp. 47-50, Spokane Convention Center, Spokane, WA, USA, July 2011.

10. Daisuke Uchida, Hiroyuki Arai, and Young Joong Yoon, "A Feeding Circuit for Switching Omni-Directional and Directive Patterns," IEEE International Workshop on Electromagnetics; Applications and Student Innovation (iWEM 2011), pp. 109-113, Oriental Institute of Technology, Taipei, Taiwan, Aug. 2011.

11. Daisuke Uchida and Hiroyuki Arai, "BER Performance Evaluation by Antenna Selections Suitable for Two-Stream MIMO Systems," International Symposium on Antennas and Propagation (ISAP 2011), FrF2-3, Lotte Hotel Jeju, Jeju, Korea, Oct. 2011.

12. Daisuke Uchida and Hiroyuki Arai, "Design of a MIMO Antenna to Enhance Channel Capacity for Indoor Base Stations," IEEE Antennas and Propagation Society International Symposium (APS-2012), (Submitted).

IEICE Technical Reports

1. Daisuke Uchida, Taihei Michihata, Hiroyuki Arai, Yuki Inoue, Keizo Cho, and Tamami Maruyama, "Directional Antenna Configuration of Indoor Base Station Antennas Considering Aspect Ratio of Rooms for MIMO systems," IEICE Technical Report, vol. 107, no. 35, AP2007-14, pp. 7-12, Kochi Green Kaikan, Kochi, May. 2007 (in Japanese).

2. Daisuke Uchida, Taihei Michihata, Hiroyuki Arai, Yuki Inoue, and Keizo Cho, "Antenna Configuration Using Directivity and Orthogonal Polarization in the Indoor MIMO Systems Assuming the Wireless LAN," IEICE Technical Report, vol. 107, no. 431, AP2007-131, pp. 51-56, Tiruru Okinawa, Okinawa, Jan. 2008 (in Japanese).

3. Daisuke Uchida, Hiroyuki Arai, Yuki Inoue, and Keizo Cho, "Optimum Conditions in Indoor MIMO Systems Using Directional Antennas at the Access Point," IEICE Technical Report, vol. 108, no. 304, AP2008-122, pp. 61-66, Kanazawa Institute of Technology, Ishikawa, Nov. 2008 (in Japanese).

4. Atsushi Suyama, Daisuke Uchida, Hiroyuki Arai, Yuki Inoue, and Keizo Cho, "A Dual Polarization 8-port MIMO Antenna with Dipole and Slot Antennas," IEICE Technical Report, vol. 108, no. 475, AP2008-234, pp. 113-116, Macao University, Macao, China, Mar. 2009.

5. Daisuke Uchida, Hiroyuki Arai, Yuki Inoue, and Keizo Cho, "Antenna Selection Based on Eigenvalue in Dual-Polarized Directional MIMO Antenna," IEICE Technical Report, vol. 109, no. 183, AP2009-80, pp. 7-12, Hachinohe Institute of Technology, Aomori, Sep. 2009 (in Japanese).

6. Daisuke Uchida, Hiroyuki Arai and Young Joong Yoon, "A Novel Feeding Circuit with Switching Function of Cardioid and Figure of Eight Radiation Patterns," IEICE Technical Report, vol. 110, no. 446, AP2010-175, pp. 7-12, Ibaraki University, Ibaraki, Mar. 2011.

7. Daisuke Uchida and Hiroyuki Arai, "A Remark of Parameters for Enhancing MIMO Channel Capacities," IEICE Technical Report, vol. 111, no. 128, AP2011-37, pp. 57-62, Shinshu University, Nagano, July 2011 (in Japanese).

8. Daisuke Uchida, Hiroyuki Arai, "Multi-Antenna System Using Radiation Patterns Wisely," IEICE Technical Report, vol. 111, no. 343, AP2011-121, pp. 13-18, Kikai-Shinko-Kaikan Building, Tokyo, Dec. 2011 (in Japanese).

IEICE General/Society Conferences

1. Daisuke Uchida, Taihei Michihata, Hiroyuki Arai, Yuki Inoue, Keizo Cho, "Antenna Configuration Using Orthogonal Polarization and Directivity at the Access Point Side in Indoor MIMO Systems," IEICE General Conference, B-1-217, Kitakyushu Science and Research Park, Fukuoka, Mar. 2008 (in Japanese).

2. Daisuke Uchida, Hiroyuki Arai, Yuki Inoue, and Keizo Cho, "Experimental Derivation of Channel Capacity and Assessment of Efficacy in Indoor MIMO Systems Using Dual-polarization," IEICE Society Conference, BS-1-6, Meiji University, Kanagawa, Sep. 2008 (in Japanese).

3. Daisuke Uchida, Atsushi Suyama, Hiroyuki Arai, Yuki Inoue, and Keizo Cho, "Experimental Assessment of Channel Capacity in Indoor MIMO Systems Using Directional Antennas," IEICE General Conference, B-1-249, Ehime University, Ehime, Mar. 2009 (in Japanese).

4. Daisuke Uchida, Hiroyuki Arai, Yuki Inoue, and Keizo Cho, "Indoor Propagation Measurement by a Low Profile Dual-Polarized Directional MIMO Antenna," IEICE Society Conference, B-1-201, Niigata University, Niigata, Sep. 2009 (in Japanese).

5. Daisuke Uchida, Hiroyuki Arai, Yuki Inoue, and Keizo Cho, "Antenna Selection Minimizing BER in Indoor MIMO Systems," IEICE General Conference, B-1-222, Tohoku University, Miyagi, Mar. 2010 (in Japanese).

6. Daisuke Uchida, Hiroyuki Arai, and Young Joong Yoon, "A Novel Feeding Circuit for Switching Multi-Shape Radiation Patterns," IEICE General Conference, B-1-182, Mar. 2011.

7. Daisuke Uchida and Hiroyuki Arai, "Experimental Discussion about Parameters for Enhancing MIMO Channel Capacity," IEICE Society Conference, BS-2-10, Hokkaido University, Hokkaido, Sep. 2011 (in Japanese).

8. Daisuke Uchida, "A Remark on Correlation Coefficient in Multi-Antenna Systems (commemorative speech)," IEICE General Conference, Okayama University, Okayama, Mar. 2012 (to be presented).

Patents

1. Yuki Inoue, Keizo Cho, Hiroyuki Arai, and Daisuke Uchida, "A Scheme for Setting Beam Characteristics in BS Antennas," JP Patent, 2008-283369 (P2008-283369A).

Joint Works

Journal Papers

1. Mitsuki Sagara, Daisuke Uchida, and Hiroyuki Arai, "Simple Selection Method by the Second Eigenvalue in Indoor 2 × 2 MIMO System," IEICE Trans. Commun. (Japanese Edition), vol. J93-B No. 9 pp. 1259-1266, Sep. 2010.

International Conferences

1. Mitsuki Sagara, Daisuke Uchida, and Hiroyuki Arai, "Simple Selection Method by the Second Eigenvalue in Indoor 2 × 2 MIMO System," International Symposium on Antennas and Propagation (ISAP 2010). 149, pp. 1009-1012, The Venetian Macao Resort Hotel, Macao, China, Nov. 2010.

2. Atsuki Mizuno, Daisuke Uchida, and Hiroyuki Arai, "BER Performance of Nonregenerative MIMO Relaying System with Phase Control," International Symposium on Antennas and Propagation (ISAP 2010). 85, pp. 571-574, The Venetian Macao Resort Hotel, Macao, China, Nov. 2010.

3. Atsuki Mizuno, Daisuke Uchida, and Hiroyuki Arai, "Broadband MIMO Relay Network with Phase Control," International Symposium on Antennas and Propagation (ISAP 2011), FrP1-66, Lotte Hotel Jeju, Jeju, Korea, Oct. 2011.

IEICE Technical Reports

1. Mitsuki Sagara, Daisuke Uchida, and Hiroyuki Arai, "Comparative Discussion of Spatial Multiplexing and Diversity Scheme by the Second Eigenvalue in Indoor 2 × 2 MIMO System," IEICE Technical Report, vol. 109, no. 304, AP2009-134, pp. 91-96, Tokyo Institute of Technology, Tokyo, Nov. 2009 (in Japanese).

2. Atsuki Mizuno, Daisuke Uchida, and Hiroyuki Arai, "Assessment of BER and Channel Capacity with Passive Nonregenarative Relaying System," IEICE Technical Report, vol. 110, no. 267, AP2010-115, pp. 137-141, Phoenix Plaza, Fukui, Nov. 2010 (in Japanese).

IEICE General/Society Conferences

1. Mitsuki Sagara, Daisuke Uchida, and Hiroyuki Arai, "Simple Selection Method by the Second Eigenvalue in Indoor 2 × 2 MIMO System," IEICE General Conference, B-1-223, Tohoku University, Miyagi, Mar. 2010 (in Japanese).

2. Atsuki Mizuno, Daisuke Uchida, and Hiroyuki Arai, "Assessment of BER and Channel Capacity of MIMO Relay System in Outdoor Environment," IEICE General Conference, B-1-229, Tohoku University, Miyagi, Mar. 2010 (in Japanese).

3. Atsuki Mizuno, Daisuke Uchida, and Hiroyuki Arai, "Assessment of BER and Channel Capacity of Passive Nonregenerative MIMO Relaying System," IEICE Society Conference, B-1-213, Osaka Prefecture University, Osaka, Sep. 2010 (in Japanese).

4. Takero Asai, Daisuke Uchida, and Hiroyuki Arai, "A Remark of Layout Method of Mobile Handset Antennas," IEICE General Conference, Okayama University, Okayama, Mar. 2012 (in Japanese) (to be presented).

The Other Research Activities

Internship

1. Hanyang University, Korea, Feb. 23rd - Mar. 8th, 2009.

2. Yonsei University, Korea, Feb. 22nd - March 7th, 2010.

3. Yonsei University, Korea, Aug. 6th - Sep. 16th, 2010 (Summer Institute, Research Communications Activities for Korean Graduate Students in Science and Technology, which is sponsored by the Japan-Korea Industrial Technology Co-Operation Foundation (JKF)).

4. Yonsei University, Korea, Feb. 10th - Feb. 23rd, 2011.

Session Chair

1. IEEE VTC-2010 Spring, Session 6C: Multiuser MIMO, Grand Hotel, Taipei, Taiwan, May 18th, 2010.

Awards

1. Daisuke Uchida, Hiroyuki Arai, Yuki Inoue, and Keizo Cho, IEEE VTS Japan 2009 Young Researcher's Encouragement Award, April 2009.

2. Daisuke Uchida, Hiroyuki Arai, Yuki Inoue, and Keizo Cho, International Symposium on Antennas and Propagation (ISAP 2009) Student Paper Award, Oct. 2009.

3. Daisuke Uchida, Junichi Ohno, and Hiroyuki Arai, International Conference on Applications of Electromagnetism and Student Innovation Competition Awards (AEM2C 2010) Best Paper Awards/The Third Prize Award, Aug. 2010.

4. Daisuke Uchida, Young Engineer Award from Technical Committee on Antennas and Propagation, 2011.